Soil Liquefaction around Offshore Pile Foundations – Scale Model Investigations

Dissertation

submitted to and approved by the

Faculty of Architecture, Civil Engineering and Environmental Sciences
University of Braunschweig – Institute of Technology

and the

Faculty of Engineering
University of Florence

in candidacy for the degree of a
Doktor-Ingenieur (Dr.-Ing.) /
Dottore di Ricerca in Risk Management on the Built Environment *)

by
Katharina Kluge
from Mainz, Germany

Submitted on	10 October 2007
Oral examination on	23 November 2007
Professorial advisors	Prof. Joachim Stahlmann
	Prof. Teresa Crespellani
	Prof. Giovanni Vannucchi

2008

*) Either the German or the Italian form of the title may be used.

The dissertation is published in an electronic form by
the Braunschweig university library at the address

http://www.biblio.tu-bs.de/ediss/data

To my parents, to my sister and to Robert

Acknowledgements

The present work was performed from 2003 to 2007, during my time as a member of the International Research Training Group "Risk Management of Natural and Civilization Hazards on Buildings and Infrastructure" at the Institut für Grundbau und Bodenmechanik of the Technical University of Braunschweig (Germany) and the Dipartimento di Ingegneria Civile of the University of Florence (Italy). I gratefully acknowledge the financial support provided by the Deutsche Forschungsgemeinschaft.

I would like to thank my tutors Professor J. Stahlmann, Professor T. Crespellani and Professor G. Vannucchi for the supervision of my research and for their constant support and advice. Furthermore, I want to thank Professor H. Oumeraci for being my examiner. I am most grateful to all of them for the interesting discussions, for the review of this dissertation and for their helpful remarks and suggestions – and, to my Italian tutors, for the nice welcome in Italy. In addition, I want to thank Dr. L. te Kamp of the Itasca Consulting Group for his help and the efficient advice he kindly gave me and for the time he hosted me at his company and Professor H. Antes for being the chairman of the board of examiners for the defence of my thesis.

At the centre of this work were the experimental test series. I still remember the first drawings of the test model set-up, the truck that delivered the tons of sand, the long hours we spent setting up everything and, of course, the many hours of shovelling sand… This would really not have been possible without the support of many helpers. Regarding the set-up and the maintenance of the test model, the precise work of our technical assistant Eckhard Feistel is deeply acknowledged; he developed and constructed the most important parts of the test model. Furthermore, I am very grateful to the technical assistants Mr. Lehmann, Mr. Neumann, Mr. Appeltauer and Mr. Kvapil of the Leichtweiß Institut für Wasserbau (LWI), who helped me in numerous situations in the experiment hall of the LWI and always contributed to a friendly atmosphere in this huge hall. I further thank Dr. Jörg Gattermann and Christian Kuhn who showed me how to handle measurement devices and data acquisition. And I thank Dr. Matthias Rosenberg and Uwe Zeemann for their support and ideas in the laboratory when carrying out various preliminary tests. However, the hardest work was done by the students that worked with me on this project: They spent hours and hours shovelling tons of sand! Besides this strenuous work, they often supplied valuable ideas and made many other contributions that helped advance my work. Jonas Hensel, Jakob Klassen, Mike Bohne, Genia Schäferhoff, Manfred Rimann, Antje Reinke, Stefan Maretzki, Jan Fischer, Kerstin Jahn, Hauke Sychla: thank you very much for your great help.

Apart from professional experience, I personally gained a lot from those four years' work: I feel very fortunate to have been a member of this international graduate course, since one of the most important experiences for me during those years was the international environment, i.e., the research stay at the University of Florence and the months I spent in Italy. I feel fortunate to have participated in this Italo-German research group, to have so many good memories of the various meetings in Florence and Braunschweig and to have met and made friends with my Italian and German colleagues. Therefore, I am grateful to Professor U. Peil and Professor C. Borri, who are the coordinators of this program.

To all of you: Danke. Thank you. Grazie. Katharina Kluge

Abstract

The present research work aims at investigating the pore pressure in the soil around offshore pile foundations when those structures are subject to wave-induced lateral loading. The understanding of the behaviour of the pore pressure in the soil is very important since the risk of soil liquefaction is self-evident for offshore structures. Even though many pile structures for the wind industry are going to be built offshore in the near future, experience concerning the probability of occurrence of soil liquefaction around dynamically loaded pile foundations is missing so far and the influencing factors are not well understood yet. It is the objective of this work to reduce this geotechnical uncertainty by means of experimental and numerical investigations and to analyse the influence of the structure's deflection and of the loading frequency on the pore pressure generation in the soil.

In the first part of the present work, the offshore wind energy structures are presented and the important facts concerning those structures are supplied. The phenomenon of soil liquefaction and its consequences is treated and the criterion for the initiation of liquefaction is discussed. An extra chapter attends to the liquefaction-inducing factors offshore. Apart from seismic excitations, those are the direct action of water waves on the subsoil and the wave-induced movement of offshore structures. Since the latter is only poorly examined and understood until now, this research focuses on the so-defined deflection-induced liquefaction with the objective to clarify the interrelations and processes going on in the soil during cyclic loading.

The second part focuses on the description of the experimental approach to analyse the pore pressure besides offshore pile foundations. Those test series represent the first investigations of their kind and are regarded as first step towards the ambitious aim to assess the risk of soil liquefaction around offshore pile foundations. Since the main indicator for liquefaction is the pore pressure, this parameter was measured and analysed in the test series. Furthermore, data were recorded for the deflection of the pile during loading. A detailed analysis of the measurement data obtained in the test series represents the central part of this thesis work. Doing so, particular emphasis is put on the likelihood of soil liquefaction due to the horizontal deflection of the pile structure. For this purpose, data from approximately 40 test series at four measurement levels are taken into account. Soil liquefaction is observed in most of the tests series. It is shown that the pore pressure strongly depends on the deflection of the structure and on the loading frequency, but also on the depth under ground surface and on the horizontal distance from the test pile.

The last part of the thesis covers the numerical simulation of the test series which were carried out with the finite-difference program FLAC. It is shown that deflection-induced pore pressure accumulation can be simulated and that this simulation is in good agreement with the results of the test series. The results of this research work supply important information on the behaviour of pore pressure near cyclically loaded pile structures and provide a sound basis for the estimation of the susceptibility of the soil to liquefaction.

Kurzfassung

Die vorliegende Arbeit hat zum Ziel, den Porenwasserdruck im Gründungsbereich von zyklisch belasteten Offshore-Pfahlgründungen zu untersuchen. Das Verständnis des Porenwasserdruckverhaltens ist sehr wichtig, da das Risiko von Bodenverflüssigung im Offshore-Bereich offensichtlich ist. Obwohl in naher Zukunft viele Pfahlstrukturen für die Windindustrie im Offshore-Bereich errichtet werden sollen, fehlen derzeit noch Erfahrungen zur Auftretenswahrscheinlichkeit von Bodenverflüssigung im Bereich dynamisch belasteter Pfahlgründungen und zu deren beeinflussenden Faktoren. Ziel dieser Arbeit ist es daher, diese geotechnische Unsicherheit mit Hilfe von experimentellen und numerischen Untersuchungen zu reduzieren und die Abhängigkeit der Porenwasserdruckentwicklung von der Strukturbewegung und der Belastungsfrequenz zu analysieren.

Im ersten Teil dieser Arbeit werden die Offshore-Strukturen der Windindustrie und die ihnen zugrunde liegenden, wichtigen Informationen vorgestellt. Das Phänomen der Bodenverflüssigung, deren Konsequenzen sowie das Kriterium für den Beginn der Verflüssigung werden diskutiert. Ein eigenes Kapitel nimmt sich der Faktoren an, die Verflüssigung im Offshore-Bereich hervorrufen. Neben seismischer Belastung sind das die direkte Belastung von Wellen und die welleninduzierte Bewegung der Strukturen selbst. Da letztere bisher kaum untersucht wurde, fokussiert diese Arbeit auf die so genannte verschiebungsinduzierte Verflüssigung mit dem Ziel, die Zusammenhänge und Prozesse im Boden während der zyklischen Belastung zu klären.

Der zweite Teil konzentriert sich auf die in der Arbeit gewählte Methode, den Porenwasserdruck im Gründungsbereich von Offshore-Pfählen experimentell zu analysieren. Diese Versuche stellen die ersten ihrer Art dar und werden als erster Schritt in Richtung des ambitionierten Ziels angesehen, das Risikos von Bodenverflüssigung bei Offshore-Pfahlgründungen zu bewerten. Da der Porenwasserdruck der Hauptindikator für Bodenverflüssigung ist, wurde dieser Parameter sowie die Pfahlverschiebung in den Modellversuchen gemessen. Im Zentrum dieser Arbeit steht die eingehende Analyse der gewonnenen Messdaten. Dabei wird das Hauptaugenmerk auf die Auftretenswahrscheinlichkeit von verschiebungsinduzierter Bodenverflüssigung gelegt. Für die Auswertung wurden Messdaten von ca. 40 Modellversuchen in vier Messebenen berücksichtigt. Bodenverflüssigung wurde in den meisten Tests beobachtet. Es wird gezeigt, dass der Porenwasserdruck stark von der Pfahlauslenkung und der Belastungsfrequenz, aber auch von der Tiefe unter GOK und dem horizontalen Abstand zum Testpfahl abhängt.

Der letzte Teil der Arbeit beinhaltet die mit dem Programm FLAC durchgeführten numerischen Simulationen der Modellversuche. Es wird gezeigt, dass die verschiebungsinduzierte Porenwasserdruckakkumulation simuliert werden kann und dass diese Simulation gut mit den in den Modellversuchen gemessenen Porenwasserdrücken übereinstimmt. Die Ergebnisse der Arbeit liefern wichtige Erkenntnisse über das Verhalten des Porenwasserdrucks im Bereich zyklisch belasteter Pfahlstrukturen und zur Bewertung der Anfälligkeit des Bodens für Verflüssigung.

Table of contents

1 Introduction

Soil liquefaction is a phenomenon which can occur in saturated sand when this sand is excited by dynamic loading. It initially causes the soil to loose its shear strength and to develop a liquid-like behaviour. Later, when the resulting excess pore water has drained, the soil structure transforms into a denser packing. When buildings or infrastructural devices are founded in liquefaction-prone areas, a risk for those structures and for the human beings using those structures arises from this phenomenon. Liquefaction and its severe consequences are known at least since the strong earthquakes in Asia and in Alaska in the 1960s. One of the damages caused by seismically induced liquefaction in Niigata in 1964 is shown in Fig. 1-1.

Since then, the triggering events causing liquefaction and the processes occurring during liquefaction were studied by many researchers. The objective is to be able to predict the occurrence of soil liquefaction and to find remedial measures against it. In the last years, the question arose whether soil liquefaction can also occur around offshore structures, not caused by an earthquake loading, but as a consequence of the dynamics during the operation of the structures. Up to now, experience in this field is still missing and, therefore, research is necessary which is focused on this question. The present work aims at analysing the probability of occurrence of soil liquefaction due to the cyclic deflection of offshore pile structures by means of experimental and numerical investigations.

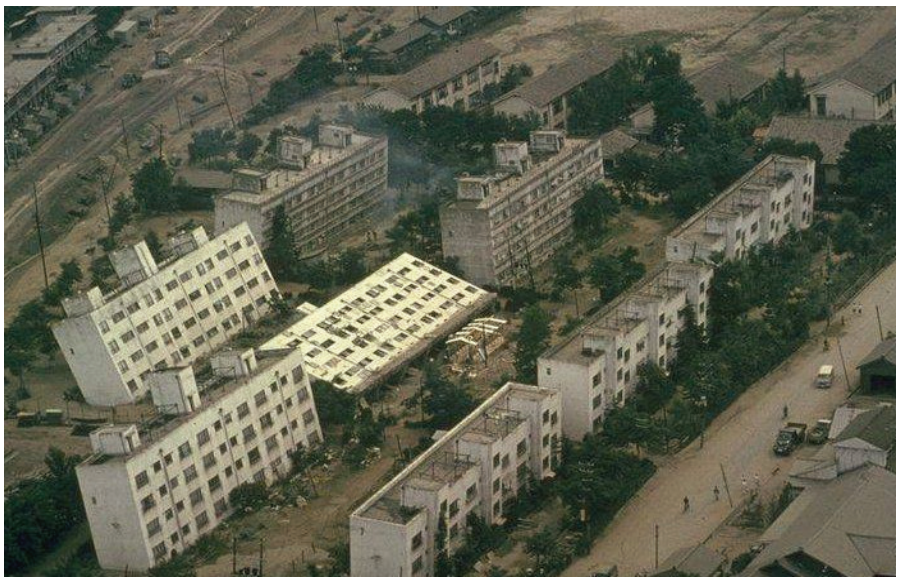

Fig. 1-1: Consequences of soil liquefaction on buildings and infrastructure in Niigata (UW (2000)).

1.1 Motivation

Some years ago, national and international regulations concerning climate protection purposes came into effect. Those regulations aim at increasing the percentage of energy production from renewable resources. A large fraction of the renewable energy production already comes from wind energy. Since the wind resources offshore are a multiple higher than on land, the potential for increased energy production offshore is regarded as very good. Another advantage offshore is the sufficient space available for installing large wind farms. In addition, from the population's point of view, the impact those offshore structures have on the landscape is minor as compared to onshore windmills.

For the wind turbines planned offshore, the monopile is a common foundation option. When waves hit the monopile, a deflection described by its amplitude and frequency is caused. This cyclic deflection leads to a rearrangement of the soil particles besides the foundation which, in turn, induces pore pressure changes in the soil. From the geotechnical point of view, the embedding of the pile in the soil under those cyclic horizontal loadings is a very important topic since the risk of soil liquefaction in offshore locations is self-evident. If the cyclic deflections of a pile cause a progressive increase in pore pressure, the soil stiffness adjacent to the pile is degraded and leads to reduced lateral restraint. The consequences of reduced lateral restraint of a monopile foundation are obvious: The structure can tilt and reach its serviceability or ultimate limit state. For the approval of offshore wind parks, according to BSH (2007), the stability of the seabed has to be proofed including the consideration of the degradation of the mechanical properties of the soil due to pore pressure accumulation and soil liquefaction. It has to be shown that either those mechanisms do not occur, that they are sufficiently considered in the design, or that they are sufficiently observed during construction and operation and, if necessary, compensated by additional measures.

Nevertheless, knowledge about pore pressure accumulation and soil liquefaction besides dynamically loaded pile foundations is not available at present since the realisation of offshore wind energy farms is only starting right now (see Fig. 2-1). Apart from that, the transfer of knowledge from laboratory tests for seismically induced liquefaction is only possible to a limited degree. Thus, it becomes evident that this gap in knowledge has to be closed. Since the generation of pore pressure is the trigger of soil liquefaction, it is important to analyse the pore pressure changes in the soil near dynamically loaded pile foundations. One possibility to do this is by measuring the pore pressure changes besides real structures, e.g., in the North Sea. Nevertheless, limit states cannot be considered in this way. Therefore, this research analyses the behaviour of the pore pressure by scaling down the structure to a test model and by analysing the pore pressure within different test series. Thus, the present investigation aims at reducing the uncertainty about soil liquefaction by increasing the understanding of the physical processes that take place in the soil during cyclic loading of monopile foundations and by revealing dependencies of the pore pressure on its inducing factors.

1.2 Placement within the framework of risk

The risk R is generally defined by the convolution integral of the probability of occurrence P_O of an uncertain event and the expected value of the damage $E(D)$ this event would have:

$$R = P_O \cdot E(D) . \tag{1-1}$$

Hence, risk is usually expressed in monetary units per year, say [€ / year]. The events that cause damages to the structures are the hazards. According to the MARINE SAFETY AGENCY (1993), a hazard is defined as "a physical situation with potential for human injury, damage to property, damage to the environment or some combination". In the present work, the hazard consists in the waves that load the structures in the offshore environment. The waves induce a cyclic deflection of the structures. This deflection, in turn, may result in pore pressure increases in the soil besides the structure and, as a consequence, in soil liquefaction.

Soil liquefaction, first of all, leads to a degradation of the resistance of the soil adjacent to the structure under consideration. As a consequence, it can also cause damages to the structure itself. Potential damages of an offshore pile structure can be its tilting or collapse. Expenses for the repair or for the replacement of parts of the structure cause economic losses. Those costs are an order of magnitude higher in the offshore environment than for onshore structures since the weather conditions and the water around the structures complicate the access to them. To fix damages of the foundation, special ships as well as divers may be necessary. In addition, the operation of wind turbines has to be interrupted when failure on the foundation occurs. This breakdown can also be evaluated monetarily. Furthermore, losses can result in indirect losses, e.g., in image losses. Since damages on offshore structures can be very severe, the present research work aims at supplying basic information that allow reducing the probability of occurrence of certain damages, namely damages due to soil liquefaction.

1.3 Methodology of research

In summary, it is the aim of the present research work to investigate and analyse the behaviour of the pore pressure in the soil around offshore pile foundations when those structures are subject to wave-induced lateral loading. The main contribution of the present research are experiments on a test pile. In the test series, the pore pressure generated in the soil due to the cyclic deflection of the pile is analysed. The test series carried out within this research represent the first investigations of their kind and, therefore, supply for the first time basic and primary information on those important issues. In this way, the geotechnical uncertainties concerning the foundation of cyclically loaded offshore structures can be reduced in terms of an extended understanding of the behaviour of pore pressure.

Fig. 1-2 shows how the present thesis work is structured. After the introduction presented in this chapter, the basic facts concerning the offshore structures under consideration are supplied in Chapter 2. This information is important in order to understand the differences between those structures and the already existing ones in the offshore environment and to understand why experience is lacking in this field. Furthermore, the properties and conditions have to be defined that will be transferred from in situ locations to the test model. Thus, this chapter provides the basis for understanding the design of the test model.

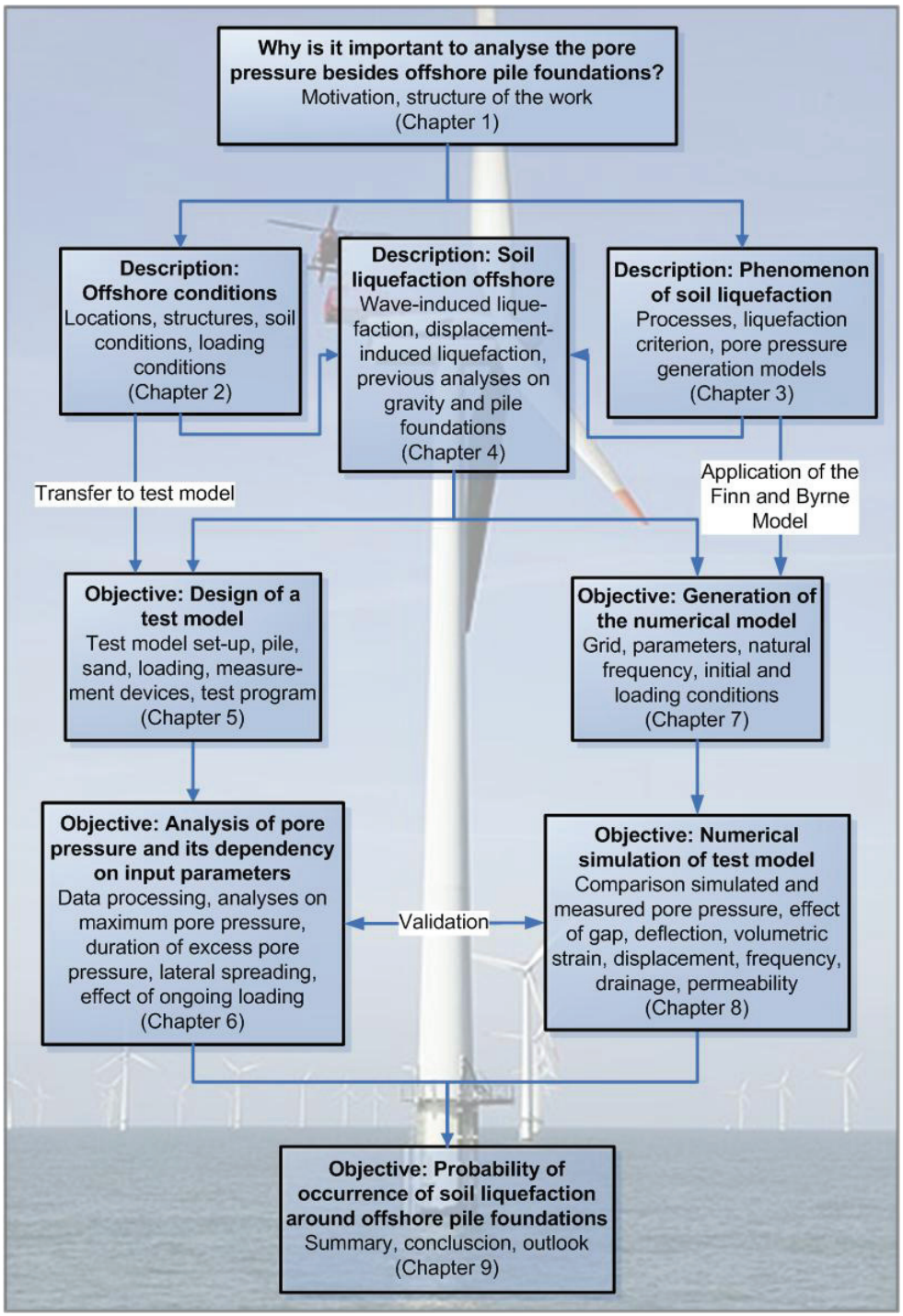

Fig. 1-2: Structure of the present research.

An extensive literature review is given in Chapter 3 with respect to the behaviour of the pore pressure in the soil when the soil is dynamically loaded. The stress-strain behaviour of dynamically loaded soils is described and three different models are presented which account for the pore pressure generation due to that loading. The so-called Finn and Byrne Model is discussed in detail since it is adopted for the numerical calculations carried out within this investigation.

Most of the research dealing with liquefaction concerns earthquake-induced loading but this is not the inducing factor analysed in this research. Therefore, Chapter 4 addresses soil liquefaction in the offshore environment. The two main factors inducing liquefaction around structures

in the offshore environment, i.e., the waves and the structures themselves, are described in this chapter. In addition, earlier analyses and studies on gravity and pile foundations are reviewed.

As already stated, experience on real structures is missing at the moment. In the last few years, test fields were installed, e.g., in the North Sea (see STAHLMANN et al. (2007)) in order to gain experience on the behaviour of real structures in the actual environment. But as consequence of costs, it will certainly never be possible to simulate the reaction of wind turbines under extreme conditions in those test fields, i.e., to study their limit states. Therefore, test models have to be realised. Such a test model was designed within the present work and is presented in detail in Chapter 5. Since the main indicator for liquefaction is the pore pressure in the soil, this parameter was measured and analysed in the test series. Therefore, a fictive but realistic offshore structure was scaled down following the similarity laws. Furthermore, the chapter describes the realisation of the test model, the emplacement of the model sand which was followed with special caution, the installed measurement devices and the data acquisition, the procedure during the test series as well as the test program.

Chapter 6 treats the analysis of the measured data with particular emphasis on the risk of soil liquefaction due to the load-induced deflection of the foundation. Those data cover the pore pressure in the soil near the pile and the deflection of the pile at two vertical positions. In order to allow different analyses, the pore pressure is split in a low- and a high-frequency part. The dependency of the pore pressure changes in the soil on the input parameters of the tests is revealed by means of the maximum pore pressure, the duration of an excess pore pressure, the amplitude of the transient pore pressure and by the correlation between displacement and pore pressure signals which were determined for all test series. In addition, the vertical as well as the horizontal spreading of excess pore pressure is examined and the effect of ongoing loading versus an interruption of loading. The applicability of the results gained from those test series and the probability of occurrence of soil liquefaction at in situ locations is discussed by means of the results of selected test series.

Chapter 7 introduces to the numerical simulation of the test series carried out within this research. After supplying basic information on the finite difference method and on the generation of the numerical model, the needed parameters of the analysis as well as the initial and loading conditions of the system are described. Further, the natural frequency of the system is determined.

Chapter 8 covers the numerical simulations carried out within this research. The calculated pore pressure during the phases of accumulation and dissipation is compared to the measured pore pressure of the test series. Furthermore, the dependency of the pore pressure on the deflection of the pile and on the volumetric strain is analysed as well as the effect of variation of input parameters and drainage. The results of the simulations are discussed and evaluated.

Chapter 9 summarises the results gained from the experimental as well as from the numerical investigations carried out within this research work. Conclusions on those results are drawn and recommendations for future research topics and improvements for both models are supplied.

The appendix covers the graphical representation of results of the test series.

2 Offshore structures of the wind energy industry

The structures that were built in the North Sea during the last decades were mainly structures of the oil and gas industry, i.e., storage tanks or oil production platforms. Those structures differ from the structures that have to be built for the wind power industry. Firstly, the structures serve different purposes. Therefore, they are differently designed, i.e., the structures themselves are different. Since wind turbines explicitly try to exploit all wind resources for their energy production, their ratio of horizontal to vertical forces is much higher than the one of the structures of the oil and gas industry. Secondly, the structures will be built in different locations and, thus, will face different environmental conditions. Until now, wind farms have only been built in areas near to the shore. Thus currently, experience from offshore locations for the wind industry is lacking. This chapter provides information concerning offshore structures of the wind energy industry which are important for the understanding of the approaches undertaken within this research work.

2.1 Political situation

In 1997, more than 160 nations signed the Kyoto Protocol. With their signature, they committed to reduce their greenhouse gas emissions for climate protection reasons. Depending on the economic development of those countries, different requirements have to be fulfilled. For example, the European Union has to reduce its emissions by a total of 8 % until 2008-2012, Germany committed to reduce its emissions by 21 % and Italy by 6.5 %. The agreement became effective in 2005.

Human activity influences the greenhouse emissions mainly by the release of carbon dioxide. According to BMU (2006, a), the largest producer of carbon dioxide emissions is the energy industry, followed by traffic, small consumers and private households. Therefore, the European Union focused on the energy industry by formulating the Directive 2001/77/EC in order to promote electricity produced from renewable energy resources (wind energy, water energy, solar energy, geothermal energy, etc.) and set differentiated bench marks for the member states. Under this Directive, the member states set up individual, national targets and chose their support mechanism.

In 2000, Germany formulated the Renewable Energy Sources Act (EEG) which is a feed-in tariff system. An amendment became effective on August 1st, 2004 (BMU (2004)). The EEG claims that the share of renewable energies on the over-all electricity consumption in Germany

should be 2010 at least doubled as compared to 2000. This equals to 12.5 % of the total power supply. A fraction of 20 % is targeted until 2020.

In contrast, Italy is one of the few countries that chose a system of tradable green certificates with binding targets as instrument to promote renewable energies (COM (2005)). The share of renewable energies on the over-all electricity consumption is targeted to 25 % by the year of 2010, thus twice as high as the target for Germany is. The green certificate system in Italy became effective in 2001.

Whereas up to now, the wind energy sector in Italy is of rather minor importance compared to, e.g., the hydropower sector, the largest part of the renewable energy produced in Germany came from the wind energy sector in 2005, namely 42.4 % (BMU (2006, b)). Regarding the installed wind power capacity, Germany is the current market-leader in the European Union. As can be seen in Table 2-1, its installed wind capacity has been 20,622 MW by the end of the year 2006 which is more than the total installed capacity of the following five European countries altogether. In Italy, wind turbines with a capacity of 2,123 MW had been installed by the end of 2006. Nevertheless, it has to be highlighted that the numbers given in Table 2-1 mainly reflect onshore wind energy plants since there are only very few farms realised offshore until now. Thus, the wind capacity in both countries will increase significantly in the next years with the beginning of the installation of offshore wind parks.

Table 2-1: Installed wind capacity of the six leading countries in Europe, end 2006 (EWEA (2006)).

Countries	Installed wind capacity [MW]
Germany	20622
Spain	11615
Denmark	3136
Italy	2123
UK	1963
Portugal	1716

According to the prognosis of BMU (2006, c), the fraction of the wind energy production on the total production of renewable energy in Germany will reach about 50 % in the year 2010. Whereas the activities in onshore wind energy production will stabilize after this year, the offshore wind industry will significantly increase from then on.

In Fig. 2-1, the forecasted expansion of the offshore wind energy until the year 2020 is shown. The bars represent the annual growth; the cumulative capacity of offshore wind energy is marked by the line. As can be seen, the installation of offshore wind turbines will start only in the present year and will increase significantly in the following years. Cautiously optimistic scenarios predict a cumulative installed output capacity of up to 12,000 MW in the year 2020. Thus, those prognoses point out the need for profound research in all fields connected to those offshore structures.

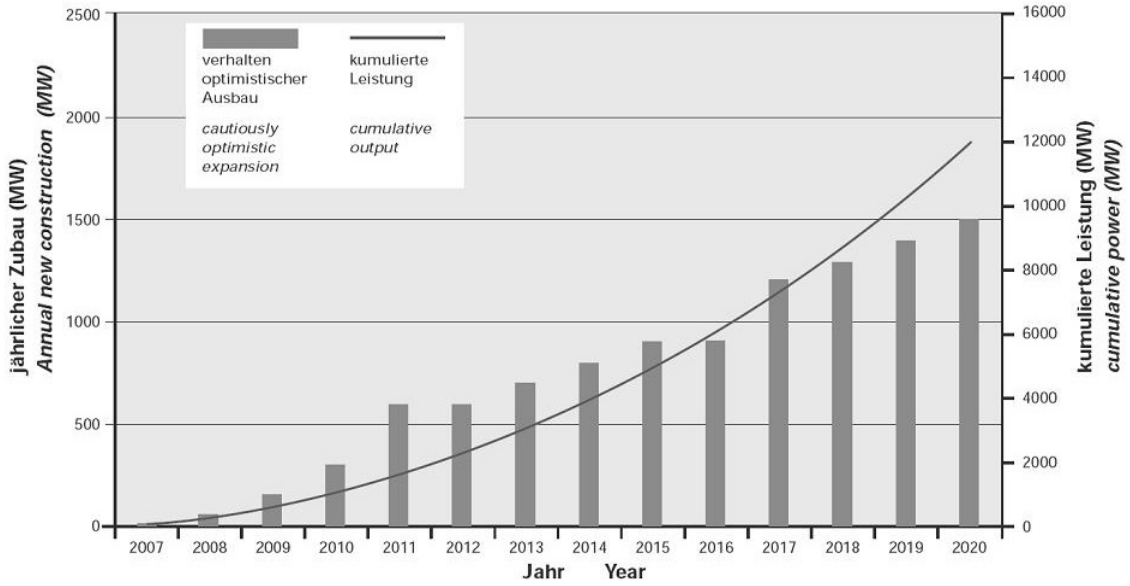

Fig. 2-1: Forecasted expansion of the capacity of the offshore wind power in Germany (BMU 2007).

2.2 Locations

Directly after its coming into effect, the regulations of the EEG triggered a high number of applications for the certification of wind farms in the North and Baltic Sea. Until beginning of 2007, almost 40 wind farms were licensed. The requirements those wind farms have to fulfil for their certification are very high. They concern, for example, the warranty of the safety and of the passage of shipping and air traffic, the correct placement of power cables or the conservation of the marine environment. Until now, fourteen wind farms have been certified in the North Sea and two wind farms in the Baltic Sea. Due to restrictions caused by the German Wadden Sea National Park and by the routing of shipping channels, the wind farms in Germany have to be constructed at a substantial distance from the coast. Therefore, they will be constructed in the so-called Exclusive Economic Zone (EEZ, up to 200 nautical miles off the German coast) beyond the territorial waters (up to 12 nautical miles off the German coast). The area in the North Sea in which the wind farms will be installed is shown in Fig. 2-2.

Those locations are 30 to 130 km away from the coast line and, therefore, the wind farms will be situated in regions with very rough environmental conditions. As can be seen in Fig. 2-2, the water depths in those areas range from 10 to 60 m. Hence, compared to the projects already realised abroad (1 to 20 km away from the coast line and water depths between 2 and 20 m), the requirements on the German facilities are higher. Furthermore, the turbines planned for the future will have power outputs up to 5 MW whereas until now the largest turbines offshore have a power output of 3.6 MW at most.

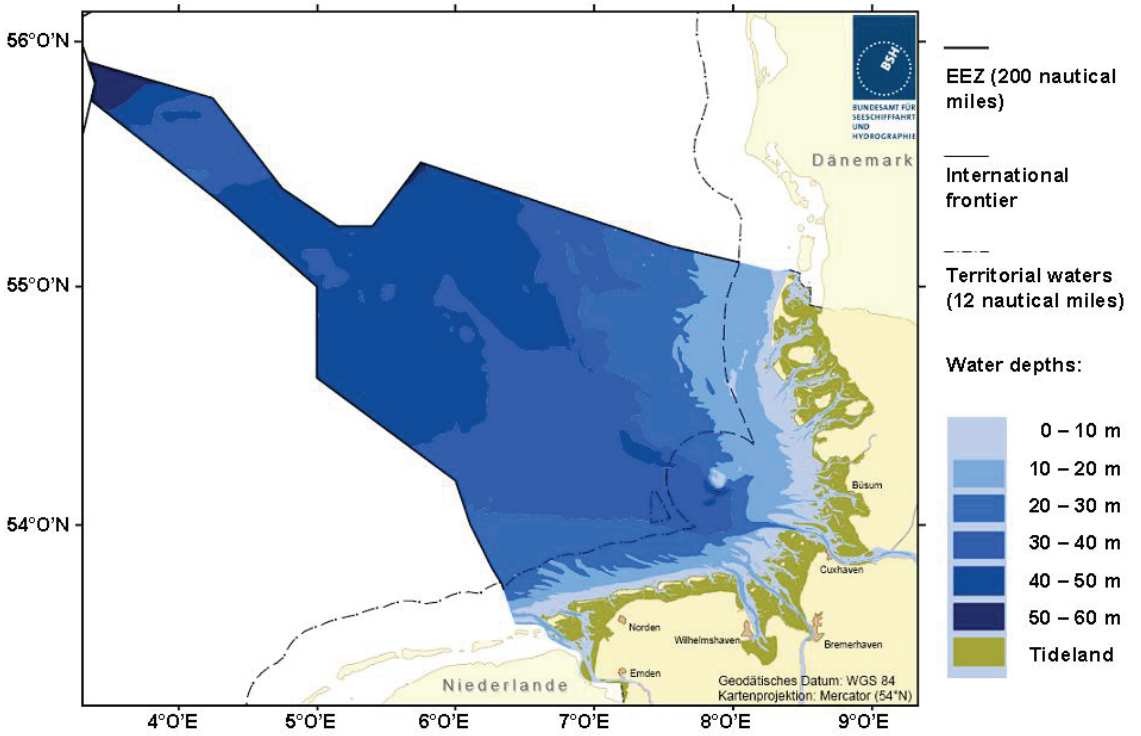

Fig. 2-2: Map of the German coast at the North Sea with indication of the Exclusive Economic Zone (EEZ) where the German offshore wind farms will be constructed. The water depths are indicated by different blue colours (after BSH (2006)).

2.3 Structures

The installation of offshore wind farms demands for foundations for which experience does not exist neither from the oil and gas industry (different structures and water depths of about 300 m) nor from near-shore structures (same structures but water depths around 5 m). Offshore structures are structures with a very high level of difficulty. According to DIN 1054 (2005), their foundations are classified in the geotechnical category 3 which covers structures with high geotechnical risk. The common foundation forms which are discussed for the structures of the wind energy industry in the North Sea are represented in Fig. 2-3. The monopile shown in (a), which is subject of the research undertaken within the present work, consists of only one single pile that is embedded in the soil. Thus, it is a very simple form with low material costs. Until now, pile diameters up to 5 m are technically feasible in terms of pile driving techniques (QUAST (2003)). Experience lacks for larger diameters and it is not known how cyclic loads affect the embedding of the pile. Common alternatives to the monopile foundation are gravity foundations, tripod or jacket foundations as shown in Fig. 2-3 (b), (c) and (d), respectively. Since those structures have often been described in literature, they will not be discussed here. Further details on those different foundation types can be found, for example, in LESNY et al. (2002) or in MITZLAFF and UECKER (2002).

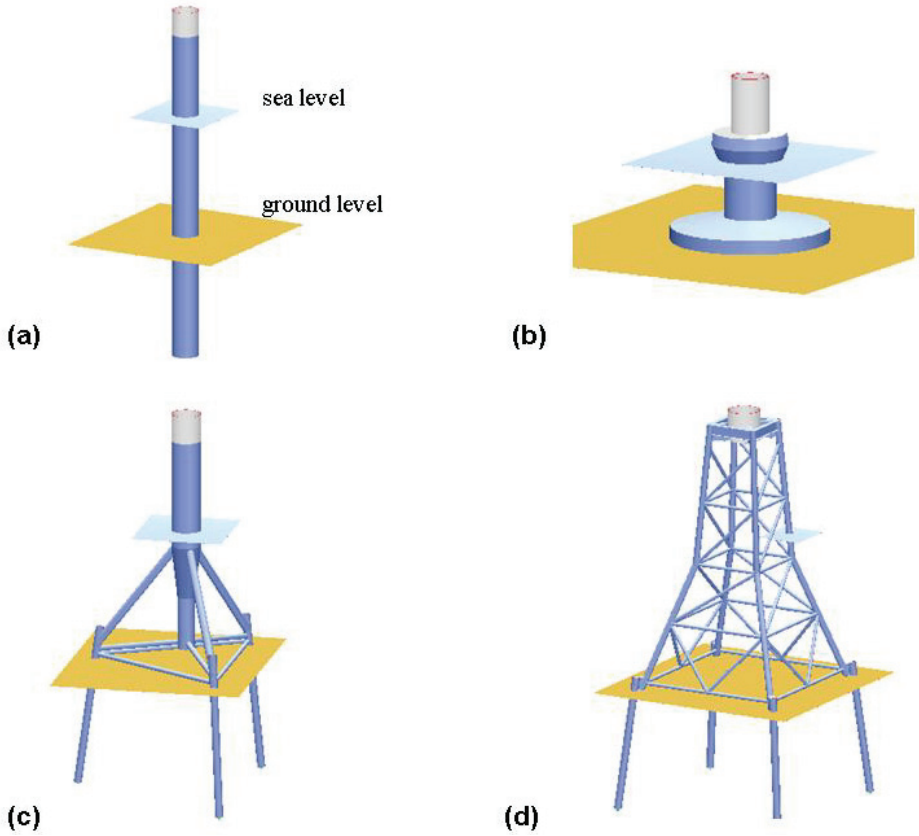

Fig. 2-3: Designs of foundation for offshore wind turbines. (a) Monopile foundation, (b) gravity foundation, (c) tripod foundation, (d) jacket foundation (after MITZLAFF and UECKER (2002)).

2.4 Soil conditions

The geology of Northern Germany and, therefore, also of the North and the Baltic Sea, is mainly characterized by diluvial sediments from the Pleistocene and by alluvial sediments from the Holocene. Both those sediments belong to the Quaternary Period. For the locations of the wind farms, it is sufficient to regard that Quaternary Period since the sediments from elder periods are in depths far under the foundations of the offshore structures. The Pleistocene, which began 1,800,000 years ago, was affected by different glacial periods. Thus, ice plates up to several hundred metres covered the landscape and lead to sediments with a very dense packing and with a high over-consolidation rate, respectively. Therefore, they are appropriate to found structures on. In contrast, when the ice melt and the Holocene began, which started about 11,500 years ago and lasts until today, the particles that sedimented above the Pleistocene materials were mainly of organic nature. Thus, they have a loose to middle dense packing. On average, the Holocene layers have a thickness of 10 to 20 m and the bearing strength of those soils is less strong. This can lead to problems in the North Sea since this region is crossed by deep subglacial valleys (up to several hundred meters) that were eroded and formed by the melting water of warm periods during the Pleistocene. Later, they were filled with looser Holocene materials. This can lead to problems for the foundations of offshore structures since the refilled valleys are not visible from the surface. For this reason, it is essential to know the position of those channels when installing structures offshore. In addition, erratic blocks in the soil with diameters of several meters can complicate the foundation, especially for the case of monopile foundations. Therefore, a careful ground survey is a very important task in order to warranty a bearing soil and uncomplicated foundation works.

The succession of strata for a potential location of a wind farm in the North Sea can be assumed to be as exemplarily shown in Fig. 2-4. In this fictive drilling profile, the soil is composed of fine and middle sand with an upper thin layer of mud. The fine sand goes down to approximately 7 m below which lays the middle sand.

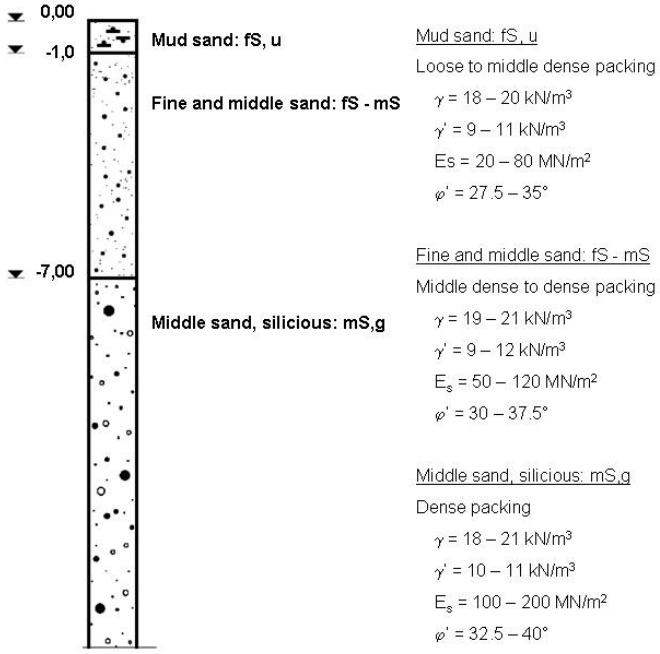

Fig. 2-4: Fictive drilling profile supplying succession of strata and mechanical properties of the soil in the North Sea (after RICHWIEN et al. (2002)).

Another important aspect is the grain size distribution of the sands in the North Sea since this is a significant property for the susceptibility of a soil for liquefaction. This phenomenon will be described in detail in the next chapter; but it should be mentioned already here that the grain size distribution of the North Sea sands given in Fig. 2-5 falls within the ranges indicating liquefaction-susceptible soil (compare Section 3.2.1). Therefore, the analysis of the behaviour of the soil in vicinity of dynamically loaded structures is all-important.

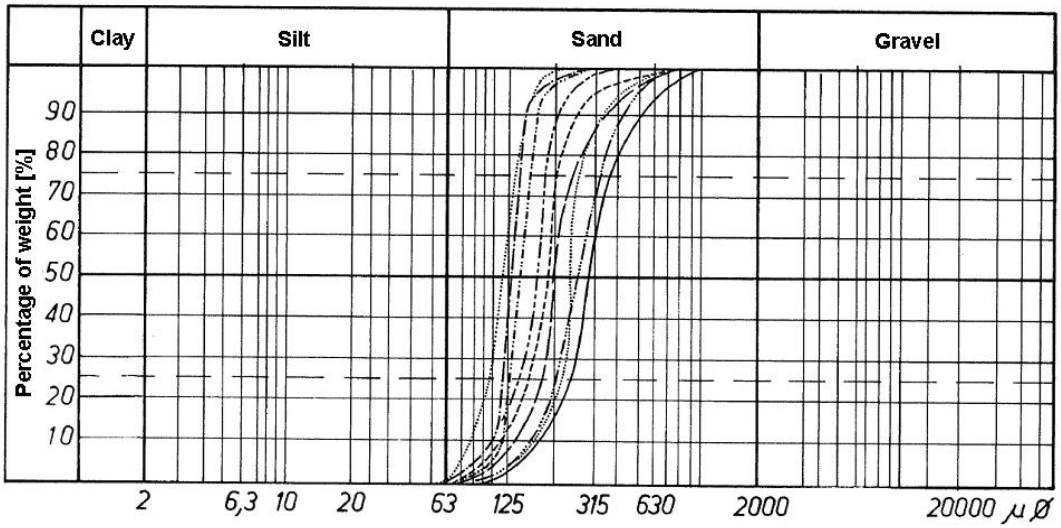

Fig. 2-5: Grain size distribution of typical Holocene sands from the North Sea (after STREIF (1990)).

Detailed information on the subsoil in the North Sea and on the therewith related field tests and laboratory tests can be found, e.g., in STREIF (1990) and in WIEMANN et al. (2002). Special requirements for the geological-geophysical and the geotechnical subsoil investigations, which have to be fulfilled within the scope of the licensing process for wind energy turbines in the North Sea, were formulated by different experts. Those required subsoil investigations are summarized by the Federal Maritime and Hydrographic Agency, in BSH (2003).

2.5 Loading conditions

The foundations of offshore structures must be designed to withstand the substantial load from the self-weight of the structures. In addition, the structures are exposed to various environmental forces including wind, waves, currents, and, for the structures in the Baltic Sea, also to ice impact. Furthermore, there are special loading conditions as earthquakes or tsunami waves. According to GERMANISCHER LLOYD (2004, b), monopile structures have to be designed such that the maximum deflection of the pile at the mud line level $u_{mud,max}$ satisfies the criterion for the serviceability limit state which is determined to

$$u_{mud,\max} = \frac{l_e}{500}, \tag{2-1}$$

in which l_e is the embedded length of the pile. For the design of offshore structures, the relevant offshore loading cases are given in design guidelines for wind turbines as, for example, in DET NORSKE VERITAS (2004) or GERMANISCHER LLOYD (2004, a). On the one hand, those loading cases describe the acting forces during normal, operational conditions which have a probability of being exceeded once a year or more often. On the other hand, the extreme loading conditions during the whole operating time of a structure have to be considered. Those conditions have a probability of being exceeded once during a certain period, for offshore structures usually during 50 or 100 years. In most cases, according to WAGNER (1990), wave loads represent the main loading condition for offshore structures. Therefore, and since the test program of the test model carried out within this research is based on wave loadings, only the wave loading will be described in the following. Information on the other loading conditions can be found in, e.g., DET NORSKE VERITAS (2004), GERMANISCHER LLOYD (2004, a) and WAGNER (1990).

2.5.1 Short-term measurements

In order to construct an offshore structure, the sea state of the location under consideration has to be analysed with respect to the probability of occurrence of certain events. Thus, the relevant occurring wave (“design wave”) and its wave parameters can be determined. Since the natural sea state is not of regular nature, but consists of a simultaneous superposition of waves with many different heights and lengths, those irregular processes can only be described by statistical functions. One approach to describe the irregular sea state is the design wave approach which defines the characteristic parameters of this sea state. Therefore, short-term measurements (20 to 30 min) are carried out in a first step during which the sea state does not change too much. The wave data of those short-term measurements can then be analysed statistically.

The mean value of all measurement values is defined as the still water level. For the determination of the wave heights, different definitions exist in literature. The zero-crossing approach is according to WAGNER (1990) a widely accepted approach. As shown in Fig. 2-6, the wave height is characterized as the distance between a wave trough and a wave crest, provided that the still water table is crossed between the trough and the crest. Hence, waves of different heights, here H_1 to H_5, and different periods, here T_1 to T_5, represent the observation period.

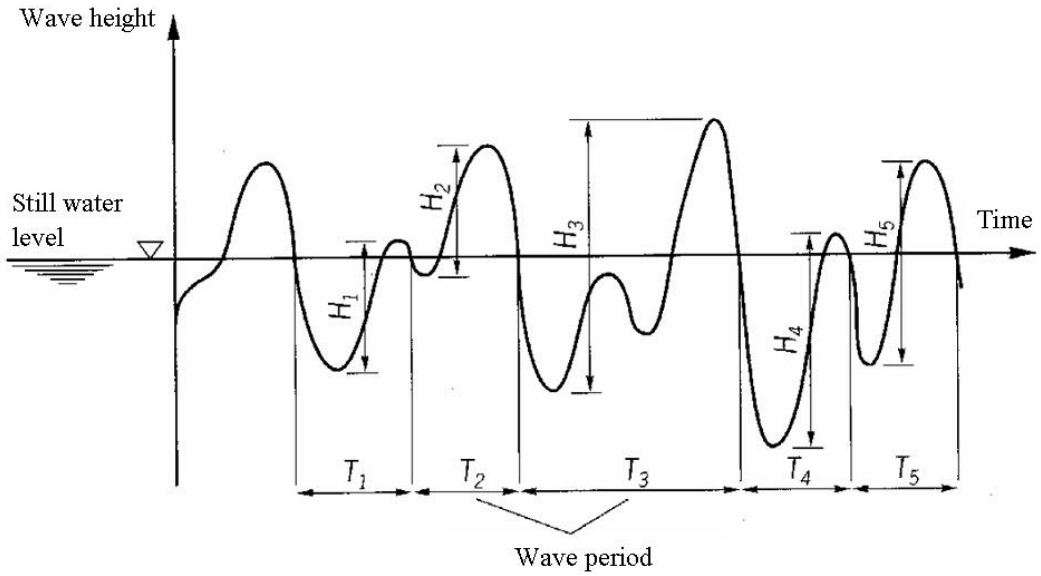

Fig. 2-6: Wave periods T_i and wave heights H_i according to the zero-crossing approach (after SCHÜTTRUMPF (1973)).

The wave design parameters from a short-term observation can be derived in the next step. First of all, the wave height H_m is the mean value of all wave heights during the measurement time under consideration. Furthermore, the mean value of the 10 % highest waves, $H_{1/10}$, or of the 1 % highest waves, $H_{1/100}$, can be determined. Special importance has the value $H_{1/3}$, the mean value of the 33 % highest waves of the observation period. It is also called the significant wave height H_s since it determines the design of offshore structures. Another important design value is the maximum wave height H_{max} of a measurement period. According to WAGNER (1990), the probability density functions of the wave heights of a short-term measurement can best be described by lognormal distributions or by the Rayleigh distribution. Those distributions result in the following relations between the wave heights:

$$H_m = 0.63 \cdot H_{1/3}, \tag{2-2}$$

$$H_{1/10} = 1.27 \cdot H_{1/3}, \tag{2-3}$$

$$H_{1/100} = 1.67 \cdot H_{1/3} \text{ and} \tag{2-4}$$

$$H_{\max} = 1.87 \cdot H_{1/3}. \tag{2-5}$$

As the name already says, short-term measurements only reflect the sea state during a short period without giving its probability of occurrence. Hence, long-term measurements are carried out additionally.

2.5.2 Long-term measurements: extreme wave

Long-term measurements consist of multiple short-term measurements repeated over a long period. According to EAU (1996), the measurements should be repeated all three or six hours. Those long-term observations provide probabilities of occurrence to the wave heights measured in the short-term measurements. Thus, they allow defining the return period of special wave events. With extrapolation techniques, the wave heights with a 50- or 100-year return period can be determined. Those data have special importance since they represent the extreme loading cases during the life time of wind turbines. The 50-year maximum wave height for different locations in the North Sea and the corresponding wave periods are shown in Fig. 2-7. As can be seen for the region of the EEZ, the maximum expected wave height with a 50-year return period is 22 to 24 m.

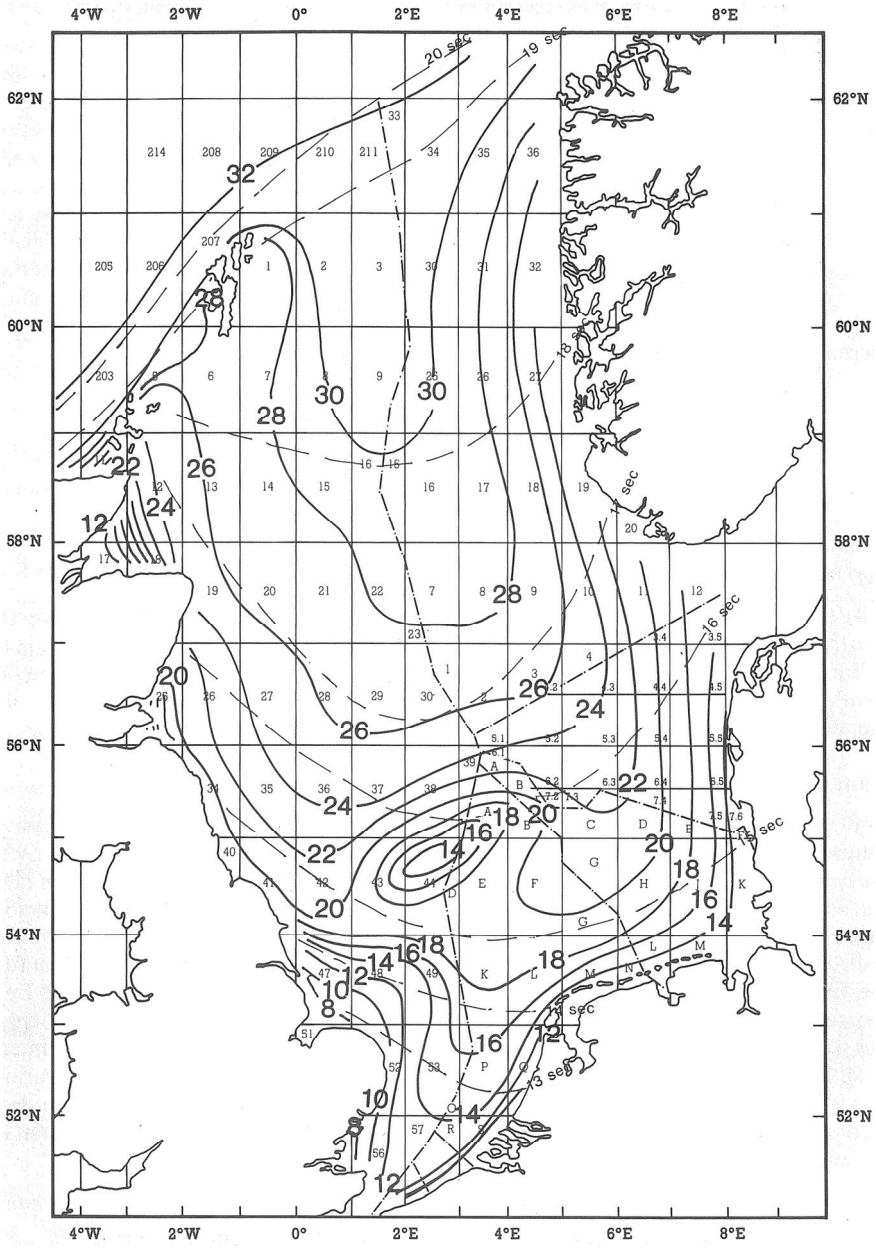

Fig. 2-7: Wave conditions in the North Sea: The solid lines represent the maximum wave height [m] with a 50-year return period; the dashed lines represent the related wave periods [s] (WAGNER (1990)).

For the location of the FINO1 research platform in the North Sea, for example, FINO (2007) gives the significant and the design wave height. At this location 45 km north of the island of Borkum with a water depth of approximately 30 m, the significant wave height with a 50-year return period is given with 7.4 m. This height was derived by means of the Weibull distribution and includes the observations of 35 years. The design wave height was derived from the long-term distribution of the significant wave height as well as from wave scatter diagrams of the site. It was determined to 15.5 m.

2.5.3 Storm profile

In order to simulate the wave conditions during a storm and to relate different wave heights and periods to their probability of occurrence during this storm, wave distributions are necessary. Since true wave distributions are often not available, storm profiles were developed for this purpose. The storm profile of NGI (1996) is generally adopted for problems in the North Sea (Fig. 2-8) and covers a storm of 42 hours. The storm profile consists of three phases. During the 18 hours build-up phase, the waves start to increase in their height from 0.5 H_s until they reach their significant wave height H_s. Then, there is a six-hour phase with stationary peak level before it the wave height decreases again during an 18 hours decay phase. Each phase consists of a certain number of waves which is also given in this figure.

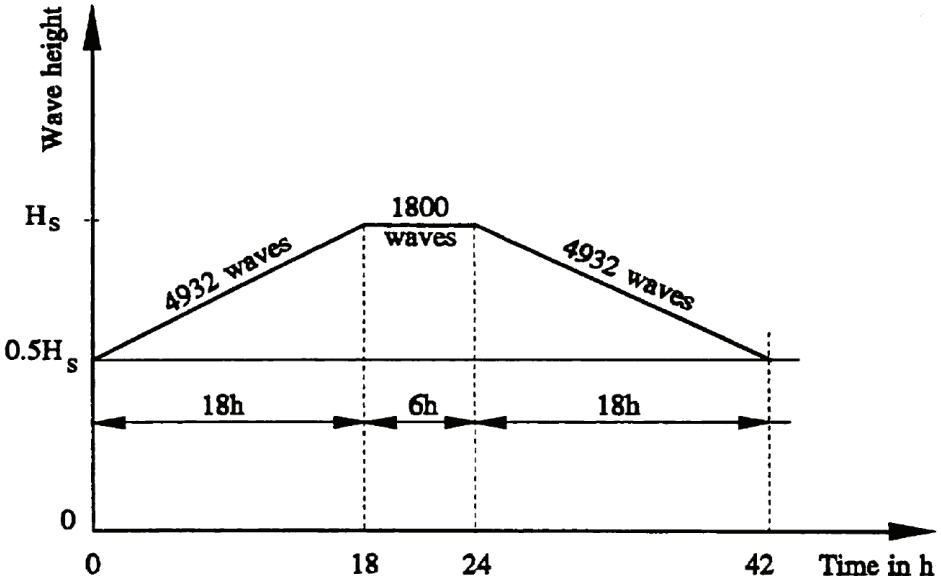

Fig. 2-8: Storm profile according to NGI (1996).

For their investigation of a pile group, REESE et al. (1988) use the more detailed storm profile given in the upper part of Fig. 2-9. It consists of seven phases. For each phase, the duration and the wave height in relation to H_s is indicated. The numbers above the columns represent the number of waves in each phase.

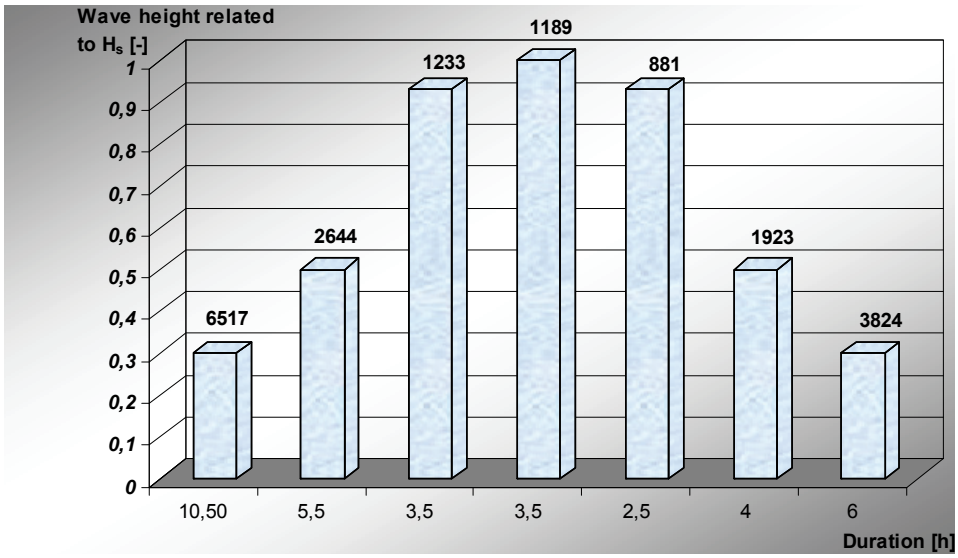

Wave height H [m]	Phase 1	Phase 2	Phase 3	Phase 4	Phase 5	Phase 6	Phase 7	T_{mean} [s]
0 - 1	968	145	20	16	14	105	553	3.2
1 - 2	2132	389	57	48	41	283	1218	4.6
2 - 3	1917	519	90	76	64	377	1095	5.6
3 - 4	1063	521	114	98	81	379	607	6.4
4 - 5	398	429	129	112	92	312	227	7.2
5 - 6	104	301	134	119	96	219	59	7.9
6 - 7	19	183	131	119	93	133	11	8.5
7 - 8	3	97	120	113	86	70	1	9.1
8 - 9		45	105	103	75	33		9.7
9 - 10		19	88	90	63	13		10.2
10 - 11		7	71	75	51	5		10.7
11 - 12		2	54	61	39	2		11.1
12 - 13		1	40	47	29			11.6
13 - 14			29	36	20			12.0
14 - 15			20	26	14			12.5
15 - 16			13	18	9			12.9
16 - 17			8	12	6			13.3
17 - 18			5	8	4			13.6
18 - 19			3	5	2			14.0
19 - 20			2	3	1			14.4
20 - 21			1	2	1			14.8
21 - 22			1	1				15.1
22 - 23				1				15.4

Fig. 2-9: Storm profile. Upper part: wave height and number of waves within the phases 1-7 shown over the duration of each phase. Lower part: Number of waves of specified height H within each phase occurring during the storm and according wave periods (following REESE et al. (1988)). See text, for the definition of the mean wave period T_{mean}.

REESE et al. (1988) choose a maximum significant wave height of H_s = 12 m and determine the probability density function *P(H)* of each wave height *H* by means of the Rayleigh equation according to

$$P(H) = \frac{4H}{(H_s)^2} e^{-2\left(\frac{H}{H_s}\right)^2} . \tag{2-6}$$

Thus, when related to the numbers of waves of each phase, the number of waves for different wave heights *H* can be determined for each phase. Those numbers are given in the lower part of the figure. As can be seen for the initial and final phase, only waves up to 8 m occur. During those phases, most of the waves have wave heights between 1 and 3 m. The wave height increases towards the climax of the storm (Phase 4) in which wave heights above 20 m are reached. The maximum wave height H_{max} = 23 m occurs once in the storm under consideration.

In order to estimate the approximate period of waves with different heights, WAGNER (1990) supplies a formula. According to this, the minimum and maximum wave period T_{min} and T_{max} can be determined from the wave heights *H* with

$$T_{\min} = \sqrt{6.5H} < T < \sqrt{15H} = T_{\max} \tag{2-7}$$

with *H* given in meters and *T* in seconds. According to this equation, the mean value $T_{mean} = (T_{min} + T_{max})/2$) was determined for wave heights of 1-23 m and is also given in Fig. 2-9.

In order to determine the hydrodynamic forces acting on the structure due to wave loading, the Morison equation can be applied. Therefore, linear and nonlinear wave theories are used. Since the test program for the test model described in Chapter 5 consists of different combinations of the amplitude and frequency of the deflection, the wave forces are not treated here. For further information on wave loadings, it is referred to, e.g., MITTENDORF (2006) and CORTE (2006).

3 Soil liquefaction: Basics and state of the art

3.1 Overview

In 1920, the term “liquefaction” firstly came up in geotechnical engineering when used by Hazen to describe the 1918 failure of Calaveras Dam in California (KRAMER (1988)). In 1936, Casagrande was the first (later followed by Castro) to start research in the field of soil liquefaction and to perform an important series of laboratory tests. Apart from his work, the literature does not show much evidence of liquefaction studies before the mid-1960s. The first event in the world where all kinds of modern infrastructure were destroyed by what came to be well known later as soil liquefaction, was the Niigata earthquake in 1964 (ISHIHARA (1993)). Slope failures occurred, failures of bridge and building foundations as well as the flotation of buried structures. Well known are the pictures from houses that were totally destroyed by tilting on their side or by sinking into the soil (see Fig. 1-1). This event as well as another severe earthquake in Alaska in the same year brought liquefaction to the attention of geotechnical engineers. Thus nowadays, liquefaction became a target of engineering concern and many researchers analyse the risk of liquefaction due to seismic loadings as, for example, it can be seen in CRESPELLANI et al. (2002).

According to CASTRO (1975), “the term liquefaction has been used to refer to a group of phenomena which have in common the development of high pore pressures in saturated sands due to static or cyclic loading under constant volume conditions.” Although this definition can be applied to a wide range of phenomena, the generation of excess pore pressure under undrained loading conditions is a hallmark of all liquefaction phenomena. Within the present research, only the cyclically induced pore pressure generation in granular soils is being covered. From the results of laboratory tests and from in situ observations during strong earthquakes, liquefaction can be distinguished into flow liquefaction and cyclic mobility. Those two phenomena mainly differ in their ratio of the static shear stress to the shear strength of the liquefied soil and are described in detail in KRAMER (1996). In situ, the severity of damage effects associated to the two phenomena during earthquakes is very different. Flow liquefaction is generally highly destructive, whereas cyclic mobility generally produces limited damages. A particular case of cyclic mobility is the so-called ‘cyclic liquefaction’ or ‘level ground liquefaction’ (compare Fig. 3-2), that occurs when the static shear stresses are zero. In the deposits, this phenomenon is characterised by some well-known and curious effects such as sand boiling or ground failures followed by large displacements.

When considering granular soils, additional stresses can be counteracted either by the grain structure of the soil or by the pore water in its voids. According to the so-called concept of effective stress introduced by TERZAGHI (1936), the total stress σ of a saturated granular soil in a probe as shown in Fig. 3-1 (a) is composed of the initial effective stress σ' which acts on the granular structure and of the neutral stress u, i.e., the pore pressure which acts on the pore fluid:

$$\sigma = \sigma' + u \,. \tag{3-1}$$

In this equation, u consists of two parts: the hydrostatic part u_h during initial steady state conditions and, possibly, the additional part Δu due to a change in loading. Since in Fig. 3-1 (a), the probe is not loaded, Δu equals to zero. If no additional stresses are considered, the total stress σ always stays constant. Hence, an increase in Δu will cause a decrease in σ'. For the probe with the height h, Eq. (3-1) can therefore be concretized to

$$\sigma = \sigma' + u_h + \Delta u = const. \,. \tag{3-2}$$

Whether stresses act on the grain structure or on the pore water, depends on the saturation of the soil and on its drainage possibilities. To explain this, the probe is regarded during loading as shown in Fig. 3-1 (b) and (c). The horizontal arrows signify a loading of, e.g., a shaking table. When the probe is loaded under drained conditions as shown in Fig. 3-1 (b), the pore water can dissipate and the volume of the grains is reduced since the grains are transferred into a denser packing. Thus, the height of the soil volume becomes h-Δh and the pore pressure does not change: $\Delta u = 0$. In contrast, when saturated soil is loaded under undrained conditions and shear deformations are possible as shown in Fig. 3-1 (c), the pore water cannot dissipate. The grains tend to be transferred into a denser packing but they are hindered by the persisting water in the voids. Therefore, the volume does not change but an excess pore pressure $\Delta u > 0$ is generated. Simultaneously, the effective stress σ' decreases to the same degree because the forces between the grains are reduced.

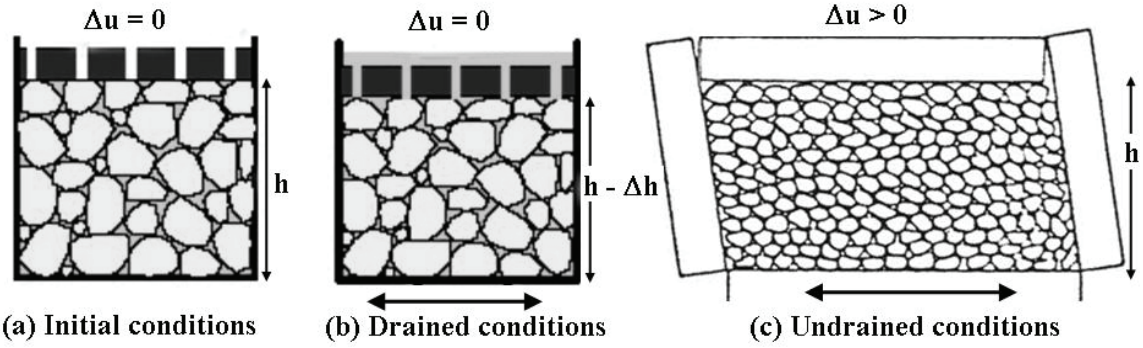

Fig. 3-1: Mechanism of change in volume and pore pressure due to dynamic loading. (a) Initial conditions, (b) drained conditions, (c) undrained conditions (after TAIEBAT (1999) and STUDER and ZIEGLER (1986), mod.).

3.2 Pore pressure generation under dynamic and cyclic loading

A rectangular element of loosely packed, contractive sand in situ may be envisaged as shown in Fig. 3-2. In the initial stress state shown in Fig. 3-2 (a), the effective overburden stress σ'_{v0} as

well as the effective lateral stress $K_0 \cdot \sigma'_{v0}$ is presented. K_0 is the coefficient of earth pressure at rest. For clarity reasons, the labelling in the figure is written besides the arrows only once but it is the same labelling for all the arrows in the same direction. During dynamic and cyclic loading, e.g., due to an earthquake, the soil element is subject to cyclic shear stress τ_{hv} and, therefore, deforms as depicted in Fig. 3-2 (b).

Corresponding to the situation shown in Fig. 3-1 (c), the soil tends to compact and to pass into a denser packing (contraction). But under undrained conditions with full saturation and low permeability, the water between the grains cannot be forced out fast because of its viscosity (RAJU (1994)). Long drainage paths around the element under consideration and high loading frequencies enforce this behaviour. Thus, the soil is inhibited to compact by the water in the pores and an excess pore pressure Δu is generated in the voids. This Δu can increase with the number of load cycles. Under the assumption that the total stress σ remains constant, the effective stress σ' is reduced to the same degree according to Eq. (3-2). A change in effective stress also affects the shear strength of the soil. Following the Mohr Coulomb approach, the shear strength τ in a cohesionless saturated soil can be expressed as

$$\tau = \sigma' \cdot \tan\varphi = (\sigma - u) \cdot \tan\varphi \tag{3-3}$$

with φ being the inner friction angle. According to this equation, an increase in u not only results in a reduction of effective stress but also of the shear strength of the soil τ. If the stresses between grains fully vanish, i.e., $\sigma' = 0$ and the excess pore pressure has the value of the initial effective stress, $\Delta u = \sigma'_0$, the shearing resistance of the soil is lost and the soil cannot transfer shear stresses any longer. At this failure state, the soil has a liquid-like behaviour. Hence, when external loads as buildings or infrastructural facilities can no longer be supported since the sand deforms like a liquid. Even if this liquefied state only exists for a short time, extensive damage may occur to the structures (see Fig. 1-1). Only when the loading ends, the consolidation process is initiated. The water drains depending on the permeability of the soil and the grains get in contact to each other again. Stresses are re-transferred to the soil skeleton and Δu relaxes and decreases. Since the water mainly dissipates towards the ground surface, a volume reduction often occurs resulting in settlements at the ground level.

Nevertheless, actual soil behaviour is more complex than the Mohr Coulomb models shows. Although many researchers continue to base the criterion for the onset of liquefaction on this approach (compare Section 3.2.2), it should be highlighted that the Mohr Coulomb approach is only a first attempt to interpret the liquefaction process that must be composed with other geotechnical considerations and experimental observations. As will be shown later, soil liquefaction only occurs if a certain threshold shear strain is exceeded (compare Fig. 3-15) and shear stresses surpass the undrained shear strength. So, in the liquefied condition the shear strength is not zero (compare Fig. 3-4). For these reasons, the scientific community has chosen as liquefaction criterion the criterion that will be described in Section 3.2.2 and that is based on the relation between excess pore pressure increase and mean effective soil stress.

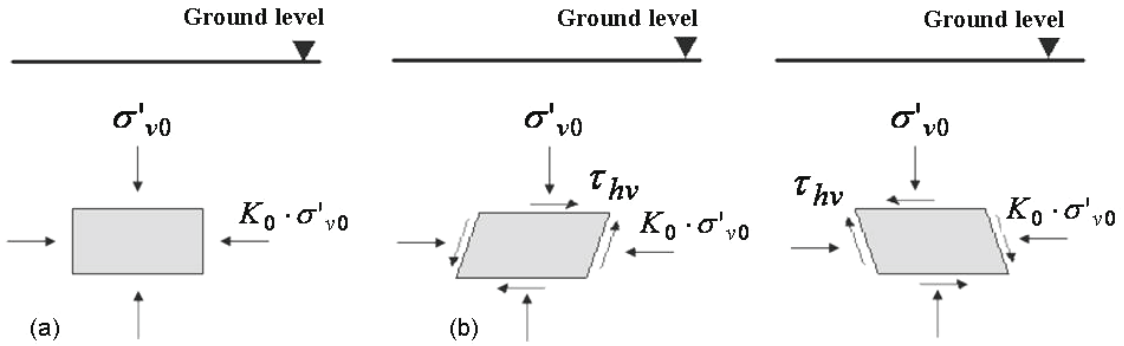

Fig. 3-2: Idealized field conditions of a soil element demonstrated (a) in the initial stress state and (b) during cyclic loading (after MARTIN et al. (1975)).

3.2.1 Laboratory tests and initiation of liquefaction

In order to better understand the processes in the soil during dynamic loading, the behaviour of corresponding soil elements was simulated in laboratory tests by many researchers (e.g., SEED et al. (1978), MARTIN et al. (1975), KHOSLA and WU (1976)). The cyclic triaxial test is the most commonly used test for the measurement of dynamic soil properties. In the simplest triaxial test, saturated soil samples are initially consolidated under ambient pressure and are then subject to a cyclic axial stress under undrained conditions. Hence, stress conditions on a plane at 45° through the soil sample are produced that approximately equal to the stresses on a horizontal plane in the ground during earthquakes (ISHIHARA (1993)). In those kinds of tests, the pore pressure u increases progressively with each cycle as can be seen in Fig. 3-3. Soil liquefaction is generally understood as the transition of the saturated, initially solid soil into a liquid. It is said to be reached when either Δu is as high as the initial effective confining stress or the strain amplitude increases to an axial strain of about 5 % (ISHIHARA (1993)).

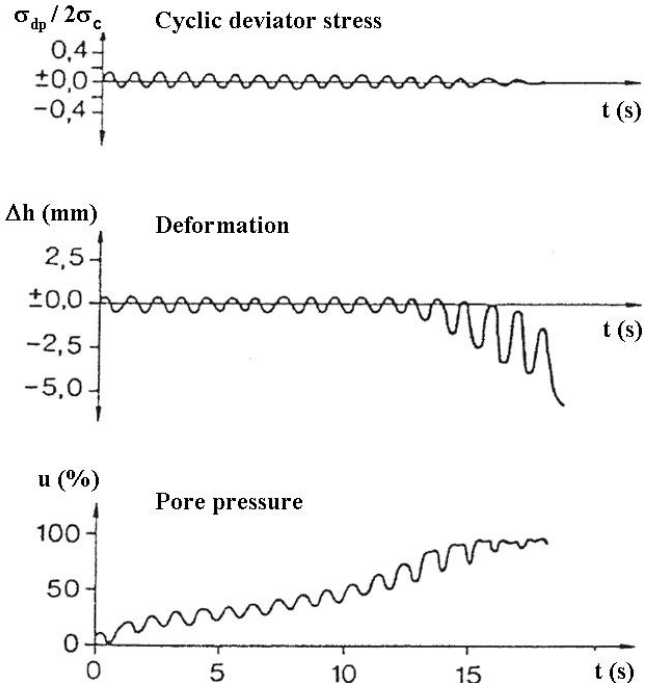

Fig. 3-3: Cyclic triaxial test of a loosely packed sand probe: applied cyclic deviator stress and the response in terms of deformation and pore pressure (after STUDER and ZIEGLER (1986)).

KRAMER (1996) considers the response of an anisotropically consolidated, triaxial specimen of loose, saturated sand. As shown in Fig. 3-4, the sand probe is initially in equilibrium (point A) under a given static shear stress. When loaded cyclically under undrained conditions, the effective stress path moves alternately to the left. Thus, the effective stress is reduced due to the build-up of pore pressure. At the same time, permanent strains accumulate. During those first loading cycles, the strains take place at only small strain levels as can be seen on the left-hand side of the figure. But when the yield strength of the soil is reached at point B, the specimen collapses. It becomes unstable and flows rapidly to large strains and low effective confining pressure. The point where this flowing behaviour is initiated lies on the so-called flow liquefaction surface. During the following strain-softening phase, additional excess pore pressure is generated. Point C represents the so-called steady state of deformation at which the soil flows continuously under constant shear stress. The shear strength mobilized at this point is the liquefied shear strength $s_u(LIQ)$ which is sometimes also called the undrained shear strength. Thus, according to the results of those undrained, triaxial tests which represented the so-called flow liquefaction, the soil has a residual shear strength in the liquefied condition and effective stresses above zero.

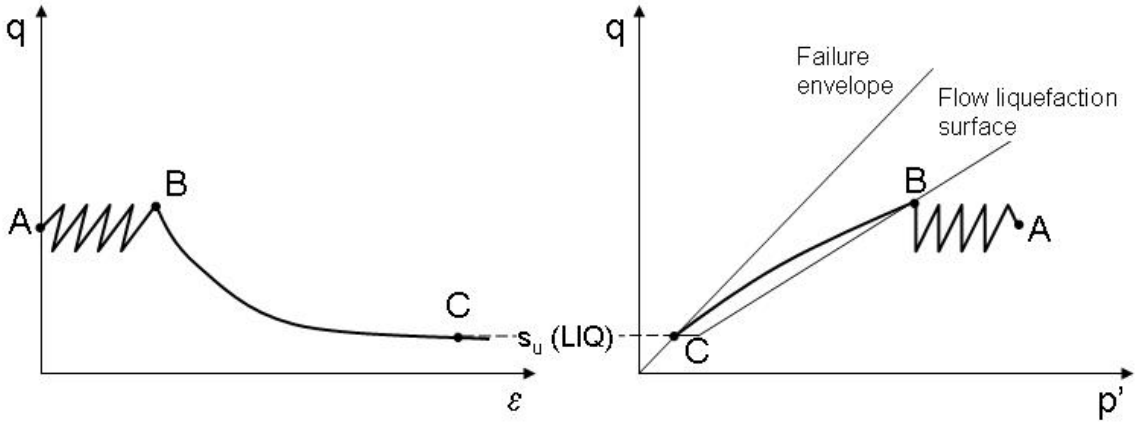

Fig. 3-4: Initiation of flow liquefaction by cyclic loading considering an anisotropically consolidated, triaxial specimen of loose, saturated sand (after KRAMER (1996)).

When the initial, static shear stress τ_{static} is smaller than the liquefied shear strength $s_u(LIQ)$, a liquefaction phenomenon called cyclic mobility can occur. Three combinations of initial conditions and cyclic loading shown in Fig. 3-5 can generate increasing pore pressure and, therewith, liquefaction. When the cyclic loading begins, the stress path moves to the left until it reaches the failure envelope (Fig. 3-5 (a)). At the same time, the effective stress decreases significantly. When the stress path touches the flow liquefaction surface (FLS) as shown in Fig. 3-5 (b), momentary periods of instability occur with significant straining. Nevertheless, when the stress returns to the static stress after the end of each cycle, the straining ceases. When the stress path reaches the failure envelope (FE), further cyclic loading causes the stress path to move up and down along the failure envelope since it cannot be crossed. Thus, the effective stress conditions stabilize but the low stiffness of the soil allows significant permanent strains to develop within each loading cycle. With changing direction of shear stress as shown in Fig. 3-5 (c), the rate of pore pressure generation increases compared to cases with no stress reversal and the stress path moves faster to the left. When reaching the failure envelope, the stress path passes twice through the origin indicating instantaneous zero effective stress conditions.

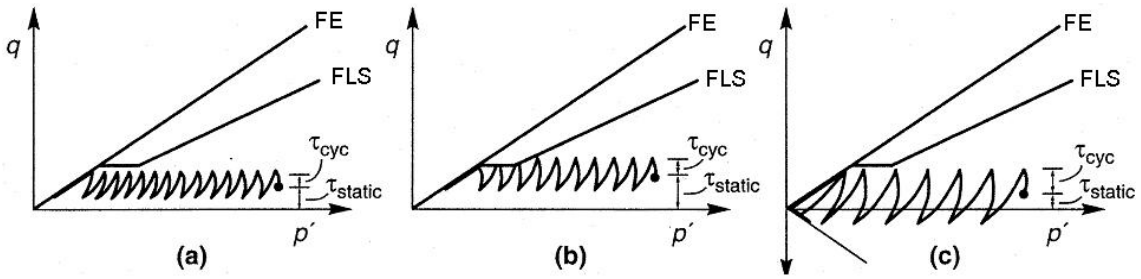

Fig. 3-5: Three cases of cyclic mobility: (a) no stress reversal and no exceedance of $s_u(LIQ)$, (b) no stress reversal and momentary exceedance of $s_u(LIQ)$, (c) stress reversal and no exceedance of $s_u(LIQ)$. FE: failure envelope and FLS: flow liquefaction surface (KRAMER (1996)).

Since cyclic triaxial tests have theoretic limitations (compare STUDER and ZIEGLER (1986) or KRAMER (1996)), the cyclic simple shear test was developed. In this test, shear stresses are generated directly and not due to a vertical alternating load with a constant horizontal stress as in the triaxial test. Hence, in situ conditions can better be represented and therefore, it is the most commonly used test for liquefaction testing. Prior to loading, samples of saturated sand are consolidated under initial vertical stress and K_0-conditions and the cylindrical specimen are restrained against lateral expansion (see Fig. 3-6). Then, a cyclic horizontal shear stress τ_{hv} is applied to the top or bottom of the sample under undrained conditions and vertical stress σ_v which deforms the specimen in almost the same way as an element of soil subject to vertically propagating shear waves. Thus, the grains are transferred into a denser packing and the probe tends to compact. Since the pore water cannot dissipate, not a volume reduction but an increase in u is caused. At the same time, σ_v' decreases with each cycle. As long as effective stress still exists, the shear strength keeps the deformation small ($\gamma < 1$ %). But when Δu exceeds the value of the initial vertical effective stress (in this example after 24 cycles), the soil practically looses its shear strength and the deformation gets large.

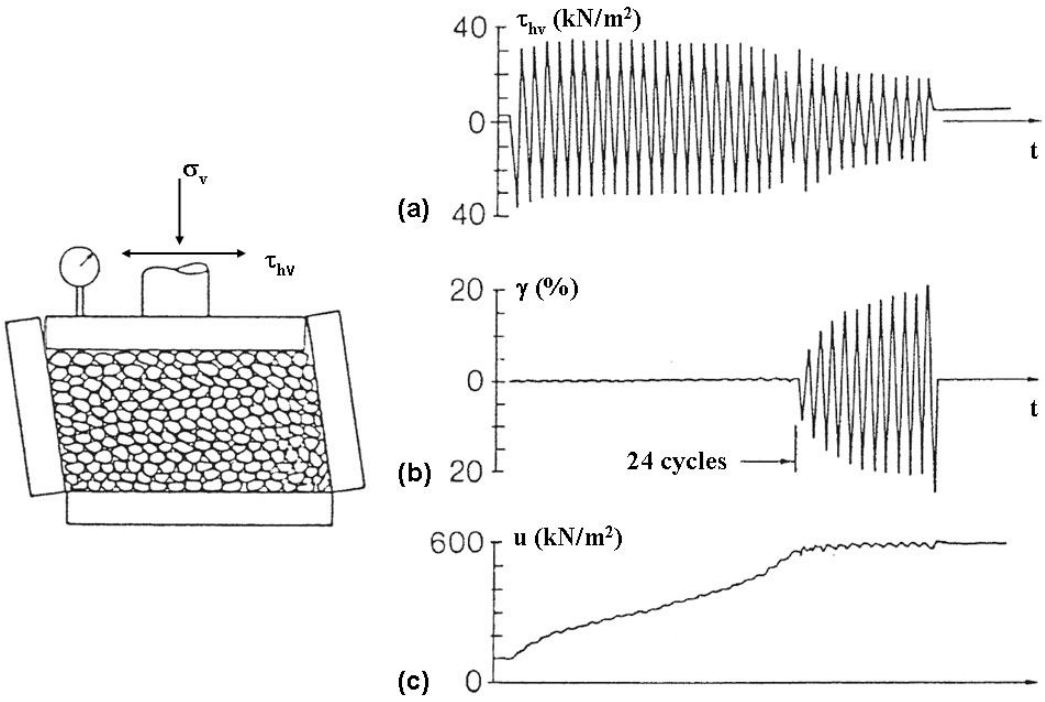

Fig. 3-6: Sketch of a cyclic shear test of a loosely packed sand probe representing (a) cyclic shear loading, (b) shear deformation and (c) pore pressure (after STUDER and ZIEGLER (1986)).

In various laboratory tests as cyclic triaxial tests, cyclic simple shear tests, cyclic torsional tests and shaking table tests, it was found that the liquefaction resistance of the soil samples strongly depends on the initial confining stress, the intensity of shaking, the number of cyclic stress applications and the void ratio or the relative density (ISHIHARA (1993)). Apart from those factors, the saturation of the soil, its permeability, the grain shape and the grain size distribution are very determining factors. According to STUDER and ZIEGLER (1986), a soil tends to liquefy if its grain size distribution lies within the regions given in Fig. 3-7. Within the region denoted with "1" falls the Niigata Sand where seismically induced liquefaction caused high damages in the 1960s. Region "2" envelopes 19 different sands from Japan for which liquefaction was observed as well. Region "3" is based on laboratory tests of LEE and FOCHT (1975). Those regions contain mostly silty or fine sandy soils with a predominantly uniformly distributed grain size distribution.

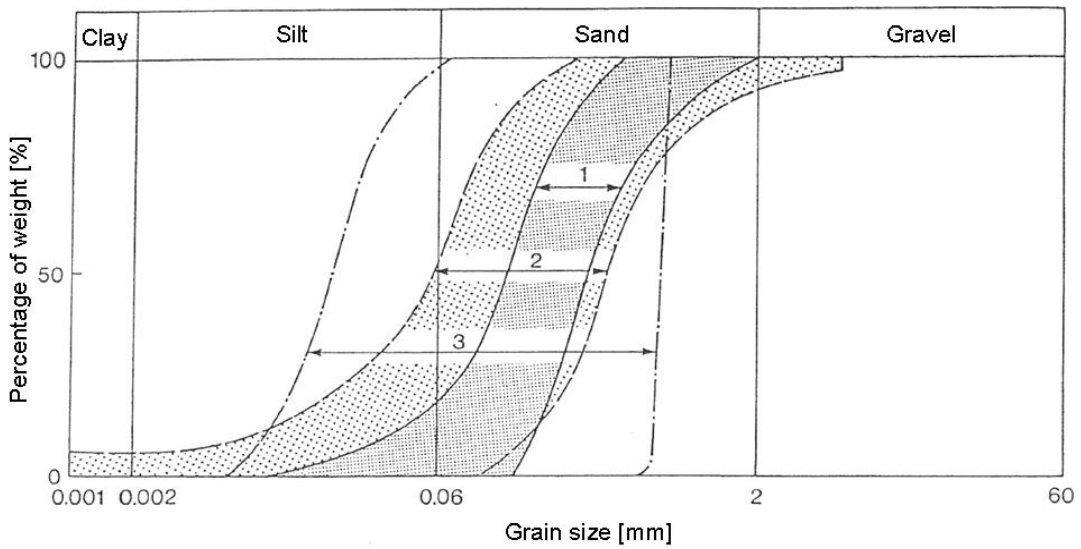

Fig. 3-7: Grain size distributions vulnerable to soil liquefaction (after STUDER and ZIEGLER (1986)): Region 1: Niigata Sand, Region 2: envelop of 19 sands from Japan that liquefied during earthquakes, Region 3: based on laboratory tests of LEE and FOCHT (1975).

3.2.2 Liquefaction criterion

As discussed in the previous section, the amount of pore pressure which is required to cause liquefaction depends on the situation or on the test under consideration. In a simple shear test, for example, liquefaction is characterized by a pore pressure increase as high as the initial vertical effective stress since sand probes are consolidated under anisotropic conditions. In contrast, in a cyclic triaxial test on isotropically consolidated soil, exceeding the mean effective stress is said to cause liquefaction. In the case of the anisotropic triaxial specimen shown in Fig. 3-4, flow liquefaction was caused even though a residual effective stress had still been present.

In order to define the onset of liquefaction for application purposes, e.g., in test models, a definition has to be formulated depending on the situation under consideration. The common definition of the onset of liquefaction found in literature is based on Eq. (3-3): Liquefaction occurs when the excess pore pressure Δu has reached the effective stress σ_0'. This relation is expressed by the liquefaction criterion

$$\sigma_0^{'} - \Delta u \leq 0\,. \tag{3-4}$$

Some authors consider the vertical effective stress as the stress to be reached for liquefaction, others only demand for the excess of the mean effective stress. Therefore, in order to discuss the transfer of stresses and the onset of liquefaction in more detail and in order to define a liquefaction criterion used for the present research, a saturated, non-cohesive sand probe is considered.

At the initial state, the stress in this probe is composed of the initial effective stress in vertical and horizontal direction, $\sigma_{v0}^{'}$ and $\sigma_{h0}^{'}$, respectively, and of the initial hydrostatic water pressure u_0 (see Eq. (3-1)). Since $\sigma_h^{'}$ is determined according to the vertical effective stress but also includes the coefficient of earth pressure at rest K_0,

$$\sigma_h^{'} = K_0 \cdot \sigma_v^{'}, \tag{3-5}$$

with

$$K_0 = 1 - \sin\varphi\,. \tag{3-6}$$

Since for non-cohesive sandy soils $K_0 \approx 0.5$, it follows that

$$\sigma_h^{'} \approx 0.5 \cdot \sigma_v^{'}\,. \tag{3-7}$$

Thus, the effective stress is higher in vertical than in horizontal direction. In the upper left part of Fig. 3-8, this initial state at the time t_0 is shown for a sand probe exemplarily consisting of six grain particles and water. The effective stress and the difference in size between the vertical and the horizontal stress are represented by the arrows and the different lengths of the arrows. The brown boxes indicate that there is grain-to-grain contact and that the inner friction is fully present at that time. The initial pore pressure u_0 is supposed to lie between $\sigma_{v0}^{'}$ and $\sigma_{h0}^{'}$ as shown in the diagram on the right-hand side of the figure.

When during loading the pore pressure increases, the effective stress decreases. The vertical and the horizontal stress decrease to the same degree since the pore pressure is an isotropic stress. On the right-hand side of Fig. 3-8, the increase in u and the decrease in σ' are schematically represented. At the same time, the inner friction decreases as a function of time. At the time t_1, the horizontal stress has completely vanished, $\sigma_h^{'} = 0$. Thus, there is no grain-to-grain contact in horizontal direction and horizontal forces cannot be transferred anymore between the grains. This is represented by the blue serrated arrows at the left. Until then, $\sigma_v^{'}$ has decreased by the same amount, but it reaches zero only at the time t_2 (see right-hand side) when the pore pressure has reached its maximum value. At that time, all effective stress is completely lost and the pore pressure is composed of u_0 and the excess pore pressure Δu.

Now the question arises when the soil is said to liquefy, i.e., when the soil looses its bearing capacity due to liquefaction. First signs of liquefaction are definitely visible at the time t_1 when the horizontal stress has fully vanished and the vertical stress has notably decreased. But only at the time t_2 when also $\sigma_v^{'}$ is zero, the effective stress is completely lost.

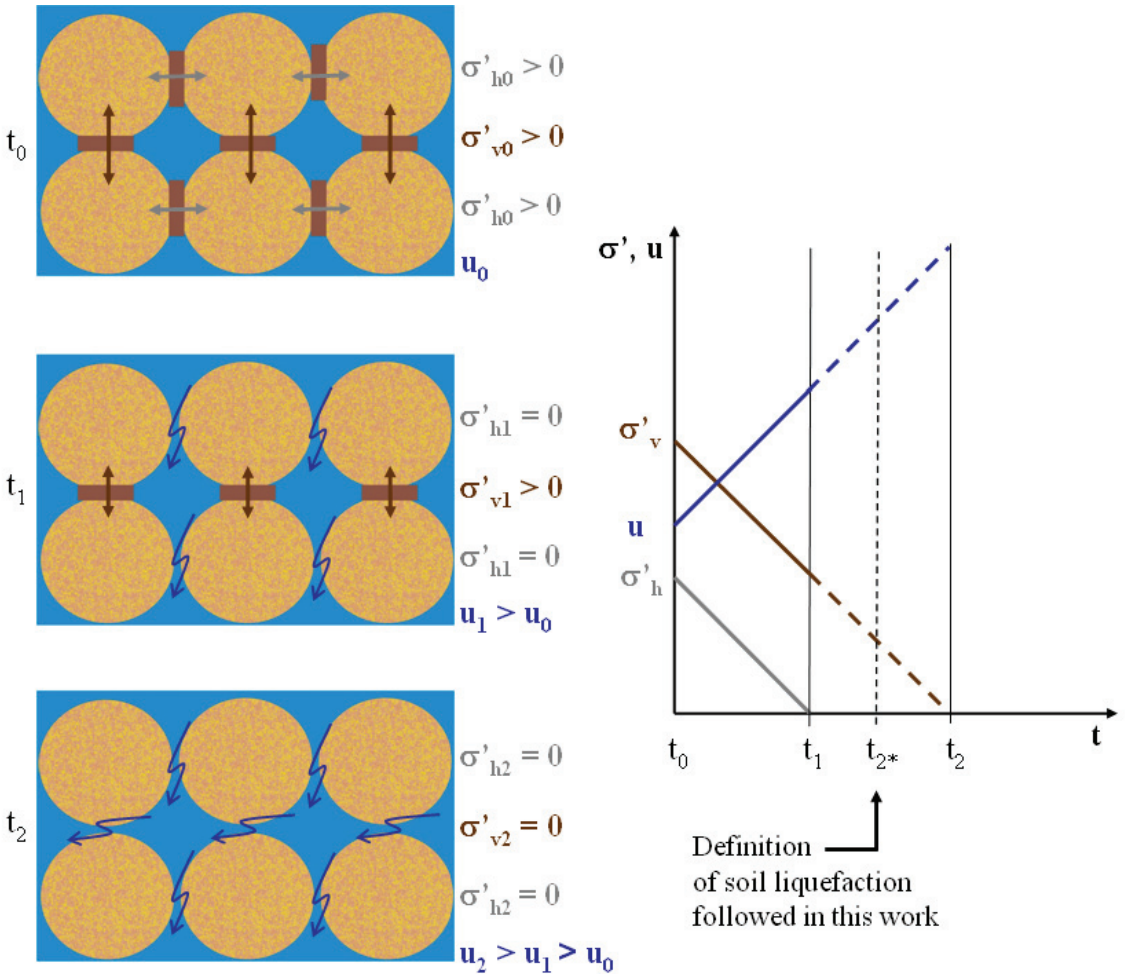

Fig. 3-8: Changes of pore pressure *u* and vertical and horizontal effective stresses *σ'* during dynamic loading of a sand probe at the time t_0 to t_2.

For the application in the field, different approaches can be found in literature to define the onset of liquefaction. FARDIS and VENEZIANO (1982) or OUMERACI and KUDELLA (2004), for example, regard the initial vertical effective stress as the stress which has to be exceeded by the pore pressure to initiate liquefaction. This approach is especially followed for the case of earthquakes. In contrast, CHENG et al. (2001), ZEN et al. (1998) or REESE et al. (1988), for example, consider the mean effective stress $\sigma'_{m0} = (\sigma'_{v0} + \sigma'_{h0})/2$ as the threshold value which signifies the onset of liquefaction. According to this definition, liquefaction is reached at the time t_{2*} indicated by the dashed vertical line in Fig. 3-8. It is argued that when using this definition, the liquefaction criterion is on the conservative side in the evaluation of the liquefaction potential.

Also FARDIS and VENEZIANO (1982) admit that phenomena similar to liquefaction already occur before $\Delta u = \sigma'_{v0}$. They state that liquefaction is already initiated when Δu reaches 96 % of σ'_{v0} as it is only necessary that most of the lateral strength or bearing capacity is lost. Furthermore, JAPANESE GEOTECHNICAL SOCIETY (1998) states that “even if the effective stress is not completely lost, the soil becomes softer as pore water pressure rises, and consequently large strain can be induced in the ground”.

Hence, depending on the definition, the characteristics of a liquefied soil are met sometime between the times t_{2*} and t_2 marked in Fig. 3-8. Since it is on the conservative side and since liquefaction definitely occurred within the test series carried out within this research (see Chapter 6), it was decided to follow the approach of the mean effective stress for these analyses. Furthermore, it is seen to be more accurate to compare a mean stress to the isotropic pore pressure than using only one component of a stress vector (σ'_v). When considering the three-dimensional case, σ'_{m0} is the mean value of the initial values of effective stress in the vertical and both horizontal directions:

$$\sigma'_{m0} = \frac{\sigma'_v + 2 \cdot \sigma'_h}{3}. \tag{3-8}$$

Thus, it is calculated by the unit weight of the soil under buoyancy γ'_s, the depths z under consideration and the coefficient of earth pressure at rest K_0:

$$\sigma'_{m0} = \gamma'_s \cdot z \cdot \frac{(1 + 2K_0)}{3} \tag{3-9}$$

The liquefaction criterion is commonly expressed in a slightly different manner as given in Eq. (3-4), namely in terms of the pore pressure ratio which refers the excess pore pressure to the initial mean effective stress:

$$r_u = \frac{\Delta u}{\sigma'_{m0}}. \tag{3-10}$$

When this ratio exceeds $r_u = 1.0$, liquefaction is said to occur.

3.3 Stress-strain behaviour of dynamically loaded soils

When dynamically loaded, monotonically or cyclically, soils behave almost linear and elastic up to a certain limit of shear strain γ_l. γ_l is named 'threshold linear strain' and is defined as that strain amplitude that causes nonlinear behaviour for the first time. The stiffness of the soil is strain-dependent but in undrained conditions, the pore water pressure does not increase. Laboratory tests (SILVER AND SEED (1971)) showed that a second limit of shear strain exists, called 'threshold shear volumetric strain' and generally indicated with the symbol γ_V. When exceeding γ_V, the stress-strain behaviour of the soil gets extremely nonlinear. Starting from this value of shear strain, when loading increases, large volume changes take place in drained conditions. In contrast, the excess pore water pressure increases and accumulates until failure in undrained conditions. In sandy soils, liquefaction can occur. In the range of deformations superior to γ_V, the stiffness of the soil changes from loading to unloading and is influenced by loading characteristics (amplitude, frequency, number of load cycles) and soil parameters (saturation of the soil, friction angle, relative density, and effective stress).

In Fig. 3-9 (a), a soil sample is subject to symmetric cyclic loading which is increased in 3 stages (labelled as I, II, III). Part (b) of the figure shows the resulting stress-strain behaviour. It can easily be seen that the hysteresis loops depend on the strain amplitude γ. The higher γ, the larger the hysteresis loops and the more decreases the mean shear modulus G_{sec} (secant

modulus, in the figure G_I, G_{II} and G_{III}, indicating the three different stages of loading). The energy dissipation per cycle due to friction is described by the dashed area A-B-0-A (shown for stage III). It is equivalent to a viscous damping. Thus, damping increases with increasing strain amplitude.

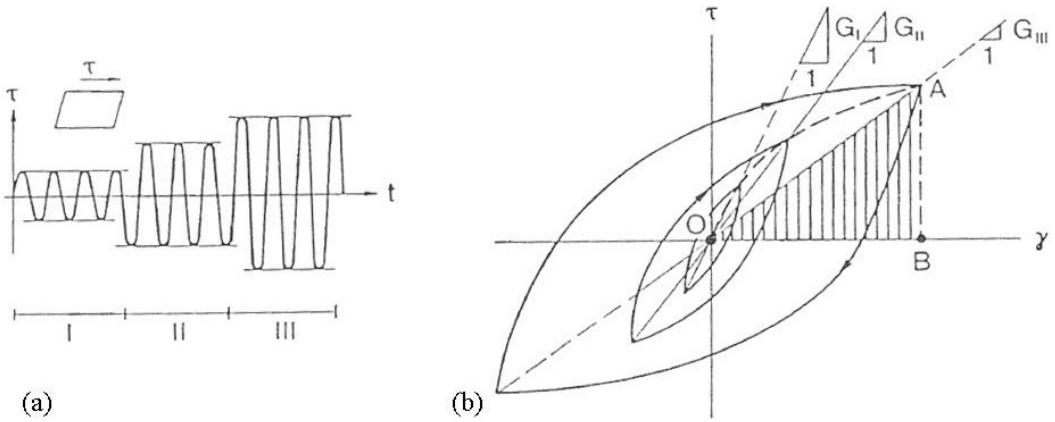

Fig. 3-9: Soil sample subject to dynamic loading, (a) loading cycles in three different stages, (b) hysteresis loop (STUDER and ZIEGLER (1986)).

If the tips of the different, strain-dependent hysteresis loops are connected, the "backbone curve" is obtained which is depicted in Fig. 3-10 (a). It shows the variation of the secant modulus G_{sec} with the shear strain amplitude γ (here shown for a certain shear strain γ_c). Obviously, the highest derivation of the curve is at its origin, G_{max}. Hence, as soon as loading begins, G_{sec} decreases. In Fig. 3-10 (b), G_{sec} is normalized to G_{max} and this ratio is plotted versus the logarithm of the shear strain γ. That curve is called the "modulus reduction curve" as it shows the reduction of the normalized shear modulus with increasing strain amplitude. According to HAUPT (1986), the reduction of this shear modulus ratio starts between $\gamma = 5 \cdot 10^{-4}$ % and $1 \cdot 10^{-2}$ %.

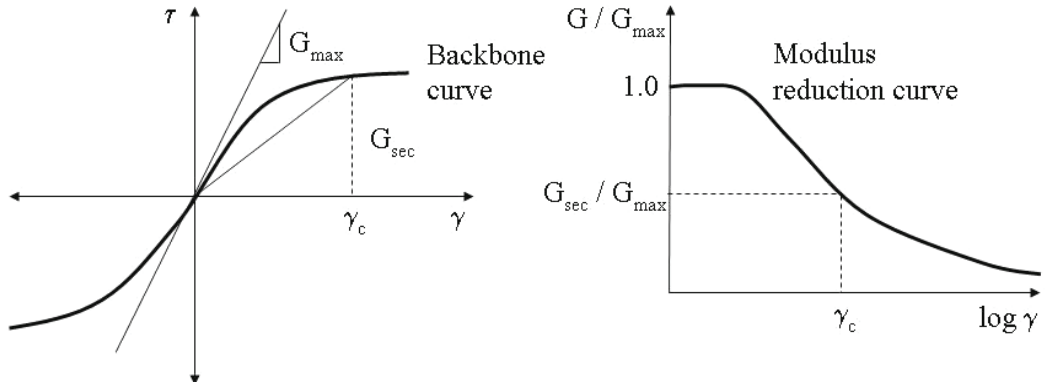

Fig. 3-10: (a) Backbone curve and (b) modulus reduction curve (after KRAMER (1996)).

Whereas the inclination of the hysteresis loops shown in Fig. 3-9 (b) characterises the stiffness of the soil, the width of each loop is related to its damping ratio. SEED and IDRISS (1970) collected data of a couple of researchers who did tests to determine the damping ratio of different sand. As it was discussed above, it was seen that damping generally increases with increasing γ. After KRAMER (1996), also other factors like the confining pressure, the void ratio and the plasticity index influence the damping ratio.

To describe the stress-strain behaviour of a soil during dynamic loading, different soil models were formulated. Those stress-strain models describe the soil behaviour either nonlinearly or, in order to simplify the models, linearly. A model incorporating all influencing factors is very complex and complicated. In order to reduce the complexity, the relevant and determining factors of a certain problem have to be identified and included in an idealized soil model.

Equivalent linear models are the simplest and most commonly used models to describe the stress-strain behaviour of soils in the range of deformations that do not exceed the threshold volumetric strains. The wide spread of those models is due to the fact that only few parameters are necessary and that those parameters can directly be determined from laboratory tests. Nevertheless, the models do not consider all details of the soil behaviour under dynamic loading conditions and imply the restriction that permanent strains at the end of the cyclic loading are not possible. Since an elastic material behaves unlimited linear, failure cannot occur and thus, those models cannot be used for complete liquefaction analyses.

The equivalent linear method uses an iterative process to take into account the nonlinear behaviour of the soil. Therefore, initial values for the strain-dependent shear modulus G_{sec} and the damping ratio ξ are assumed. This first approximation of G_{sec} and ξ can be done with correlations and empirical formulas from literature (compare STUDER and ZIEGLER (1986) or KRAMER (1996)). Then, the response of the soil due to dynamic loading in terms of mean strains is determined in a linear calculation. According to the so-determined strains, new values for the shear modulus and the damping ratio can be calculated which are iteratively improved until there is no further change in properties. According to STUDER and ZIEGLER (1986), this method is suitable for applications in geotechnical engineering even if it leads to deformations that are underestimated by about 50 %. The maximum stresses are overestimated by about 25 %.

Cyclic nonlinear models do not use equivalent linear material parameters but the actual path of the hysteresis loop during cyclic loading. So, the stress-strain behaviour can be represented more appropriately. Since liquefaction can take place only if the deformations exceed the threshold volumetric strain γ_V, only those nonlinear models can be used for liquefaction predictions. The models can represent the shear strength of a soil and, by applying an appropriate pore pressure generation model, they can also predict changes in pore pressure and effective stress during undrained cyclic loading. Many cyclic nonlinear models have been developed. They are all characterized by a backbone curve and by a series of "rules" that determine the unloading-reloading behaviour, stiffness degradation, etc.. Backbone curves are usually described by simple functions that correlate the shear strength of a soil to the strain amplitude and thus, represent the transition from the initial stiffness at low strains to the ultimate strength at high strains. G_{max} and τ_{max} are measured, computed or obtained by empirical correlations. The "rules" concretize the stress-strain behaviour for unloading and reloading. The more "rules" are incorporated in the model, the more accurate is the model and the better it simulates certain soil behaviours. However, the number of problems decreases to which it can be applied to. An example model for a given backbone curve and "rules" can be found in KRAMER (1996).

One of the most important advantages of cyclic nonlinear models compared to equivalent linear models is that they can simulate the development of permanent strains. Another advantage is

their ability to represent pore pressure changes and changes in effective stress when coupled with pore pressure generation models (see Section 3.4). Hence, pore pressure generation under cyclic loading as well as soil liquefaction can be predicted.

Advanced constitutive models are able to deal with many details of dynamic soil behaviour. They describe the soil behaviour for general initial stress conditions and are able to handle cyclic loading, high or low strain rates, and drained or undrained conditions. As a consequence, they imply more material parameters than the equivalent linear or the cyclic nonlinear models. However, those parameters are sometimes difficult to determine. The nonlinear material behaviour is expressed by introducing elastic as well as plastic strains. In general, they also require the formulation of a yield surface, a hardening law and a flow rule. The increased generality of those models is accompanied by an increased complexity. Therefore, they are often unhandy and inefficient for engineering practice.

3.4 Pore pressure generation models

The potential of a soil to liquefy is generally evaluated by comparing the loading conditions with the resistance of the soil. To understand the relation of the applied loadings and the pore pressure generation, a lot of laboratory tests were carried out to simulate the earthquake loads. Based on those tests, pore pressure generation models were formulated to predict the pore pressure generation for given loadings. Those approaches link the pore pressure generation to certain parameters as to the applied stresses, to the energy dissipation or to the applied strains. According to KAGAWA et al. (1981), most of the models explicitly or implicitly include the interrelation of the volume change of a drained soil with the pore pressure generation of an undrained soil during cyclic loading. The cyclic stress and the cyclic strain approach are the most important approaches and, therefore, are going to be discussed in the next sections.

3.4.1 Cyclic stress approach

H.B. Seed was one of the pioneers in evaluating the liquefaction susceptibility of a soil. Since his approach was based on cyclic stresses, this approach has come to be known later as the cyclic stress approach. The cyclic stress approach assumes that pore pressure generation is fundamentally related to the cyclic shear stresses generated by the loading. To simplify the irregular loading, it is expressed in terms of the amplitude of an equivalent uniform cyclic shear stress with a certain number of cycles. Most commonly used is the level of 65 % of the peak cyclic shear stress as amplitude of the equivalent shear stress. The number of equivalent uniform stress cycles depends on the earthquake magnitude. In a second step, the amplitude of an equivalent uniform cyclic shear stress which is required to cause liquefaction is determined for the same number of loading cycles. This is done by laboratory or in situ tests and described in detail in KRAMER (1996). After determining the equivalent uniform action and resistance shear stress amplitudes, their values are compared. At depths where the shear stress induced by the loading exceeds the shear strength of the soil, the soil is expected to liquefy (see Fig. 3-11). The condition for the onset of liquefaction is that the factor of safety FS becomes less than 1:

$$FS = \frac{cyclic\ shear\ stress\ required\ to\ cause\ liquefaction}{equivalent\ cyclic\ shear\ stress\ induced\ by\ earthquake}. \tag{3-11}$$

Although there is a large number of factors that influence the cyclic stresses required to initiate liquefaction (like the density, the strain history, the overconsolidation ratio, etc.), this approach is the most often applied approach in practice.

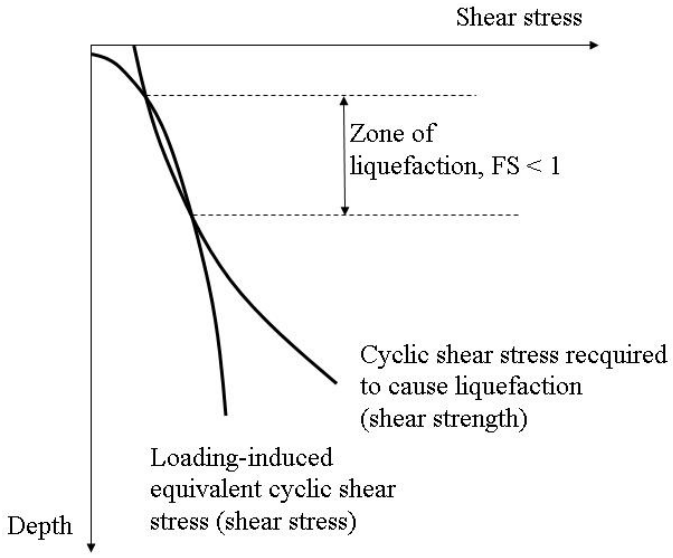

Fig. 3-11: Identification of liquefied zone by means of cyclic stress approach (after KRAMER (1996)).

3.4.2 Cyclic strain approach

SILVER AND SEED (1971) could show in laboratory tests that the densification of dry sands is rather controlled by cyclic strains than by cyclic stresses and that a threshold volumetric shear strain exists. Only when this threshold is exceeded, volume changes occur. Because the volume reduction of dry sand is coupled to the development of excess pore pressure during cyclic loading of saturated sand, one can educe that also the pore pressure generation is fundamentally related rather to cyclic shear strains than to cyclic shear stresses. That is why this approach is called the cyclic strain approach. Consequently, the loading is expressed in terms of strains. Therefore, the loading (which is in the majority of cases irregular in nature) is transferred to an equivalent series of uniform strain cycles (see KRAMER (1996) for more details and formulas). Laboratory tests are carried out for the characterization of the liquefaction resistance. Even if, compared to cyclic stresses, the cyclic strains are considerably more difficult to predict accurately, the advantage of the strain approach overweighs: The factors discussed in Section 3.4.1 that influence the cyclic stresses τ_{cyc} required to initiate liquefaction (e.g., the density, strain history, over-consolidation ratio) similarly influence the shear modulus G of the soil. Thus, the cyclic shear strain which is expressed by $\gamma_{cyc} = \tau_{cyc} / G$ is influenced by the upper mentioned factors in its numerator as well as in its denominator. Hence, the influence on γ_{cyc} is much smaller than on τ_{cyc} alone.

DOBRY and LADD (1980) could prove this assumption by their measurements presented in Fig. 3-12: the pore pressure ratio $r_u = \Delta u / \sigma'$, produced by ten strain-controlled cycles of loading, is plotted over the cyclic shear strain γ_{cyc}. The interesting result of those investigations is the following: the data lie more or less on one single curve. This is surprising since two different sands were used, since those sands were prepared by three different methods, and since three

different initial effective confining pressures were applied. This is the hallmark of the cyclic strain approach: the pore pressure generation is insensitive to those factors and it is highly correlated to the applied shear strain γ_{cyc}.

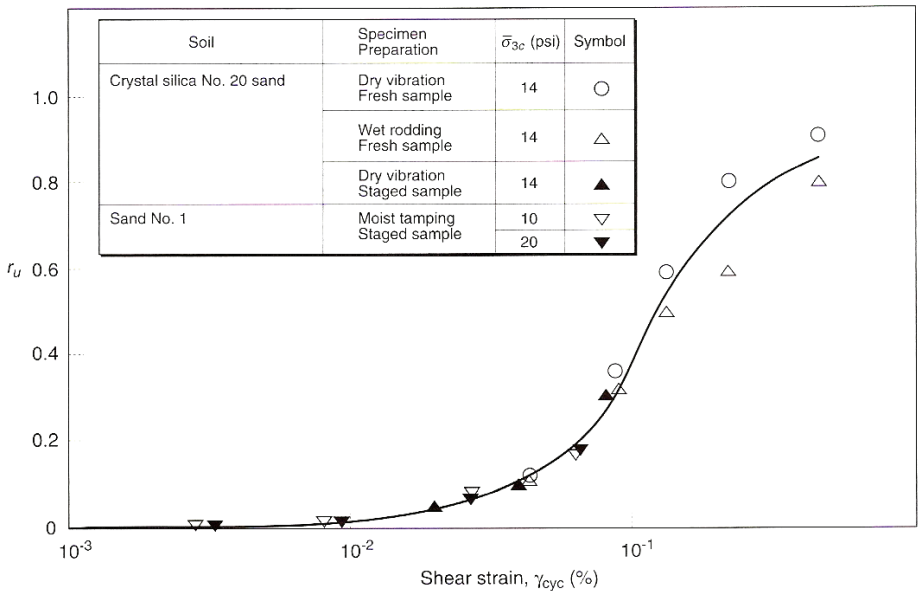

Fig. 3-12: Pore pressure ratio r_u over shear strain γ_{cyc} after 10 cycles of loading in strain-controlled cyclic triaxial tests. The tests include two different sands, three different preparation techniques and three different levels of initial effective stress. (DOBRY and LADD (1980)).

The evaluation of the liquefaction potential is comparable to the evaluation in the cyclic stress approach (compare Fig. 3-11): the equivalent cyclic shear strains induced by the earthquake loading are compared to the ones required to cause liquefaction. When the latter (the resistance) are smaller, liquefaction occurs in these regions.

3.4.3 Finn and Byrne Model

The Finn and Byrne Model is an advanced model within the cyclic strain approaches. It is an effective stress-based approach with a stress-strain law that includes a coupling between the cyclic shear strains and the volumetric response of the sand. It incorporates two extensions into the standard Mohr Coulomb plasticity model which will be derived in the following.

In a cyclic shear test under drained conditions, a soil sample undergoes an incremental volumetric compaction strain $\Delta\varepsilon_{vd}$ which is caused due to slipping at grain-to-grain contacts (FINN et al. (1977)). For $\gamma < 0.3$ %, this volumetric response of the sand is proportional to the shear strain amplitude γ. Now, a sample subject to the same shear strain amplitude but under undrained conditions is considered. According to MARTIN et al. (1975), it is known from experimental results that the cyclic pore pressure changes are low for small shear strain amplitudes. Also, the residual pore pressure build-up during one cycle is relatively small compared to the initial pore pressure. Thus, the contact forces between the grains due to shearing in the undrained condition are comparable to the ones in the drained condition. Therefore, it can be assumed that the intergranular slip leading to the volume change $\Delta\varepsilon_{vd}$ also occurs in the undrained situation.

Prior to loading, the vertical stresses are carried by the granular structure. When loaded, the sand skeleton transfers those stresses to the less compressible pore water. With each cycle of shear strain, an increase in pore pressure Δu is caused. The corresponding reduction in effective stress leads to a release of an increment of recoverable volumetric strain $\Delta\varepsilon_{vr}$. This volumetric expansive strain increment $\Delta\varepsilon_{vr}$ is traced back to elastic deformations at the grain contacts due to the relaxing sand skeleton. It can be expressed by the ratio of Δu and the tangent modulus $\overline{E_r}$. Because of volumetric compatibility, the change in volume of voids at the end of one loading cycle has to equal the net volume change of the sand structure, i.e., $\Delta\varepsilon_{vd}$ - $\Delta\varepsilon_{vr}$. This leads to

$$\frac{\Delta u \cdot n}{K_W} = \Delta\varepsilon_{vd} - \Delta\varepsilon_{vr} . \tag{3-12}$$

With $\Delta\varepsilon_{vr} = \Delta u / \overline{E_r}$, one obtains

$$\frac{\Delta u \cdot n}{K_W} = \Delta\varepsilon_{vd} - \frac{\Delta u}{\overline{E_r}} , \tag{3-13}$$

where the following abbreviations are used:

$\frac{\Delta u \cdot n}{K_W}$: change in volume of voids

Δu: pore pressure increment for one cycle

n: porosity of the soil sample

K_W: bulk modulus of water

$\overline{E}_r$: unloading modulus (tangent modulus of the one-dimensional unloading / rebound curve at σ'_{v0})

$\Delta\varepsilon_{vd}$: volumetric change of the sand structure due to slip

$\Delta\varepsilon_{vr}$: volumetric change of sand structure due to recoverable volumetric strain

From this follows for Δu in a saturated sand sample subject to one cycle of loading in simple shear under undrained conditions:

$$\Delta u = \frac{\Delta\varepsilon_{vd}}{\frac{1}{\overline{E_r}} + \frac{n}{K_W}} . \tag{3-14}$$

The bulk modulus $K_W \approx 2 \cdot 10^6$ kN/m^2 is approximately two orders of magnitude higher than $\overline{E_r}$ for confining pressures < 190 kN/m^2 which corresponds to depths in which liquefaction can occur. MARTIN et al. (1987) assume that the water in saturated soil samples is effectively not compressible ($n / K_W \rightarrow 0$). This means that the volume changes are zero and Eq. (3-13) is simplified to

$$\Delta\varepsilon_{vd} = \Delta\varepsilon_{vr} = \frac{\Delta u}{\overline{E_r}} \tag{3-15}$$

or

$$\Delta u = \Delta \varepsilon_{vd} \cdot \overline{E_r} \; . \tag{3-16}$$

This simplification is only valid for fully saturated soil samples (saturation $S_r = 1$). For partially saturated soil samples ($S_r < 1$), K_W decreases relatively fast and reaches the orders of $\overline{E_r}$ (already for $S_r \approx 0.99$). So, Eq. (3-13) cannot be simplified as for the saturated case and it can easily be seen that when K_W decreases, also Δu gets considerably smaller. SILVER AND SEED (1971) showed that $\Delta \varepsilon_{vd}$ is independent of vertical effective stress. Considering a saturated soil sample that is loaded by the initial vertical stress σ'_{v0} and that undergoes the elastic volumetric strain ε_{vr0}, one observes liquefaction when a cyclic strain is applied that causes a volumetric strain $\varepsilon_{vd} = \varepsilon_{vr0}$ under drained conditions.

Natural loadings, like earthquakes, blasting, machine vibration or wind and wave loading mainly differ in one property from the conditions mentioned above: they are irregular and non-uniform. So, $\Delta \varepsilon_{vd}$ needs to be computed also for those non-uniform sequences of cyclic strain amplitudes when this model should be applied. MARTIN et al. (1975) carried out a series of cyclic shear tests and could find a method to predict volumetric strains during non-uniform or random shear strain amplitude sequences. Firstly, they experimentally established the volumetric strain curves shown in Fig. 3-13 (a) that were found for different constant shear strain amplitudes γ. They assume that the volumetric strain of a new cycle (N+1) depends on the already accumulated strain during N previous cycles and of the shear strain amplitude applied in the (N+1)th cycle, no matter if the loading is uniform or non-uniform. Having, e.g., an accumulated volumetric strain of $\varepsilon_{vd} = 0.4$ % and a shear strain amplitude of $\gamma = 0.2$ % for cycle (N+1), this would result in an increment of volumetric strain of $\Delta \varepsilon_{vd} = 0.06$ % for the subsequent cycle. In order to use this procedure for numerical calculations, the very same data shown in Fig. 3-13 (a) are plotted in terms of volumetric strain increments versus shear strain amplitude for different accumulated volumetric strains in Fig. 3-13 (b). It was observed in the tests that when the volumetric accumulated strain has a certain high level, additional cyclic shear strain amplitudes may not result in further volumetric changes. This is consistent with the volumetric strain asymptotically approaching the cyclic shear strain axis in Fig. 3-13 (b) where $\Delta \varepsilon_{vd} = 0$.

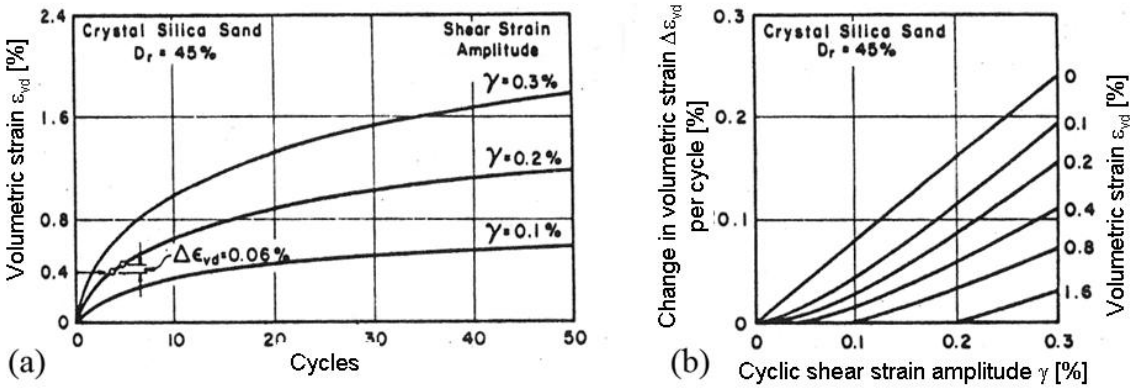

Fig. 3-13: (a) Volumetric strain curves for constant cyclic shear strain amplitude tests, (b) same data, alternative plotting representation (MARTIN et al. (1975)).

The analytic expression for the curves shown in Fig. 3-13 (b) is given by the so-called Finn Constitutive Law:

$$\Delta\varepsilon_{vd} = C_1 \cdot (\gamma - C_2\varepsilon_{vd}) + \left(\frac{C_3(\varepsilon_{vd})^2}{\gamma + C_4\varepsilon_{vd}} \right). \tag{3-17}$$

C_1 to C_4 are experimentally determined constants which depend on the sand type and the relative density. The incremental pore pressure Δu during a given loading cycle is linked to that volumetric strain increment in Eq. (3-16). It can be calculated by means of the unloading modulus $\overline{E}_r$ which is analytically expressed as

$$\overline{E_r} = \frac{(\sigma_v')^{1-m}}{mk_2(\sigma_{v0}')^{n-m}}. \tag{3-18}$$

σ_v' and σ_{v0}' are the values of the current and the initial vertical effective stress, respectively, and m, n and k_2 are experimentally determined constants. Those constants can be obtained from a series of three unloading oedometric curves from different initial vertical stresses σ_{v0}' as exemplarily shown in CRESPELLANI and MADIAI (2002). An increase in Δu causes a decrease in σ_v'. The new calculated effective stress will affect the maximum initial shear modulus G_{max} and the maximum shear stress τ_{max} that will be applied to the next cycle of loading (FINN et al. (1977)). Hence, the current shear modulus is modified progressively for the changing effective stresses in each time interval. So, the stress-strain curve for unloading and reloading is continually updated.

A disadvantage of the formula developed by MARTIN et al. (1975) is that Eq. (3-17) is based on laboratory data of a specific sand at a specified relative density of 45 % only. According to investigations done by BYRNE (1991), this equation was found to be not stable for other relative densities. Therefore, BYRNE (1991) later modified this model and could even give a simplified formula. Firstly, he plotted the data shown in Fig. 3-13 in a different way: in Fig. 3-14 (a), they are plotted for the three levels of shear strain amplitudes in terms of volumetric strain increments versus accumulated volumetric strain. Secondly, he divided the axes by the shear strain amplitude. Thus, the analytic expression given in Eq. (3-17) results in

$$\frac{\Delta\varepsilon_{vd}}{\gamma} = C_1 \cdot \left(1 - C_2 \frac{\varepsilon_{vd}}{\gamma}\right) + \frac{C_3\left(\frac{\varepsilon_{vd}}{\gamma}\right)^2}{1 + C_4 \frac{\varepsilon_{vd}}{\gamma}}. \tag{3-19}$$

Hence, the data represented by the three curves of Fig. 3-14 (a) collapse on one single curve. This is presented in the dimensionless plot in Fig. 3-14 (b) which BYRNE (1991) describes by only two constants C_1 and C_2. The analytic expression of this fitting curve, the Byrne Constitutive Law, is also applicable for other relative densities and has the form

$$\frac{\Delta\varepsilon_{vd}}{\gamma} = C_1 \cdot \exp\left(-C_2\left(\frac{\varepsilon_{vd}}{\gamma}\right)\right). \tag{3-20}$$

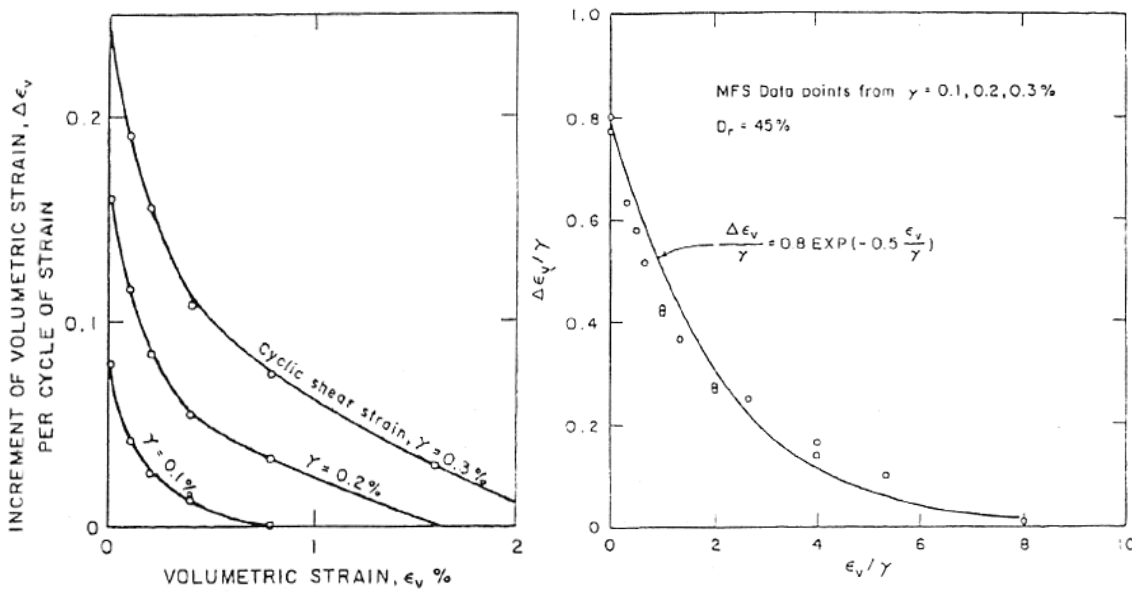

(a) **(b)**

Fig. 3-14: (a) Alternative volumetric strain curves from the data of Fig. 3-13, (b) normalized incremental volumetric strain (BYRNE (1991)).

Here, C_1 and C_2 are constants that can easily be defined by empirical correlations (for the tests carried out here: $C_1 = 0.8$, $C_2 = 0.5$). C_1 controls the amount of volume change and can either be calculated by means of the relative density D_r (in percent) or by the values of standard penetration tests N_{60}:

$$C_1 = 7600 \cdot (D_r)^{-2.5} = 8.7 \cdot N_{60}^{-1.25}. \tag{3-21}$$

The constant C_2 controls the shape of the accumulated volume change with number of cycles. Since the shape is the same for all densities, C_2 is a constant fraction of C_1 for all densities:

$$C_2 = \frac{0.4}{C_1}. \tag{3-22}$$

To compute the resulting changes in pore pressure, Eq. (3-20) is modified such that volumetric strains are defined per ½ cycles. Those strains are not recoverable but plastic strains and are therefore referred to as $\Delta\varepsilon_{vd}^{p}$:

$$\Delta\varepsilon_{vd}^{p} = (\Delta\varepsilon_{vd})_{1/2 cycle} = 0.5 \cdot \gamma \cdot C_1 \cdot \exp\left(-C_2 \left(\frac{\varepsilon_{vd}}{\gamma}\right)\right). \tag{3-23}$$

Similar to Eq. (3-16), the volumetric strains are related to the excess pore pressure increments Δu over a rebound constrained tangent modulus M:

$$\Delta u = M \cdot \Delta\varepsilon_{vd}^{p}. \tag{3-24}$$

For $K_m \approx 1600$, $m = 0.5$ and P_a being the atmospheric pressure (with the same units as σ_v'), M can be calculated according to

$$M = K_m P_a \left(\frac{\sigma_v'}{P_a}\right)^m \tag{3-25}$$

and is said to be in good agreement with the values reported by MARTIN et al. (1975). On the left-hand side of Eq. (3-24), Δu is calculated for fully undrained conditions whereas it is counterbalanced on the right-hand side of the equation by the volumetric strain under fully drained conditions and by the factor M mainly including the effective stress. The generated pore pressure u_g is calculated in Eq. (3-26) by summing up the pore pressure increments Δu:

$$u_g = \sum \Delta u \tag{3-26}$$

To verify those formulae for the build-up of pore pressure, BYRNE (1991) used a large number of resonant column tests shown in Fig. 3-15 and determined the pore pressure ratio $r_u = \Delta u / \sigma_0'$ in dependency of the shear strain amplitude. As can be seen in Fig. 3-15, there is a threshold shear strain γ_V, below which pore pressure build-up will not occur and which was already reported by SILVER AND SEED (1971). Calculating the pore pressure build-up by Eq. (3-23) without considering such a threshold ($\gamma_V = 0$), the pore pressure ratio is over-predicted (see dotted line on the left). Introducing a threshold shear strain $\gamma_V = 0.005$ % and substituting γ in Eq. (3-23) by $\gamma^* = \gamma - \gamma_V$, the pore pressure ratio is under-predicted (see dotted line on the right). With a threshold strain amplitude of $\gamma_V = 0.002$ %, the prediction of the model is very good (for reasons of clarity, it is not depicted in the figure). Nevertheless, test data of other researchers showed that having only few load cycles, the threshold strain is 0.01 %. BYRNE (1991) decided to take a value of $\gamma_V = 0.005$ % as a compromise for the calibration of his model. A listing of studies containing information on the threshold shear strains can be found in VUCETIC (1994).

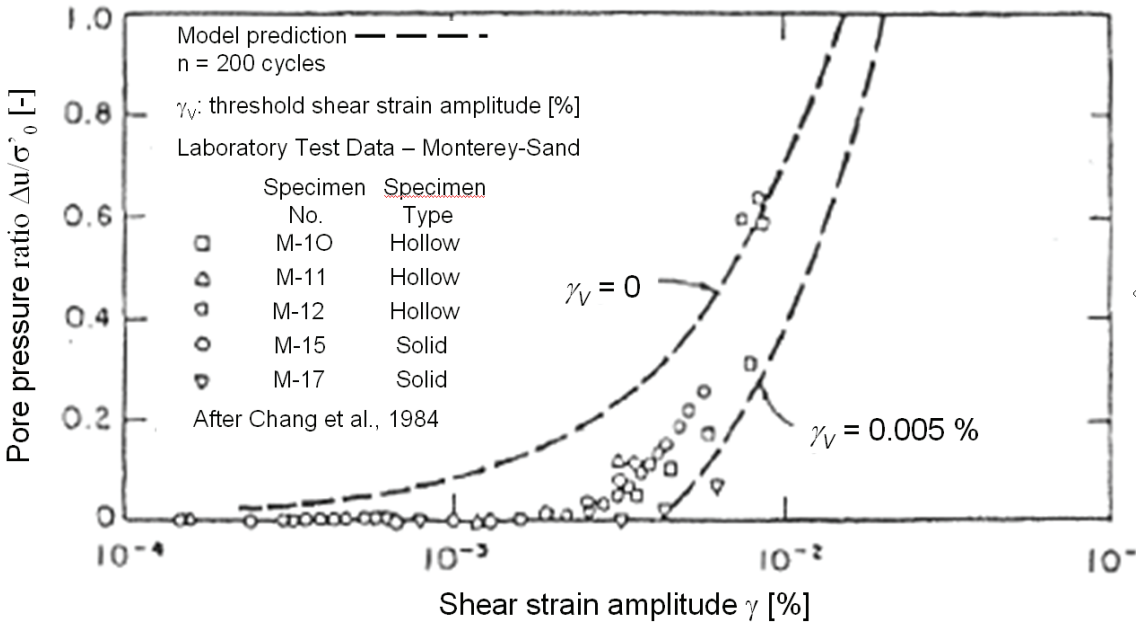

Fig. 3-15: Pore pressure ratio observed in resonant column tests depending on the shear strain amplitude. The signs indicate the test results of different sand specimen, the dotted lines correspond to model predictions for 200 cycles including a threshold shear strain γ_V. (BYRNE (1991)).

BYRNE (1991) uses the stress-strain law proposed by HARDIN and DRNEVICH (1972) to compute strains from stresses. Within this approach, G is a function of the vertical effective stress and the shear strain, i.e., G decreases with decreasing effective stress. It has the form

$$G = G_{\max} \cdot \left(\frac{1}{1+\gamma_h} \right) \tag{3-27}$$

in which γ_h is the hyperbolic strain which includes among other variables the number of cycles and the vertical effective stress. More details are given in BYRNE (1991). The model predictions were compared to the results of laboratory tests and to field experience during earthquakes and showed an excellent agreement.

Up to now, the Finn and Byrne Model was used for different earthquake studies as they can be found in COOKE (2000), CHAWLA (2003) or MARTINO and SCARASCIA MUGNOZZA (2005) and others. In those studies, the impact of seismic shaking to soil-structure interaction was examined. Thus, the seismic excitation is the reason for changes in stresses in the soil. To the best of the knowledge of the author, the model was not yet used in a dynamic study in which a pile structure itself acts as exciting source causing changes in stresses in the soil. This is the case analysed in the present research.

4 Soil liquefaction in the offshore environment

As the subsoil in the offshore environment often corresponds to the grain size distribution marked in Fig. 3-7, this area can be said to be susceptible to liquefaction. As stated in Chapter 3, research on the liquefaction phenomenon began in the middle of the 20th century after two severe earthquakes occurred in Japan and Alaska which both led to high damages and could be traced back to soil liquefaction. But of course, also in the offshore environment, soil liquefaction can be induced by earthquakes and can cause severe damages on the structures built there. The triggers to cause soil liquefaction are the seismic waves generated in the hypocenter of an earthquake. There are body waves (P-waves and S-waves) that propagate radially from the source through the interior of the earth. When they reach the surface, they are diffracted and reflected. Thus, surface waves (Rayleigh waves and Love waves) are generated that travel in parallel to the surface. The upward propagating shear waves induce a cyclic shear stress in the ground. When a relatively loose saturated soil is shaken by seismic waves, it tends to compact and to move into a denser packing. But during a seismic disturbance, there is normally not enough time for the water in the pores to drain. It is trapped between the grains and the seismic loading leads to an excess pore pressure. When the soil passes into a liquid and looses its shear resistance, it is not capable to support structures anymore. According to SEED et al. (1976), excess pore pressure in fine sand may be found also one hour or more after an earthquake. The risk of earthquake-induced soil liquefaction plays a very important role in the offshore environment. The structures have to be designed to endure the earthquake loading case. Therefore, a lot of emphasis was put on the development of seismic design guidelines for the offshore industry structures (see FERRITTO et al. (1999) for more details).

But leaving this inducing factor aside, there are two other factors that can evoke soil liquefaction in the offshore environment: the direct action of the water waves on the subsoil and the indirect wave-induced lateral deflection of a structure which is embedded in the soil. In Fig. 4-1, both inducing factors and the pore pressure changes in the soil caused by them are shown. Whereas on the left-hand side, a pore pressure change in the soil is induced directly by the water waves due to the water pressure changes caused by them (compare Section 4.1), the pore pressure in the soil close to the foundation can change as well due to the movement, i.e., due to the deflection of the pile (compare Section 4.2). As a matter of course, both inducing factors can also interfere with each other.

According to CHANEY and FANG (1991), the loadings generated by an earthquake and the loadings generated by storm waves (directly or indirectly) differ in the following aspects: Firstly, storm waves have frequencies considerably lower than earthquake loadings (< 0.1-1 Hz vs. 10 Hz). But as storms last longer than earthquakes, they load the structures for a longer time (some hours vs. few seconds). Secondly, the probability that a structure subject to a storm loading has been subject to similar loadings before is higher than the same probability for the earthquake case. And thirdly, the direction of propagation is different: In the case where the liquefaction is wave or displacement-induced, the excitation propagates from the mud line or the structure, respectively, in the subsoil. Whereas when the liquefaction is induced by an earthquake, the shear waves propagate from a lower level in the ground upward in direction of the mud line or of a structure if present.

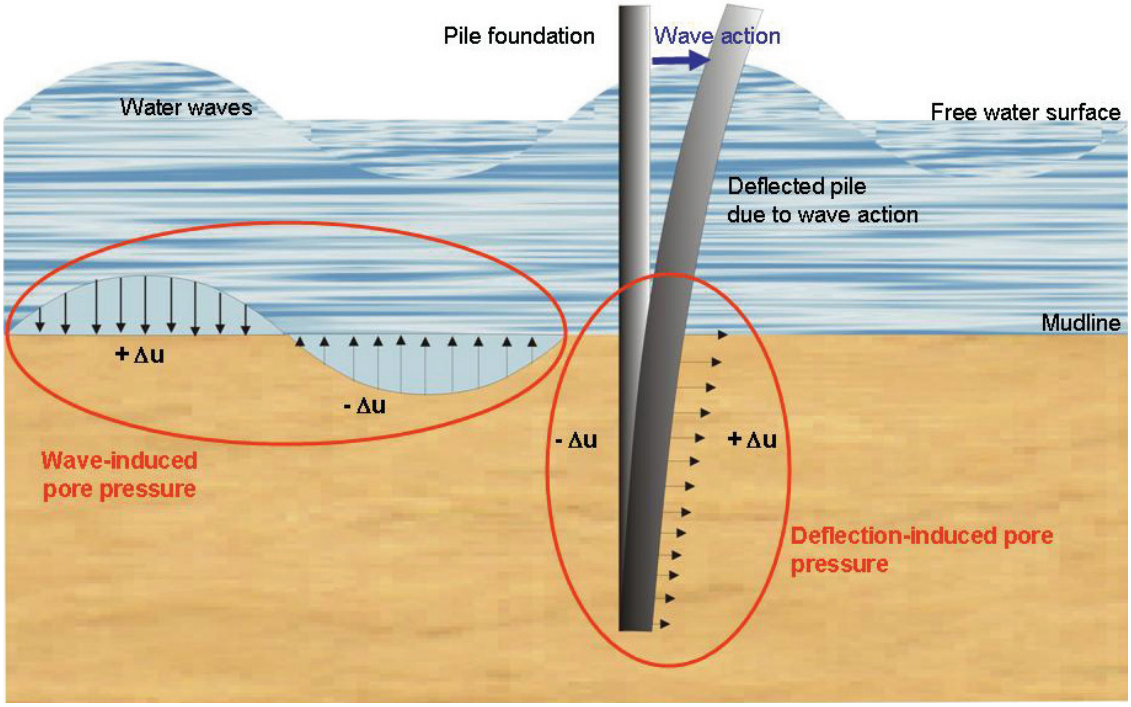

Fig. 4-1: Wave-induced pore pressure in a seabed and deflection-induced pore pressure due to the movement of a foundation structure.

Whereas seismic risk analyses for offshore structures already exist, it still has also to be ensured that structures built offshore are also safe against directly or indirectly induced liquefaction due to water waves. Because of the high horizontal forces and, therefore, the high lateral displacement, the wind turbines planned in the last years are vulnerable for deflection-induced liquefaction and thus, have to be investigated carefully.

4.1 Soil liquefaction due to oscillating water pressure

SEED and IDRISS (1982) report the failure of a steel pipeline in Lake Ontario during a storm which was traced back to soil liquefaction due to oscillating water pressure. According to SUMER and FREDSØE (2002), there are two different mechanisms of liquefaction: the “momentary liquefaction” and the “residual liquefaction”. A water wave propagating over the ocean

causes pressure oscillations in the sea bed as it is presented in Fig. 4-2 and, consequently, results in the development of shear stress in the soil. The pressure oscillations in the depth z below the mudline depend on the wave characteristic L, T and H (length, time, height) and on the water depth h. In addition, because of the propagation of the wave, they also depend on the time. The amplitude p_0 of the wave-induced pressure p is high under the crest of the wave whereas it is low under its trough. The momentary liquefaction originates from the temporarily upward directed pressure gradient in the sea bed under a wave trough. It causes buoyancy in the soil resulting in momentary or transient liquefaction of the soil and is, therefore, relevant for structures embedded in the upper soil layers. In contrast, the residual liquefaction is characterized by a residual pore pressure generation due to the cyclic shear stresses in the soil which can increase with every wave. To determine the pressure oscillations, it is customary to use the linear Airy wave theory. It is assumed that the wave height is small compared to the water depth ($H < h$) and that the sea bed is rigid and nearly impermeable.

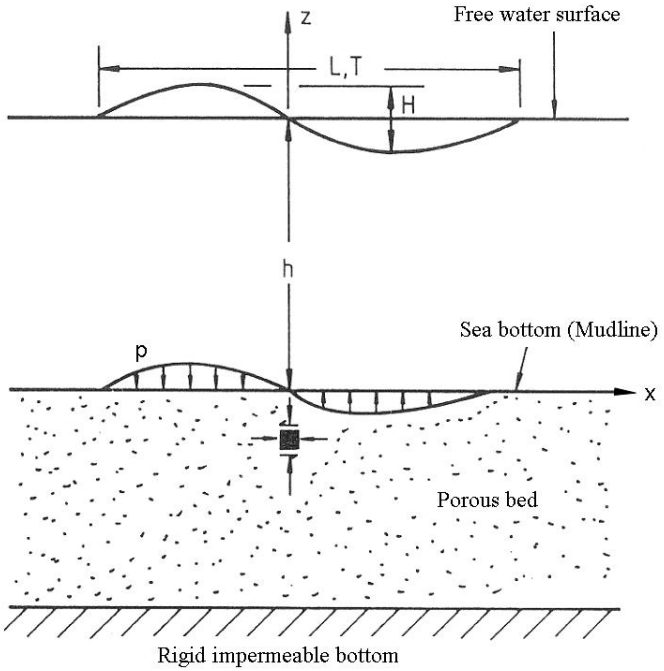

Fig. 4-2: Pressure distribution in the ocean soil due to oscillating water pressure (POULOS (1988)).

According to POULOUS (1988), the wave motion generates the vertical stress σ_v and the cyclic shear stress τ_{hv} which are calculated for a soil element in the depth z of the sea bed as

$$\sigma_v = p_0 \cdot (1 + kz) \cdot \exp(-kz) \cdot \cos(kx - \omega t) \tag{4-1}$$

and

$$\tau_{hv} = p_0 \cdot kz \cdot \exp(-kz) \cdot \sin(kx - \omega t)\,. \tag{4-2}$$

The wave number k is determined from $k = 2\pi / L$ and the angular frequency $\omega = 2\pi / T$. It has to be considered that the stresses are subject to permanent variations. The excess pore pressure under the wave crest tends to dissipate in the adjacent regions under negative pressure. When

the wave trough is above this point, water begins to flow back from the adjacent regions until again the wave crest supersedes the trough. Hence, pore pressure generation is permanently accompanied by pore pressure dissipation. Nevertheless, a long-term accumulation of pore pressure can be observed under certain circumstances. This is represented in Fig. 4-3.

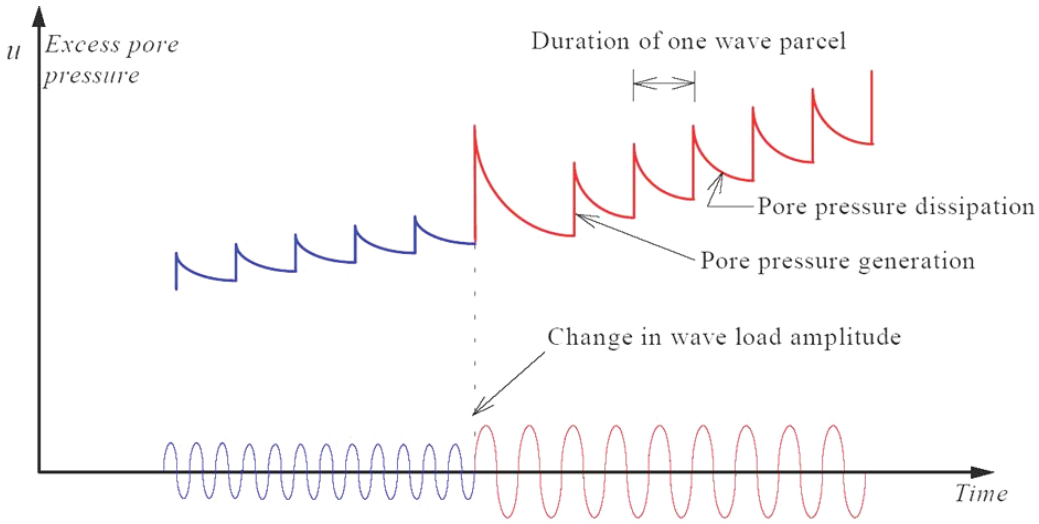

Fig. 4-3: Pore pressure generation and dissipation due to oscillating water pressure. A change in the wave load amplitude leads to higher pore pressure generation (TAIEBAT and CARTER (2000)).

To check whether the pore pressure accumulation leads to a liquefaction of the ocean soil or not, POULOS (1988) presents two approaches that both are based on the comparison of the wave-induced shear stress (the action) with the values required to cause liquefaction (the resistance). The approach of NATARAJA and GILL (1983) makes use of data from standard penetration tests (SPT). Firstly, the wave-induced shear stress τ_{hv} at various depths is estimated according to Eq. (4-2). Then, τ_{hv} is compared to the cyclic shear strength of the soil which is empirically estimated from the SPT-data. In the depths, where the actual stress is higher than the strength of the soil, the soil is said to be liquefied. The approach of ISHIHARA and YAMAZAKI (1984) uses an empirical estimate which depends on the relative density of the soil to determine the cyclic stress ratio τ / σ_v to cause liquefaction. A limit value of 0.23 is defined. If τ / σ_v exceeds this limit value, liquefaction is unlikely to occur. If the ratio is smaller than 0.23, liquefaction is possible. By means of a diagram, the depth below the mudline where liquefaction occurs can then be determined.

The approaches were applied for a water wave travelling over the sea bed with a wave height of 14 m, a wave length of 168 m and a wave period of 13 s. The water depth was assumed to be 20 m; the relative density 0.61. The wave-induced stress exceeds the stress to cause liquefaction down to a depth of 20 m under the mudline when following the approach of NATARAJA and GILL (1983). When applying the approach of ISHIHARA and YAMAZAKI (1984), liquefaction occurs down to 30 m under the mudline. Hence, a wide range of depths can be affected by wave-induced liquefaction. Thus, in the case of an offshore pile foundation, liquefaction would occur over a large part of the embedded length. But it has to be noted that the results of both approaches strongly depend on the wave and the soil parameters. Hence, definite predictions

cannot be derived from the previous findings. Therefore, more in situ measurements must be performed and examined carefully. More details on the wave-induced pore pressure generation can be found, e.g., in VERRUIJT (1982), NAGO and MAENO (1987), ZEN et al. (1998) and CHENG et al. (2001).

4.2 Soil liquefaction due to the displacement of marine structures

During an ocean storm, waves do not only load the sea bed but also the structures which are founded on the sea bed. A wave exerts a lateral force on the structure (gravity foundation, pile foundation, etc.) that varies with the propagation of the wave. The structure is firstly loaded in direction of the wave propagation, then in the opposite direction. The forces are transferred over the structure to the subsoil and cause a rearrangement of the soil particles in vicinity of the structure. According to the cyclic strain approach, e.g., of Finn and Byrne (Section 3.4.3), volume reductions lead to a generation of pore pressure. Depending on the characteristics of the loading and the soil, this pore pressure can accumulate resulting in soil liquefaction.

OUMERACI and KUDELLA (2004) showed within their experiments on a caisson foundation that a part of the pore pressure generation can be traced back directly to the displacement of the structure under consideration (compare Section 4.3.1): The waves that load the structure cause a tilting of the structure back and forth resulting in a build-up of pore pressure in the underlying sand. Equivalent studies on pile foundations do not exist and experiences from earthquake studies cannot be transferred. Therefore, the examination of the deflection-induced pore pressure generation around pile foundations was the objective of the investigations carried out within this doctoral work.

4.3 Previous analyses on offshore structures

Although most of the studies dealing with the liquefaction phenomenon concentrate on earthquakes, there are also some studies of liquefaction around offshore structures for the non-earthquake case. TAIEBAT (1999) gives a broad, chronological review of the literature dedicated to that topic. Here, the review begins with the literature that covers analyses of gravity foundations as most of the analyses deal with that type of structures. But as the loading and drainage characteristics of gravity foundations strongly differ from the ones of pile foundations, the studies that deal with the liquefaction phenomenon around pile foundations are resumed in an extra section.

4.3.1 Gravity structures

Section 4.1 considered the pore pressure generation due to the oscillating water pressure in the sea bed without structures. In the 1970s, research on the liquefaction susceptibility of ocean soil also began to include marine structures as interest in that topic rose with the construction of the Ekofisk tank. This concrete structure was installed in 1973 in the Norwegian North Sea and serves as production platform and oil storage tank. As can be seen in Fig. 4-4, the Ekofisk tank has a diameter of 93 m and is placed in a water depth of 90 m. It is founded on a layer of fine sand with a thickness of 26 m, below there is clay. To check if the sand under the tank could

liquefy under storm wave loadings, an extensive testing program was carried out. The tank was filled with water for several months prior to filling it with oil because the risk of failure was not known (LEE and FOCHT (1975)). It was instrumented with devices to measure oceanographic data, pore pressures in the soil directly under the foundation, and the settlement and tilt of the tank (CLAUSEN et al. (1975)). The tank was subject to several minor and major storms and liquefaction was found to be a possibility that had to be considered carefully in the design of offshore structures. Therefore, before and after the installation of the tank, the liquefaction potential in the subsoil of the Ekofisk tank was analysed in many studies.

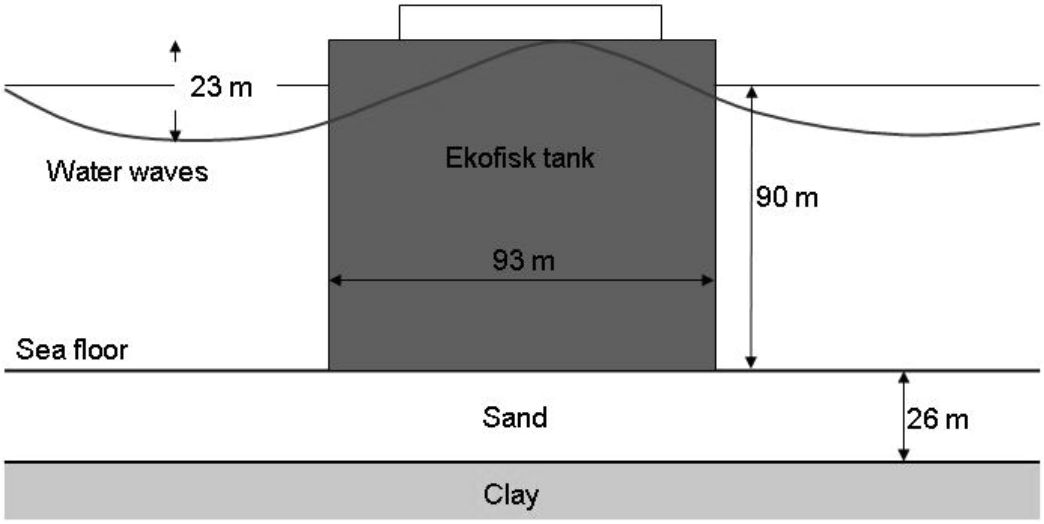

Fig. 4-4: Geometry of the Ekofisk tank (after TAIEBAT (1999)).

BJERRUM (1973) was the first to recognize and analyse the possibility of liquefaction occurring in saturated sea bed sediments. Contrary to the case with no additional structure, the Ekofisk tank makes it difficult for the water under the structure to dissipate. A design storm with a return period of 100 years was used in the analysis. In spite of the assumption of no drainage, it was concluded that liquefaction due to the cyclic wave loads would not occur. LEE and FOCHT (1975) carried out cyclic triaxial tests to determine the cyclic loading strength of the Ekofisk soil, also under undrained conditions. In their tests, the loading frequency firstly corresponded to the frequency of ocean waves which was taken as 1/12 Hz. But it was experienced that the frequency seemed to have only little influence on the cyclic loading strength of the sand. Hence, it was set to 1 Hz in order to speed up the testing program. The liquefaction potential was evaluated by considering all possible configurations of waves for the design storm. It was found that liquefaction would occur for the lower relative densities of the soil. This method was then extended by additionally considering the pore pressure dissipation which would take place between the storm events and also between the storm waves themselves (a fact that strongly differs from the assumptions taken for earthquakes). This showed positive effects on the strength of the soil, but could not completely prevent liquefaction. RAHMAN et al. (1977) were the first to present a numerical solution of the Ekofisk problem. Cyclic simple shear tests were used to evaluate the pore pressure generation as well as its dissipation. A complete time history of pore pressure was provided for selected points under the tank during the storm. The results were compared to Bjerrum's undrained analysis and also here, liquefaction did not occur.

VERRUIJT and SONG (1991) came to the same result by a finite element analysis: the Ekofisk tank would be safe against liquefaction. TAIEBAT (1999) performed calculations with an advanced model based on the work of RAHMAN et al. (1977). The constitutive model is an elasto-plastic model based on the Mohr-Coulomb failure criterion. To incorporate the effects of cyclic loading, it includes additional plastic volumetric strains. Liquefaction-induced failure was predicted within this analysis but the predicted pore pressures as well as the predicted settlements were slightly larger than the measured values. Other studies dealing with the risk of liquefaction near offshore caisson foundations can be found in JESSBERGER and JORDAN (1980) or in SCHUPPENER (1980).

In the test series carried out by OUMERACI and KUDELLA (2004), the pore pressure generation was traced back not only to the direct action of the waves but, for the first time, also to the motion of the structure itself. Large scale experiments were carried out in the large wave channel of Hanover and the pore pressure generation process was studied under a caisson structure when loaded by waves. The terms “wave motion mode” and “caisson motion mode” are used by the authors. The wave motion mode causes pore pressure changes in the subsoil due to the direct influence of waves (independent of the closeness to the caisson). The caisson motion mode generates pore pressure changes in the subsoil due to the motion of the structure itself (the pore pressure generation due to this mode corresponds to the here so-called deflection-induced pore pressure generation). Within the test program, pulsating and braking wave impact loads were analysed. According to the measurements, the generation of transient pore pressure outside the sea bed was dominated by the wave mode, whereas the pore pressure measured directly under the edge of the caisson was rather dominated by the caisson motion mode. The caisson motion mode strongly influences the transient pore pressure but its influence decreases with increasing distance from the caisson. Furthermore, it was seen that impact loads induce a higher caisson motion than the pulsation loads and that only impact loading exceeded the threshold value of the frequency and amplitude of the caisson motion which is required for the initiation of residual pore pressure generation.

Another aspect that was studied was the pore pressure generation with time. In Fig. 4-5, the measured motion of the caisson (at the posterior edge of the caisson) as well as the resulting moment and the thereby induced pore pressure is represented. Although the moment does not vary significantly over the total number of wave cycles, the deformation as well as the pore pressure increases (the transient as well as the residual pore pressure). This increase starts after about 130 cycles (Inflexion point I): both the deformation and the transient pore pressure get larger and the residual pore pressure begins to build up significantly. When exceeding a “Saturation point” S, the residual pore pressure begins to decrease while the residual soil deformation still increases. From there on, the dissipation of the pore pressure dominates its generation. Total residual liquefaction was not achieved even a strong accumulation of pore pressure due to the motion of the structure was shown.

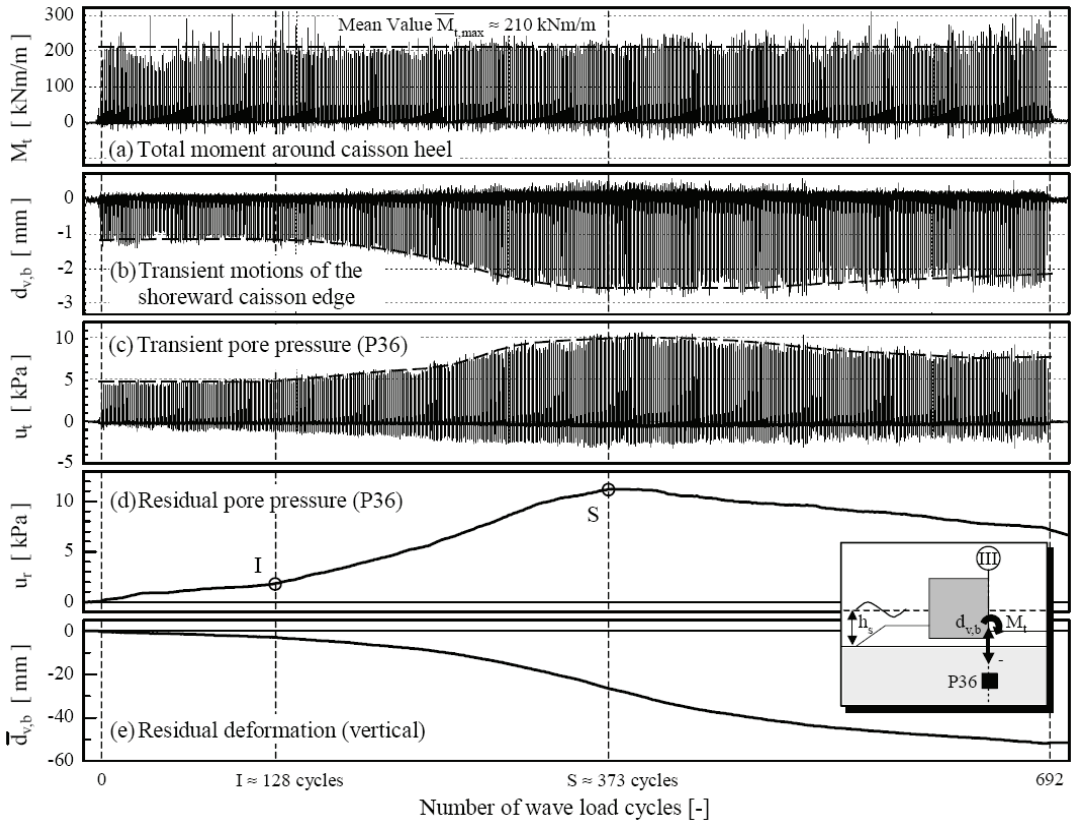

Fig. 4-5: Wave load, soil deformation and pore pressure response of a test model caisson structure loaded by waves (OUMERACI and KUDELLA (2004)).

4.3.2 Pile foundations

As the wave-induced motion of caissons is different from the motion of pile foundations (and also the drainage possibilities differ from one foundation to the other), the pore pressure generation induced by the motion of pile foundations should be examined. However until now, there are only few studies that can be found in literature that deal with the liquefaction phenomena around pile structures offshore.

Studies that were done earlier as, e.g., the analysis of HETTLER (1981) or the load tests of LONG and VANNESTE (1994) focus on the deflection of the pile during cyclic loading and on the thereby induced displacements but do not consider the pore pressure response in the soil. As mentioned in Section 3.4.3, MARTIN et al. (1975), FINN et al. (1977) and MARTIN et al. (1978) developed basic equations to relate the shear stress, the shear strain and the pore pressure in saturated granular soil during cyclic loading. Based on that research, MARTIN et al. (1980) studied the lateral soil pile interaction due to earthquakes with respect to pore pressure generation and dissipation. The presented analytical solutions show that the extent of dissipation or redistribution of pore pressure generated during cyclic loading can be significant and mainly depend on the permeability of the soil, the drainage path length and the distance from the pile. LEE and POULOS (1988) used the method of RAHMAN et al. (1977) to study the influence of excess pore pressure on the axial response of offshore piles. The waves of the design storm were assumed to induce only cyclic axial loading on the pile. The skin friction as well as the elastic

soil modulus was reduced during cyclic loading and the changes in the bearing capacity of the pile were studied for various values of soil permeability. REESE et al. (1988) analysed an offshore platform founded on four groups of piles and subject to cyclic lateral load induced by storm loading. In a first step, a design storm was defined and its wave heights and forces were determined. In a second step, the wave-induced deflection was calculated using the p-y method. The strain field resulting from those deflections was determined by a hybrid, finite element formulation. Then, a pore pressure generation model was developed based on cyclic strain-controlled triaxial tests on saturated sand. Thus, the pore pressure resulting from the strains due to the wave-induced deflection could be determined. A simplified computation of dissipating pore water was included to the model and thus, the pore pressure was predicted for the storm peak and for the end of the storm.

Apart from analytical and numerical investigations, another approach to analyse the unknown processes would be to model them in a smaller scale, i.e., to carry out experiments. Although this is a very promising approach, final results of such experiments cannot be found in literature. Some investigations have only been carried out in the very last years by different researchers (STAHLMANN and KLUGE (2003), SAVIDIS et al. (2004), GRABE et al. (2004), KOHLHASE et al. (2005), ACHMUS et al. (2007)). Nevertheless, most of them consider the displacement due to the cyclic loading but not the pore pressure response in the soil and final conclusions are not available yet.

4.4 Summary and conclusions

First investigations of soil liquefaction in the offshore environment considered the infrastructural devices of the oil and gas industry. Waves as liquefaction-inducing factor were examined and it was shown that also this loading with a lower frequency could evoke soil liquefaction. A relatively new research field is related to the infrastructural devices of the wind energy industry that explicitly want to exploit the natural forces offshore and are, therefore, characterized by high horizontal forces. It was shown in the investigations carried out so far and described in the previous sections that cyclic loading of soils may result in an excess pore pressure leading to a progressive degradation of the soil resistance. Due to the lack of experimental tests on pile foundations, it is not known whether the cyclic loading of, e.g., monopile foundations for the wind energy industry can also lead to the build-up of excess pore pressure and to a degradation of the resistance of the soil in vicinity of an offshore foundation.

The present research work attends to these open questions by investigating the pore pressure in a test model and by simulating this pore pressure numerically. The conduction of the test model is considered as a very important task in order to allow the verification and validation of numerical models. Hence, the aim of the investigations undertaken within this work is to examine the reaction of the pore pressure on the cyclic loading of a monopile foundation and to reveal the dependency of the pore pressure on its input parameters. The test series represent the first investigations of their kind and are regarded as first step towards the ambitious aim to assess the risk of soil liquefaction around offshore pile foundations. Thus, they supply important information on the behaviour of pore pressure besides cyclically loaded pile foundations.

5 Test model to analyse the deflection-induced pore pressure

5.1 Objectives and procedures

As already discussed, experiences concerning the foundation of offshore structures are mainly based on experiences of the oil and gas industry. In addition, few wind farms have been built near shore in the last years. Thus, there are neither measurements nor experience on foundations of the offshore wind industry until now. Numerical models can be applied to the situation, but they are not validated yet. So, the aim of this research work is to analyse the geotechnical processes in the soil by means of a test model, i.e., to enable an analysis of the pore pressure changes in the soil due to the loading-induced deflection of the pile foundation. Since test models with caisson structures were already carried out and since the monopile foundation is a common foundation option for the wind turbines, a pile foundation is considered in the test model.

First test series were carried out with a pneumatically-driven, force-controlled loading system. It pulled the pile in one direction and then, permitted it to swing back freely. Thus, very realistic loading conditions could be reproduced. But those preliminary tests showed many degrees of freedom and were not reproducible. Hence, it was decided to carry out displacement-controlled test series first. In those displacement-controlled tests, the pile is deflected by a motor-driven con-rod (compare Section 5.3.4). Only doing so, it is possible to analyse the pore pressure changes in the soil and to detect dependencies of those pore pressure changes on the input parameters. Force-driven test series and the so-permitted possible tilting of the structures have to be analysed in further test series.

The test stand, which was designed within this research work, is depicted in Fig. 5-1. It consists of a box (area: 2 x 3 m, height: 3 m) which is filled with water and sand. The test pile is placed in the middle of the stand. It is a pile (3 m long) which is embedded with 1.5 m of its length in the sand. Above the sand level, there is 1 m of water. The structures in front and behind the pile are frame structures that hold the loading system and the measurement devices. The response of the loading in terms of pore pressure is measured at four levels next to the pile. All those parts will be discussed in the next sections.

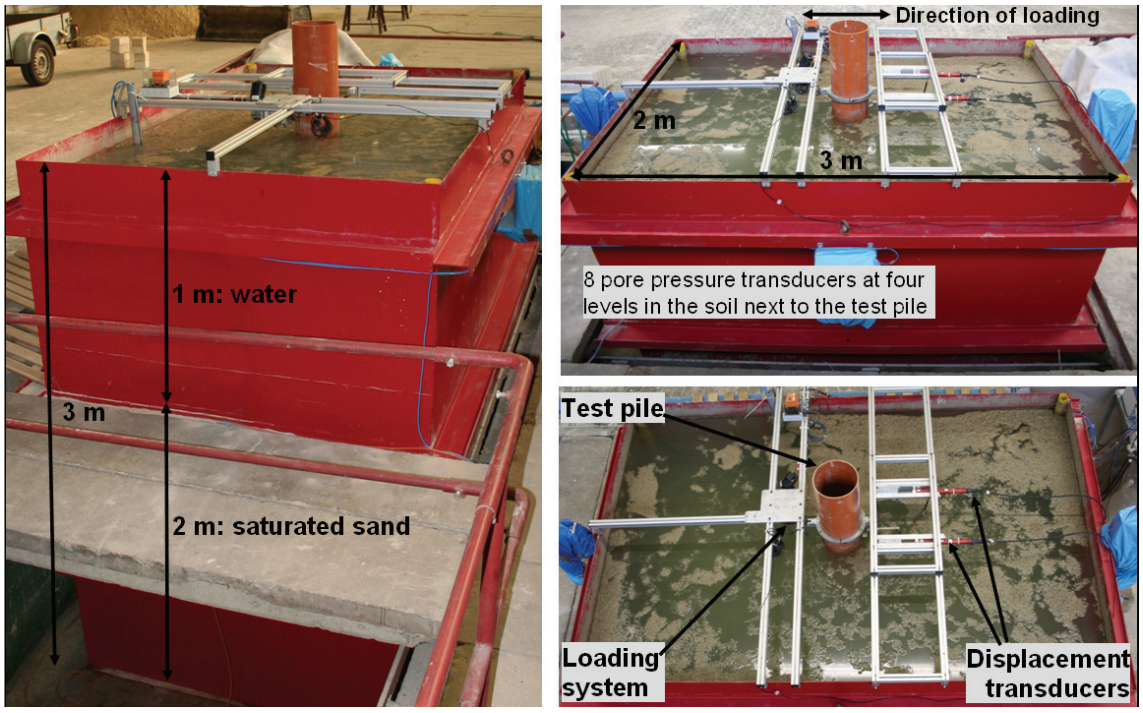

Fig. 5-1: Set-up of the test model.

In the displacement-controlled test series carried out within this research, the deflection of the pile is characterized by its amplitude and by the frequency of the cyclic loading. As it was described in Section 3.4.2, volumetric strains that accumulate during dynamic loading can cause the generation of pore pressure. Hence, it has to be analysed on the one hand whether the deflection of a pile also causes volumetric strains which lead to the same result. On the other hand, the loading frequency influences the drainage rate of the pore water: low frequencies allow a higher drainage than high frequencies. Therefore, to determine the influence of those two factors on the pore pressure generation, different test series were carried out in which those parameters were varied.

5.2 Similarity laws

To allow the transfer from reality to a test model (and vice versa), the offshore structure itself as well as the soil around its foundation has to be modelled properly. Since the costs of a test model increase with the scale of the model to the power of three, the model scale should be kept as small as possible on the one hand (OUMERACI (1994)). On the other hand, the chosen scale must be large enough in order to achieve appropriate data that help to explain a certain phenomenon and that allow the transfer back to nature. Thus, an appropriate scale must be found that fulfils those requirements best at acceptable costs and at minimized scaling errors.

Dimension analyses are performed to assure the proper reproduction of the physical processes under investigation in an experiment. The basic theoretical principles for this task were developed among others by BUCKINGHAM (1915) who developed the most widely accepted theorem called “Buckingham π-theorem”. The aim of this theorem is to transfer the most important physical variables of a system into dimensionless key figures that have to be equal in reality and

in the model. Therefrom, scaling factors can be obtained which determine how the physical variables are scaled down to the model. The π-theorem can be broken down as follows:

- All governing physical properties of the system under consideration are determined. They consist of the parameters describing the structure, the soil and the loading conditions.
- Reference values are defined that are used to transfer those values into dimensionless form which is achieved by simple multiplications or divisions. If only geometric dimensions are to be transferred to a model, it is obvious that the value "length" with the dimension [m] can be used as reference value for that purpose. Considering the example given in Fig. 5-2 for example, the length of the pile $l_{p,o}$ and $l_{p,m}$, respectively, can be chosen as reference values (o being the index for the original system; m for the model).

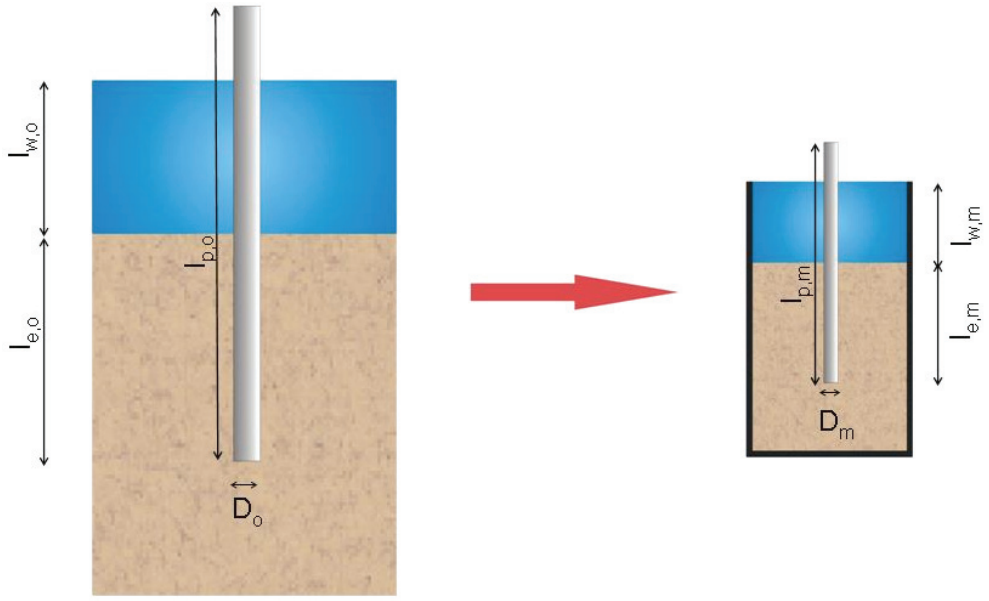

Fig. 5-2: Transfer of geometrical dimensions from the real world to a model.

- All geometric dimensions are brought in dimensionless form by the reference lengths l_p and all so-achieved key figures have to be equal for the original system and the model. This is exemplarily shown for the embedded length l_e of the pile:

$$\frac{l_{e,o}}{l_{p,o}} = \frac{l_{e,m}}{l_{p,m}} \quad . \qquad \frac{[m]}{[m]} = [-] \tag{5-1}$$

- This expression is valid for all scales. Thus, the scaling factor λ is chosen and can be expressed by

$$\lambda = \frac{l_{p,o}}{l_{p,m}} = \frac{l_{e,o}}{l_{e,m}} . \tag{5-2}$$

- If other dimensions are involved, additional reference values have to be chosen, e.g., the specific unit weight of soil γ_s [kN/m^3]. A force F, for example, can then be turned in dimensionless form by the division with the product of γ_s and the reference length l_p to the power or 3:

$$\left(\frac{F_o}{\gamma_{s,o}\cdot l_{p,o}^3}\right)=\left(\frac{F_m}{\gamma_{s,m}\cdot l_{p,m}^3}\right). \qquad \frac{[kN]}{[kN/m^3]\cdot[m^3]}=[-] \tag{5-3}$$

- When the specific unit weight of soil γ_s is the same for the reality system and for the model ($\gamma_{s,m}=\gamma_{s,o}$), the scaling factor for the forces is given by the expression of Eq. (5-4). According to this procedure, all scaling factors for the transfer of the variables from the real world to the model can be determined. The results are summarized in Table 5-1.

$$\left(\frac{F_o}{F_m}\right)=\left(\frac{l_{p,m}^3}{l_{p,o}^3}\right)=\left(\frac{1}{\lambda^3}\right) \tag{5-4}$$

Table 5-1: Variables of a system and their scaling factors.

Variable	Denotation	Dimension	Size in the test model
Length	l	m	$l_m = l_o / \lambda$
Area	A	m^2	$A_m = A_o / \lambda^2$
Volume	V	m^3	$V_m = V_o / \lambda^3$
Unit weight	γ_s	kN/m^3	$\gamma_m = \gamma_o$
Force	F	kN	$F_m = F_o / \lambda^3$
Line load	P	kN/m	$P_m = P_o / \lambda^2$
Stress	σ	kN/m^2	$\sigma_m = \sigma_o / \lambda$
Moment	M	kNm	$M_m = M_o / \lambda^4$
Time	t	s	$t_m = t_o / \sqrt{\lambda}$
Velocity	v	m/s	$v_m = v_o / \sqrt{\lambda}$
Viscosity	ν	m^2/s	$\nu_m = \left(\frac{1}{\lambda}\right)^{3/2} \cdot \nu_o$

The scaling rules given explicitly in Table 5-1 also apply to other variables with the same dimension. For example, the modulus of elasticity E has the same scaling factor as the stress σ. Since sometimes, it is not possible to find a material that fulfils the required scaling factors for, e.g., the modulus of elasticity E, the relevant structural property can be modelled instead, e.g., the flexural stiffness EI of a pile structure. With $\gamma_{s,m}=\gamma_{s,o}$, the scaling factor for the flexural stiffness is defined to $(E\cdot I)_m = (E\cdot I)_o / \lambda^5$. Doing so, not only another material but also different profiles can be used which then changes the moment of inertia I. An alternative procedure is proposed by WALZ (1982) who calculates the required wall thickness of the model pile by scaling-down the elastic length of the pile following geometric similarity. It has to be decided from case to case which methods are the most appropriate for the problem under consideration.

Even though, all rules cannot always be followed. Hence, it has to be assured that at least the most important variables that influence the system are properly transferred to the model. The others are neglected. This negligence leads to scaling errors that should be minimized. Looking at the viscosity of water, for example, it can easily be seen that not all similarity laws can be properly applied when reproducing the original in a smaller scale. For a test model in a scale of, for example, 1:20 ($\lambda = 20$), a fluid with a viscosity of almost 90 times lower than that of water would be required. But such a thin fluid practically does not exist and so, water with its usual viscosity is commonly used in down-scaled test models accepting that dynamic similarity is not totally achieved. Also for the test model described here, usual water was used.

5.3 Test model set-up

Present-day, it is feasible to drive offshore pile foundations with diameters of approximately 5 m. Therefore, a diameter of 5 m was taken for the in situ pile to be scaled down in the model. The water depth was assumed to be 20 m and the embedded length of the pile in the soil was taken to 30 m. Those relevant geometric dimensions from in situ were scaled down for the test model by the factor $\lambda = 20$ and determine the test model set-up. The geometric dimensions of the in situ pile as well as those of the test pile are given in Table 5-2.

A box consisting of steel-plates and with an area of 2 m x 3 m and a height of 3 m was constructed (see Fig. 5-1). In direction of the applied loading, it is 3 m long (= 12 times the diameter of the pile) which is supposed to be large enough in terms of minimized reflections. The tank is filled with saturated sand up to approximately a height of 2 m and with water up to a height of 3 m. In Fig. 5-3, a sketch of the test model with its dimensions is given.

Table 5-2: Geometric dimensions of a monopile foundation (in situ and test model).

Dimension	In situ [m]	Test model [m]
External diameter (pile)	5.00	0.25
Embedded length (pile)	30.00	1.50
Water table over sand bed	20.00	1.00

In order to easily pump out the water from the box after each test, a drainage layer of poroton stones was placed at the bottom of the box and a drainage pipe was installed in every corner of the box. The stones in the drainage layer were covered by a fleece which was fixed to the box and sealed by a bitumen layer. So, only water can pass through the fleece which is essential for the protection of the pumps inserted in the pipes against damage by sand. Small pumps with low pumping speed were placed in every corner of the box in order to ensure a very slow drawdown of the water level and, in this way, a very little change of the soil density.

In order to place the pore pressure transducers that are installed in the model (compare Section 5.4.1), a frame with a holder was constructed for those devices. In Fig. 5-3, this frame is shown in grey whereas the red circles represent the position of the measurement devices. Deci-

sive for the shape of this structure was the demand that the disturbance of the soil should be as small as possible. Therefore, the vertical steel bars of the frame were placed not directly in the loading direction of the pile, but approximately 20 cm aside. Smaller horizontal bars permit to place the measurement devices directly in front of the pile. Those bars are flexible and thus, can be fixed at different heights and different distances from the pile.

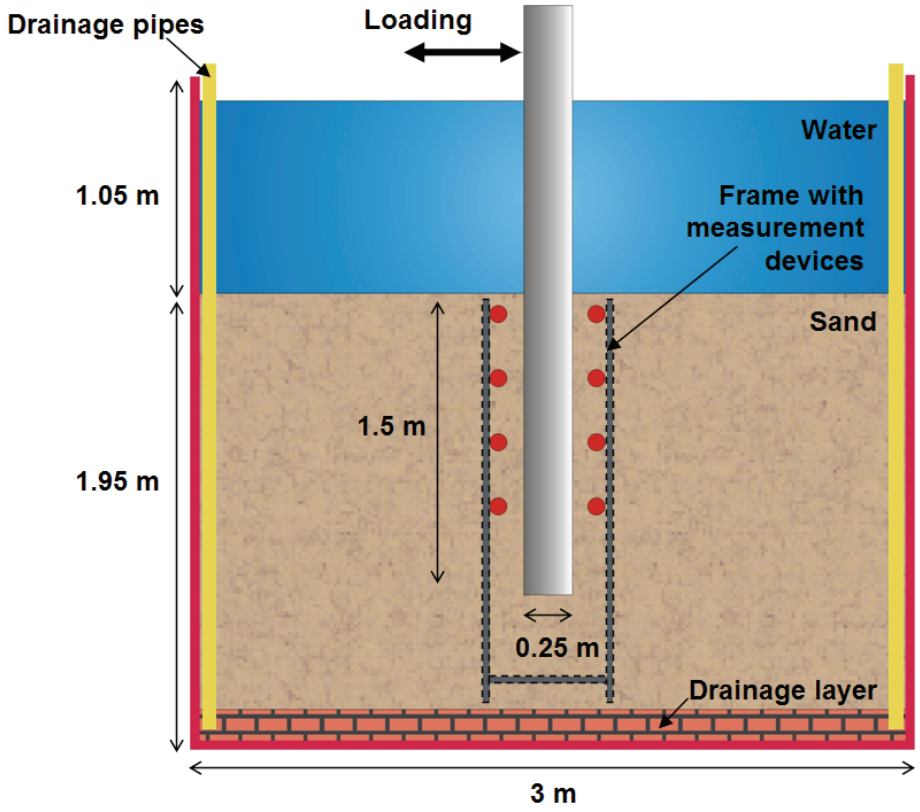

Fig. 5-3: Sketch of the test model: dimensions and placing of pore pressure transducers.

5.3.1 Model pile

It is not sufficient to scale only down the geometric dimensions, but also the stiffness of the pile plays an important role. Therefore, as it was discussed in Section 5.2, the stiffness has to be scaled down with λ to the power of 5. Alternatively, the pile can be dimensioned according to WALZ (1982). The test series carried out within this research were performed with a PVC pile with a diameter of 0.25 m and a wall thickness of 6.5 mm. It had a length of 3 m. A template was constructed that ensured the identical position of the pile and the measurement devices in the test series.

5.3.2 Model sand

Two things have to be considered when choosing sand for an experimental test. Firstly, the grains of the model sand have to fulfil geometrical similarity, i.e., they have to be λ-times smaller than the grains of the in situ soil. Secondly, the governing properties of the model sand have to equal the properties of the in situ sand. That means that granular soils cannot be mod-

elled with cohesive soils since they totally differ in their mechanical behaviour. When geometrically scaled down, the sand of the North Sea (compare Section 2.4) would fall into the grain sizes of cohesive soil. This would not be appropriate. Therefore, sand as fine as possible was chosen for the test series and it was assured that the permeability of the sand which is an important soil parameter regarding soil liquefaction was scaled down properly. According to Table 5-1, the coefficient of permeability k has to be scaled down from the original to the model according to

$$k_m = \frac{1}{\sqrt{\lambda}} \cdot k_o \tag{5-5}$$

For sand, the permeability can be estimated by means of the d_{10}-value (grain size of 10% passing) according to the Hazen law:

$$k\left[m/s\right] = d_{10}^2\left[cm\right] \tag{5-6}$$

Thus, with λ being 20, the d_{10}-value for the required model sand can be determined to:

$$d_{10,m} = \sqrt{k_m} = \sqrt{\frac{1}{\sqrt{\lambda}} \cdot k_o} = \sqrt{\frac{1}{\sqrt{\lambda}} \cdot d_{10,o}^2} = \sqrt{\frac{1}{\sqrt{\lambda}}} \cdot d_{10,o} = 0.47 \cdot d_{10,o} \tag{5-7}$$

Thus, sand from the Schlingmeyer Company, denoted as “Feinstsand G”, was chosen. Its grain size distribution is shown in Fig. 5-4. Using the existent d_{10}-values of this model sand and the North Sea sand (0.066 mm and 0.125 mm, respectively), the ratio of $d_{10,m}$ and $d_{10,o}$ (should be 0.47 according to (5-7)) is 0.53. This means that $d_{10,m}$ and consequently also k_m are slightly larger than demanded (approximately 12 %). Nevertheless, this is compensated by the fact that the same fluid as in reality is used in the test model. It is thicker than it should be and thus, this results in a slightly smaller k than demanded. Considering those compensating effects, the model sand was seen to well represent the soil conditions in the North Sea.

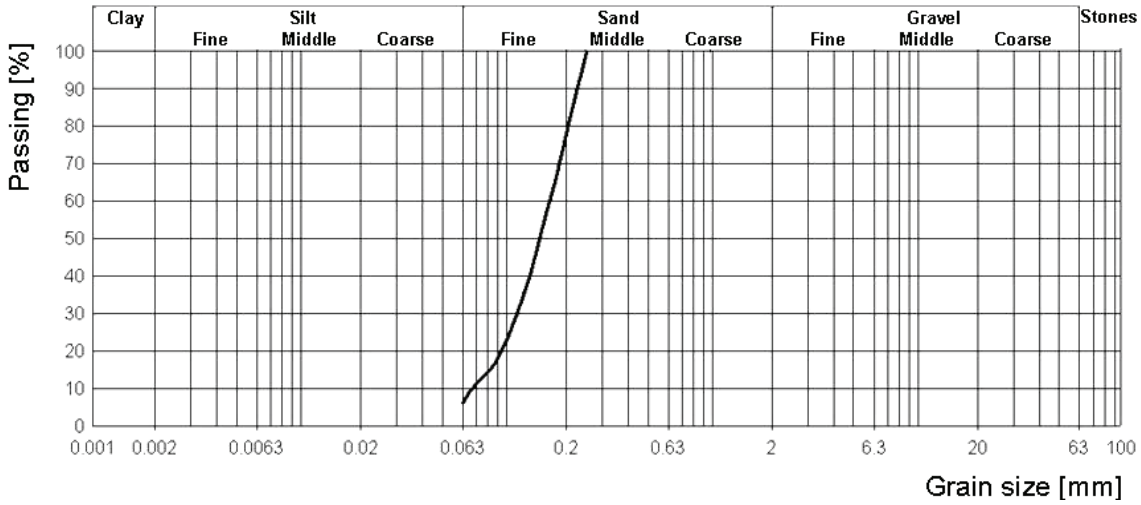

Fig. 5-4: Grain size distribution of the sand “Feinstsand G”.

As can be seen from the grain size distribution, the sand used in the test model is fine sand with a low fraction of medium sand. The coefficient of uniformity is 2.4 and the permeability coefficient is $2 \cdot 10^{-5}$ m/s. The density of the sand at the loosest and the densest packing was determined by the shaking table test (DIN 18126 (1996)). The friction angle was determined in a direct shear test. The mechanic properties of the sand are compiled in Table 5-3.

Table 5-3: Mechanic properties of the sand "Feinstsand G".

Density of dry soil		**Porosity**		**Void ratio**		**Friction angle**
$\rho_{d,min}$ [g/cm^3]	$\rho_{d,max}$ [g/cm^3]	n_{min} [-]	n_{max} [-]	e_{min} [-]	e_{max} [-]	φ [°]
1.219	1.583	0.403	0.540	0.674	1.175	36

5.3.3 Emplacement of the model sand

To ensure comparable test series, the test conditions concerning the compactness of the sand have always to be the same. Therefore, the sand is removed after each test and brought back before the start of a new experiment following always the same procedures. This preparation is mandatory for good results. In Fig. 5-5 and Fig. 5-6, the first 200 s of the data obtained by one of the pore pressure transducers is representatively shown for two different test series. The signals represent the pore pressure ratio r_u according to Eq. (3-10). Both tests were carried out with a forced displacement of ±0.75 cm at the point of load application and with a loading frequency of 1.5 Hz. In the first test (Fig. 5-5), the soil was removed and brought back before the test as it is done in the usual procedure. The second test (Fig. 5-6) was carried out 24 hours after the first one but without removing the sand. Thus, the sand was already loaded before. It can clearly be seen that preloading highly influences the results of the tests. Whereas the pore pressure ratio r_u in the test without preloading increases to approximately a value of $r_u = 1.2$ directly after the loading begins, r_u in the test with preloading oscillates with a nearly constant amplitude of approximately $r_u = 0.2$. This amplitude of the pore pressure ratio is reached after approximately 200 s for the case when the sand was removed and brought back and then, does not change considerably anymore. Hence, conditions are reached after 200 s for the case "without preloading" very similar to the ones obtained for the case "with preloading".

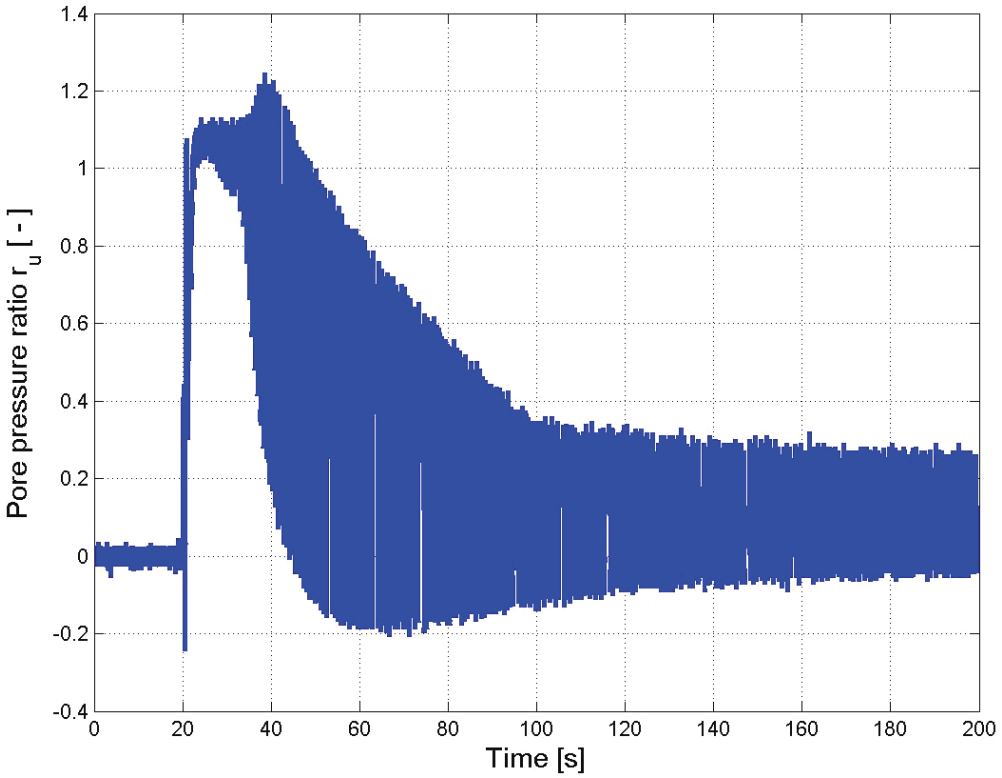

Fig. 5-5: First 200 s of the pore pressure signal in terms of the pore pressure ratio r_u without the soil being preloaded before. The loading starts after 20 s of data recording.

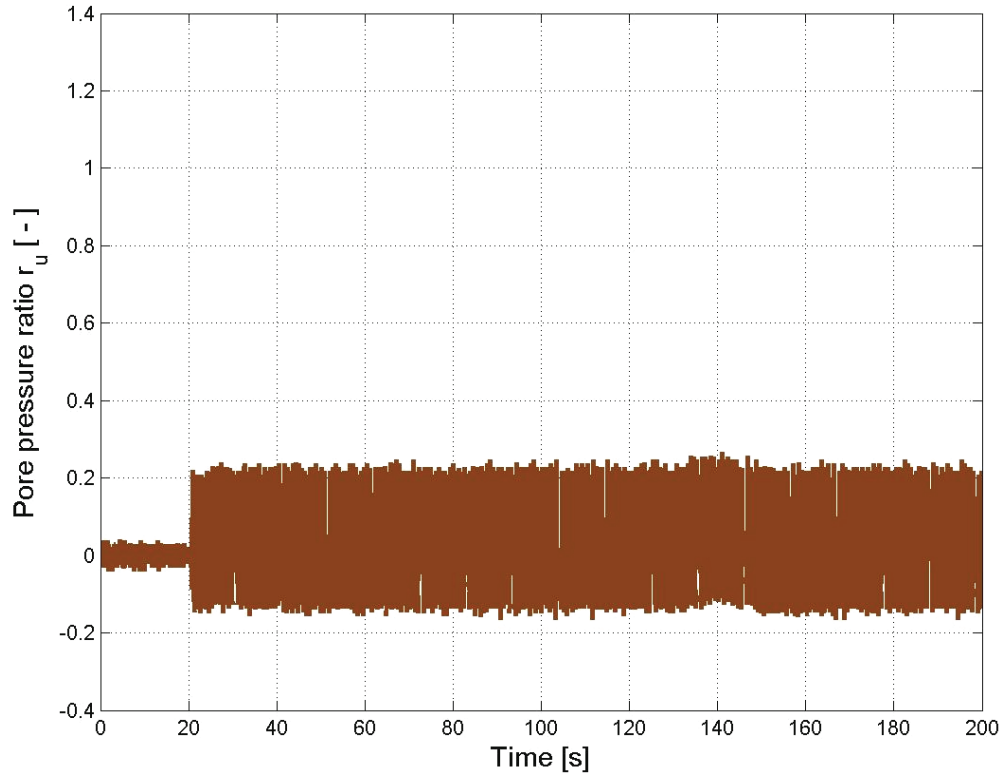

Fig. 5-6: First 200 s of the pore pressure signal in terms of the pore pressure ratio r_u with the soil being preloaded before. The loading starts after 20 s of data recording.

The results shown in Fig. 5-5 and Fig. 5-6 make clear that special emphasis has to be put on the emplacement of the sand. Therefore, before starting the test series, preliminary tests were conducted in a smaller scale as well as in the test model to define a special procedure for the emplacement of the sand. The aim was to ensure a homogenous emplacement which results in reproducible compactness and void content. The following procedure was chosen: Firstly, the test model is filled with approximately 10 m^3 of water which corresponds to a height of approximately 1.7 m. This filling process is interrupted three times because the pore pressure transducers need to be filled up with distilled water. Secondly, the sand is placed into the test model by means of a crane and a bucket. In doing so, the bucket is immersed in the water with about 2/3 of its height. It is then opened carefully and the sand begins to sink down slowly.

In a smaller-scale laboratory test it was observed that clusters of sand disintegrate as soon as they get in contact with water and that the sand sinks to ground very uniformly. Pilot tests confirmed this procedure in terms of a uniform density and a uniform surface of the sand. The so-achieved compactness of the sand was investigated by dynamic penetration tests and by cylindrical probes. For this purpose, soundings were carried out with a sounding rod developed by the IGB TUBS. This was necessary as usual sounding rods are not suitable for test models. The sounding rod that was used here has a drop weight of 2 kg and a drop height of 40 cm. It was assured that all tests had a loose to medium dense relative density.

When the process of filling in the sand is finished, all pore pressure transducers are covered with sand. The test model then contains sand up to a height of approximately 2 m and is filled with water to a level of about 3 m.

5.3.4 Loading system

The loading system is fixed on a frame on the top edge of the test stand. A motor driven con-rod is connected to a ring attached to the test pile as can be seen in Fig. 5-7. Two parameters can be set: the amplitude of displacement x_w and the frequency f. The displacement is given by the eccentricity of the con-rod. The frequency is controlled by the power supply of the motor: it linearly rises with the input voltage. The input voltage is controlled by a power supply unit.

Deflections of the pile with an amplitude up to $x_w = \pm 1.5$ cm (at the top of the pile at the load application) and a frequency of up to $f = 2.0$ Hz were realised within the test series. Those input parameters are shown in Fig. 5-8 for a test series with $x_w = \pm 1.5$ cm in (a) and $f = 2.0$ Hz in (b). The frequency was obtained by a Fast Fourier Transform of the signal shown in (a). In addition, it was recorded by an inductive proximity switch which was placed next to the con-rod and served for the real-time monitoring of this input parameter.

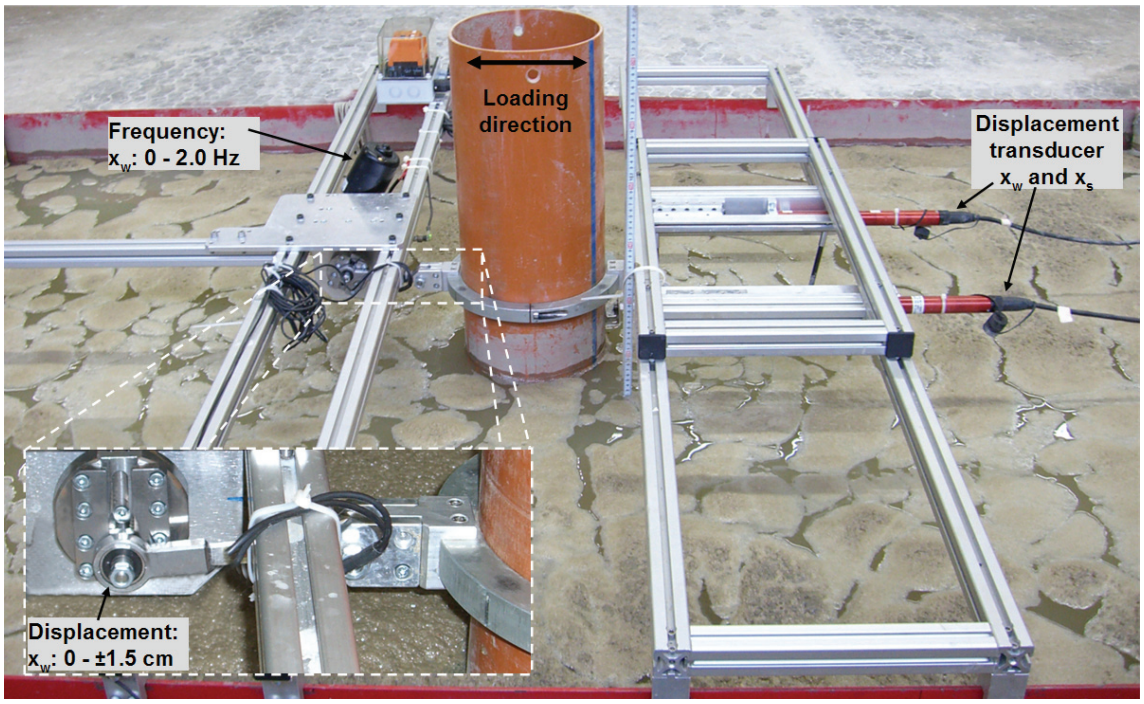

Fig. 5-7: Loading system.

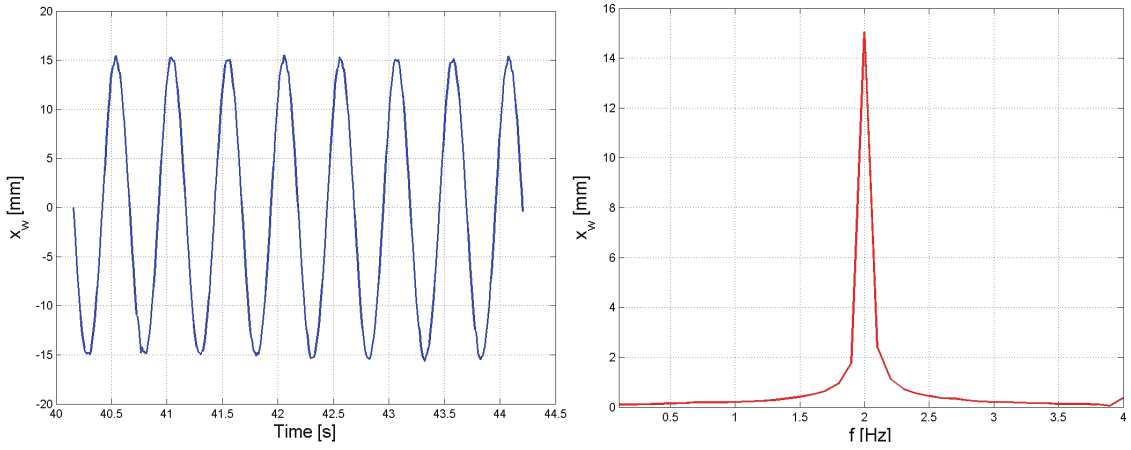

(a) **(b)**

Fig. 5-8: (a) Deflection x_w due to loading and (b) frequency of the loading as obtained by a Fast Fourier Transform of the signal shown in (a).

5.4 Measurement devices and data acquisition

To measure the pore pressure in the soil, eight pore pressure transducers are installed around the test pile. Those transducers are miniature transducers especially designed for test models with a pressure range of 0-0.3 (upper four transducers) and 0-0.5 bar (lower four transducers), respectively. Since the atmospheric pressure highly influences the measured values of those supersensitive transducers, an atmospheric pressure transducer is also used. Two displacement transducers measure the displacement of the pile during loading at two different levels. Furthermore, a frequency counter registers the loading frequency. The assembly of those measurement devices is schematically shown in Fig. 5-9.

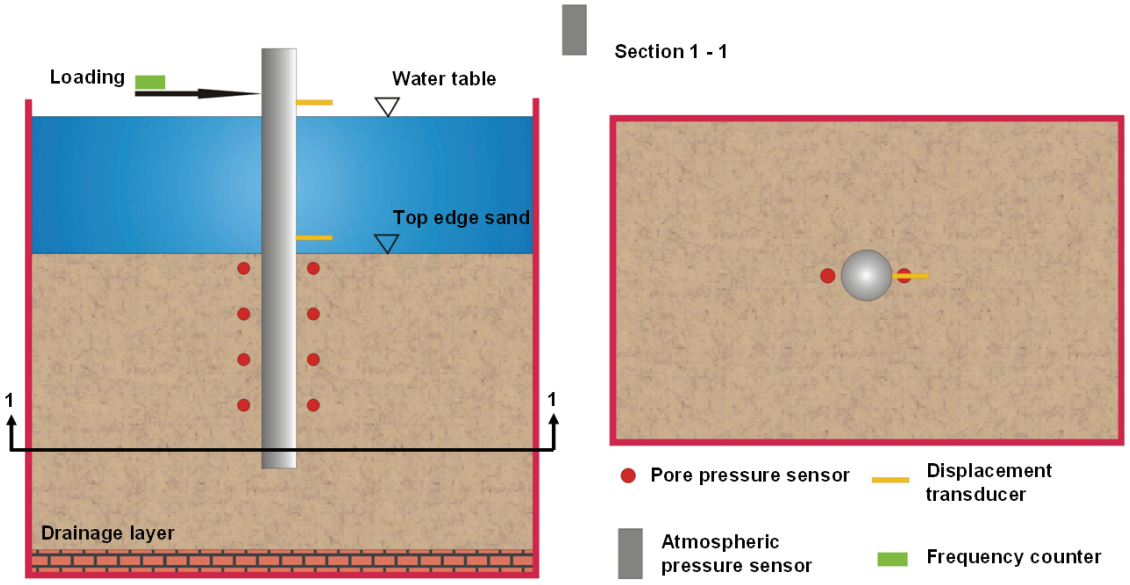

Fig. 5-9: Measurement devices installed in the test model.

All experimental data were acquired by a data acquisition instrument (National Instruments) and were converted into digital signals. The sampling rate was chosen according to DISYNET (2007) which demands a sampling rate of at least 5 times higher than the highest frequency to be measured in the system. To ameliorate the quality of the signals, the sampling rate was set to 100 Hz (50 times higher than the highest frequency of the system). The program LabVIEW was used for the control of the experiments, for data acquisition and for the graphical real-time presentation of the data. The data were recorded by a computer and then transferred to Matlab for the data analysis. Fig. 5-10 gives an overview of the data acquisition and of all measurement devices used within the tests.

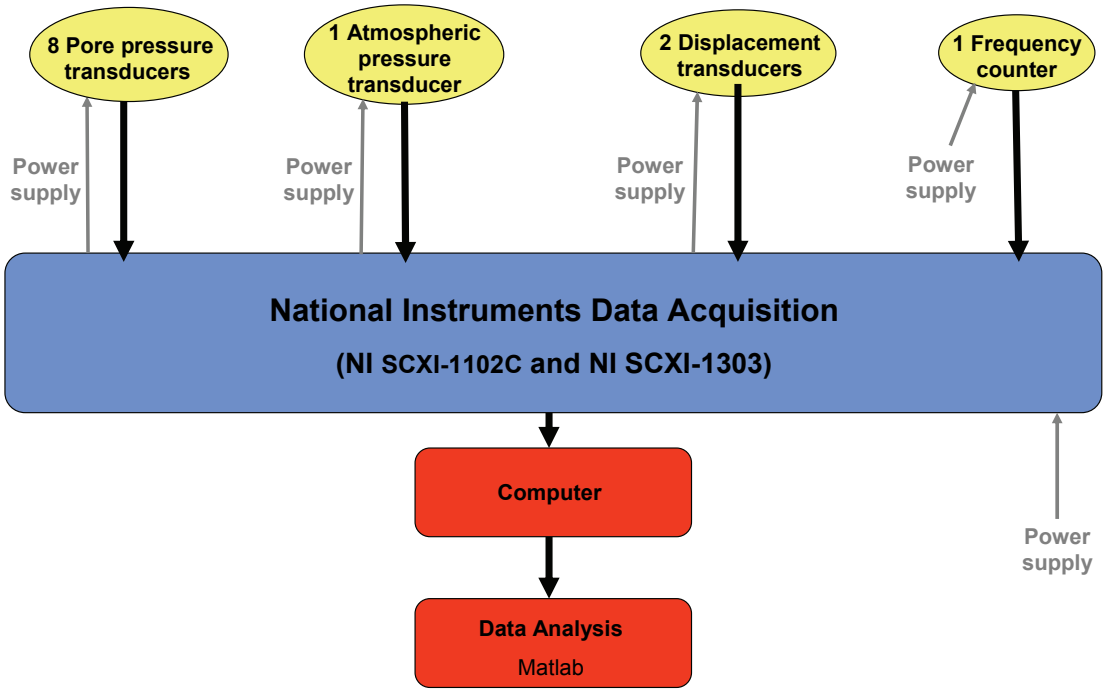

Fig. 5-10: Scheme of the data acquisition and the measurement devices.

5.4.1 Pore pressure transducers

Eight pore pressure transducers are installed around the test pile. They are fixed on a steel frame and placed right next to the pile. The measurement devices were installed at four levels before and behind the pile (in loading direction, see Fig. 5-11). The distance between those levels was 28 cm for every test series. In most tests, they were located 2.5 cm away from the pile. In two tests, in order to analyse the lateral spreading of excess pore pressure, the pore pressure was also measured at a distance of 10 and 20 cm from the pile. In all test series, the top level was covered by approximately 10 cm of soil. So, stresses were recorded in depths down to approximately 95 cm which corresponds to two thirds of the embedded length of the pile.

In order to calibrate the transducers before the test series, they were immersed in a cylindrical vessel filled with water. The measurement output of the transducers was recorded for different depths. Thus, a calibration curve (pressure versus voltage output) was obtained and calibration factors could be determined for each transducer.

It was seen that since the pressure transducers are miniature transducers for pressure ranges up to 0.3 bar and 0.5 bar, respectively, they are very sensitive to changes of the atmospheric pressure. For example, on a high-pressure day with 1030 mbar, the overpressure of +30 mbar, compared to 1000 mbar, equals to the pressure of a 30 cm water column. As an accurate measurement of pore pressure is the most important issue when assessing soil liquefaction, those atmospheric pressure changes had to be compensated. Therefore, an atmospheric pressure transducer was added to the test model. Also sampled with 100 Hz, the values of this transducer were incorporated in the calculation of the pore pressure. Doing so, the data of the pore pressure is always referenced to 1000 mbar and hence, is comparable for every test series. The sensitivity of the pore pressure transducers to transient changes in pressure was also tested and showed that the transducers react very fast to those variations.

Fig. 5-11: Steel frame for the pore pressure transducers.

5.4.2 Other measurement devices

Two displacement transducers are used to measure the deflection of the pile. As can be seen in Fig. 5-12, they are fixed on a metal frame just next to the pile and measure the deflection of the pile by means of extension arms that are attached to the pile. One transducer measures the deflection of the pile approximately at the location where the loading was applied on the pile. This is the left transducer shown on the pictures in Fig. 5-12. It is labelled x_w since it is placed near the water level. This mainly controls the displacement that is forced to the pile by the con-rod. The other transducer (labelled x_s since it is placed near the sand level) measures the deflection of the pile just above its embedding in the sand, approximately 1 m under x_w. Therefore, the second extension arm is immersed in the water and only the transducer itself can be seen in the picture.

An inductive proximity switch monitors and counts the loading frequency in real-time. So, it is possible to control the frequency during the test series. Its signals completely agreed with the frequencies chosen for the tests and with the Fourier Transforms of both the displacement and the pore pressure (see Section 5.3.4 and 6.1.2).

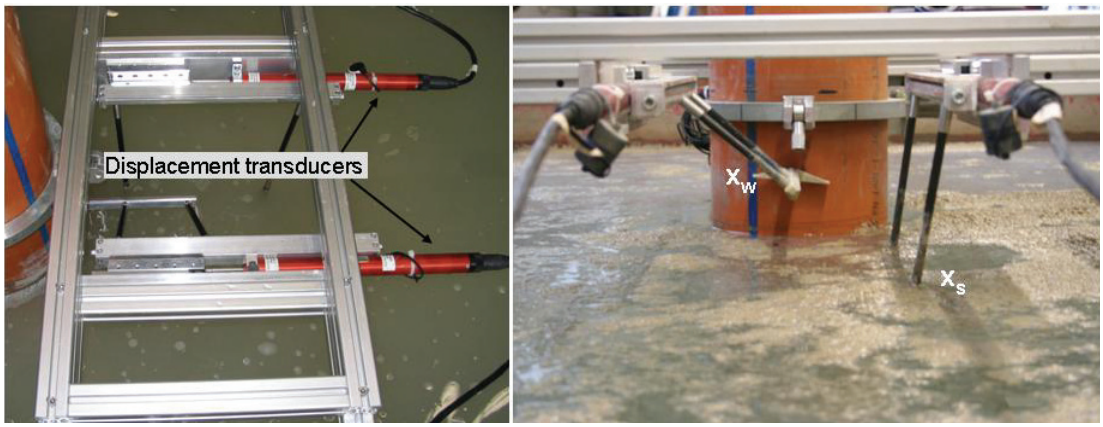

Fig. 5-12: Set-up of the displacement transducers x_w (measuring the deflection of the pile at the water level) and x_s (measuring the deflection of the pile at the level of the sand).

5.5 Test program and realisation

The emplacement of the sand was discussed in Section 5.3.3. As it was said, the sand was removed and brought back before each test series. To allow the sand and water to settle down and to ensure comparable measurement conditions, the test series took place 24 hours after the insertion of the sand had been finished. In order to analyse the influences of the pile deflection and of the loading frequency on the stress conditions of the soil, those two parameters were varied.

The maximum deflection of the pile $u_{mud,max}$ at the mud line level was defined following Eq. (2-1). The so-calculated maximum deflection at the mud line of the test model is $u_{mud,,max} = 0.3$ cm. It equals to the measured deflection x_s. Further, $x_s = \pm 0.3$ cm corresponds to a forced deflection at the water level of approximately $x_w = \pm 1.0$ cm (compare Fig. 6-6). Thus, the smallest deflection at the water level was chosen to $x_w = \pm 0.5$ cm and, to enlarge the analysed spectrum, the maximum deflection was set to $x_w = \pm 1.5$ cm for some test series.

The frequency was varied from 0.3 to 2.0 Hz. The lower bound of 0.3 Hz was chosen according to the maximum wave period in a storm (compare Fig. 2-9) which was scaled down following the formula for time variables given in Table 5-1. Thus, the period of the wave with the lowest height corresponds to approximately 0.7 s in the test model, i.e., to a frequency of 1.4 Hz. In order to analyse a slightly larger spectrum, test series were carried out until an upper frequency of 2.0 Hz. Nevertheless, special emphasis was put on small amplitudes of displacement and low frequencies since those conditions reflect the operating in situ conditions (compare Section 2.5) and since it is of interest if liquefaction also occurs under those conditions. The natural frequency of the system was determined within the numerical studies (see Section 7.4.2). It corresponds to approximately 4.9 Hz. Since it is beyond the input frequencies studied within the test series, the problem of resonance can be neglected here.

Table 5-4 shows the test program carried out within this research. The character 'R' indicates the test series realised within this test program. The index '2' signifies that at least two tests were done with this combination of input parameters to guarantee reproducibility. '*' indicates the tests after which another test with preloading was carried out afterwards. The test with '10/20' indicates the test in which the influence of the pore pressure on the distance from the test pile was examined. In each of those test series, the test pile was loaded for 60 min which corresponds to 1080-10800 loading cycles (depending on the frequency of the test series under consideration). Only in the test with the index 'Stop', the loading was stopped after approximately 20 seconds to analyse the effect of drainage. After all test series, the settlement around the pile was measured. The compactness of the sand was controlled by dynamic penetration tests.

In each test, the pile was loaded for 60 min. This time was chosen since OUMERACI and KUDELLA (2004) could measure an accumulation of pore pressure only after a certain number of load cycles. As it was seen after the first tests, a shorter measurement time would be sufficient since the changes in pore pressure only occur in the first minutes after the beginning of load application. Nevertheless, the 60 min measurement time was kept for uniformity reasons.

Table 5-4: Test program ('R': test series realised, '2': more than one test, '*': additional tests with preloading, '10/20': additional tests with pore pressure measurements at 10 and 20 cm distance from the test pile, 'Stop': test in which the loading was stopped after approximately 20 s).

f [Hz] / x_w [cm]	0.3	0.5	1.0	1.5	2.0
0.50	R2	R*	R2	R2	R
0.75	R2*	R2	R*10/20	R	R
1.00	R2	R*	R2	R	R2Stop
1.50		R	R2		R

6 Analysis and results of the test series

The labelling of the measurement devices and their position in the test model is given in Fig. 6-1. The pile is deflected by a forced displacement (corresponding to x_w since it is measured at approximately the same height) and with a given frequency f. Thus, the experimental data include the displacement of the pile at two levels (x_w near the water level and x_s near the sand level), the loading frequency as well as the pore pressure response at four levels (B1 – B4 and F1 – F4). In the following analyses, the measurement levels of the pore pressure transducers will be called level 1 (B1 and F1), level 2 (B2 and F2), level 3 (B3 and F3) and level 4 (B4 and F4). One group of pore pressure transducers will be denoted as group F since this is the direction in which the pile moves *forward* when the signals of the pile deflection increase in value. When the pile is deflected *backward*, the values of the displacement signals decrease and the pile moves towards the sensors of group B (compare Fig. 6-2).

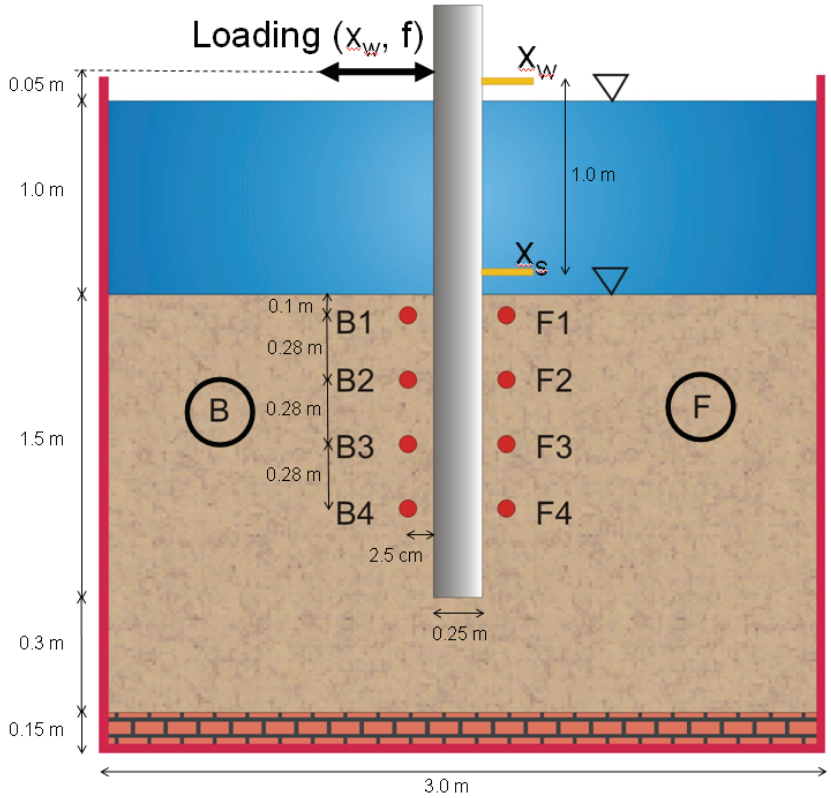

Fig. 6-1: Labelling and position of the measurement devices of the test model.

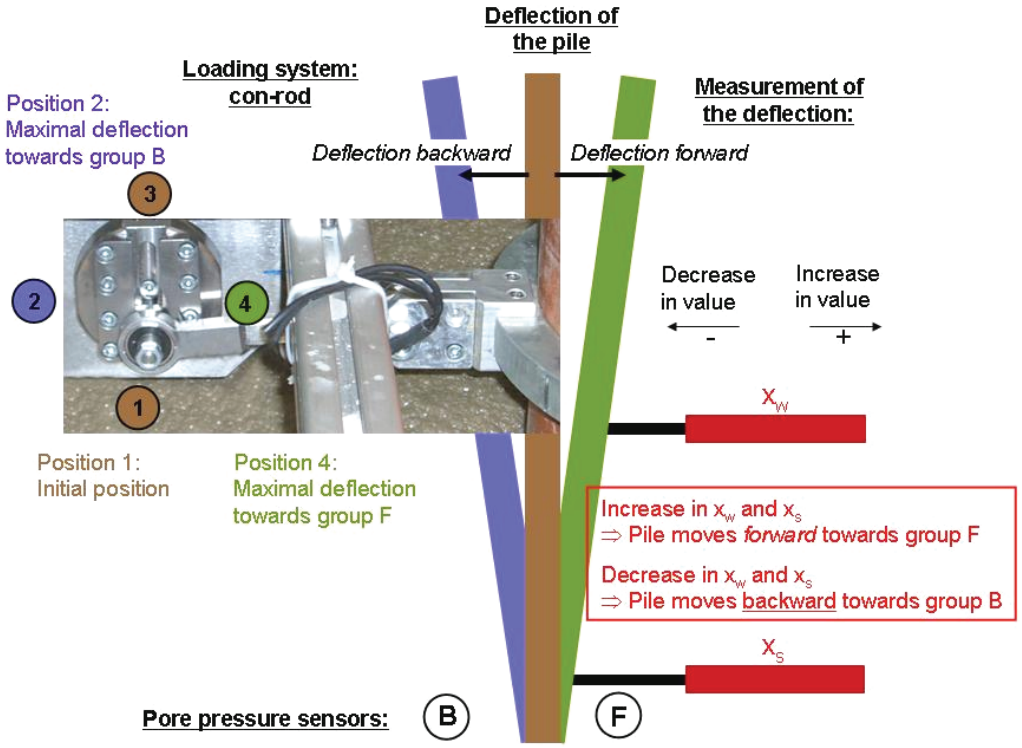

Fig. 6-2: Sketch of the pile with the loading system and the displacement transducers.

When used as characterization for the test series, the term "displacement" generally means the displacement of the pile x_w at the point of load application since this is the displacement that is forced during the loading. Nevertheless in some analyses, the displacement x_s at the embedding of the pile is used as reference value for the pore pressure as it is closer to the transducers. It will be shown in Section 6.1.3 that the relation to either x_w or x_s is allowed since the correlation of those displacement signals is very high.

6.1 Preliminary calculations

Fig. 6-3 represents the signals of the pore pressure transducers of group B for a test series with $x_s = \pm 0.75$ cm and $f = 1.0$ Hz. The signals strongly differ from each other. Firstly, the starting values of the signals vary since the hydrostatic pressures depend on the location of the transducers (B1: approximately 11.5 kN/m^2; B4: approximately 19 kN/m^2). Therefore, also the maxima cannot be directly compared to each other. Secondly, the signals differ in their progression with time: Whereas the maxima of the pore pressure at level 1, for example, last for about 70 seconds, the pore pressure at the other levels decreases very fast after reaching its maxima. Thirdly, also the transient pore pressure, i.e., the oscillation around the mean value depends on the level under consideration and thus, cannot be compared directly to the values observed at the other levels.

In order to be able to compare the pore pressures measured at the different levels, two steps are performed. Firstly, the signals are standardised by subtracting the hydrostatic pore pressure and by referring the excess pore pressure to the effective stress of the level under consideration. Hence, they are referred to the location of the transducers (see Section 6.1.1). Secondly, the

signals are separated in their low- and high-frequency parts in order to consider the signals' general progression and their transient fluctuations separately from each other (see Section 6.1.2).

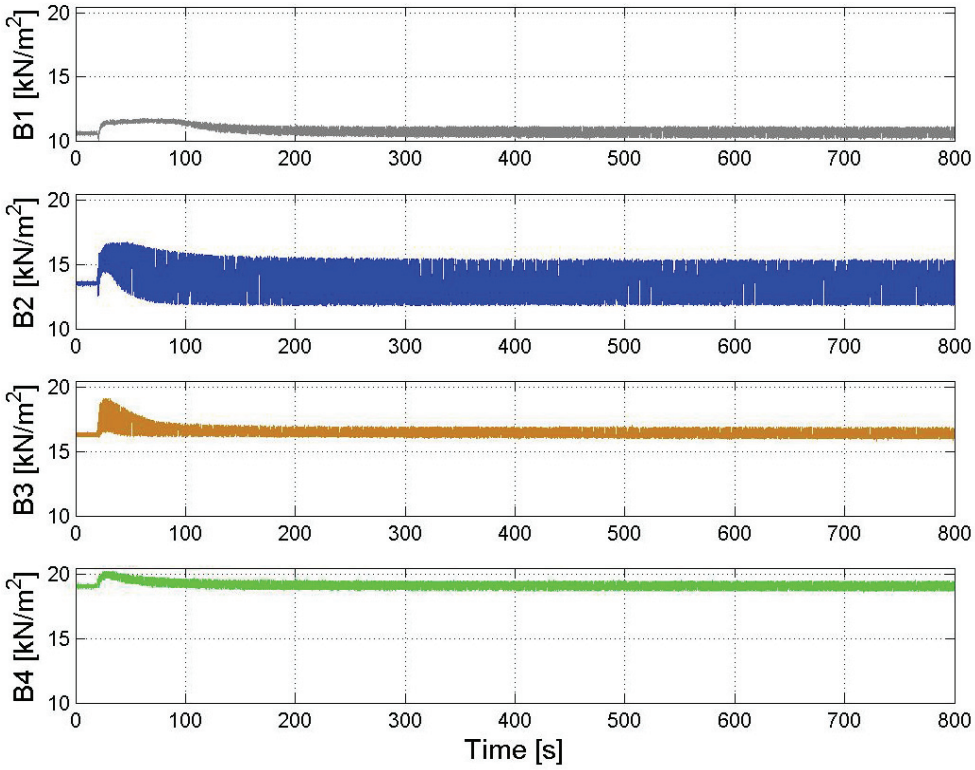

Fig. 6-3: Pore pressure signals of the transducers B1 – B4 (x_w: ±0.75 cm, f: 1.0 Hz).

6.1.1 Standardization

The pore pressure needs to be standardised in order to allow a comparison of the signals determined at the four different levels. This standardization is exemplarily illustrated in Fig. 6-4 for pore pressure transducer B1. Considering the pore pressure signal of a transducer ($signal_i$) which is shown by the grey curve in Fig. 6-4 for transducer i = B1, the first step is to subtract the hydrostatic pore pressure u_h:

$$\Delta u_i = signal_i - u_h \,. \tag{6-1}$$

u_h depends on the measurement level and is calculated according to $u_h = \gamma_w \cdot h$ (γ_w being the unit weight of water and h being the height of the water level to the depth where the transducer i is located). Δu_i represents the change in pore pressure (residual as well as transient) that begins to develop directly after the loading starts. It corresponds to the excess or to the negative pore pressure, respectively. This variation of the pore pressure with time is shown by the orange curve in Fig. 6-4. However, Δu_i alone does not allow one to draw conclusions concerning the state of the soil (liquefied / not liquefied). Only if Δu_i is related to the initial effective stress σ'_{m0}, the quotient

$$r_u = \frac{\Delta u_i}{\sigma'_{m0}} \tag{6-2}$$

represents a criterion for soil liquefaction (see Section 3.2.2). For the analyses carried out here, it was decided to consider the exceedance of the initial mean effective stress given by Eq. (3-9) as decisive for the onset of liquefaction since this is the lower bound for liquefaction and since liquefaction definitely occurred during the test series. Hence, liquefaction is said to occur when

$$r_u \geq 1\,. \tag{6-3}$$

The pore pressure ratio r_u is represented by the red curve in Fig. 6-4. During the first approximately 100 seconds after the beginning of loading $\Delta u_i \,/\, \sigma'_{m0} > 1$, thus indicating that liquefaction occurred during that time. Thereafter, as $r_u < 1$, the effective stress dominates over the excess pore pressure again.

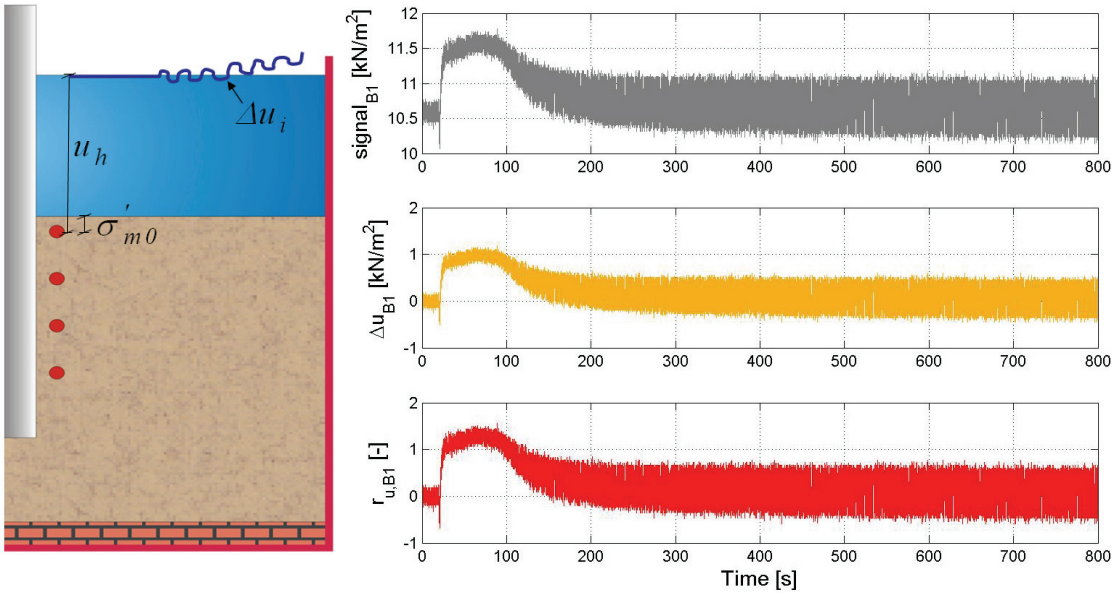

Fig. 6-4: Standardization of the pore pressure (original signal → excess or negative pore pressure → pore pressure ratio) exemplarily shown for transducer B1.

6.1.2 Fast Fourier Transform

The second calculation step announced in Section 6.1 is the splitting of the signals in two frequency parts. The low-frequency part describes the general progression of a signal without the transient fluctuations and is comparable to the mean or residual pore pressure ratio over the time. High frequencies only contain the transient fluctuations of a signal (that are generated due to every single loading cycle) without considering the actual residual value of the pore pressure ratio. Thus, by splitting the signals, the two frequency parts can be analysed independently from each other.

In Fig. 6-5 (a), the standardised signal r_u of transducer F2 is shown in the time domain over the first 800 s of a test series. By a Fast Fourier Transform (FFT), the signal is transferred to the

frequency domain. As can be seen in the resulting magnitude spectrum in Fig. 6-5 (b), the first peak is at a very low frequency and represents the general progression of the signal. The peak at 2.0 Hz represents the loading frequency; the multiples of the loading frequency can be seen as well. In order to split the signals into their general progression and into their loading-induced oscillations, a filter was applied for further processing. The filter has a cut-off frequency of one quarter of the loading frequency (red line, here 0.5 Hz). This filter is firstly designed as a low-pass filter that transfers the low frequencies of the frequency spectrum back to the time domain. This is done by means of an inverse FFT. The resulting signal in the time domain is represented by the curve in Fig. 6-5 (c) showing the low-frequency component of the signal. Secondly, the filter is designed as a high-pass filter which only transfers frequencies higher than 0.5 Hz back to the time domain. Fig. 6-5 (d) shows this high-frequency component, i.e., the transient oscillations of the signal. The cut-off frequency of one quarter of the loading frequency was seen to be reasonable to divide the high-frequency parts from the low-frequency parts and showed good results for all test series. Minor changes of that frequency did not influence the resulting time series significantly. The splitting in low- and high-frequency parts was done for every pore pressure signal in order to enable and to facilitate the comparison of the signals. Whereas the original signal is used for general analyses described in the Sections 6.1.4 and 6.3, the low-frequency part of the pore pressure ratio is used in the sections 6.2.1 to 6.2.3 and Section 6.2.4 regards the high-frequency part.

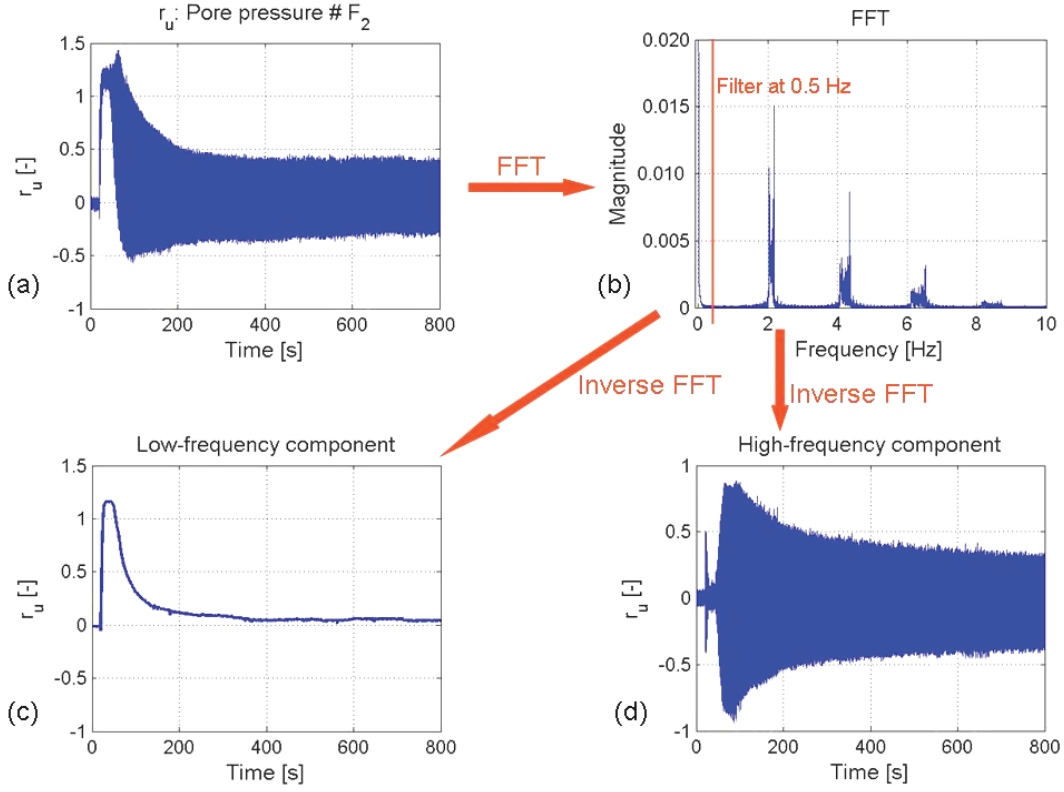

Fig. 6-5: Transformation of r_u-signal in its low- and high-frequency part (exemplarily shown for transducer F2 for a test with $x_w = \pm 0.5$ cm and $f = 2.0$ Hz). (a) r_u in time domain, (b) r_u in frequency domain, (c) low-frequency part of r_u in time domain, (d) high-frequency part of r_u in time domain.

6.1.3 Cross-correlation of displacement signals

Fig. 6-6 shows typical signals of x_w and x_s during a test series. In the test under consideration, the displacement x_w was adjusted to about ±0.1 cm (upper curve in Fig. 6-6). Because of the low stiffness of the pile, the displacement x_s amounts only to ±2.5 mm (lower curve in Fig. 6-6).

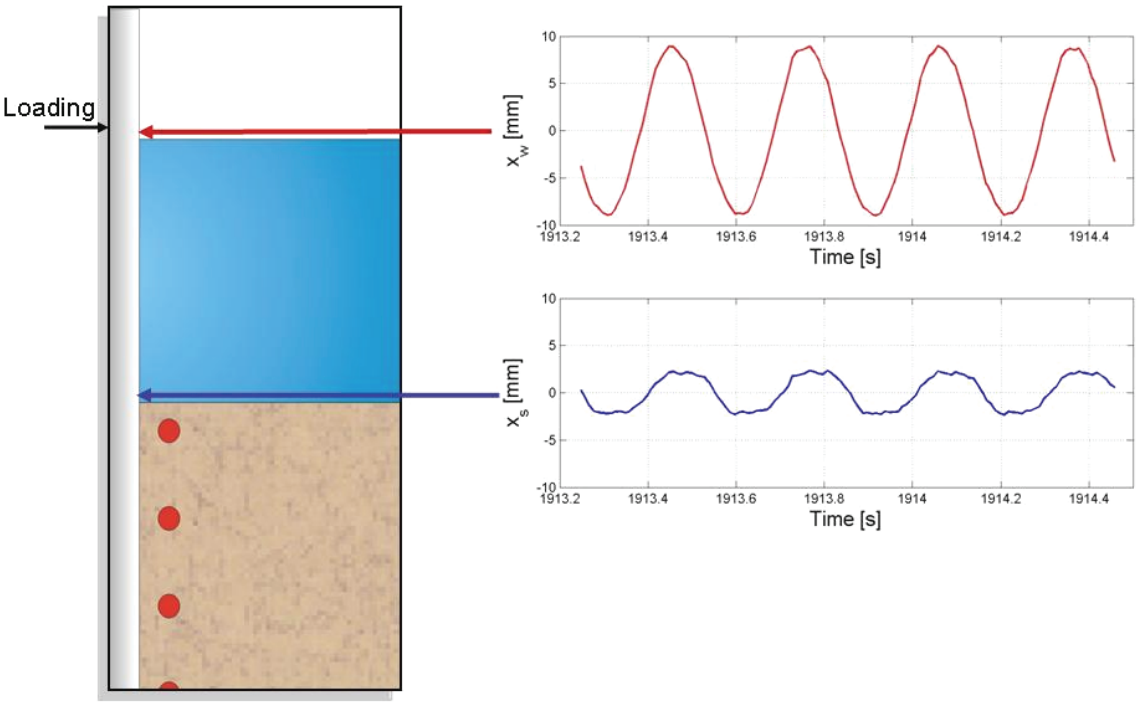

Fig. 6-6: Characteristic signals for the displacement measurements x_w and x_s.

In order to show that the two signals are highly correlated to each other, the cross-correlation function was used. This function statistically compares two different sequences and provides their cross-correlation as a measure of dependency on each other and the time shift between the two signals. According to BENDAT and PIERSOL (2000), the cross-correlation function $R_{xy}(\tau)$ is defined as

$$R_{xy}(\tau) = E[x(t) \cdot y(t+\tau)] = \int_{-\infty}^{\infty} x(t) \cdot y(t+\tau) dt \,. \tag{6-4}$$

$x(t)$ is a time series, say x_w, where t is a variable that is interpreted as time and $y(t+\tau)$ is another time series, say x_s, with the time shift τ. When applying Eq. (6-4) to two signals of a defined time of observation (τ_{min} to τ_{max}), Eq. (6-4) is varied to

$$R_{xy}(\tau) = E[x(t) \cdot y(t+\tau)] = \int_{\tau_{min}}^{\tau_{max}} x(t) \cdot y(t+\tau) dt \,. \tag{6-5}$$

The signals are shifted in time by the multiples of the value of τ (which corresponds to the sampling frequency, here $\tau = 0.01$ s) and τ_{min} and τ_{max} represent the lowest and highest multiples of τ, respectively, until which the signals are shifted against each other. Those values are generally determined such that the function y is shifted by about 20 % of its period of observation. For

each τ, the values of the signals are multiplied with each other and are integrated. This integration for each $(t+\tau)$ is represented by the cross-correlation function shown in Fig. 6-7 (a). The maximum peak signifies the integration of the signals when shifted such that the correlation is the highest, i.e., when the maximum values of the signals superpose each other for the first time. The next peak is caused when the signals are shifted by exactly one phase. The values of $R_{xy}(\tau)$ only depend on the values of the signals. When $R_{xy}(\tau)$ is normalized by use of the standard deviations of both signals (σ_x and σ_y), one obtains the cross-correlation coefficient function $\rho_{xy}(\tau)$

$$\rho_{xy}(\tau) = \frac{R_{xy}(\tau)}{\sigma_x \cdot \sigma_y} \tag{6-6}$$

with

$$-1 \le \rho_{xy}(\tau) \le 1\,. \tag{6-7}$$

Whereas $\rho_{xy} = -1$ or 1 shows full correlation of the two signals, $\rho_{xy} = 0$ indicates no correlation. The cross-correlation coefficient function of x_w and x_s is depicted in Fig. 6-7 (b).

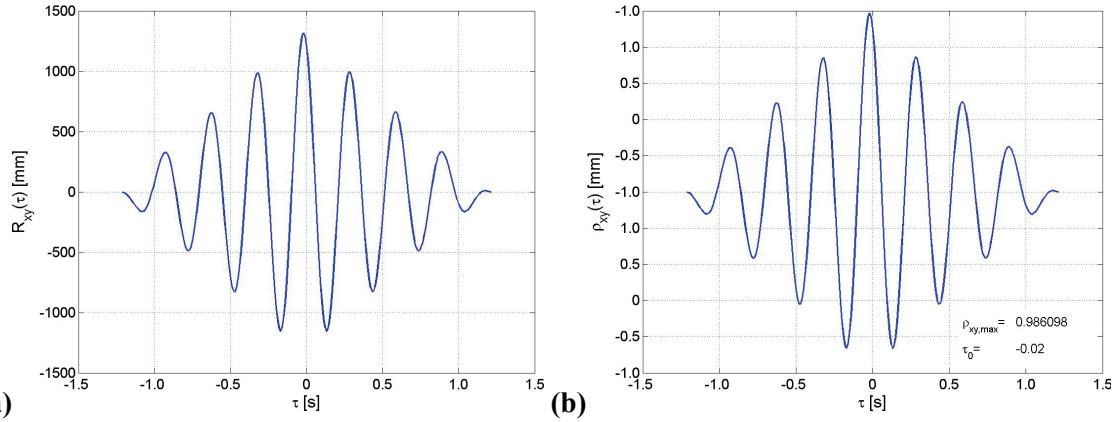

(a) **(b)**

Fig. 6-7: (a) Cross-correlation function of x_w and x_s according to Eq. (6-5) and (b) cross-correlation coefficient function of x_w and x_s according to Eq. (6-6).

As can be seen, the highest peak is $\rho_{xy,max} = 0.98$ which signifies a very strong correlation of the signals. This is not surprising since the deflection x_w is certainly very much correlated with the deflection x_s. With increasing τ, the coefficient ρ_{xy} tends to decrease and approaches zero for τ_{min} and τ_{max}. This is due to the shifting of the signals: they have to have the same length when being subject to this analysis. Therefore, they are zero-padded at the beginning and at the end, respectively, when shifted and thus, the integration gets smaller ($\rightarrow$ multiplication with 0). The time shift τ_0 between $\rho_{xy,\max}$ and $\tau = 0$ signifies the temporal delay between the displacement x_w and the displacement x_s or in case of periodic signals, their phase shift. Here, $\tau_0 = 0.02$ s which means the deflection of the pile at the level of x_s reaches its maximum deflection 0.02 s later than at the level of x_w. The cross-correlation coefficient ρ_{xy} and the time shift of the signals τ_0 were determined for each test series and show similar behaviour in all tests.

6.1.4 Cross-correlation of displacement and pore pressure over entire test

To detect the dependency of the pore pressure on the deflection of the pile, those signals were cross-correlated as well. Therefore, the cross-correlation coefficients of the deflection x_s and the pore pressure signals of group B were determined for 18 time periods during a test (time periods of approximately 1.5 s all 200 s). The values of the resulting cross-correlation coefficients over the entire duration of the test are exemplarily represented in Fig. 6-8 by dots which are connected by lines. Obviously, two phases have to be distinguished. Phase 1 comprises the first minutes of a test (in this test, approximately 500 seconds) in which the cross correlation coefficients of all signals are rather arbitrary and non-uniform. This means that during the 1.5 s-periods of observation, the pore pressure does not constantly depend on the deflection of the pile. Nevertheless, general trends can be observed within this phase. The discussion of this first phase will be given in Section 6.2 in detail and will reveal those general dependencies of several pore pressure characteristics on the amplitude and the frequency of the pile deflection. Phase 2 includes the time after Phase 1 until the end of the test. It is characterized by rather uniform and high cross-correlation coefficients. For the transducers B2 – B4, the coefficients mostly lie between 0.9 and 1.0 representing a very high correlation of the pore pressure and the deflection of the test pile during the analysed 1.5 s-periods of observation. In contrast for transducer B1, the cross-correlation coefficients lie in the range of $\rho_{xy,max}$ = 0.5-0.7. Whereas at level 1 and 2, the cross-correlation coefficients are negative, they are positive at level 3 and 4 indicating that a rotation point of the pile exists between the levels 2 and 3. This second phase will be treated in Section 6.3.

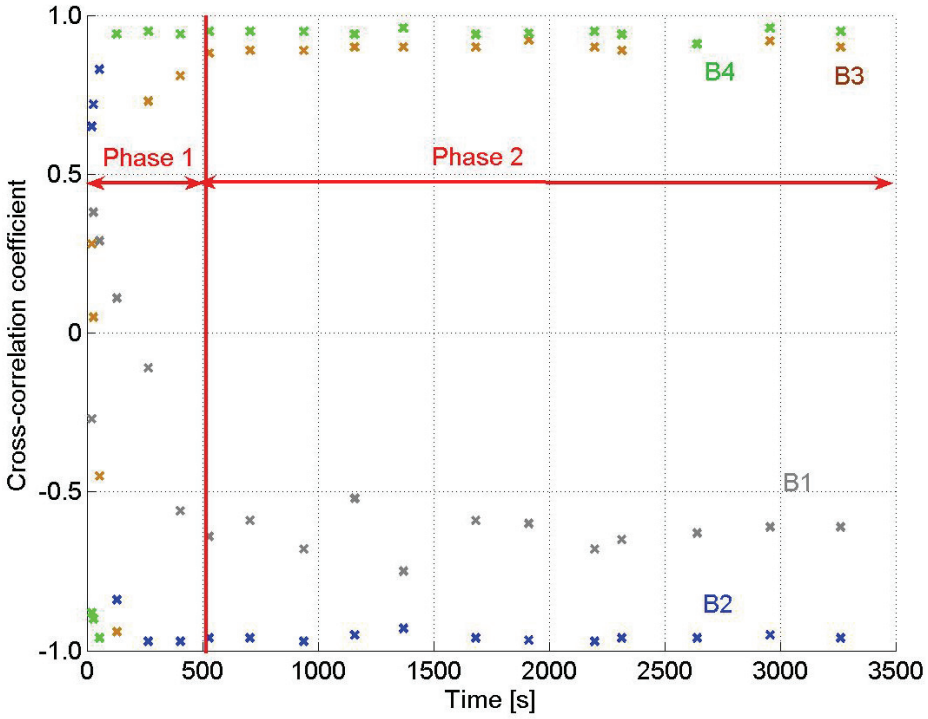

Fig. 6-8: Cross-correlation coefficients of x_s and the pore pressure of B1 – B4 during observation periods of 1.5 s over the entire duration of the test. Two phases 1 and 2 are defined.

6.2 Analysis I: Analysis of the initial conditions (Phase 1)

For the analysis of Phase 1 indicated in Fig. 6-8, the measurement data will be analyse with respect to the maximum pore pressure, the duration of liquefaction, etc., by considering the signals' transformation in low- and high-frequency parts (Section 6.1.2). All analyses are referred to the displacement x_w at the level of load application although x_s is the measured displacement which is closer to the pore pressure transducers. The reference to x_w was chosen for the sake of clarity. As it was shown in Section 6.1.3, this simplification is permitted since the signals are highly correlated to each other.

6.2.1 Maximum ratio of mean pore pressure

In order to analyse the maximum value of the mean pore pressure ratio $r_{u,max}$, the maximum values of the low-frequency parts of the signals were determined for all test series. In Fig. 6-9, the low-frequency part of the pore pressure ratio r_u is exemplarily shown for one test series with $x_w = \pm 1.0$ cm and $f = 2.0$ Hz. Here, the pore pressure transducers B1 – B4 in a distance of 2.5 cm from the pile surface are considered. According to all other test series, the pore pressure begins to accumulate directly when the loading is applied and reaches its maximum value after only a small number of load cycles (9 on average, minimum: 3 loading cycle, maximum: 24 loading cycles, a dependency on the input parameters could not be observed). The maximum values of the pore pressure ratio are marked for all levels in Fig. 6-9.

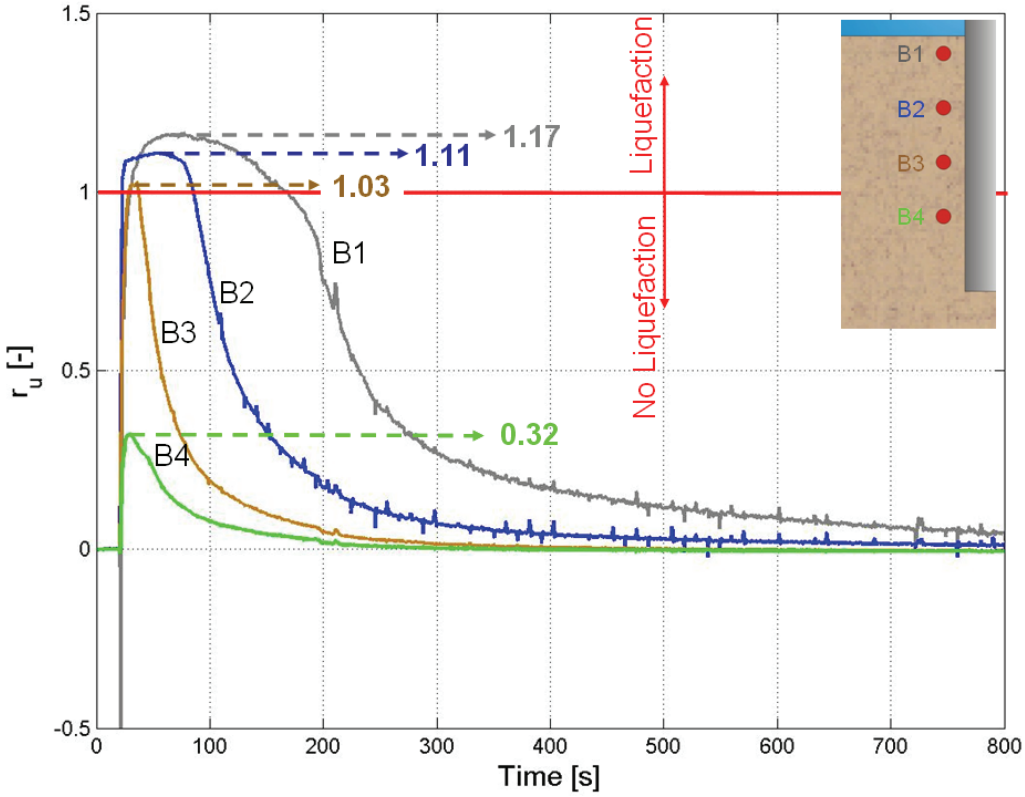

Fig. 6-9: Low-frequency part of the pore pressure ratio r_u as a function of time for the backward transducers B1 – B4 at different levels 2.5 cm away from the surface of the pile ($x_w = \pm 1.0$ cm and $f = 2.0$ Hz). The maximum values $r_{u,max}$ and the liquefaction criterion are marked.

The $r_{u,max}$-values shown in this figure decrease from the first level (B1: $r_{u,max} = 1.17$) to the bottom level (B4: $r_{u,max} = 0.32$). At the levels 1, 2 and 3, $r_{u,max}$ exceeds the threshold of $r_u = 1.0$ above which liquefaction is expected to occur (see liquefaction criterion in Section 3.2.2 and Eq. (6-2)). At level 4, in contrast, the pore pressure reaches only around one third of the initial effective mean stress. Thus, the soil did not liquefy at this level. It is conspicuous that in this test, liquefaction occurred at level 2 first and only afterwards at level 1. This is due to the bad drainage capabilities at this lower level compared to level 1 which is closer to the surface (see also Section 6.3.1).

As described in Section 5.4.1, the pore pressure transducers were mostly installed at a distance of 2.5 cm from the test pile, thus providing a vertical profile of the pore pressure during loading as it is shown in Fig. 6-9 (position of measurement devices as shown in Fig. 6-1). In order to analyse the horizontal profile as well, i.e., the lateral spreading of excess pore pressure, two additional test series were carried out. In those tests, the pore pressure transducers were not only positioned in vertical but also in horizontal direction as can be seen in Fig. 6-10 (only at level 3, data are lacking). Hence, four transducers were left in their usual position (group B, 2.5 cm from the pile surface) and served as reference signals. Therefore, the maximum pore pressure ratio at 2.5 cm from the test pile is called $r_{u,max,ref}$. The four transducers of group F were also installed on side B, but were placed further away from the test pile than the other transducers (first test: 10 cm, second test: 20 cm). In the following sections, the labelling B1 (10 cm), for example, signifies the transducer at the first level at a distance of 10 cm from the pile surface.

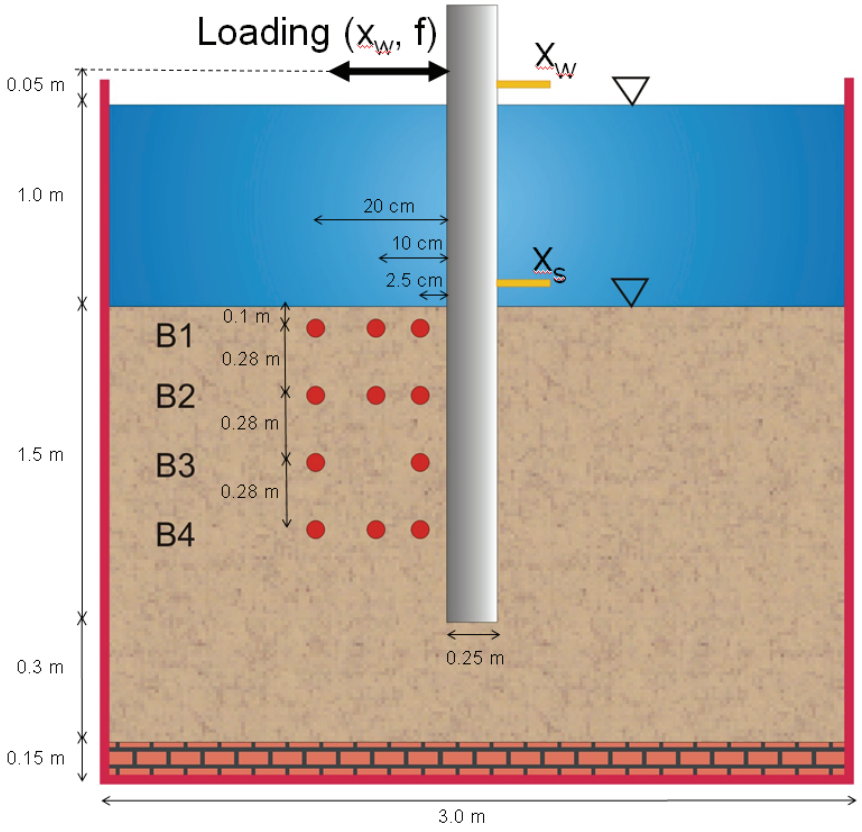

Fig. 6-10: Position of the measurement devices for the analysis of lateral spreading of excess pore pressure.

6.2.1.1 Vertical and horizontal profile

In order to investigate the vertical and horizontal profile of excess pore pressure, the results of two test series with a displacement of $x_w = \pm 0.75$ cm and a frequency of $f = 1.0$ Hz are considered (compare Table 5-4). In Fig. 6-11 (a), the vertical profile is exemplarily shown for the mean pore pressure ratio r_u of the transducers at a distance of 2.5 cm from the test pile. The horizontal profile of r_u at level 2 is shown in Fig. 6-11 (b). As can be seen, the pore pressure decreases with depth and with distance to the pile.

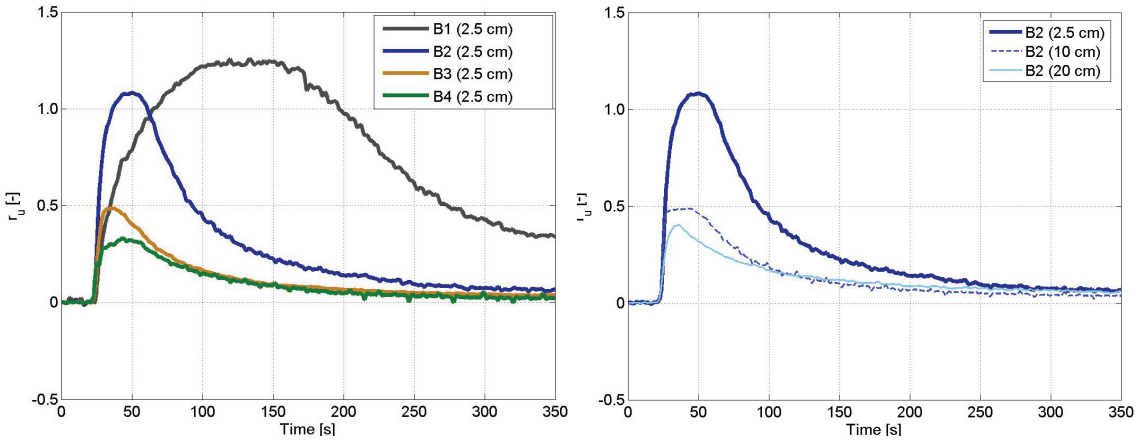

(a) **(b)**

Fig. 6-11: Low-frequency part of the pore pressure ratio r_u as a function of time for the backward transducers. The vertical profile is shown in (a) for a distance of 2.5 cm from the test pile. The horizontal profile is shown in (b) for level 2.

In order to analyse the maximum pore pressure ratio vertically for all three distances from the test pile (2.5 cm, 10 cm and 20 cm) and horizontally for all four levels (B1, B2, B3, and B4), all pore pressure signals of the test series under consideration were considered. $r_{u,max}$ was determined for every signal and yield data points in the vertical profile shown in Fig. 6-12 as well as in the horizontal profile represented in Fig. 6-13. Those data points are indicated by markers. The lines connecting those markers represent a possible gradient for $r_{u,max}$ in horizontal and vertical direction, respectively. More test series would be necessary to ascertain the exact pore pressure decrease with depth and distance, respectively.

For three different distances from the pile (2.5 cm, 10 cm and 20 cm), the vertical profile shows $r_{u,max}$ over the depth (for B1 to B4). The black markers (2.5 cm) represent the maximum values of the pore pressure ratio determined for the signals shown in Fig. 6-11 (a), i.e., at a distance of 2.5 cm from the test pile. The other markers indicate those values for a distance of 10 cm and 20 cm. Since data for B3 (10 cm) was lacking, the pore pressure ratio was interpolated for this location. The red line represents the liquefaction criterion. It can be seen that for all distances from the test pile, the $r_{u,max}$-values are the highest for level 1 and decrease with depth.

The horizontal profile represented in Fig. 6-13 shows the $r_{u,max}$-values measured at the same levels but at different distances from the pile. The blue line (B2) represents the maximum values of r_u determined for the signals shown in Fig. 6-11 (b), i.e., for level 2. For all levels, $r_{u,max}$ is the

highest in immediate vicinity of the test pile (i.e., at a distance of 2.5 cm to the test pile) and decreases with increasing distance from the test pile. Whereas at level 3 and 4, the maximum pore pressure ratio decreases almost linearly with distance to the test pile, this relation is not clear at level 1 and 2. More test series would be necessary to detect the function of the decrease of $r_{u,max}$ with distance from the pile. Also in this figure, the red line signifies the liquefaction criterion. Hence, liquefaction was observed for B1 (2.5 cm), B1 (10 cm) and B2 (2.5 cm).

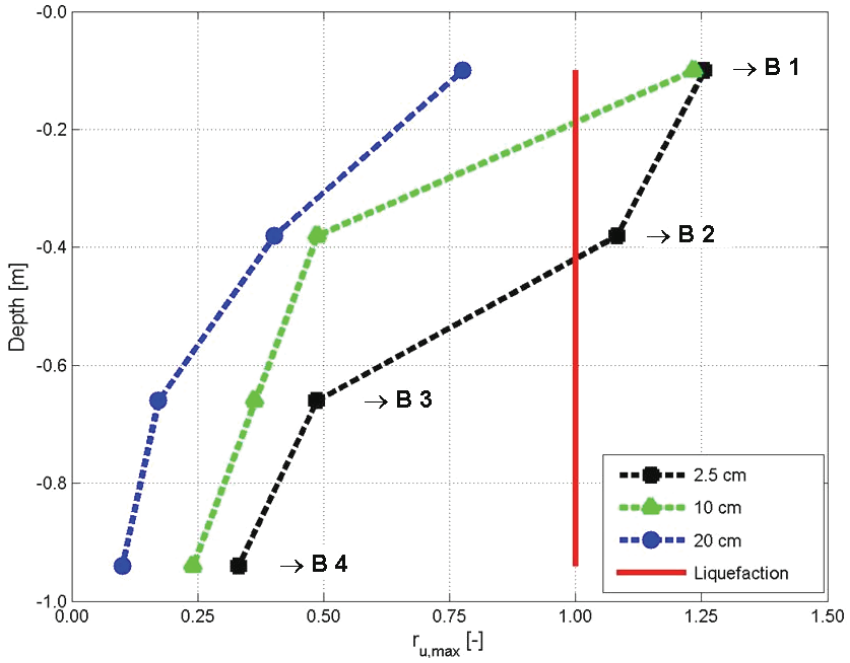

Fig. 6-12: Vertical profile of the maximum pore pressure ratio of group B for three different distances from the test pile. The test series were carried out with x_w = ±0.75 cm and f = 1.0 Hz.

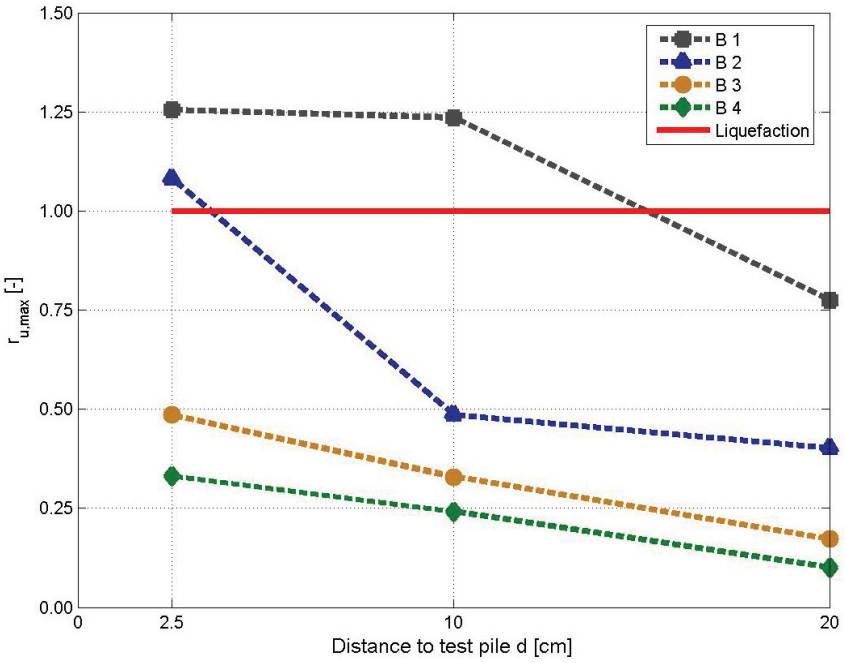

Fig. 6-13: Horizontal profile of the maximum pore pressure ratio of group B for the levels 1-4. The test series were carried out with x_w = ±0.75 cm and f = 1.0 Hz.

6.2.1.2 Detailed analysis: vertical profile

In order to analyse the vertical profile in more detail, all test series carried out within this research work (compare Table 5-4) are analysed with respect to $r_{u,max}$. It should be recalled that those tests were carried out with the position of measurement devices as shown in Fig. 6-1. For all tests and transducers, the maximum values of the pore pressure ratio were determined. Those values are represented for all levels individually in two different plots shown in Fig. 6-14 to Fig. 6-17: a surface plot (above) and an isoline plot (below). The surfaces are defined by the $r_{u,max}$ -values that are spanned over x_w and f. Thus, a $r_{u,max}$ -value is provided for all combinations of x_w and f. For this purpose, the values of the transducers under consideration of group F and B were averaged. For the two tests which were not carried out within this range of parameters (compare Table 5-4), the values were interpolated. The red plane signifies the liquefaction criterion where $\Delta u = \sigma'_{m0}$. Exceeding this surface indicates that liquefaction occurred at the level under consideration. Below the surface plots, $r_{u,max}$ is plotted in terms of isolines. Thus, the dependency of the maximum pore pressure ratio on the input parameters x_w and f can better be revealed.

Considering level 1 of the vertical profile, liquefaction occurred in most of the tests. Only in the test series with very low amplitudes of deflection and low frequencies, the liquefaction criterion was not matched. According to the experimental results of SILVER AND SEED (1971) and BYRNE (1991), this could be due to a threshold shear strain for the onset of liquefaction that is mostly exceeded at this level. Only in the tests with very low displacements and frequencies, the deflection leads to strains not high enough to cause an excess pore pressure as high as the initial mean effective stress. Furthermore, the low frequencies of those tests could provide enough time for the pore water to dissipate and thus, could prevent a pore pressure accumulation resulting in liquefaction. Nevertheless, although liquefaction occurred in most of the tests, a dependency of $r_{u,max}$ on x_w and f cannot be identified unambiguously for this upper level as can be seen in the isoline plot.

In contrast to level 1, a strong dependency of $r_{u,max}$ on x_w and f is found at the levels 2 to 4: $r_{u,max}$ predominantly increases with increasing deflection and frequency. According to Section 3.4.3, dynamic loading of a soil causes cyclic shear strains in the soil that can be coupled to the pore pressure. Whereas under drained conditions, a volume reduction would occur, an excess pore pressure is generated in an undrained soil. The observed dependency of $r_{u,max}$ on the displacement at the levels 2 to 4 can be explained according to the strain approach: higher displacements lead to higher strains and thus, to higher volume reductions. This will, in turn, result in higher pore pressure. Apart from the dependency on the deflection, the dependency on the loading frequency plays an important role. If low frequencies are applied to a soil, the pore water has sufficient time to dissipate. Thus, the ratio $\Delta u_{acc} / \Delta u_{diss}$ of pore pressure accumulation or generation and pore pressure dissipation is smaller compared to the same ratio when a loading with higher frequencies is applied (supposed the permeability of the soil is the same). As the pore pressure only accumulates when the pore pressure generation is higher than its dissipation, the pore pressure ratio thus strongly depends on the loading frequency.

At level 2, the isolines have in general an angle of approximately 45° indicating that $r_{u,max}$ at this level depends equally strong on x_w and on f. As soon as the maximum value either of x_w or of f is reached, a further increase in frequency or displacement does not change the pore pressure ratio significantly. In the cases of level 3 and level 4, their angle of inclination gets steeper. Hence, it is evident that the dependency of $r_{u,max}$ on x_w increases with increasing depth, whereas the influence of f on $r_{u,max}$ decreases with depth to almost no dependency at level 4 (see isoline plot). This can be due to the fact that the drainage possibilities of the soil at upper levels are more efficient compared to the drainage possibilities at the bottom level. The following conclusions can be drawn: Whereas at the upper level, a higher frequency interferes the drainage of water and, therefore, allows a higher accumulation of pore pressure (generation > dissipation), the frequency at the bottom level does not have a strong influence since the dissipation of water in this level is very slow in any case. The influence of x_w increases with depth since the drainage possibilities are worse at those bottom levels.

Since the deflection of the pile decreases with increasing depth, the highest $r_{u,max}$-values occur in the upper level and decrease with depth, too. Regarding the number of test series which result in liquefied soil, this number decreases from level 1 to 4. Table 6-1 lists the percentage of tests resulting in liquefaction for the levels 1 to 4. As can be seen, liquefaction was observed in 75 % of the test series at level 1, in 60 % of the tests at level 2, in 35 % at level 3 and still in 15 % at level 4. The depth of the levels 1 to 4 was given in Section 5.4.1 and is once more listed in the table in terms of the so-defined minimum liquefied depth. Thus, when liquefaction occurred at level 3, for example, the soil down to at least 0.66 m under the sand surface is liquefied. The forth column supplies this depth in terms of the fraction of the entire embedded length. Hence, in 35 % of the tests, liquefaction occurred at level 3, resulting in at least 0.66 m of liquefied sand which corresponds to 44 % of the embedded length of the pile. As can be seen in Fig. 6-17 for level 4, the liquefied state was only achieved in tests with very high x_w and f. Nevertheless, three tests resulted in soil liquefaction also at level 4. That means, in those tests, the soil was liquefied down to a depth of approximately 1 m which corresponds to almost two thirds of the embedded length of the pile.

Table 6-1: Percentage of tests resulting in liquefaction at level 1-4 and minimum liquefied depth in [m] and as a fraction of the embedded length of the pile.

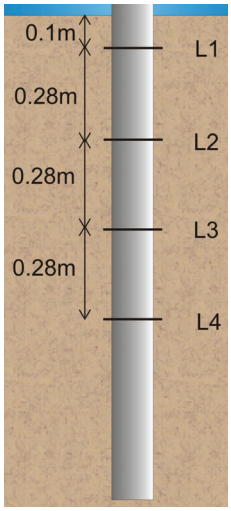

Level	Percentage of tests with liquefaction [%]	Minimum liquefied depth [m]	Minimum liquefied depth [%] Depth / Embedded length
Level 1	75	0.1	6.7
Level 2	60	0.38	25.3
Level 3	35	0.66	44.0
Level 4	15	0.94	62.7

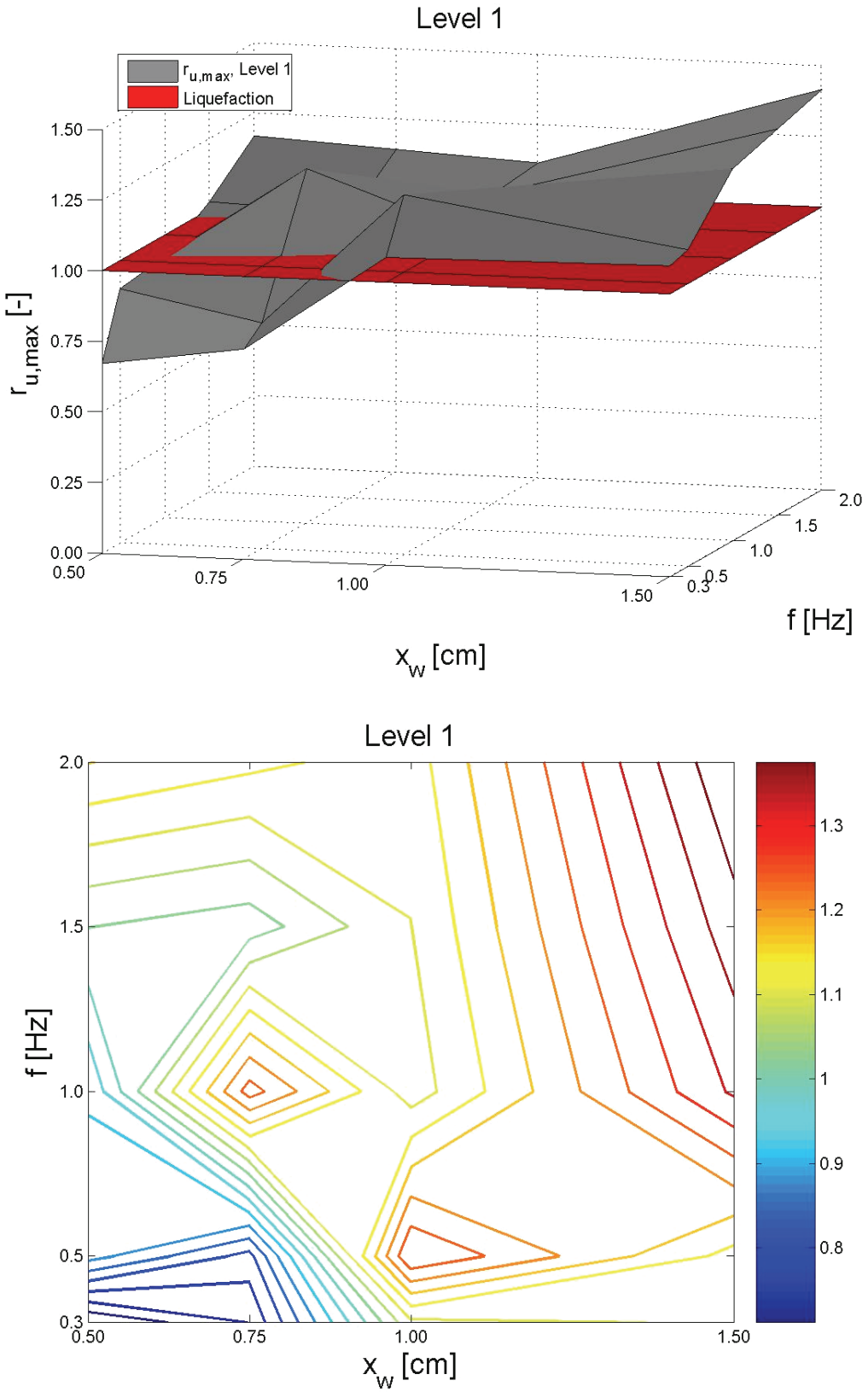

Fig. 6-14: Above: Maximum pore pressure ratio $r_{u,max}$ for level 1 versus displacement x_w and frequency f. Below: Isolines of the maximum pore pressure ratio $r_{u,max}$ for level 1 as a function of displacement x_w and frequency f.

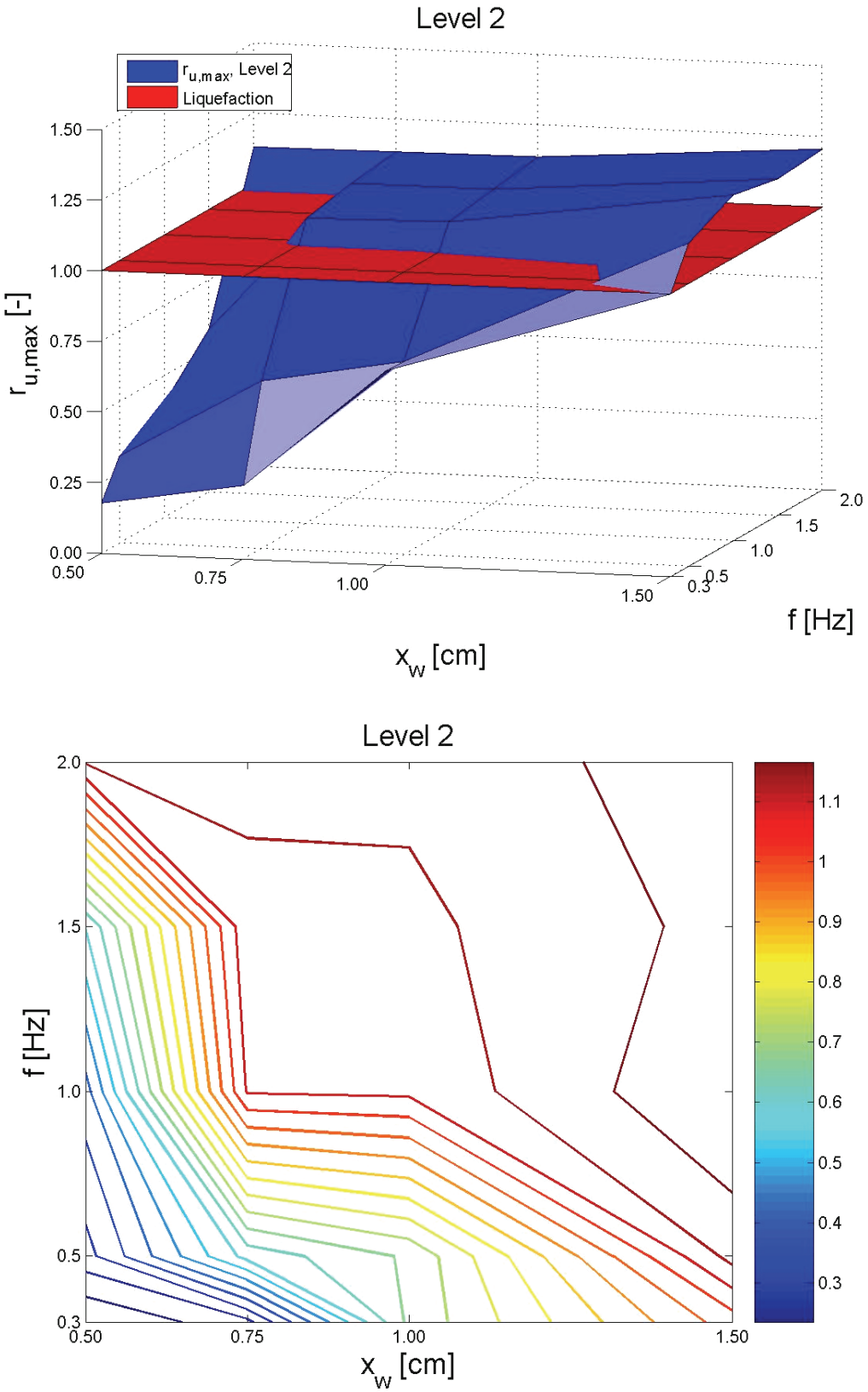

Fig. 6-15: Above: Maximum pore pressure ratio $r_{u,max}$ for level 2 versus displacement x_w and frequency f. Below: Isolines of the maximum pore pressure ratio $r_{u,max}$ for level 2 as a function of displacement x_w and frequency f.

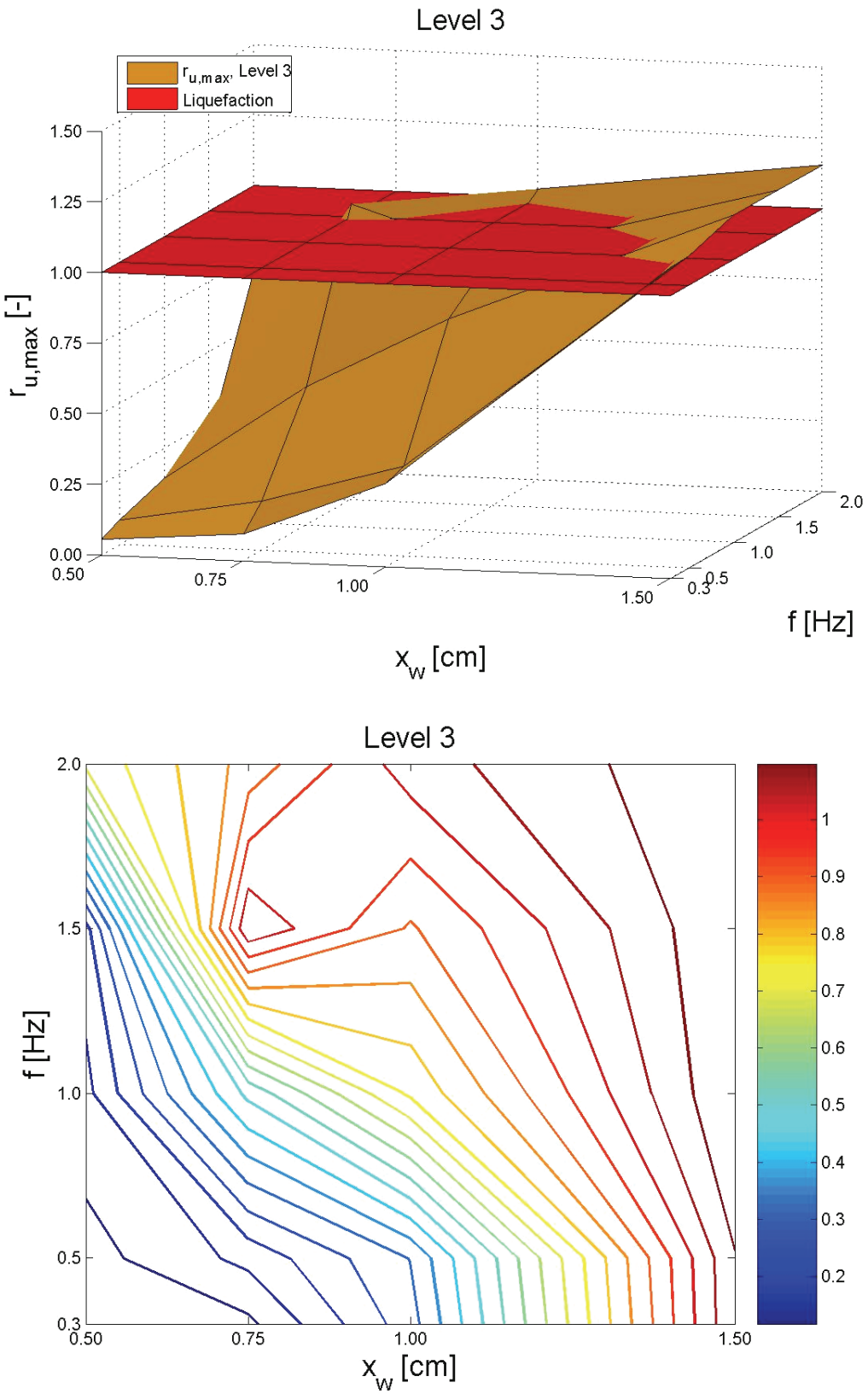

Fig. 6-16: Above: Maximum pore pressure ratio $r_{u,max}$ for level 3 versus displacement x_w and frequency f. Below: Isolines of the maximum pore pressure ratio $r_{u,max}$ for level 3 as a function of displacement x_w and frequency f.

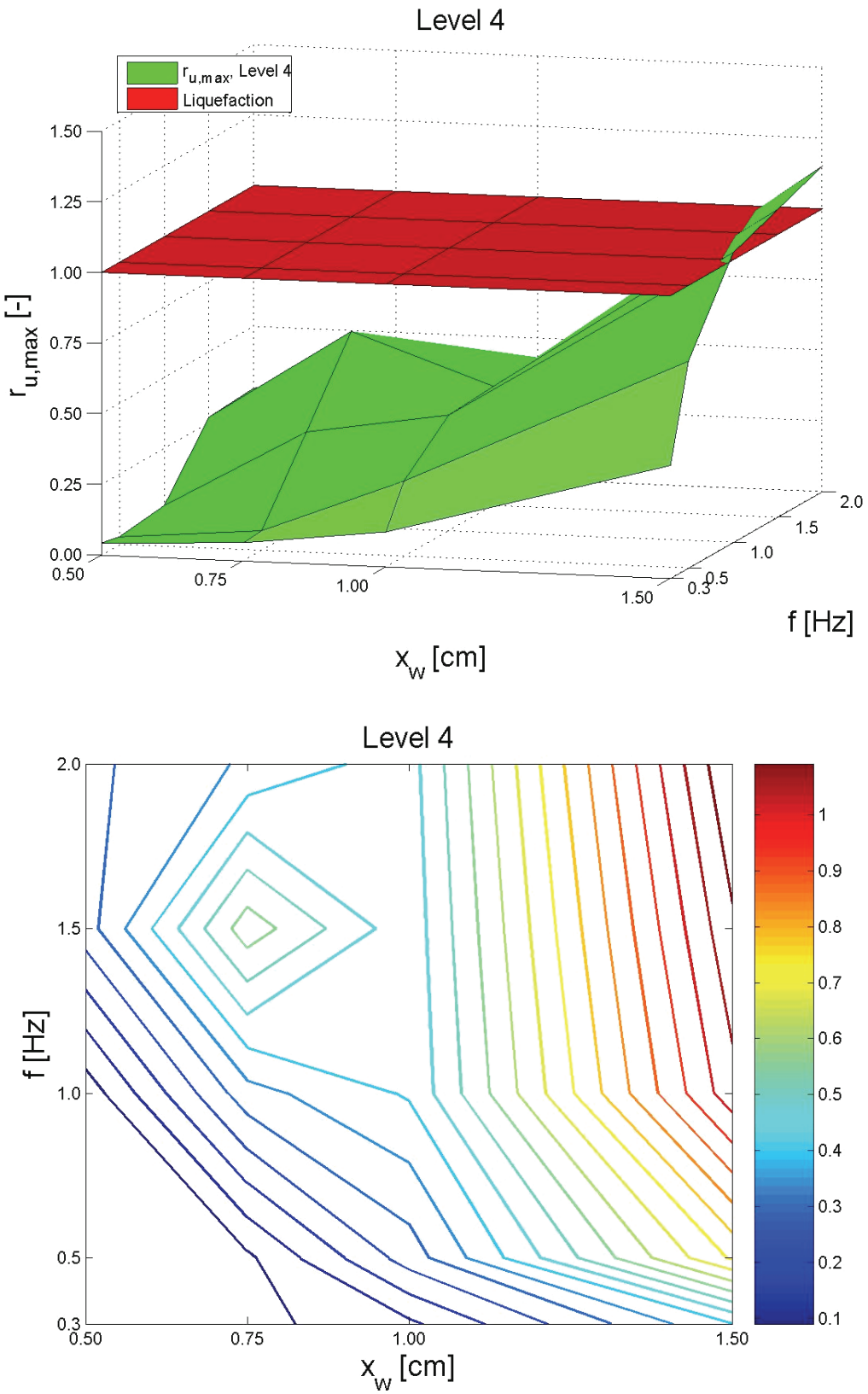

Fig. 6-17: Above: Maximum pore pressure ratio $r_{u,max}$ for level 4 versus displacement x_w and frequency f. Below: Isolines of the maximum pore pressure ratio $r_{u,max}$ for level 4 as a function of displacement x_w and frequency f.

6.2.1.3 Detailed analysis: horizontal profile

In order to report the detailed results of the horizontal spreading of the pore pressure, the first 350 seconds of the two tests discussed in Section 6.2.1.1 are looked at in a more detailed way. Those tests were carried out with the same given displacement and frequency but with the transducers being installed at different distances d to the test pile (2.5 cm, 10 cm and 20 cm). The position of the pore pressure transducers is indicated in Fig. 6-10. The result of the tests, i.e., the low-frequency part of the pore pressure signals at different distances from the test pile, is presented separately for each level in Fig. 6-18 to Fig. 6-21. As can be seen for all levels, the maximum pore pressure is a function of the horizontal distance from the pile. It is highest in immediate vicinity to the test pile and decreases with distance. This is obviously due to the fact that the deflection and, therefore, also strains and volume changes, are the highest in immediate vicinity of the test pile. Nevertheless at level 1, the maximum pore pressure measured 10 cm away from the pile is almost as high as 2.5 cm away from the pile (≈ 98 % of $r_{u,max,ref}$). Thus, the lateral spreading of the excess pore pressure is relatively high at this level since the soil liquefies also at that distance. The only difference to the signal of the pore pressure being measured at a distance of 2.5 cm to the pile is that the pore water dissipates slightly faster at this location. At a distance of 20 cm to the pile, the pore pressure increases much less (to slightly more than 60 % of $r_{u,max,ref}$). The soil does not liquefy and the pore water dissipates immediately after reaching its maximum value. Thus, the area which is strongly influenced by the deflection of the pile in terms of liquefied soil has a radius of at least 10 cm at that upper level. Assuming a linear degradation of pore pressure between a distance of 10 and 20 cm of the pile, liquefaction would occur up to approximately 15 cm. But this linear behaviour is not likely and further test series should be carried out in order to ascertain the range of excess pore pressure. At the second level, liquefaction only occurs directly at the test pile. The maximum value of the pore pressure ratio at 10 and 20 cm distance from the pile reaches a value of only approximately 0.5 and 0.4, respectively. Hence, the lateral spreading of excess pore pressure is not as high as at level 1. At level 3 and 4, liquefaction never occurred but the tendency of the pore pressure ratio to decrease with increasing horizontal distance is also valid there.

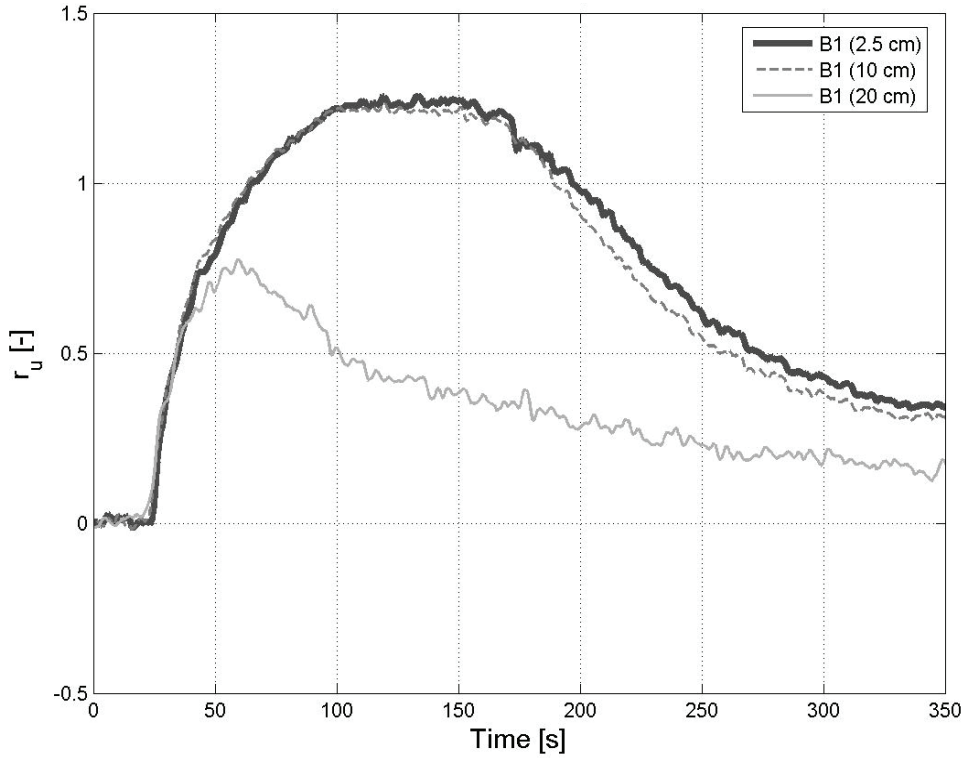

Fig. 6-18: Low-frequency part of the pore pressure ratio r_u at level 1 as a function of time for the backward transducers at different distances from the pile as indicated (2.5 cm, 10 cm and 20 cm). The test series were carried out with $x_w = \pm 0.75$ cm and $f = 1.0$ Hz.

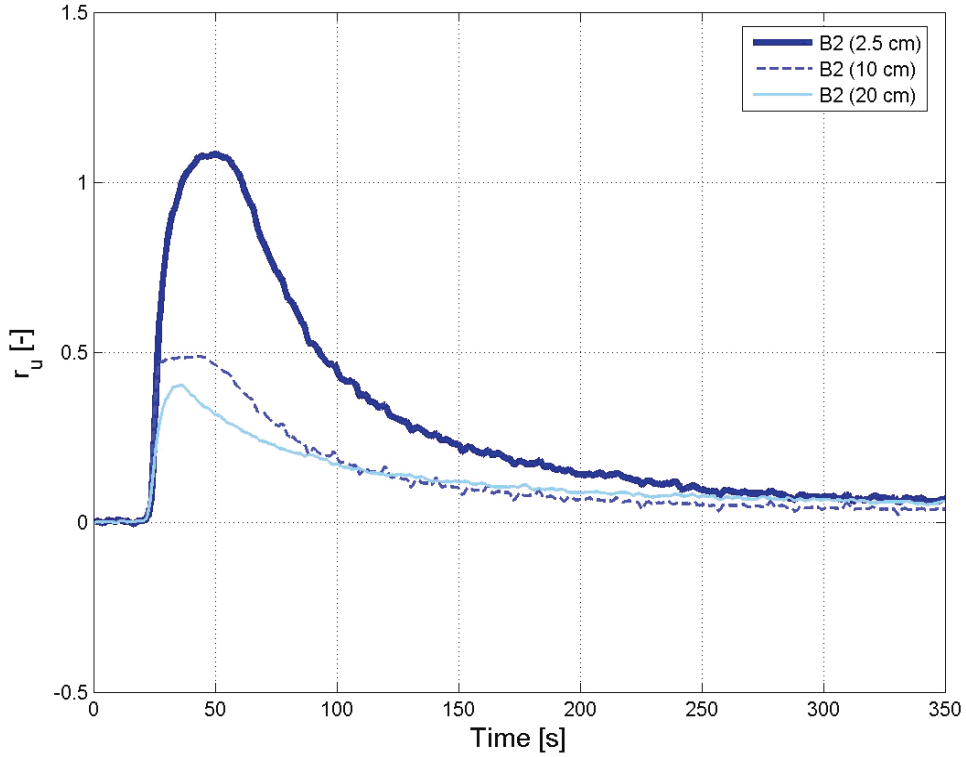

Fig. 6-19: Low-frequency part of the pore pressure ratio r_u at level 2 as a function of time for the backward transducers at different distances from the pile as indicated (2.5 cm, 10 cm and 20 cm). The test series were carried out with $x_w = \pm 0.75$ cm and $f = 1.0$ Hz.

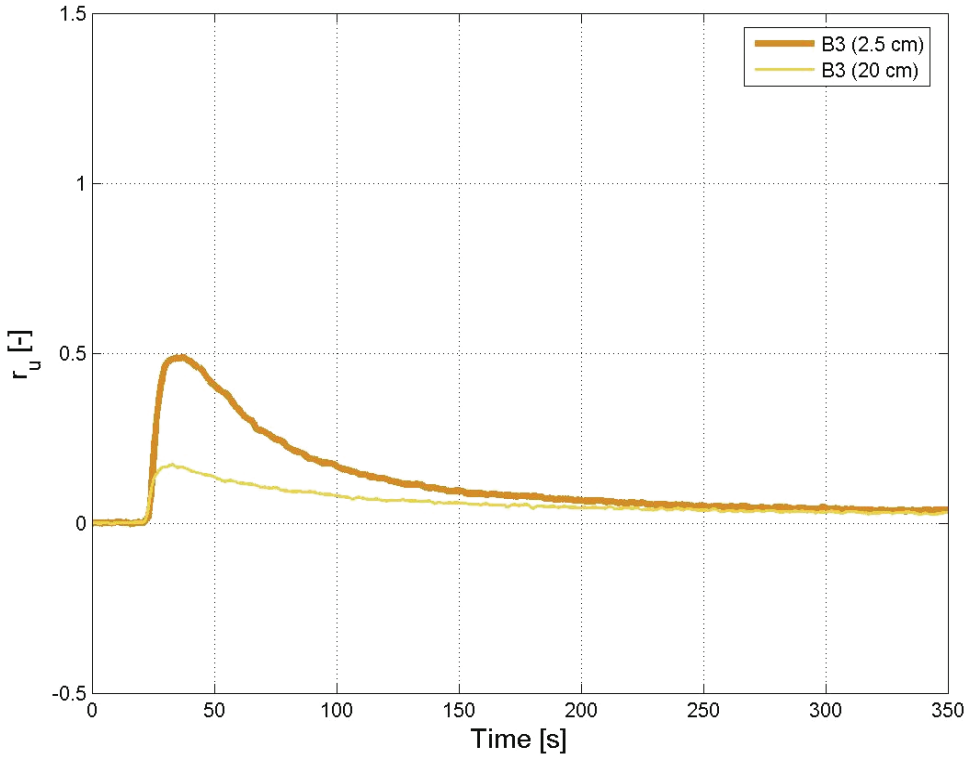

Fig. 6-20: Low-frequency part of the pore pressure ratio r_u at level 3 as a function of time for the backward transducers at different distances from the pile as indicated (2.5 cm, 10 cm and 20 cm). The test series were carried out with $x_w = \pm 0.75$ cm and $f = 1.0$ Hz.

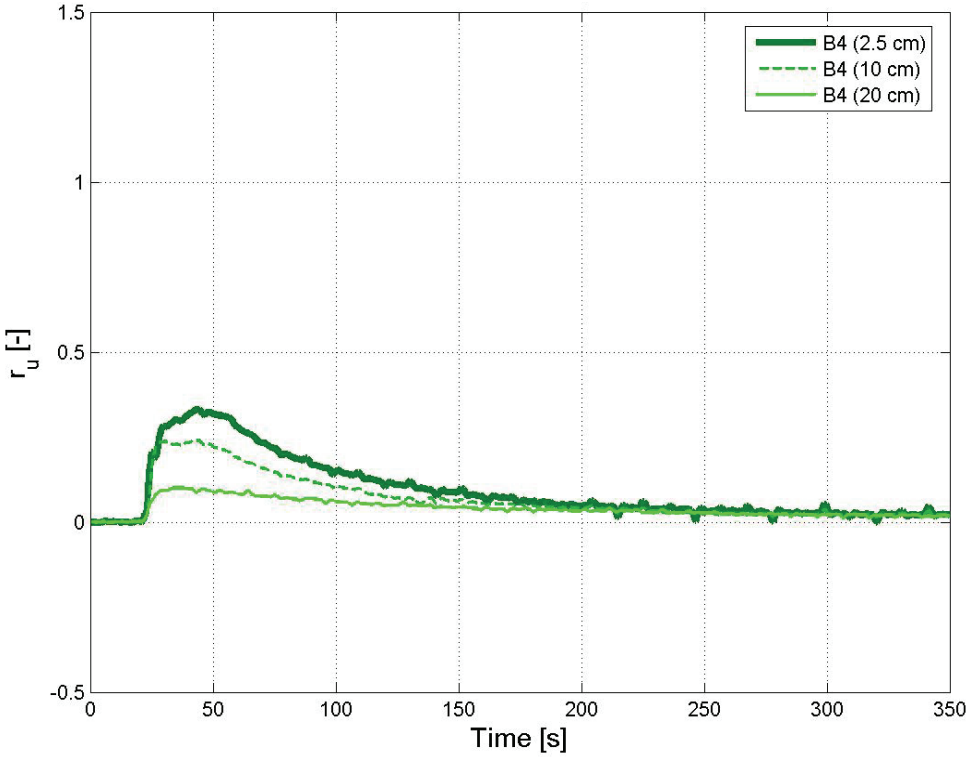

Fig. 6-21: Low-frequency part of the pore pressure ratio r_u at level 4 as a function of time for the backward transducers at different distances from the pile as indicated (2.5 cm, 10 cm and 20 cm). The test series were carried out with $x_w = \pm 0.75$ cm and $f = 1.0$ Hz.

6.2.1.4 Determination of $r_{u,max}$ from the input parameters x_w and f

As it was discussed in the preceding sections, a dependency of $r_{u,max}$ on x_w and f was observed for the levels 2 to 4 in vertical as well as in horizontal direction. In contrast, a dependency at level 1 could only be found for horizontal distances to the pile. In the vertical profile, $r_{u,max}$ increased with increasing pile deflection and loading frequency at the levels 2 to 4. In the horizontal profile, decreasing values of excess pore pressure were found for increasing distance from the pile at all levels. In order to roughly estimate the magnitude of $r_{u,max}$ for future test series, the $r_{u,max}$-values were approximated by linear equations depending on x_w and f. They are represented by planes which are spanned over x_w and f and are shown in Fig. 6-22. Those planes were determined by least-squares regression and thus, are planes of best fit. The coefficient of determination is $R^2 = 0.77$ for level 2, $R^2 = 0.85$ for level 3 and $R^2 = 0.84$ for level 4. Fig. 6-22 contains the generated planes as well as the surfaces representing the measurement data (compare Fig. 6-15 to Fig. 6-17). The equations defining the planes for the levels 2 to 4 are:

$$r_{u,\max,L2}[-] = 0.58 \cdot x_w[cm] + 0.34 \cdot f[Hz] - 0.05\,, \tag{6-8}$$

$$r_{u,\max,L3}[-] = 0.68 \cdot x_w[cm] + 0.34 \cdot f[Hz] - 0.53 \text{ and} \tag{6-9}$$

$$r_{u,\max,L4}[-] = 0.74 \cdot x_w[cm] + 0.24 \cdot f[Hz] - 0.54\,. \tag{6-10}$$

Using those equations, the maximum pore pressure ratio $r_{u,max}$ of the test series carried out within the present research can be calculated as a first approximation by inserting x_w and f of the actual test series in the equations. Since a dependency of $r_{u,max}$ on x_w and f could not be determined for level 1, an equation to estimate values for this level cannot be supplied. For a more accurate estimation of the maximum pore pressure ratio, more test series would be necessary. Hence, the linear interrelation of input parameters and maximum pore pressure ratio could be improved or a nonlinear function could be found to describe the dependencies. In order to account for the horizontal degradation of excess pore pressure, the $r_{u,max}$-values determined by Eqs. (6-8) to (6-10) have to be reduced when considering locations further away from the test pile. Provided that the results of Section 6.2.1.3 are valid for all combinations of x_w and f, the $r_{u,max}$-values have to be reduced by the fractions given in Table 6-2. Nevertheless an equation for the estimation of $r_{u,max}$ cannot be given for level 1, it was found that the excess pore pressure at a distance of 10 cm from the test pile is 2 % below $r_{u,max,ref}$ whereas at a distance of 20 cm, the excess pore pressure is reduced by 40 %.

Table 6-2: Reduction of $r_{u,max}$ for the levels 1-4 for the distances d from the test pile.

	d = 10 cm	d = 20 cm
Level 1	- 2 %	- 40 %
Level 2	- 55 %	- 65 %
Level 3	not available	- 65 %
Level 4	- 30 %	- 70 %

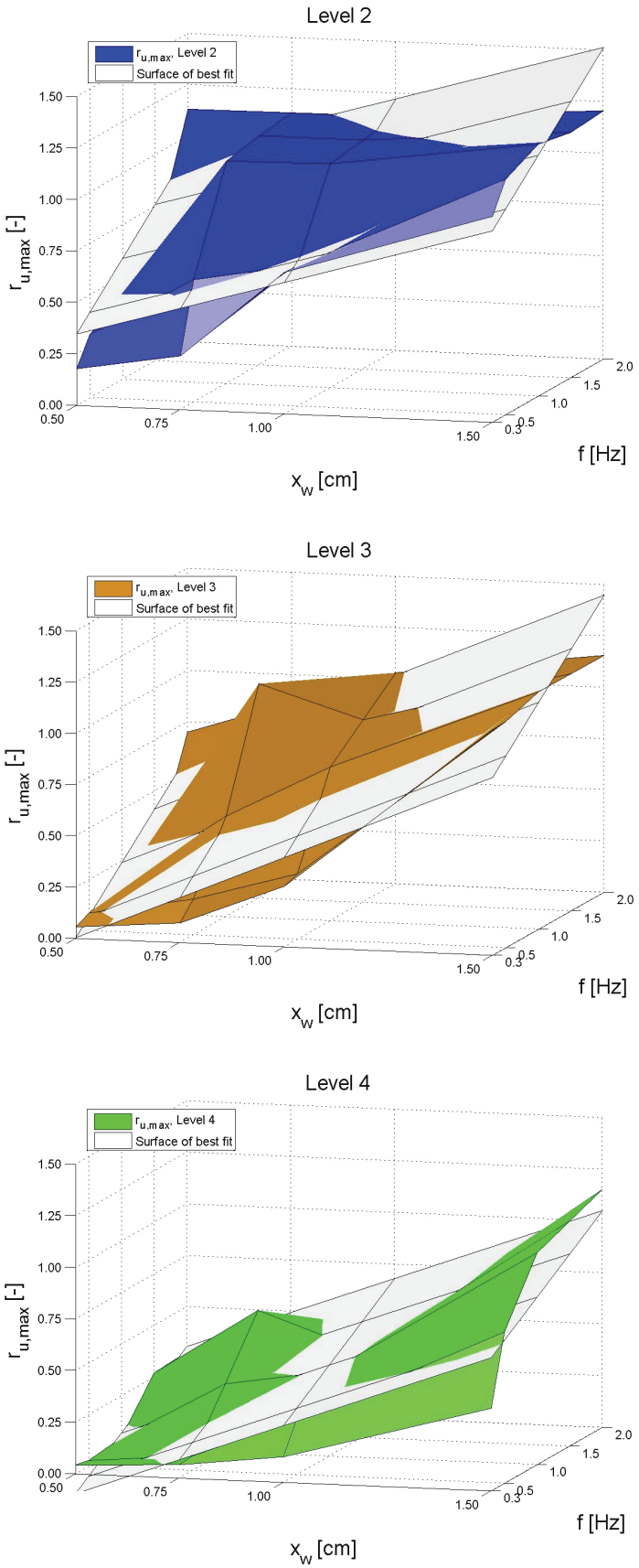

Fig. 6-22: Maximum pore pressure ratio $r_{u,\max}$ for the levels 2-4 and planes of best fit determined for those values.

6.2.2 Temporal analysis of mean pore pressure

Section 6.2.1 revealed at which locations and in which test series liquefaction occurred and how the maximum pore pressure ratio $r_{u,max}$ depends on the input parameters x_w and f. Liquefaction was mostly detected at level 1 but in some test series, the pore pressure ratio also signified soil liquefaction at other levels. However, the pore pressure in the different test series not only differs in the maximum magnitude of the r_u but also in its temporal behaviour after reaching the maxima: sometimes the pore pressure decreases very fast to about the hydrostatic pressure, sometimes this dissipation is delayed. Within this section, the pore pressure ratio will be analysed with respect to the duration of the liquefied state and of the excess pore pressure.

6.2.2.1 Duration of liquefaction

It is important to know not only if or if not liquefaction occurred but also the duration of the liquefied state is important in order to assess the risk of soil liquefaction for structures. Structures founded on liquefied soil can, for example, tilt and tilting is a function of time. So, given that the soil liquefies, it is crucial to know for how long the $r_{u,max}$ -values exceed the threshold value of $r_u = 1$ and if the parameters x_w and f influence this duration. To answer those questions, Fig. 6-9 is once more depicted in Fig. 6-23. Now, the time is analysed for which the signals exceed the liquefaction criterion. This time period is named t_{liq}. It should be noted that it is not entirely correct to speak about the duration of liquefaction when considering this time. The analysed time t_{liq} is the time during which $r_u > 1$ but the ratio r_u refers to the initial effective stress and stresses may change during loading. Anyway, in order to compare the different test series qualitatively, it is appropriate to use this time as a measure for the duration of liquefaction.

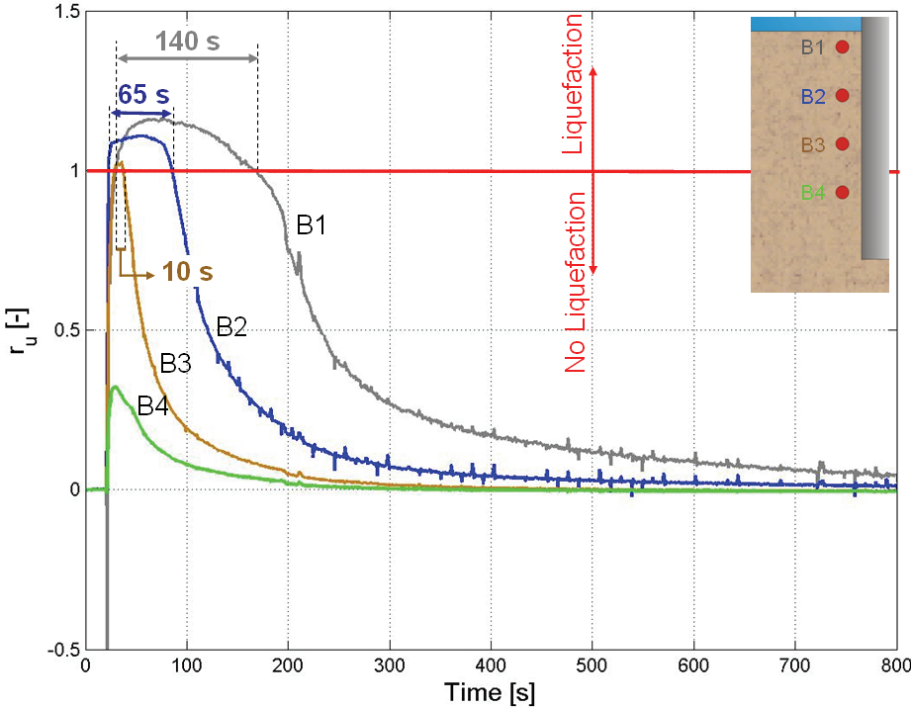

Fig. 6-23: Low-frequency part of the pore pressure ratio r_u as a function of time for the backward transducers B1 – B4 at different levels 2.5 cm away from the surface of the pile ($x_w = \pm 1.0$ cm and $f = 2.0$ Hz). The duration of the liquefied state t_{liq} and the liquefaction criterion are marked.

In the test under consideration represented in Fig. 6-9, t_{liq} of the pore pressure transducer B1 was approximately 140 s. The duration of liquefaction $t_{liq} \approx 65$ s for B2 and $t_{liq} \approx 10$ s for B3. The signal of B4 did not exceed the threshold value of $r_u = 1$, i.e., no liquefaction occurred at that level.

To analyse the duration of the liquefied state at the different measurement levels and to reveal its dependency on x_w and f, the t_{liq}-values for all transducers and tests were analysed accordingly to Section 6.2.1 in a surface and an isoline plot. Those plots showing the duration of the liquefied state for the different combinations of x_w and f are shown in Fig. A-1 to A-4 for all measurement levels individually. Also here, t_{liq} was averaged for group B and group F. For all levels, the liquefied state lasted the longest for test with maximum displacement and frequency. Furthermore, on average, the t_{liq}-values are the highest at level 1 (the scale goes up to 400 s at this level!) and decrease with increasing depth. At level 4, tests with no liquefaction dominate (t_{liq} equals to zero indicates that no liquefaction occurred). Also for this analysis, the dependency of t_{liq} on x_w and f was analysed by means of an isoline plot. As already discussed, the duration of liquefaction increases steeply for high displacements and frequencies. For those combinations, t_{liq} depends strongly on both x_w and f at all levels. The dependency on x_w is due to the larger regions that are affected by the deflection of the pile. Thus, also the process of pore pressure dissipation takes longer since the drainage paths are longer. Since pore pressure only decreases when the pore water can dissipate and since higher frequencies prevent dissipation, it becomes obvious that the duration of the liquefied state is also longer for high loading frequencies. For low x_w and f, t_{liq} is either very low and a dependency cannot be determined (level 1) or a liquefaction does not happen at all ($t_{liq} = 0$). This is the case at level 2, 3 and 4.

6.2.2.2 Duration of excess pore pressure

Since the duration of liquefaction can only be determined for test series and locations where liquefaction occurred, those data are only available for some tests. In order to allow conclusions on the dissipation process also under the condition of no liquefaction, the duration of the dissipation process should be considered as well for all signals. Most of the signals reach their starting value after the excess pore water has drained. But since not all signals come back to exactly this value (compare Section 6.3.2), it is more appropriate to examine the half-life of the excess pore pressure. It is defined as the time until the pore pressure ratio has decreased half of its maximum value. Although the half-life normally describes the exponential decay of a physical quantity, it was seen to be appropriate for the analyses carried out here. Since the highest $r_{u,max}$-value is approximately 1.4, this duration is longer than the duration of liquefaction for all tests. Thus, this half-life $t_{50\%}$ can be readout for every signal even if liquefaction did not occur. In Fig. 6-24, the arrows signify this time for the pore pressure ratio at the four levels. For transducer B1, this half-life is approximately 200 s, $t_{50\%} \approx 95$ s for B2, $t_{50\%} \approx 30$ s for B3 and $t_{50\%} \approx 40$ s for B4.

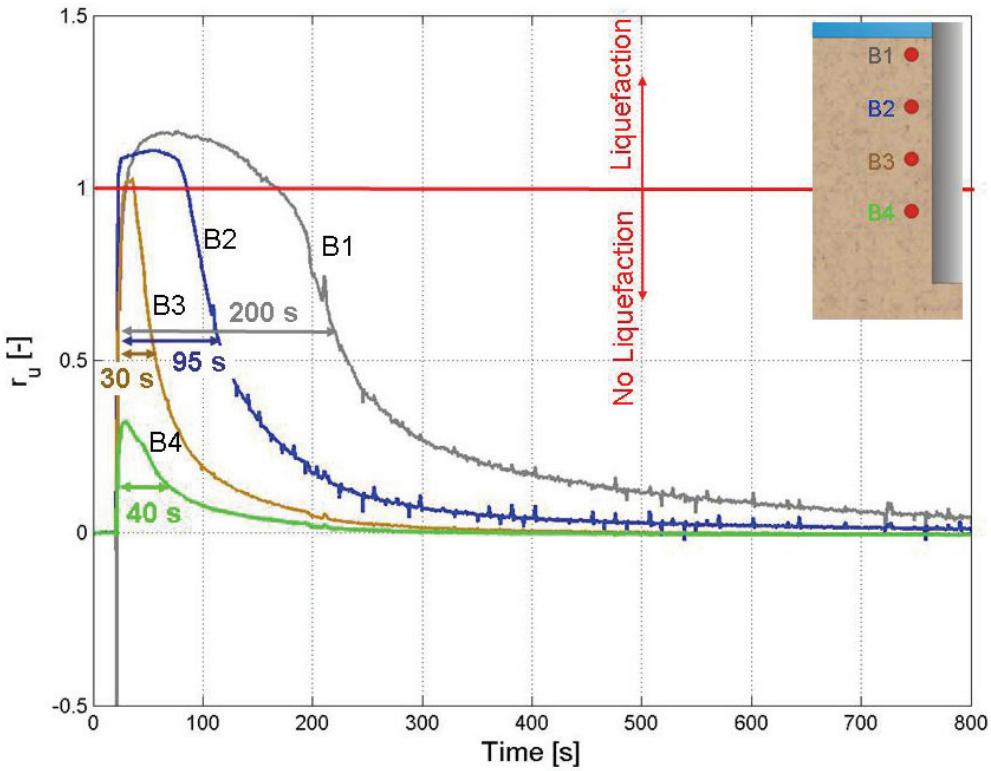

Fig. 6-24: Low-frequency part of the pore pressure ratio r_u as a function of time for the backward transducers B1 – B4 at different levels 2.5 cm away from the surface of the pile (x_w = ±1.0 cm and f = 2.0 Hz). The half-life of the excess pore pressure $t_{50\%}$ after reaching its maximum is marked.

In the appendix B, see Fig. B-1 to B-4, the half-life $t_{50\%}$ (average values of group B and group F) is plotted separately for each measurement level in dependency on x_w and f. Also here, surface as well as isoline plots are provided. The duration of excess pore pressure $t_{50\%}$ generally lasted the longest for tests with maximum displacement and frequency. The levels 1 and 2 differ from the levels 3 and 4. In the upper two levels, $t_{50\%}$ predominantly increases with increasing pile displacement and increasing frequency whereas the longest durations are reached at level 1 (the scale goes up to 500 seconds at this level!). The dependency on x_w can be explained by the larger regions that are embraced by the process of pore pressure dissipation (see spatial spreading in Section 6.2.1.3). Thus, the drainage paths are longer and the dissipation takes more time. Since an excess pore pressure can only be sustained if the generation of pore pressure is higher than its dissipation and since the dissipation depends strongly on the loading frequency, it becomes obvious that the duration of the excess pore pressure is also longer for high loading frequencies. For level 3 and 4, a dependency of $t_{50\%}$ on the input parameters cannot be identified. Instead, the values are relatively constant for low displacements and frequencies as well as for high displacements and frequencies. In addition, $t_{50\%}$-values are lower at level 3 and 4 than at level 1 and 2. Since the pore pressure ratio $r_{u,max}$ does not increase as much at level 3 and 4 as at the upper levels, also the duration $t_{50\%}$ is lower at those levels.

6.2.3 Effect of ongoing loading

In order to analyse the effect of ongoing loading on the pore pressure dissipation, a test was carried out in which the loading was stopped exactly at the beginning of the dissipation process of the pore water. The usual dissipation behaviour of a test with the same input parameters x_w and f ($x_w = \pm 1.0$ cm and $f = 2.0$ Hz) but without stopping the loading is considered comparatively. In Fig. 6-25, the low-frequency part of two pore pressure signals for transducer B 3 are shown. The blue line represents the pore pressure ratio of the normal test (test "N") in which the loading was applied until the end of the test. It is called "normal" test since the loading corresponds to the other tests analysed until now, e.g., shown in Fig. 6-9. The red line represents the test in which the loading was stopped (test "S"). In both tests, the pore pressure strongly increases directly after the loading starts ($t = 20$ s). After approximately 7 s, both signals reach their maximum $r_u \approx 1.05$. The input parameters x_w and f were chosen regarding the fact that the maximum pore pressure does not dissipate immediately after reaching its maximum value but only starts to dissipate after some seconds. Thus, the effect of drainage can well be observed. Since in test "N", the pore water started to dissipate at the time t = 40 s, the loading in test "S" was stopped at the same time.

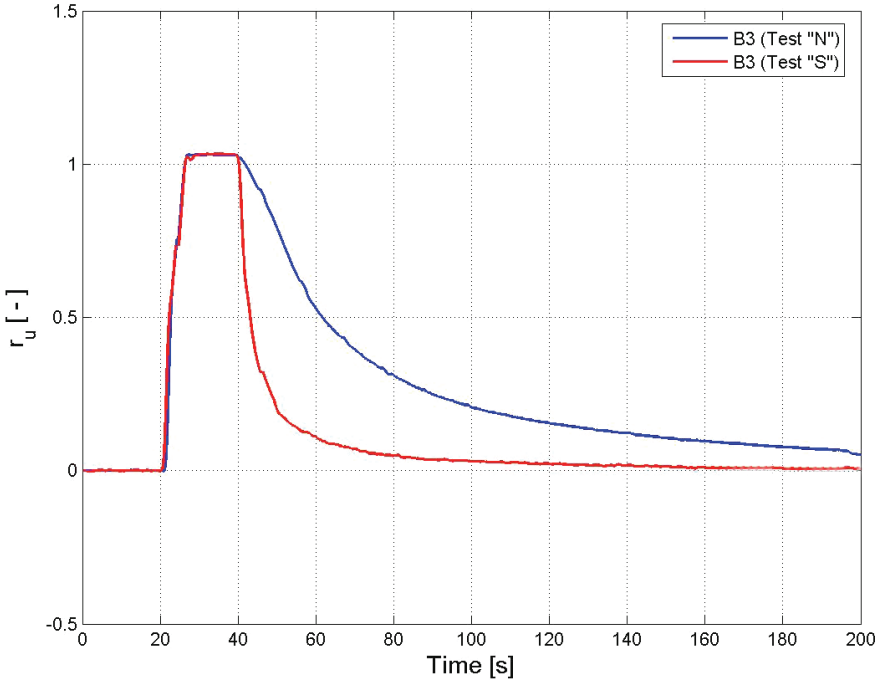

Fig. 6-25: Low-frequency part of the pore pressure ratio r_u at level 3 as a function of time for the backward transducers of a normal test "N" (blue line) and of test "S" which was stopped after 20 s of loading (red curve). Both tests were carried out with $x_w = \pm 1.0$ cm and $f = 2.0$ Hz.

As can be seen in the figure, the pore water in test "S" immediately starts to drain when the loading is stopped. The ratio r_u strongly decreases and the pore pressure reaches its starting value $r_u = 0$ at approximately $t = 160$ s. When considering the first seconds of the dissipation process until the pore pressure has decreased to its half, the gradient g for test "S" can be expressed as

$$g_S = \frac{\Delta u_S}{\Delta t_S} = \frac{2.5\,kN/m^2}{4s} = 0.63\,\frac{kN/m^2}{s}. \tag{6-11}$$

In contrast, the pore pressure in test "N" decreases with a lower gradient, i.e., the pore water drains slower than in test "S". The gradient for test "N" is

$$g_N = \frac{\Delta u_N}{\Delta t_N} = \frac{2.5\,kN/m^2}{22\,s} = 0.11\,\frac{kN/m^2}{s}. \tag{6-12}$$

Those gradients quantify the different dissipation behaviours of the pore water in tests with ongoing and with stopped loading. The dissipation process in test "N" is almost 6 times slower than in test "S" regarding the pore pressure degradation to the half of the pore pressure maximum. At the time $t = 160$ s, the pore pressure ratio in test "N" has still the value of $r_u \approx 0.1$. Only at $t = 400$ s, it reaches its starting value (for the sake of clarity, it is not shown in this figure).

In order to analyse the rate of the pore pressure increase and decrease, the pore pressure increments per loading cycle $\Delta u_{(1\,cycle)}$ were determined for both tests. For a new cycle $n+1$, the increment is calculated by subtraction of the pore pressure of cycle $n+1$ and of cycle n according to

$$\Delta u_{(1\,cycle)} = \Delta u_{n+1} = u_{n+1} - u_n. \tag{6-13}$$

Since during a loading cycle, pore pressure not only accumulates due to the loading but also dissipates due to drainage, the pore pressure rate of a loading cycle consists of two terms:

$$\Delta u_{(1\,cycle)} = (\Delta u_{acc} + \Delta u_{diss})_{(1\,cycle)} \tag{6-14}$$

Hence, $\Delta u_{(1\,cycle)}$ is positive when the accumulated pore pressure of a loading cycle is higher than the dissipated pore pressure. Accordingly, $\Delta u_{(1\,cycle)}$ is negative for $\Delta u_{acc} > \Delta u_{diss}$.

For the analysis of $\Delta u_{(1\,cycle)}$, the time characterized by increasing pore pressure and the time characterized by pore water dissipation are looked at separately. Firstly, the increasing pore pressure during the first 15 s is considered. Fig. 6-26 shows the pore pressure rates $\Delta u_{(1\,cycle)}$ for test "N" (a) and test "S" (b). As could already be seen in Fig. 6-25, the increases in pore pressure at the beginning of the test are relatively equal for both pore pressure signals. They start at $t = 20$ s and end at $t \approx 27$ s. Since $\Delta u_{(1\,cycle)}$ is positive during this period, the increments of the accumulated pore water are higher than the increments of the dissipated pore water. Between $t \approx 27$ s and $t \approx 35$ s, increases in pore pressure Δu_{acc} and decreases in pore pressure Δu_{diss} are balanced, thus $\Delta u_{(1\,cycle)} \approx 0$. This is the time at which the maximum of the pore pressure is reached.

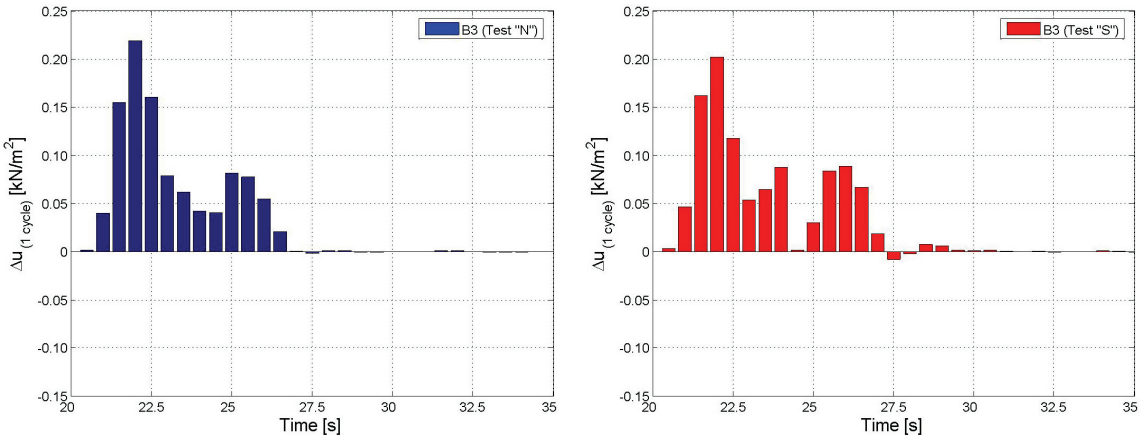

(a) (b)

Fig. 6-26: Pore pressure rate per loading cycle of transducer B3 during the first loading cycles of a usual test (a) and a test which was stopped after approximately 20 seconds of loading (b).

Secondly, the dissipation process is considered, i.e., the time after the pore pressure has reached its maximum. The pore pressure rates for the first loading cycles during this dissipation process are shown in Fig. 6-27 (a) for test "N" and in (b) for test "S". The pore pressure dissipation starts at $t = 40$ s which is shown by negative rates of the pore pressure per loading cycle (hence $\Delta u_{diss} > \Delta u_{acc}$ during this time). The pore pressure rates $\Delta u_{(1\ cycle)}$ are relatively small for test "N" and do not exceed -0.04 kN/m^2·s. In contrast, a very high amount of pore pressure is lost per loading cycle in test "S" in which the loading is stopped. Four cycles after the loading has stopped, those losses go up to nearly -0.30 kN/m^2·s. Since the loading and, therewith, the source of pore pressure accumulation, has been stopped in this test, $\Delta u_{acc} = 0$ from $t = 40$ s on and, therefore, $\Delta u_{(1\ cycle)} = \Delta u_{diss}$. Hence in this test, the pore pressure dissipates without restraint, whereas the ongoing loading in test "N" inhibits the pore water to drain, i.e., slows down the dissipation process. A slower decrease of the excess pore pressure also implies that the effective stress in test "S" recovers slower than it does in test "N" (see Eq. (3-2)). Furthermore, it can be followed that the loading of test "N" is responsible for delayed pore water dissipation in this test, thus for the difference $\Delta u_{(1\ cycle),N} - \Delta u_{(1\ cycle),S}$.

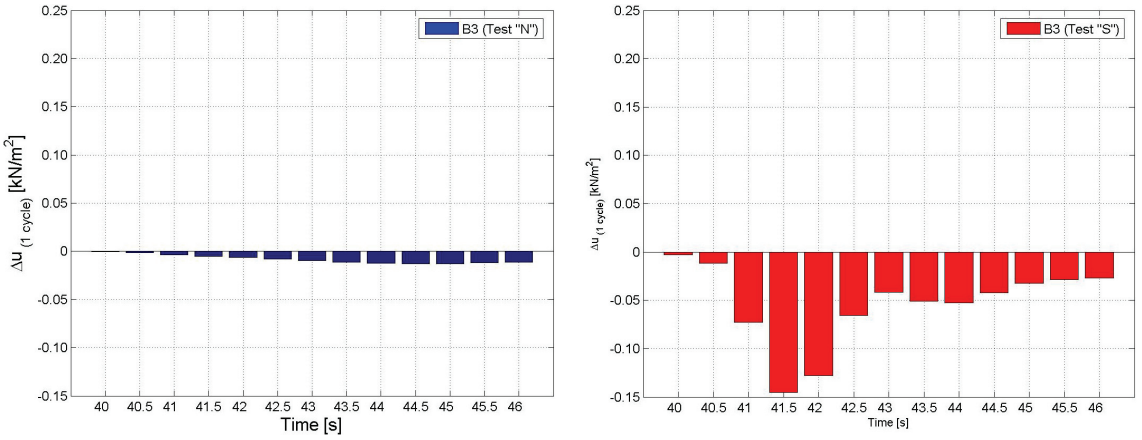

(a) (b)

Fig. 6-27: Pore pressure rate per loading cycle of transducer B3 of test "N" (a) and test "S" (b) during fifteen loading cycles at the beginning of the dissipation process.

6.2.4 Amplitudes of transient pore pressure

In the last sections, the low-frequency parts of the signals were examined with respect to the maximum pore pressure ratio, its dependency on the input parameters, its duration and the effect of ongoing loading. In this section, the transient parts will be analysed, i.e., the high-frequency component of the signal. In contrast to the analyses done before which dealt with the pore pressure ratio r_u, the analysis of the transient pore pressure refers to the pore pressure changes Δu since this parameter has more significance for such investigations. In Fig. 6-28, the transient pore pressure Δu_{trans} is plotted exemplarily for group B for the first 800 s of a test. It becomes evident that Δu_{trans} strongly differs from level to level. In the test shown here, it is the lowest at level 1 ($\Delta u_{trans} = \pm 1.3$ kN/m^2), the highest at level 2 ($\Delta u_{trans} = \pm 4.0$ kN/m^2) and then decreases with depth. As discussed before, Δu_{trans} reflects the transient oscillations of the pore pressure signals per cycle without considering pore pressure accumulation. For level 1, e.g., this means that apart from the residual pore pressure, there is a transient excess pore pressure in each load cycle of maximally 1.3 kN/m^2 followed by a suction of the same value. As can be seen qualitatively in Fig. 6-9, the low-frequency parts of the signals reach their starting value after some hundred seconds of each test. Hence, they fall back to approximately the hydrostatic pressure. Thus, a suction of 1.3 kN/m^2 means that the pore pressure transiently falls below the hydrostatic pressure. In addition, the amplitude of the signals varies over time as can be seen most drastically for transducer B3. For the following analysis of Δu_{trans}, the maximum amplitude of the transient pore pressure was examined.

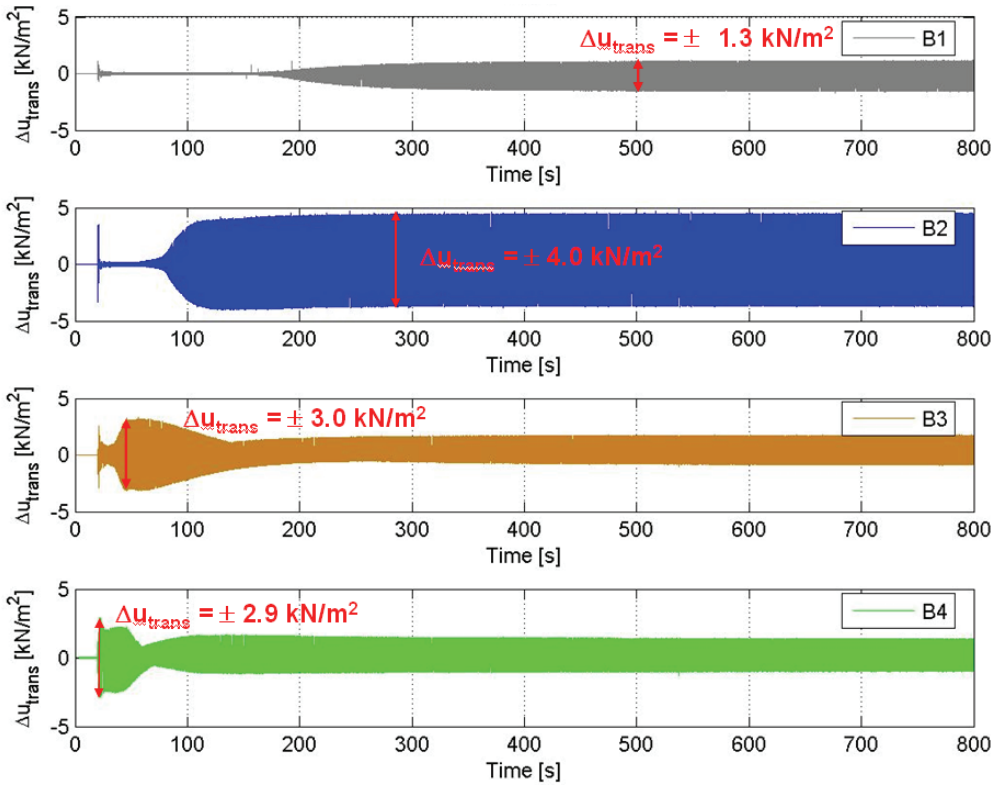

Fig. 6-28: High-frequency part of the pore pressure Δu_{trans} as a function of time for the backward transducers B1 – B4 at different levels 2.5 cm away from the surface of the pile ($x_w = \pm 1.0$ cm and $f = 2.0$ Hz). The maximum values of Δu_{trans} are marked.

In the appendix C, the transient pore pressure is shown separately for all the four levels in a surface and an isoline plot in Fig. C-1 to C-4. Again, the average value of group B and group F is represented. Regarding level 1, the Δu_{trans} values are rather small (0.4 kN/m^2 to 2.6 kN/m^2) and fluctuate. There seems to be no dependency on the parameters x_w and f at all. This is due to the fact, that level 1 is very near to the sand surface and, though, the pore pressure dissipates very fast. For the levels 2 to 4, however, a strong correlation can be noticed: Δu_{trans} increases with increasing x_w and f. As indicated by the straight lines, the correlation between transient pore pressure and either displacement or frequency is quite similar. At level 2, this leads to a very steep increase in Δu_{trans} up to approximately 14 kN/m^2. This means that the excess pore pressure is approximately four times higher than the initial mean effective stress. At level 3, the transient pore pressure is generally smaller and only increases to around Δu_{trans} = 5.5 kN/m^2. At level 4, Δu_{trans} is again higher and goes up to approximately 14 kN/m^2. Therefrom, it can be concluded that the pile has a rotation point between level 2 and 3. Because of the low values of Δu_{trans} at level 3, it can be concluded that this rotation point is closer to level 3 than to level 2, probably directly above the level 3. This was already mentioned in the analyses of the correlation of displacement and pore pressure in Section 6.1.4 and will be confirmed by the cross-correlation analyses of the pile deflection and the pore pressure in Section 6.3.1. Thus, the deflection of the pile at level 3 is very small, resulting in very small transient pore pressure oscillations. The dependency of Δu_{trans} on x_w can be explained with Δu_{trans} following the pressure and suction effects of the pile. As the deflection is higher at the levels 2 and 4 compared to level 3 (due to the vicinity of the rotation point), also Δu_{trans} is higher at level 2 and 4 compared to level 3. It was seen that not only the deflection but also the loading frequency influences Δu_{trans}: with increasing f, Δu_{trans} increases at the levels 2 to 4. A reason for this dependency is the inertia of the water that leads to higher amplitudes for increased frequencies.

6.3 Analysis II: Analysis of the final conditions (Phase 2)

In this section, the final test conditions will be analysed, i.e., the time after the first 800 seconds. At this stage, the initial soil rearrangements are completed, the excess pore pressure has dissipated and the measurement data are characterized by a steady behaviour. Thus, Phase 2 allows analysing the correlation of the pore pressure and the displacement when the initial soil rearrangements are finished. Apart from that, it can be investigated whether at the end of the test series, an increased pore pressure can be measured compared to the initial hydrostatic pore pressure or not.

6.3.1 Cross-correlation of displacement and pore pressure in Phase 2

In order to start with the analysis of the correlation of displacement and pore pressure, the sketch in Fig. 6-2 is recalled which shows the test pile in its different positions during one loading cycle. The system of load application is represented on the left-hand side and the displacement measurement on the right-hand side of the pile. The position of the pore pressure transducers is marked by ‘B’ and ‘F’ at the bottom of the figure. At the beginning, the test pile is in its starting position marked by the brown coloured pile in the middle of the sketch. Hence, the con-rod is in position ‘1’. When the test starts, the loading system first pulls the pile towards

position ‘2’. At this position, the pile (represented in blue) experiences its maximum deflection in direction of the pore pressure transducers of group B and the displacement transducers reach their minimum value. Then, the test pile is pushed back in the other direction, over position ‘3’ to position ‘4’. At this point, it has its maximum deflection in direction of the pore pressure transducers of group F and the displacement transducers reach their maximum value.

Fig. 6-29 exemplarily represents the signals x_s and the pore pressure of group B during a period of 1.3 s in Phase 2. On the left-hand side of the figure, the displacement x_s and the pore pressure B1 to B4 are shown for approximately four loading cycles. On the right-hand side, the according cross-correlation functions of the signals under consideration are given.

As could already be seen in Fig. 6-8, the correlation between x_s and the pore pressure at the first level is not very high. The maximum cross-correlation coefficient in the period under consideration is determined to $\rho_{xy,max}$ = -0.6. The negative correlation signifies that the pore pressure decreases with increasing x_s and vice versa. The low correlation is due to the fact that the pore pressure at this level fluctuates most. This again, is because of the vicinity of the interface between sand and water which allows a better drainage of the pore water and prevents its accumulation. As can best be seen for level 2, the forward deflection of the pile, i.e., the deflection away from the transducers of group B (increase in x_s) causes the pore pressure B2 to decrease (marked by the solid line in the figure). This corresponds to the theory (Section 3.4.3) which connects volume decreases and pore pressure increases. After the pile reaches its maximum deflection (marked by the dashed line in that figure), it moves back in direction of the transducer and the pore pressure increases. The maximum cross-correlation coefficient at level and period under consideration equals to $\rho_{xy,max}$ = -0.97. This indicates a very high negative correlation between the displacement and the pore pressure. Looking at the cross-correlation coefficient function of this level shown on the right-hand side of the figure, it can be seen that the pore pressure has a delay in time of τ_0 = 0.01 s compared to the deflection of the pile.

Contrary to the upper levels, the pore pressure at the levels 3 and 4 increases with increasing x_s and thus, the cross-correlation coefficients are positive. Since this increase in x_s is measured above the embedding of the pile in the sand, it can be concluded that the pile has a rotation point between levels 2 and 3. A deflection of the pile to the one side at the level of load application leads to a deflection to the other side in those bottom levels. The maximum cross-correlation coefficient at levels 3 and 4 is 0.92 and 0.94, respectively, and, therefore, almost as high as at level 2. When comparing the time shifts τ_0, it can be seen that those time shifts are very small for all levels (0 to 0.03 s). This means that the pore pressure reacts very fast to changes of the deflection of the pile. Nevertheless, it is obvious for the two bottom levels that the pore pressure begins to decreases in value before the pile has reached its maximum deflection (dashed line). At first glance, this is surprising. But it can be explained by a decrease of deflection over the length of the pile. Due to the ratio of the stiffness of the soil and the pile and, thus, due to the embedding of the pile, the deflection of the pile at level 3 and 4 is much less than at the sand level. Hence, when the pile is still deflected at the sand level (x_s), it experiences no deflection at level 3 and 4 anymore resulting in the immediate initiation of pore water dissipation. In contrast,

only a small impulse of the pile towards group B seems to suffice to stop the dissipation process and to result in pore pressure increases again (solid line).

Results very similar to the results presented here were seen for all test series. Concluding, it can be resumed that after a certain time of loading, namely in the second phase indicated in Fig. 6-8, the algebraic signs of the cross-correlation coefficients $\rho_{xy,max}$ are always opposite for the two upper and the two bottom levels. This signifies that there is a rotation point between the levels 2 and 3. Furthermore, they are opposite for group B and for group F. Further, the cross-correlation coefficients are usually very high for the levels 2-4 whereas at level 1, the signals are less correlated.

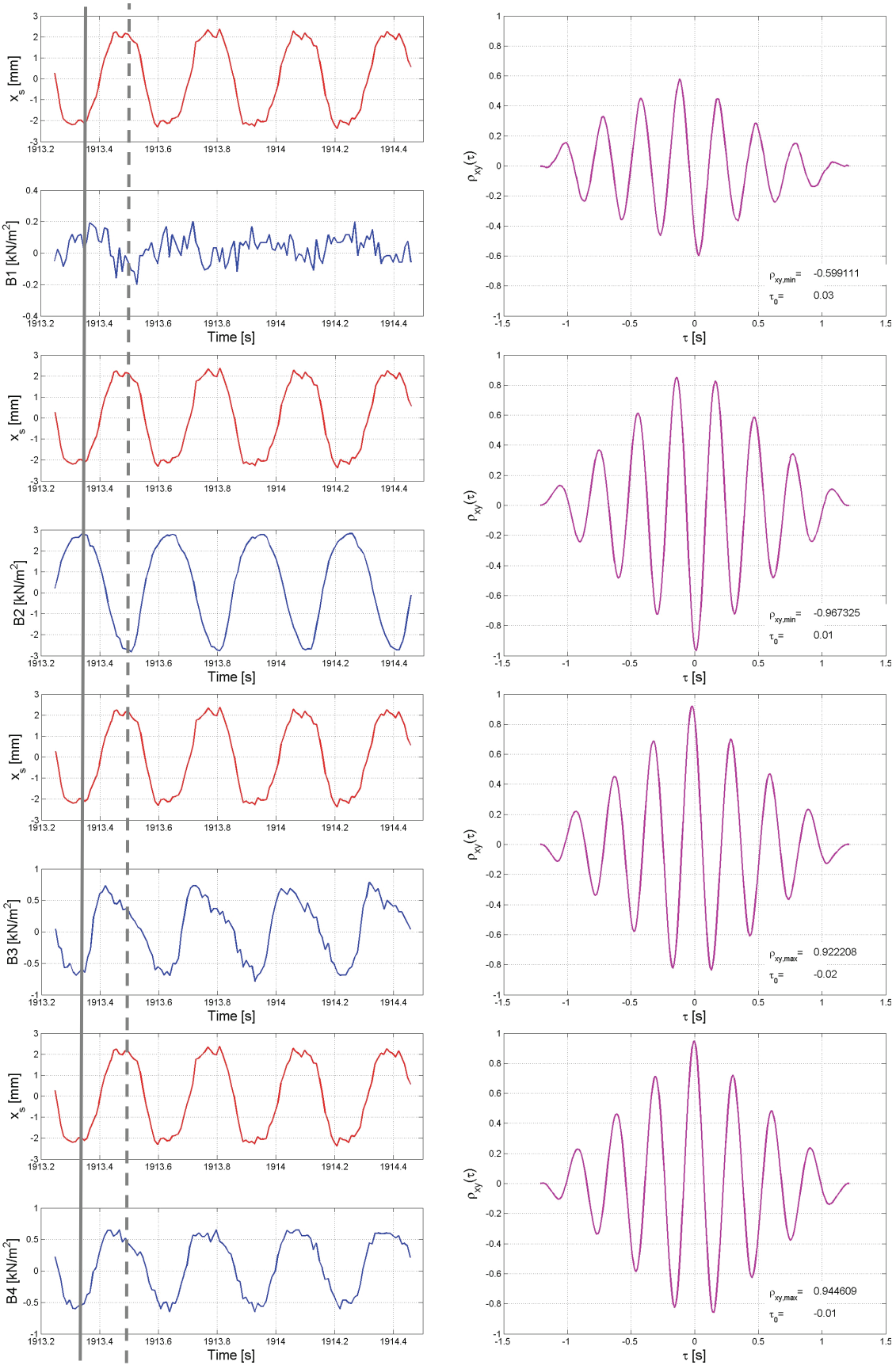

Fig. 6-29: Displacement x_s and pore pressure signals of group B (left-hand side) and the associated cross-correlation coefficient function (right-hand side).

6.3.2 Comparison of initial and final pore pressure

As discussed in Chapter 4, an earthquake-induced excess pore pressure in the soil may be observed more than one hour after the seismic loading. Also in the analyses of OUMERACI and KUDELLA (2004) carried out on a caisson breakwater, it was noticed that the pore pressure under the caisson accumulated only slowly and reached its maximum value after many cycles without dissipating significantly. In contrast, as could already be seen by the general progression of the pore pressure signals, the pore pressure measured in the test series carried out here increased rapidly immediately after the beginning of the loading but also dissipated relatively fast and went back to approximately the value of hydrostatic pressure. To reveal if in the present case, a residual excess pore pressure would persist in the soil after the loading, the very final values of the pore pressure measurements of the test series were compared with the initial values (hydrostatic pore pressure). This comparison was done for all tests and transducers by use of the mean initial and mean final values of the original data.

It was seen that the deviations were very small: they mostly even did not exceed 1 %. In addition, no trend could be identified for increased or decreased pore pressure at the end of the test series. This indicates that the values of the pore pressure at the end of the test approximately correspond to the initial values. Therefore, a residual pore pressure at the end of the loading, as it can be found after earthquakes, cannot be confirmed for the test series carried out in the present work. Nevertheless, this does not imply that liquefaction did not occur. In contrast, liquefaction was observed. Neither, this signifies that the changes in pore pressure can be neglected and do not imply a risk for the structures. It has to be remembered that the test series carried out within the present research are displacement-driven tests. Thus, a tilting of the structure is not possible. In reality, when affected by wave forces, structures can tilt although the soil is only liquefied for some moments.

6.4 Key results of the experimental test series

The experimental investigations carried out within this research analysed the occurrence of soil liquefaction in vicinity of a cyclically loaded pile. The test program combined a wide range of input parameters in order to reveal the dependencies of the pore pressure on those parameters. A summary of the key results of those analyses is given in Table 6-3 and is resumed in the following.

In a first analysis, the maximum values of the pore pressure ratio $r_{u,max}$ were analysed in the vertical as well as in the horizontal profile. It was seen that the highest $r_{u,max}$-values were generally reached at level 1. At this level, liquefaction occurred in 75 % of the tests carried out. Also at distances further away from the test pile, considerable excess pore pressure was measured. Nevertheless, a dependency on the input parameters x_w and f could not be observed for this level. This means that liquefaction also occurred in tests characterised by deflections with low amplitudes and frequencies. It was further observed that the $r_{u,max}$-values decreased from level 1 to level 4 as well as with horizontal distance to the pile. Whereas at level 2, an equal dependency of $r_{u,max}$ on x_w and f was detected ($r_{u,max}$ increased with increasing x_w and f), the dependency on x_w became stronger with depth. In three test series, liquefaction was observed at all levels,

i.e., over 63 % of the embedded length of the pile. Although large vertical displacements of the pile were prevented by the pile being fixed to the system of load application, it was seen that the pile slightly sank into the soil within those test series. In order to extrapolate values of $r_{u,max}$ for different combinations of the input parameters, equations were developed for the levels 2 to 4 which express $r_{u,max}$ in dependency of x_w and f.

It was not only analysed whether or not liquefaction occurred but also for how long the soil was liquefied or experienced significant excess pore pressure. The liquefied state generally lasted in the range of seconds to minutes (the longest duration of liquefaction was approximately 7 min). The duration of liquefaction t_{liq} was seen to be the longest at level 1 and to decrease with depth. Nevertheless, a dependency of t_{liq} on the input parameters was observed for all levels which was similarly strong for x_w and f.

For the cases where liquefaction was not reached, the duration of liquefaction could not be determined. Nevertheless, the duration of excess pore pressure (the time until the pore pressure ratio has decreased to the half of its maximum value) $t_{50\%}$ could be analysed for all cases. It was seen that $t_{50\%}$ generally decreased from level 1 to level 4. At the levels 1 and 2, a correlation of $t_{50\%}$ on x_w and f, equally strong for both parameters, was observed. In contrast, $t_{50\%}$ was relatively constant at the bottom levels 3 and 4 and a dependency could not be detected. A test, in which the loading was stopped after the pore pressure ratio had reached its maximum value, showed that $t_{50\%}$ was six times smaller than in the usual tests with ongoing loading. Thus, $t_{50\%}$ can be seen as a measure for the dissipation process.

For all test series, not only the general process of the signals was analysed, i.e., their low-frequency parts but also the amplitude of their high-frequency parts, i.e., the amplitude of the transient oscillations Δu_{trans}. This analysis revealed that Δu_{trans} was higher at the levels 2 and 4 than at the levels 1 and 3. In addition, it could be seen that Δu_{trans} did not depend on the input parameters at level 1 but increased with increasing x_w and f at the other levels. Obviously, the reason for the behaviour of Δu_{trans} at level 1 is its location close to the sand surface which allowed the pore water to drain relatively fast. The small amplitudes of Δu_{trans} at level 3 and the higher amplitudes at the levels 2 and 4 lead to the conclusion that there is a rotation point close to level 3.

The analysis of the final phase showed that the pore pressure and the deflection of the pile are highly correlated to each other in this phase at the levels 2 to 4. It was observed that the rotation point must be located between the levels 2 and 3. Furthermore, an analysis of the deviation of the final pore pressure values from the initial values showed that an excess pore pressure did not persist in the soil over the entire duration of the test series. In contrast, the pore pressure dissipated very fast after reaching its maximum value and went back to approximately the hydrostatic pore pressure.

Table 6-3: Summary of the key results of the pore pressure analyses.

Predominant behaviour of $r_{u,max}$ when…	**x_w ↑**	**f ↑**
at level 1:	No dependency, but mostly liquefaction	
at levels 2, 3, 4:	$r_{u,max}$ ↑	$r_{u,max}$ ↑
Further comments: • $r_{u,max}$ decreases from level 1 to level 4 • Influence of x_w increases with depth (level 2: $r_{u,max}$ equally depends on x_w and f, level 4: $r_{u,max}$ mainly depends on x_w) • $r_{u,max}$ decreases with distance from test pile (only analysed in two test series) • The spatial spreading is the highest at level 1 and decreases with depth		

Predominant behaviour of t_{liq} when…	**x_w ↑**	**f ↑**
at levels 1, 2, 3, 4:	t_{liq} ↑	t_{liq} ↑
Further comments: • t_{liq} decreases from level 1 to level 4 • The correlation of t_{liq} with x_w and f is similarly strong		

Predominant behaviour of $t_{50\%}$ when…	**x_w ↑**	**f ↑**
at level 1, 2:	$t_{50\%}$ ↑	$t_{50\%}$ ↑
at levels 3, 4:	No dependency, $t_{50\%}$ relatively constant	
Further comments: • $t_{50\%}$ decreases from level 1 to level 4 • At the levels 1 and 2, the correlation of t_{liq} with x_w and f is similarly strong • $t_{50\%}$ is six times smaller when the loading is stopped after the pore pressure has reached its maximum value (only analysed in one test series)		

Predominant behaviour of Δu_{trans} when…	**x_w ↑**	**f ↑**
at level 1:	No dependency	
at levels 2, 3, 4:	Δu_{trans} ↑	Δu_{trans} ↑
Further comments: • Δu_{trans} is higher at the levels 2 and 4 compared to the levels 1 and 3 • The correlation of Δu_{trans} with x_w and f is similarly strong for the levels 2, 3 and 4		

Further results from analysis of final conditions
• The pore pressure u and the pile deflection x_s are highly correlated at the levels 2 to 4 • Rotation point between the levels 2 and 3 • No residual pore pressure at the end of the test series

6.5 Discussion on the probability of occurrence of soil liquefaction

In the analyses, it was found that liquefaction at level 1 occurred in most of the test series, namely in 75 %. In 60 % of the tests, the liquefied soil also included the second level, in 35 % also the third level and in 15 % of the tests, also level 4 was affected by soil liquefaction. Liquefaction over all four levels indicates that the so-defined minimum liquefied depth corresponds to a fraction of approximately 63 % of the embedded length of the pile. Strong dependencies on the amplitude of deflection and on the loading frequency were found for all analysed parameters. Those dependencies are summarised in Table 6-3. The test program included forced displacements from ±0.5 cm to ±1.5 cm and frequencies from 0.3 Hz to 2.0 Hz.

Remembering the motivation for the test program shown in Table 5-4, it can be recognized that the tests with displacements smaller than 1.0 cm and with frequencies below 1.4 Hz are interesting for the transfer back to real offshore conditions (compare Section 5.2). The tests with higher input parameters were carried out to enlarge the analysed spectrum in order to determine dependencies on those parameters. Nine test series fall into the range of $x_w \leq 1.0$ cm and $f \leq 1.4$ Hz and thus, those nine tests should be considered in more detail in order to discuss the probability of occurrence of soil liquefaction at in situ locations. Nevertheless by doing so, it has to be recalled that the conditions represented in the test model slightly differ from the conditions in situ (uniform displacement-driven load application, lower pile stiffness) and, thus, do not allow the direct transfer of the results. However, it is necessary to analyse those tests with respect to this transfer in order to draw conclusions for further research.

The vertical profiles of the maximum pore pressure ratio of those nine tests are represented in Fig. 6-30. For the sake of clarity, the labelling of the axes was omitted. According to Fig. 6-12, the maximum pore pressure ratio is represented by the x-axis whereas the y-axis represents the depths under ground surface. Again, the red line signifies the liquefaction criterion $r_u = 1$. As can be seen for the tests within this range, soil liquefaction occurred in four of those nine tests. In the other tests, the pore pressure also accumulated but did not exceed the threshold of $r_u = 1$. The four tests in which liquefaction was observed are indicated by the labelling T1 to T4. It is obvious that liquefaction in those tests only occurred at level 1 and 2. Nevertheless, as it was seen in Table 6-1, liquefaction observed at level 2 means that at least the upper 0.38 m of soil were liquefied, i.e., at least 25 % of the embedded length of the pile. Furthermore, the maximum duration of the liquefied state was 75 s at maximum (test T3, level 1). Nevertheless, those smaller input values fall in the range in which only small increases in amplitude of deflection and frequency cause relatively strong increases of the maximum values of pore pressure. This can be seen most notably in the isoline plots in Fig. 6-15 and Fig. 6-16 and, therefore, should be considered with caution.

As mentioned before, the loading frequencies of 0.3-1.0 Hz correspond to in situ wave periods of approximately 4.5-15 s (compare Section 5.2). In order to estimate the probability of occurrence of the wave events represented by the tests T1 to T4 in an ocean storm, Fig. 2-9 is considered. This figure supplies the probability of occurrence of certain wave heights and the corresponding wave periods which were derived by Eq. (2-7). The maximum permitted deflection was determined by means of the serviceability criterion given in Eq. (2-1) to 1.0 cm ($=x_w$).

This deflection is supposed to be only reached under extreme, unfavourable conditions. Therefrom, the following conclusions for the test series T1 to T4 can be qualitatively drawn:

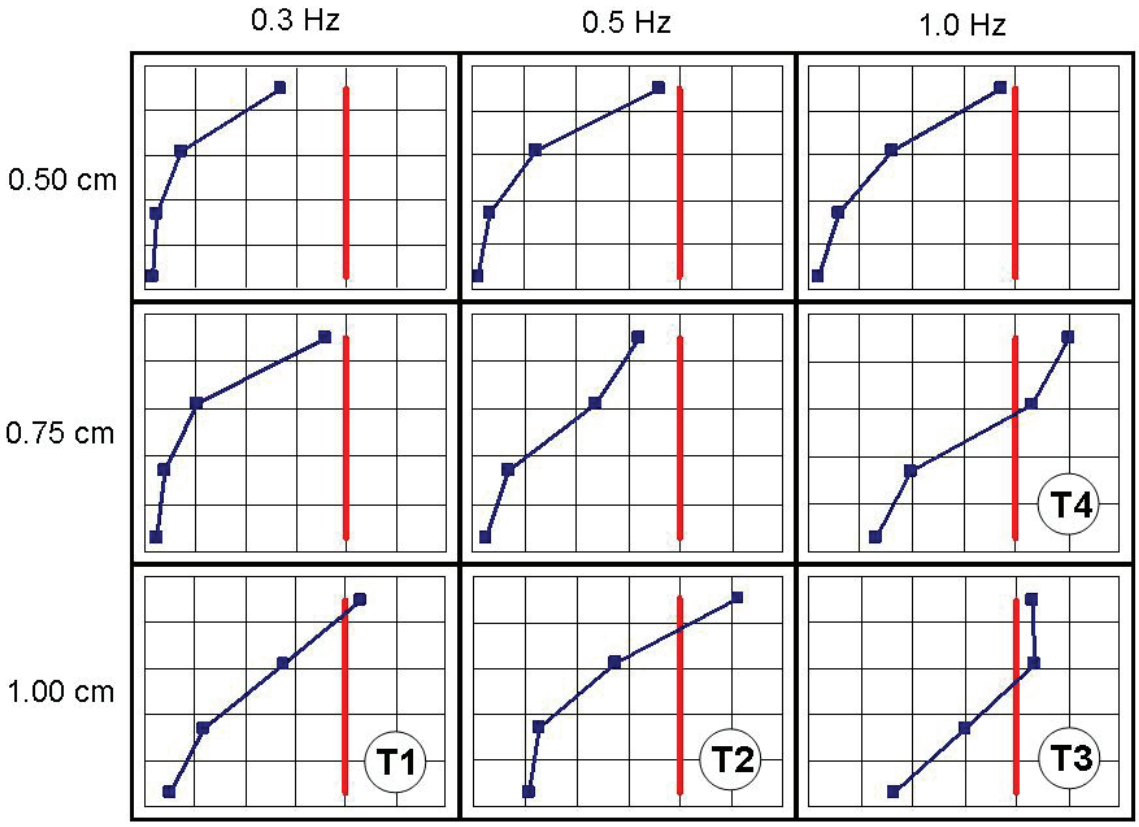

Fig. 6-30: Vertical profiles of $r_{u,max}$ for the tests within the range of x_w = ±0.50 - 1.00 cm and f = 0.3 - 1.0 Hz measured at a distance of 2.5 cm from the test pile. The axes are according to Fig. 6-12 (x-axis: $r_{u,max}$ [-], y-axis: depth [m]) and T1 – T4 indicate the tests in which liquefaction occurred.

T1: Waves with this frequency have a very low probability of occurrence in an ocean storm. In the storm profile under consideration (Fig. 2-9), only one single wave with the corresponding height (23 m) hits the structure during the 36-hour storm (in Phase 4). Since this wave height corresponds to the maximum wave height in a storm and applies high forces to the structure, a large deflection of the pile is expected.

⇒ Frequency: Unlikely to occur (according to the storm profile: 0.005 %).
Deflection: Possible to occur for frequency under consideration.

T2: The loading frequency of 0.5 Hz in the test model corresponds to waves with a wave period of approximately 9 s at in situ locations. Regarding the storm profile given in Fig. 2-9, those waves occur during Phase 2 to Phase 6. Their over-all probability of occurrence is 2.4 %. Considering the fact that those waves produce forces considerably smaller than the forces produced by waves with the maximum wave height, a deflection of 6 cm in situ (corresponds to the deflection of this test) is not very likely.

⇒ Frequency: Likely to occur (according to the storm profile: 2.4 %).
Deflection: Unlikely to occur for frequency under consideration.

T3: Transferred to nature, waves with the frequency chosen in test T3 have a period of approximately 4.5 s. Hence, more than one-fifth of the waves during an ocean storm are waves which fall in this range (20.6 %). They especially occur during Phase 1 and Phase 7, namely to 16.5 %. Thus, those waves would also hit the structures during normal conditions, i.e., non-storm conditions. Nevertheless, due to their low wave height, the forces they apply on the structures are marginal and thus, it is very unlikely that the structure is deflected by 6 cm.

⇒ Frequency: Very likely to occur (according to the storm profile: 20.6 %).
Deflection: Very unlikely to occur for frequency under consideration.

T4: The test represented by T4 was carried out with the same frequency as test T3. Hence, its frequency also applies to 20.6 % of the waves during an ocean storm. Since the deflection here was only 0.75 cm, those conditions are more likely to be encountered in situ than the ones represented by test T3. Nevertheless, also a deflection of approximately 4 cm in situ (corresponds to $x_w \approx \pm 0.75$ cm) seems to be very unlikely to be caused by a wave with a height of 1 to 2 m.

⇒ Frequency: Very likely to occur (according to the storm profile: 20.6 %).
Deflection: Very unlikely to occur for frequency under consideration.

The discussion of those four tests makes clear that the conditions represented by the other tests shown in Fig. 6-30 are more probable to be encountered than those of the tests T1 to T4. Recapitulating, it can be concluded that for the tests T2 to T4 which were carried out with frequencies likely to occur during normal or storm conditions, the low wave heights imply low wave forces which would not suffice to cause deflections of 4 cm or higher. Hence, the combined amplitude and frequency of deflection are not probable to occur at one and the same time.

In contrast to the tests T2 to T4, a wave with a frequency represented by test T1 has a very high impact when striking the pile structure and thus, a high deflection is probable. Assuming that this reflection would be as high as the limit deflection, nevertheless, such a wave only occurs once according to the storm profile under consideration (compare Fig. 2-9). Hence, before and after this wave, waves with lower heights and forces hit the structure. However, since waves progressively increase and decrease in height during the storm, the maximum wave is presumably followed by waves with only slightly lower heights. Thus, it should be investigated whether those loading conditions could evoke soil liquefaction as well.

Assuming that the soil would also liquefy under those loading conditions and that the vertical spreading of liquefaction would equal to the one of test T1, the minimum liquefied depth defined in Section 6.2.1.2 would equal to 6.7 % of the embedded length of the pile (level 1) but to not more than 25.3 % of this length (level 2). When transferring those results to a real offshore pile with an embedded length of 30 m, this would equal to a minimum liquefied depth of 2 m or 7.6 m, respectively. Now regarding scour, a phenomenon described in, e.g., SUMER and FREDSØE (2002), losses in the embedding of the pile can also occur due to this scour phenomenon. The depth of the so-induced scour holes is estimated to equal two times the diameter of the pile. Thus, for the offshore monopile foundation given in Table 5-2, for example, the

minimum liquefied depth would correspond to only one-fifth of the scour hole depth or to three-fourth of it, respectively. Thus, in both cases, the minimum liquefied depth would be smaller than the scour hole depth. According to DET NORSKE VERITAS (2004), the formation of scour holes has either be taken into account when designing the dimensions of the foundation or it has to be prevented by adequate means for scour protection which have to be installed around the structures as early as possible. Hence, regarding the first case, the loss of pile embedding due to soil liquefaction would already be considered by the design. Regarding the second case, means for scour protection would have to ensure a protection against soil liquefaction as well or additional means for soil liquefaction would be necessary. Nevertheless, since also scour is not finally examined yet, further investigations on the soil liquefaction phenomenon should be conducted in order to verify those assumptions.

Within the test series carried out in this research, uniform displacement-driven loading conditions were applied to the test pile. This driving mode was seen to be important in order to achieve reproducible results that allow a profound understanding of the ongoing processes in the soil. The dependency of the pore pressure on the amplitude of deflection, on the loading frequency and on the distance from the pile, for example, could hence be analysed. Nevertheless, the probability of occurrence of soil liquefaction can only be quantitatively determined for the test series carried out within this research. Due to the displacement-driven, uniform loading conditions, the results of those test series cannot be transferred directly to in situ conditions since they do not correspond to the conditions met there. Hence, for definite predictions concerning the pore pressure changes during real offshore loading conditions, further test series would be necessary that study

- force-driven instead of displacement-driven loading conditions and
- non-uniform instead of uniform loading conditions.

Thus, the set-up of the test model should be adjusted for further test series such that a force-driven loading will be possible. First test series of this kind were already carried out by means of a pneumatically-driven loading system. Based on the knowledge gained by the displacement-driven test series described here, such test series should be further developed and conducted. Hence, forces down-scaled from in situ conditions could be applied to the test pile and would allow free oscillations of the pile due to those forces. This is important since doing so, the reaction of the pile towards soil liquefaction, i.e., a liquefaction-caused tilting or sinking of the pile could be analysed.

Further, not only uniform loading conditions (be them displacement-driven or force-driven) but rather non-uniform conditions should be simulated in further test series in order to better reproduce the loading conditions offshore. Hence, the storm profile given in Chapter 2.5.3, for example, with its seven phases, the corresponding wave numbers and wave heights could be adopted. By carrying out test series according to this storm profile, a very good simulation of the real loading conditions offshore during a storm would be achieved. Furthermore, when specific locations are to be modelled, the test pile as well as the subsoil properties should be adapted to the special in situ conditions under consideration.

7 Numerical simulation

As discussed in Chapter 4, numerical investigations related to the topic of this research mostly dealt with seismically induced liquefaction, with pore pressure increases beneath caisson breakwaters or with accumulating displacements around cyclically loaded piles. Therefore, it is the objective of this research to investigate whether an accumulation of pore pressure due to the cyclic deflection of a pile can also be simulated numerically. Consequently, all characteristics of the test model described in Chapter 5 are transferred to a numerical model and the same uniform displacement-driven loading is applied to the modelled pile structure. Hence, it can be analysed whether the numerically calculated pore pressure is in good agreement to the measured pore pressure from the test series and if the dependencies on the input parameters found in the analysis of the test series can also be observed in the numerical simulation. If this is the case, further investigations can focus on the numerical simulation and can analyse the influences of pile stiffness as well as of non-uniform and force-driven loading conditions. Furthermore, the transferability of the probability of soil liquefaction discussed in the previous chapter can be ascertained. Concluding, it is the aim of the numerical simulations to properly model the deflection-induced pore pressure measured in the test series.

For this numerical simulation, the finite-difference program FLAC (Fast Langrangian Analysis of Continua) was used. This program originally developed by Peter Cundhall in 1986 is commercially released by the ITASCA Consultants GmbH. FLAC is based on the explicit finite difference method. It incorporates eleven basic constitutive models and, in addition, provides a pore pressure generation model which can be used in the dynamic analysis option. This is the so-called Finn and Byrne model presented in Section 3.4.3. FLAC contains a programming language, FISH (short form of FLACish) which allows the user to define functions and variables and to customize constitutive models and analyses. For more details, see ITASCA (2002).

7.1 Theoretical background

FLAC is a computer code that incrementally solves differential equations which are very difficult to solve analytically due to the high computational effort required for this task. The method used by FLAC for this problem is the finite difference method (FDM). To solve differential equations numerically, a discretisation in time and space is necessary. Therefore, the time continuum is replaced by discrete points in time. In order to do this, two solution schemes exist, namely an explicit and an implicit one. In explicit solution schemes, the calculation of a new

increment only requires the nodal values of the known time step *n*. In contrast, the implicit solution scheme also demands for the solution of the nodes at the new time step *n+1*. Hence, a coupled differential equation system has to be solved when using this time integration algorithm. The discretisation in time will be treated in Section 7.1.2.

Apart from the discretisation in time, the modelled area can no longer be seen as a spatial continuum but as an area discretised by a grid. In the FDM, partial derivatives in the differential equations are replaced by finite difference approximations assuming linear variations of those variables over finite intervals. Those finite differential approximations are expressed in discrete nodes of the system. Hence, calculations are done discretely at the grid nodes. The discretisation in space is discussed in Section 7.1.1.

Thus, derivatives for time and space have to be formulated independently from each other. Doing so, the differential equation is transferred to a large algebraic system of equations which can easily be solved by means of a computer. As Euler (1707 – 1783) was the first one to use finite difference schemes, this technique is often referred to as the Euler technique (see D'ACUNTO (2004)). After 1945, research on finite differences was driven forward strongly because of the new possibilities offered by the development of computers. Today, equations with variable coefficients as well as nonlinear problems can be handled by the FDM.

7.1.1 Discretisation in space

To approximate a derivative of a function by finite differences and to estimate the error in this finite difference approximation, the Taylor's series expansion is used. In its general form, it is given by

$$\begin{aligned} f(x+\Delta x) &= f(x) + \sum_{h=0}^{\infty} f^{(h)}(x)\frac{(\Delta x)^h}{h!} \\ &= f(x) + f'(x)\cdot\Delta x + f''(x)\frac{\Delta x^2}{2!} + f'''(x)\frac{\Delta x^3}{3!} + \dots . \end{aligned} \tag{7-1}$$

In terms of the derivative, it becomes

$$f'(x) = \frac{f(x+\Delta x) - f(x)}{\Delta x} - f''(x)\frac{\Delta x^2}{2!} - f'''(x)\frac{\Delta x^3}{3!} - \dots . \tag{7-2}$$

Because $f''(x), f'''(x), \dots$ are not known, those terms are handled as the error $O((\Delta x)^n)$:

$$f'(x) = \frac{f(x+\Delta x) - f(x)}{\Delta x} - O((\Delta x)^n) . \tag{7-3}$$

The function $u(x_j)$ depicted in Fig. 7-1 represents a function of only one variable which can be differentiated many times. The derivative of that function at the point x_j is $u'(x_j)$. Geometrically seen, it is the tangent at the point $(x_j, u(x_j))$. In order to approximate that derivative, the finite difference method is used. There are three possibilities for the approximation: the forward, the backward and the centred approximation.

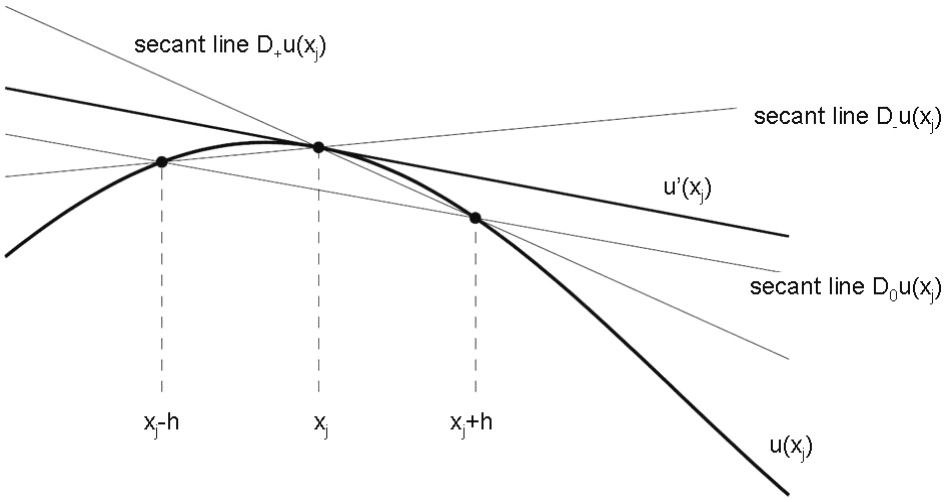

Fig. 7-1: Function *u(x$_j$)*, its derivative *u'(x$_j$)* and three different approximations to *u(x$_j$)* interpreted as the slope of secant lines (after LEVEQUE (2005)).

According to Eq. (7-3), *u'(x$_j$)* can be approximated by

$$u'_f(x_j) = \frac{u(x_j + h) - u(x_j)}{h} - O((h)^n). \tag{7-4}$$

This approximation *u'$_f$(x$_j$)* is called forward approximation as it starts at point *x$_j$+h* whereas *h* is the grid size. Geometrically seen, *u'$_f$(x$_j$)* is the slope of the secant lines that connects the points *(x$_j$, u(x$_j$))* and *(x$_j$+h, u(x$_j$+h))*. In Fig. 7-2, this secant line is named *D$_+$u(x$_j$)*.

Furthermore, there is the backward approximation *u'$_b$(x$_j$)* given by

$$u'_b(x_j) = \frac{u(x_j) - u(x_j - h)}{h} - O((h)^n) \tag{7-5}$$

and represented in Fig. 7-1 by the secant line *D$_-$u(x$_j$)*. As said before, *O((h)^n)* estimates the error of this approximation. Knowing that

$$u'(x_j) = \lim_{h \to 0} \frac{u(x_j + h) - u(x_j)}{h} \tag{7-6}$$

is the proper expression for *h* becoming zero, it is clear that the error *O((h)^n)* depends on the grid size *h*. For *u'$_f$(x$_j$)* and *u'$_b$(x$_j$)*, the size of the error is roughly proportional to *h*. Therefore, this kind of approximation is called a first-order accurate approximation.

As can be seen from Fig. 7-1 by the secant line *D$_0$u(x$_j$)*, the centred approximation *u'$_c$(x$_j$)* is a third possibility to approximate *u'(x$_j$)* by

$$u'_c(x) = \frac{u(x + h) - u(x - h)}{2h}. \tag{7-7}$$

This expression gives a better approximation since the error *O((h)^n)* is proportional to *h^2*. Therefore, it is called a second-order accurate approximation. Formulas involving even more grid points, i.e., higher-order derivatives, will have still smaller errors.

7.1.2 Discretisation in time

Whereas the discretisation in space leads to almost identical results no matter what kind of method is used, the way of integrating the time can strongly influence the solution progress of a problem. The most important characteristic of a numerical solution scheme is the way of integrating time derivatives in a nonlinear differential equation. This can be done either implicitly or explicitly. The dynamic analysis in FLAC uses an explicit finite difference approach in time. With explicit time integration algorithms, nonlinear problems can be computed in almost the same time as linear ones whereas implicit time integration algorithms take significantly longer to solve nonlinear problems. Furthermore, it is not necessary to solve systems of coupled equations and to store any matrices. This results in fewer requirements for computer time and memory. In order to discuss the different methods of discretisation in time, Fig. 7-2 is considered which shows different nodal solutions during different time steps. For both methods, the nodal increment u_j^t at the spatial location x_j is known for the time step t and the solution u_j^{t+1} for the new time step t+1 is supposed to be calculated.

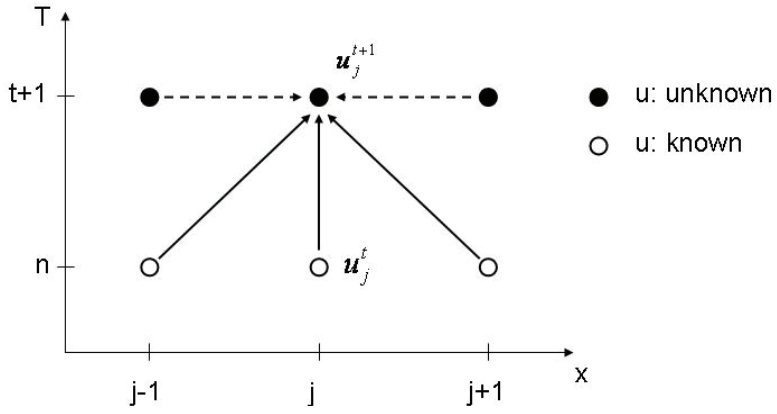

Fig. 7-2: Discretisation in time.

Implicit solution schemes

In implicit solution schemes, the solution of the nodal increment u_j^{t+1} is not only influenced by the solution of the neighbouring nodes at the time step t (represented in Fig. 7-2 by the solid arrows) but also by the neighbouring nodes at the new time step $t+1$ (represented by the dotted arrows). Hence, the implicit discretisation in time at the grid point x_j at time T_t is

$$\left[\frac{\partial u}{\partial t}\right]_j^t = \frac{u_j^{t+1} - u^t}{\Delta t} = A \cdot u^{t+1}, \tag{7-8}$$

whereas A includes a number of factors which will not be explained here. According to Eq. (7-8), the differential equations at every node depend on each other. The complete system is considered until a stable solution is approached and a system of dependent algebraic equations has to be solved. This results in slight deviations of the solution path and in an iterative process of improvement. Depending on the algorithm used for those iterations, different methods as the Newton-Raphson method, the secant method, the arc length method, or the Line Search (see WILL (1996)) may be distinguished. Because the algebraic equations depend on each other, the solution at each node is not known until the entire solution is found.

Explicit solution schemes

Also in explicit solution schemes, the solution of the neighbouring nodes is needed when calculating the new increment. But here, equilibrium is only specified for discrete nodes and only the values of the known time step t are needed (represented in Fig. 7-2 by the solid arrows). So, the differential equations of the new nodal increments can be solved independently of each other at the grid point x_j at time T_t by

$$\left[\frac{\partial u}{\partial t}\right]_j^t = \frac{u^{t+1} - u^t}{\Delta t} = A \cdot u^t . \tag{7-9}$$

The most complex part of explicit solution schemes is the choice of the critical time step. This time step has to be small enough so that the numerical propagation velocity of information between two spatial nodes is smaller than the maximum propagation velocity of the physical process. Thus, the critical time step depends on the speed of wave propagation and on the geometric situation, i.e., the grid definition. Using that time step, the system matrices (M, C, and K) become diagonal. Hence, the equations of motion of all nodes are uncoupled and can be solved independently from one another. Whereas the time step in implicit solution schemes can be arbitrarily large, it has to be relatively small in explicit calculations. That means a high number of computation cycles has to be carried out before a static equilibrium is reached. But with this small time step, deviations from the solution path are very small and the loadings in the system propagate according to the material model. The deviations are corrected in the next time step; iterations are not necessary. Hence, the small time step of explicit solution schemes results in small amounts of computational effort per time step whereas the computational effort per time step is larger for implicit solution schemes.

7.1.3 Implementation of the Finn and Byrne model in FLAC

FLAC can perform coupled dynamic-groundwater flow calculations. By default, the pore fluid simply responds to changes in pore volume caused by the mechanical dynamic loading. The average pore pressure remains essentially constant in the analysis. However, pore pressure can build up in sands during cyclic shear loading, leading to liquefaction. There are a number of models that attempt to account for pore pressure build-up, but they are often referred to specific laboratory tests. But since in nature, the stress and strain paths do not correspond to those uniform tests but follow arbitrary rules, an adequate model must be robust and general. The Finn and Byrne model is considered as an appropriate model that accounts for the basic physical processes. Both formulations of this pore pressure generation model, Eq. (3-17) and Eq. (3-20), are formulated in FLAC and can be incorporated in the standard Mohr Coulomb plasticity model.

In MARTIN et al. (1975) and most other publications on this topic, the notion of a strain reversal is clear because they consider one-dimensional measures of strain. In 2-D analyses, however, there are at least three components of the strain rate tensor. By eliminating the volumetric strain, the strain increments of the two-dimensional strain space at time step t are accumulated at time step $t+1$ as follows:

$$\varepsilon_1^{t+1} = \varepsilon_1^t + \Delta e_{11} - \Delta e_{22} \tag{7-10}$$

and

$$\varepsilon_2^{t+1} = \varepsilon_2^t + 2\Delta e_{12}\,. \tag{7-11}$$

To locate the extreme points in strain space, the preceding unit vector in strain space n_i^t is computed as

$$n_i^t = \frac{v_i}{|v_i|}, \tag{7-12}$$

where

$$v_i = \varepsilon_i^t - \varepsilon_i^{t-1}. \tag{7-13}$$

The subscript *i* takes the values 1 and 2. Repeated indices imply summation. The projection of the new vector, $\varepsilon_i^{t+1} - \varepsilon_i^t$, from one iteration step to the next, is given by the dot product of the new vector with the previous unit vector:

$$d = (\varepsilon_i^{t+1} - \varepsilon_i^t) \cdot n_i^t\,. \tag{7-14}$$

Thus, a negative *d* indicates a reversal in strain. The absolute value of *d* is checked and when a maximum d_{max} is reached after a minimum number of time steps, the updates

$$\gamma = d_{\max}\,, \tag{7-15}$$

$$\varepsilon_i^{t-1} = \varepsilon_i^t\,, \tag{7-16}$$

and

$$\varepsilon_i^t = \varepsilon_i^{t+1} \tag{7-17}$$

are done. The γ derived in this way is inserted into Eq. (3-17) or Eq. (3-23), and $\Delta\varepsilon_{vd}$ is obtained. The accumulated volumetric strain is then updated to

$$\varepsilon_{vd}^{t+1} = \varepsilon_{vd}^t + \Delta\varepsilon_{vd} \tag{7-18}$$

and is saved in order to use it again in Eq. (3-17) or Eq. (3-23). Also, one-third of $\Delta\varepsilon_{vd}$ is saved and the direct strain increment inputs are adjusted to the model at the next cycle *c+1* by

$$\Delta e_{11}^{c+1} = \Delta e_{11}^c + \frac{\Delta\varepsilon_{vd}}{3}, \tag{7-19}$$

$$\Delta e_{22}^{c+1} = \Delta e_{22}^c + \frac{\Delta\varepsilon_{vd}}{3} \tag{7-20}$$

and

$$\Delta e_{33}^{c+1} = \Delta e_{33}^{c} + \frac{\Delta \varepsilon_{vd}}{3} . \tag{7-21}$$

The normal strain increment adjusts the effective stresses (calculated as mean total stress plus pore pressure). As compressive strain increments are negative in FLAC and $\Delta\varepsilon_{vd}$ is positive, the effective stress decreases and the pore pressure increases.

7.2 Test of the Finn and Byrne Model

Most of the applications of the Finn and Byrne Model described in Section 3.4.3 deal with earthquake loadings. But within the present research, soil liquefaction due to the movement of a structure in the offshore environment is analysed. As discussed before, earthquake loadings differ from wave loading in the offshore environment in certain points. Therefore, it is tested in a preliminary study if the Finn and Byrne model is also applicable to properly model the deflection-induced pore pressure generation studied within this research. As it could be seen in Fig. 3-13 (b), the volumetric strain increment $\Delta\varepsilon_{vd}$ of a new loading cycle depends on the level of the accumulated volumetric strain ε_{vd} of the previous cycles and of the applied cyclic shear strain amplitude γ during the cycle under consideration. After each cycle, ε_{vd} is updated with the new increment $\Delta\varepsilon_{vd}$ until it reaches a level where no further increase in ε_{vd} is possible. The volumetric strain increments are coupled to the pore pressure: with increasing compaction, also the pore pressure increases. Since $\Delta\varepsilon_{vd}$ always increases in Fig. 3-13, the pore pressure always accumulates but does not decrease in value. Since it is not evident if also dilatation of the soil, leading to a decrease in pore pressure, can be simulated, a simplified 25-zone test model is studied first. This model consists of 5 x 5 zones and is depicted in Fig. 7-3.

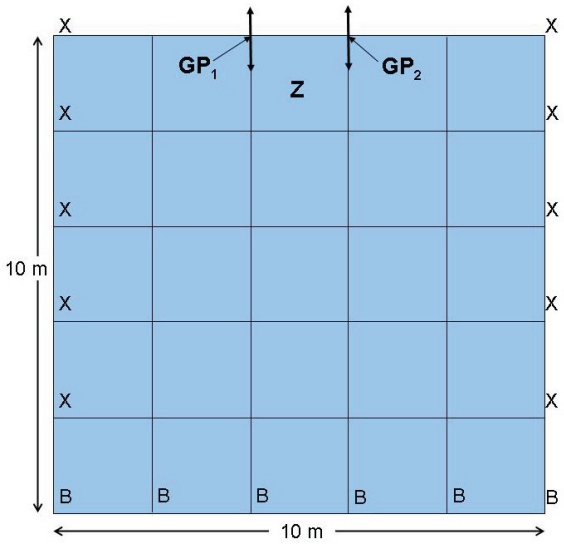

Parameters	Value
Soil density	2000 kg/m^3
Bulk modulus, soil	1.26·10^5 kN/m^2
Shear modulus	5.8·10^4 kN/m^2
Inner friction angle	35°
Porosity	0.4
Saturation	1
Water density	1000 kg/m^3
Bulk modulus, water	2·10^6 kN/m^2

Fig. 7-3: 25-zone test model with boundaries fixed in x-direction (X) and in both x- and y-direction (B), respectively. Grid points *GP$_1$* and *GP$_2$* are sinusoidally loaded to analyse the volumetric strain and pore pressure response in zone *Z*. The material parameters are given in the table.

A sinusoidal normal loading is applied to two grid points GP_1 and GP_2 as indicated by the black arrows. The pore pressure response is analysed for the zone that is enclosed by those grid points, named *Z*. The loading results in displacements of the grid points shown in the upper part of the diagram of Fig. 7-4 (black curve). The grid points oscillate around their initial position and due to this displacement, the volumetric strain ε_{vd} in *Z* changes. ε_{vd} of *Z* is shown by the green curve. When the grid points are displaced upward (dilatation), this displacement causes an increasing ε_{vd} (positive increments $\Delta\varepsilon_{vd}$). A displacement in downward direction (compression) causes a decreasing ε_{vd} (negative increments $\Delta\varepsilon_{vd}$). The therefrom resulting pore pressure changes in *Z* are shown in the plot below. It can be seen that when the zone experiences positive $\Delta\varepsilon_{vd}$ (dilatation), the pore pressure decreases and vice versa. Thus, it could be shown that the volumetric strain cannot only cause an increase but can also lead to a decrease in pore pressure.

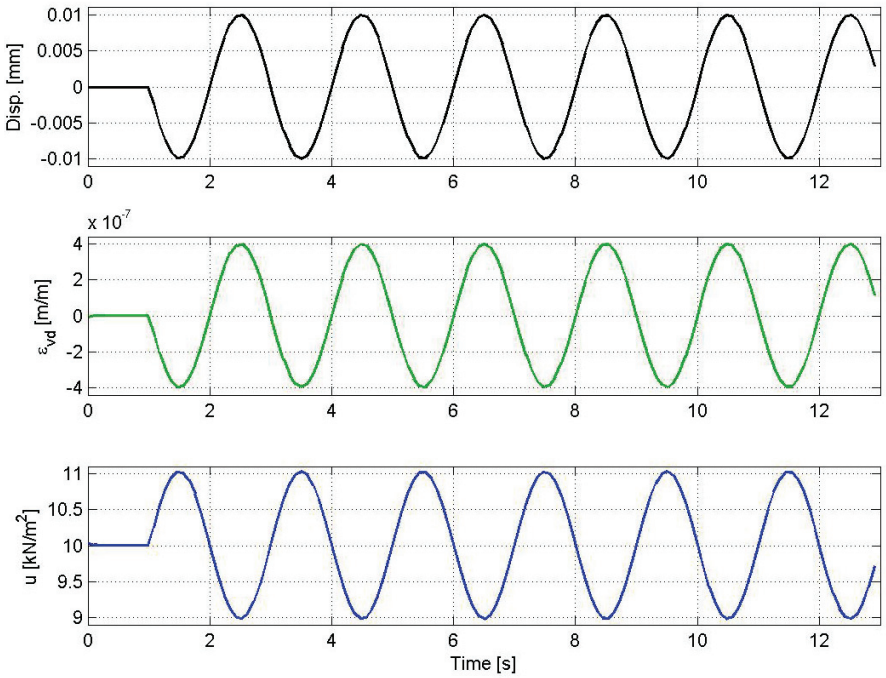

Fig. 7-4: Loading at gridpoint GP_1 and GP_2 and responses in zone *Z* over the time. Upper curve: forced displacement of the grid points GP_1 and GP_2; middle curve: volumetric strain increment ε_{vd} in zone *Z;* lower curve: pore pressure response *u* in zone *Z*.

7.3 Generation of the numerical model

This section supplies basic information on the generation of the numerical model for the simulation of the test series described in the previous chapters. Due to long computational times, the model was simulated with the two-dimensional FLAC program. This simplification from the three-dimensional to the two-dimensional simulation is justified for the pore pressure generation since this pore pressure generation is caused by the deflection of the pile in the x,y-plane. The pore pressure is also allowed to dissipate in parallel to this x,y-plane. The dissipating excess pore water Δu per time *t* can be expressed by the differential equation of consolidation in this plane by

$$\frac{\partial \Delta u}{\partial t} = c_v \cdot \left(\frac{\partial^2 \Delta u}{\partial x^2} + \frac{\partial^2 \Delta u}{\partial y^2} \right). \tag{7-22}$$

In this equation, c_v is the coefficient of consolidation, including the coefficient of permeability k, the compressibility of the soil K_s and the unit weight of water γ_w:

$$c_v = \frac{k \cdot K_s}{\gamma_w}. \tag{7-23}$$

Whereas the pore pressure generation induced by the deflection of the pile can be well represented by the two-dimensional simulation, the pore pressure dissipation is underestimated by neglecting the third dimension. According to LANG et al. (2007), the radial pore pressure dissipation perpendicular to the y-axis is represented by

$$\frac{\partial \Delta u}{\partial t} = c_v \cdot \left(\frac{\partial^2 \Delta u}{\partial r^2} + \frac{1}{r} \frac{\partial \Delta u}{\partial r} \right), \tag{7-24}$$

assuming that the permeability of the soil is equal in vertical and horizontal direction and with r being the radial distance of a considered point from the centre of the pile. Since the gradient of excess pore pressure in radial direction and the associated flow were neglected in this analysis, the pore pressure dissipation is under-predicted by the amount given in Eq. (7-24).

7.3.1 Wave transmission

In order to avoid distortion of propagating ground motions, it has to be assured that the wave transmission in the model is accurate. Therefore, the dimensions of the finite difference zones have to be chosen properly. KUHLEMEYER and LYSMER (1973) postulate that for accurate representation of wave transmission through a model, the spatial element size Δl must be smaller than approximately one-tenth to one-eighth of the wavelength λ associated with the highest frequency component of the input wave

$$\Delta l \leq \frac{\lambda}{10}. \tag{7-25}$$

According to ITASCA (2002), the maximum frequency f which can be modelled accurately depends on the speed of wave propagation C and on the wavelength λ of the input wave:

$$f = \frac{C}{\lambda}. \tag{7-26}$$

In this equation, C is the smallest wave speed in the system, either the speed of compression waves C_p or the speed of shear waves C_s:

$$C_p = \sqrt{\frac{K_s + \frac{4}{3}G}{\rho}} \qquad \text{and} \tag{7-27}$$

$$C_s = \sqrt{\frac{G}{\rho}} \tag{7-28}$$

with K_s being the bulk modulus of the soil, G its shear modulus and ρ its mass density. For the soil parameters chosen for this simulation (see Section 7.3.5.1), the minimum wave speed is C_s = 170 m/s. Since the maximum input frequency to be modelled is f = 2.0 Hz (see Table 5-4), the maximum element size should be $\Delta l \leq 8.75$ m in order to avoid numerical distortion. Since the test model analysed within this research has a height and a width of 3 m, those requirements on the grid are met in any cases (see Section 7.3.2).

The critical time step Δt_{crit} for the numerical calculations (see Section 7.1.2) depends on the element size. It is given by

$$\Delta t_{crit} = \min\left\{\frac{A_Z}{C_p \cdot \Delta l_{\max}}\right\} \tag{7-29}$$

where A_Z is the area of the zone and Δl_{max} is the maximum length of the area (so that Az/Δl_{max} is the minimum propagation distance for the zone under consideration). The {min}-function is taken over all zones of the model (ITASCA (2002)). As consequence, the smallest critical time step in the model becomes decisive for the calculation. This time step is set to be calculated automatically by FLAC. For the simulations calculated here, the time step is approximately $\Delta t = 1 \cdot 10^{-5}$ s. Due to the dependency on the zone size given in Eq. (7-29), this time step is larger for larger zone sizes and vice versa.

7.3.2 Grid generation for the soil

Requirements on the grid are given by the test model set-up on the one hand and by the numerical method on the other hand. The pore pressure in the test model was analysed at a distance of 2.5 cm from the pile surface. Thus also in the model, the pore pressure should be analysed at this location which demands for very small zones in immediate vicinity of the pile. According to ITASCA (2002), the greatest accuracy of numerical results is obtained for a model with equal square zones. To improve the calculation time, the aspect ratio of a zone (ratio of side length) can be chosen until a ratio of 1 : 5. In order to enlarge the zones from the pile in direction of the boundaries, a gradual variation in size is recommended. Under those conditions, the grid is generated as shown in Fig. 7-5. According to the sand filling of the test model setup, its width is 3 m and its height 2 m. Up to a distance of 0.4 m from the pile, the zones gradually increase in width. From 0.4 m to 1.5 m, the zones are all equal. For all zones, the criterion for the aspect ratio is kept. The model consists of approximately 2000 zones. At the bottom of the model, the boundary is fixed in both x- and y-direction whereas at the sides, it is fixed in x-direction. The

locations of the grid points at which the pore pressure is analysed are indicated by the red circles in the insert of Fig. 7-5. The material properties for the soil will be given in Section 7.3.5.1.

7.3.3 Grid generation for the pile

FLAC supplies structural elements to model structures as tunnel liners, pile foundations, cables, etc. Within this simulation, pile elements were used to model the pile. Those pile elements are two-dimensional elements with three degrees of freedom (two displacements and one rotation). They interact with the grid via normal coupling springs. Those nonlinear connectors transfer forces and displacements between the pile elements and the grid at the pile element nodes. The formulation of the coupling springs is similar to the load-displacement relations formulated by the "p-y-curves" (ITASCA (2002)). Within the simulations of this research work, the pile consists of 30 segments. Node 1 is situated at the sand surface; node 31 is located 1.5 m below. The load is applied to node 1 and thus, corresponds to the displacement x_s measured within the test series. The element nodes fall together with the grid as can be seen in Fig. 7-5. The geometric and material properties of the pile are given in Section 7.3.5.3.

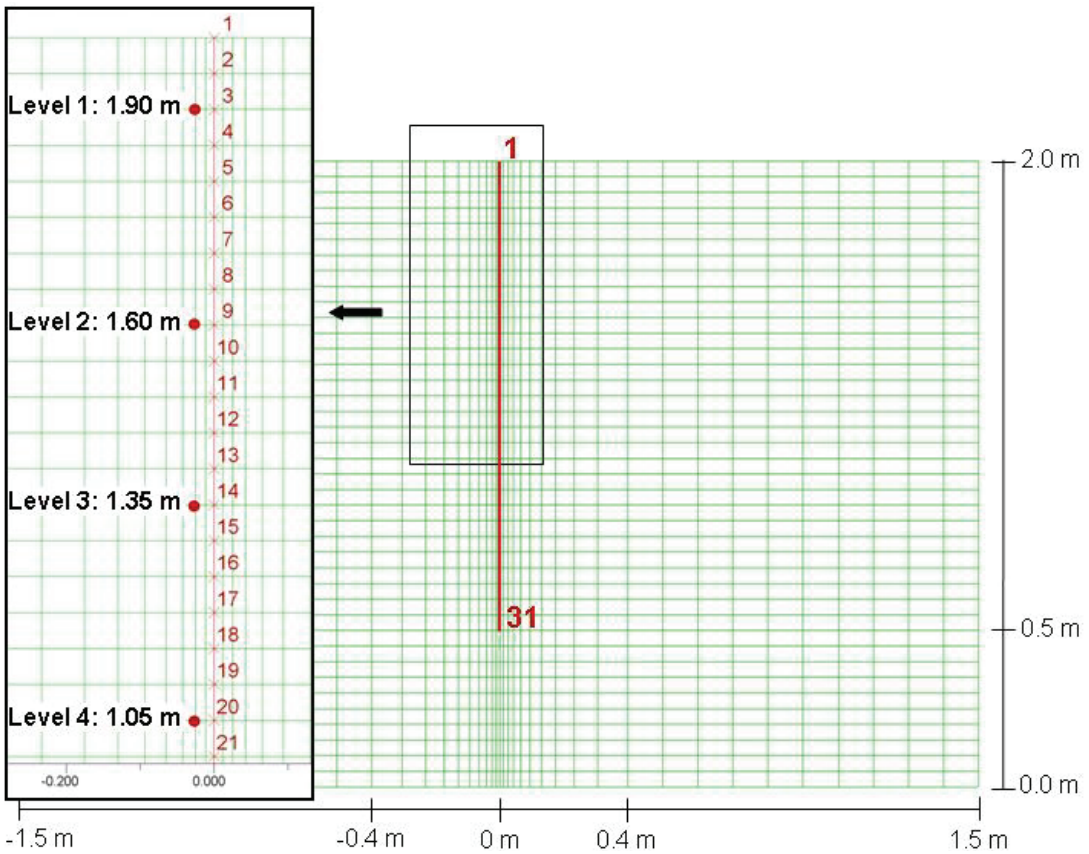

Fig. 7-5: Grid and pile structure indicated by the red line. The pile node numbers and the locations where the pore pressure is analysed are indicated in the insert.

7.3.4 Damping

As discussed above, the differential equations of all nodes are coupled in the implicit solution scheme. So, carrying out a static calculation, inertia and damping can be neglected. But in ex-

plicit solution schemes, the equation system is uncoupled. Therefore, inertia as well as damping have to be considered and not only a dynamic but also a static problem is solved in the dynamical calculation mode. Hence, the inertial terms in the equations of motion are used as numerical means to reach the equilibrium state of the system under consideration. As quasi-static calculations of nonlinear systems are not allowed to evoke oscillations in the system and should result in non-inertial solutions, the equations of motion must be damped. To bring static simulations to equilibrium, a critical damping is necessary (WILL (1999)).

When a soil is dynamically loaded, it begins to oscillate and waves propagate from the loading source in all directions. When travelling through the soil, those waves are damped and loose energy as a result of internal friction and slippage along interfaces. The damping in soil is mainly hysteretic, i.e., independent of frequency (ITASCA (2002)). But it is difficult to reproduce this type of damping numerically, especially when several wave forms are superimposed. The dynamic hysteretic behaviour is not sufficiently considered in FLAC. Therefore, additional damping is necessary. Firstly, a Rayleigh damping is provided in FLAC which is approximately frequency-independent over a certain range of frequencies. Secondly, local damping (originally designed for static calculations) can be used in dynamic analyses. It operates by adding and subtracting mass to/from the nodes at certain times during a cycle of oscillation: Mass is added when the velocity changes sign and is subtracted when the velocity has a maximum or minimum point. Choosing the damping coefficient appropriate to wave propagation, it simulates the hysteretic damping quite well. This local damping coefficient α_L is given by

$$\alpha_L = \pi \cdot D, \tag{7-30}$$

where D is the critical damping. Thus, there is no need to specify the frequency. According to DHAKAL (2004), the damping for geological materials lies between 2% and 5%. Since for dynamic analyses 5% damping is a typical value, the local damping coefficient is set to $\alpha_L = 0.05\pi = 0.16$.

7.3.5 Parameters of the numerical analysis

In order to simulate the results of the test series described in Chapter 6, the same material parameters were used in the numerical analysis as they were present in the test model. Only some parameters have to be converted for the FLAC calculation as, for example, the permeability since FLAC asks for the entry of this variable in other units as usual. The following sections supply the parameters of the soil, the water and the pile.

7.3.5.1 Soil parameters

For the soil parameters, the values assembled in Table 7-1 are used. The parameters were determined in laboratory tests, were derived from equations or were chosen from literature. The permeability has to be adjusted since FLAC uses the mobility coefficient κ [m^2/Pa·s] for its analyses. In laboratory tests, the permeability was determined to 1.68e^{-4} m/s. The mobility coefficient κ is calculated according to ITASCA (2002) by the permeability k and the unit weight of water γ_w according to

$$\kappa = \frac{k}{\gamma_w} . \tag{7-31}$$

Table 7-1: Soil parameters used in the numerical analysis.

Parameter	Value	Source
Density	1900 kg/m^3	Laboratory tests
Dynamic shear modulus	$5.8 \cdot 10^4$ kN/m^2	According to DGGT (2002)
Dynamic bulk modulus	$1.26 \cdot 10^5$ kN/m^2	According to DGGT (2002)
Inner friction angle	36°	Laboratory tests
Permeability	$1.71 \cdot 10^{-8}$ m^2/ Pa·s	According to Eq. (7-31)
Porosity	0.4	Laboratory tests
Void ratio	0.67	Laboratory tests
Poisson's ratio	0.3	According to DGGT (2002)
Constant C_1 (Finn and Byrne)	0.3	According to Eq. (3-21)
Constant C_2 (Finn and Byrne)	1.35	According to Eq. (3-22)

7.3.5.2 Water parameters

For the water, only the density and the bulk modulus have to be set. Those parameters are given in Table 7-2. Furthermore, the fluid flow can be set on or set off. This will be discussed in Chapter 8.

Table 7-2: Water parameters used in the numerical analysis.

Parameter	Value	Source
Density	1000 kg/m^3	According to ITASCA (2002)
Bulk modulus	$2 \cdot 10^6$ kN/m^2	According to ITASCA (2002)

7.3.5.3 Pile parameters

The pile parameters used in the numerical analyses are summarized in Table 7-3. In order to assign the appropriate values for the density and the Young's modulus to the pile elements, some calculations have to be done since the pile in the test model is a hollow pile filled with sand and the parameters given in Table 7-3 represent the values for a full pile section. Hence, the density ρ_{total} is calculated by adding the products of the density and the area of the soil and the pile, respectively, and by dividing it by the total cross-sectional area:

$$\rho_{total} = \frac{\rho_{soil} \cdot A_{soil} + \rho_{pile} \cdot A_{pile}}{A_{total}} . \quad (7\text{-}32)$$

The density of the pile was set to 1500 kg/m^3 according to the density of PVC.

As an approximation, the Young's modulus E_{total} is calculated accordingly, by summing up the products of the Young's modulus and the moment of inertia of the soil and the pile, respectively, and by dividing the resulting stiffness by the total moment of inertia:

$$E_{total} = \frac{E_{soil} \cdot I_{soil} + E_{pile} \cdot I_{pile}}{I_{total}} . \quad (7\text{-}33)$$

The Young's modulus of the soil was taken according to Table 7-1; the Young's modulus of PVC was set to $2.5 \cdot 10^6$ kN/m^2. The perimeter $2\pi r$ is the exposed perimeter of the element to the soil, i.e., the length of the pile surface that is in contact with the soil. When deflected, the pile interacts with the soil via normal coupling springs which transfer motion and forces between the structural element nodes and the grid. This load-displacement relation is described by the code parameters of the normal coupling springs: stiffness (cs_nstiff), cohesive strength (cs_ncoh) and friction angle (cs_nfric). ITASCA (2002) supplies guide values for those parameters.

Table 7-3: Pile parameters used in the numerical analysis.

Parameter	Value	Source
Radius	0.125 m	According to Table 5-2
Density	1861 kg/m^3	According to Eq. (7-32)
Young's modulus	$5.83 \cdot 10^5$ kN/m^2	According to Eq. (7-33)
Perimeter	1.571 m	According to ITASCA (2002)
Poisson's ratio	0.3	Internet
cs_nstiff (normal coupling springs)	$1 \cdot 10^3$ kN/m^2	According to ITASCA (2002)
cs_ncoh (normal coupling springs)	$1 \cdot 10^3$ kN/m^2	According to ITASCA (2002)
cs_nfric (normal coupling springs)	36°	According to ITASCA (2002)

7.4 Preliminary calculations

Prior to performing the dynamic analysis, the initial equilibrium state has to be calculated and the pile structure has to be activated. In addition, the natural frequency of the system should be determined since this is a very important value when carrying out dynamic analyses.

7.4.1 Initial conditions

The water height of 3 m is considered but in order to save computational time, the water zones are deactivated (compare Fig. 7-5). The pore pressure is assigned by initial conditions. The system is brought in mechanical as well as fluid equilibrium and the coefficients for the Finn and Byrne formulation are assigned to the soil. After having reached this equilibrium state, the pile structure is activated. The initial conditions before the loading is applied to the pile are shown in Fig. 7-6.

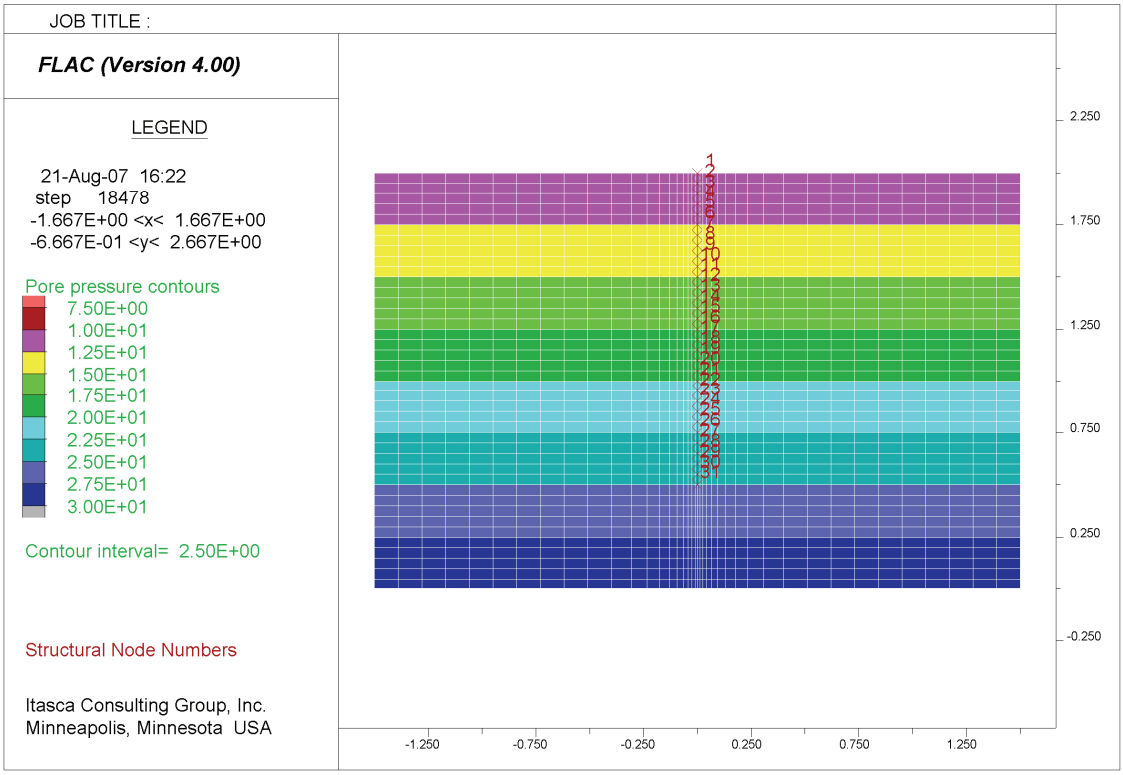

Fig. 7-6: Initial pore pressure conditions shown as contour plot and pile structure with node numbers indicated in red.

7.4.2 Natural frequency of the system

The natural frequency of a system is the frequency with which a free system oscillates after being deflected. When damping is neglected, this natural frequency corresponds to the resonance frequency of the system. If excitations with frequencies that approach this resonance frequency are applied to a system, the amplitudes increase strongly and those increasing amplitudes can lead to the collapse of the system.

Regarding offshore pile foundations, it is evident that loading with the natural frequency of the system can lead to increasing deflections and can cause considerable damage to those structures. Therefore, it is important to determine the natural frequency of the system and to ensure that the loading frequencies do not correspond to this natural frequency. The natural frequency is a function of the stiffness and the mass of the system, including the mass of the pile, the added hydrodynamic and the added geodynamic mass. Here, the natural frequency of the model is

determined by means of the numerical model. Therefore, the pile node number 1 is deflected by 0.2 cm and allowed to freely oscillate afterwards. Damping is set off. The resulting displacement of pile node number 1 is shown in Fig. 7-7 (a). As can be seen, the pile head oscillates with a certain frequency. The decreasing amplitude of the deflection is due to geometric damping. The oscillating frequency, i.e., the natural frequency of the system is determined to $f_N = 4.91$ Hz by means of a Fast Fourier Transform which is shown in Fig. 7-7 (b). Since the maximum frequency of loading applied to the test pile is 2.0 Hz, resonance it not a problem to be considered for the laterally loaded pile studied within this research.

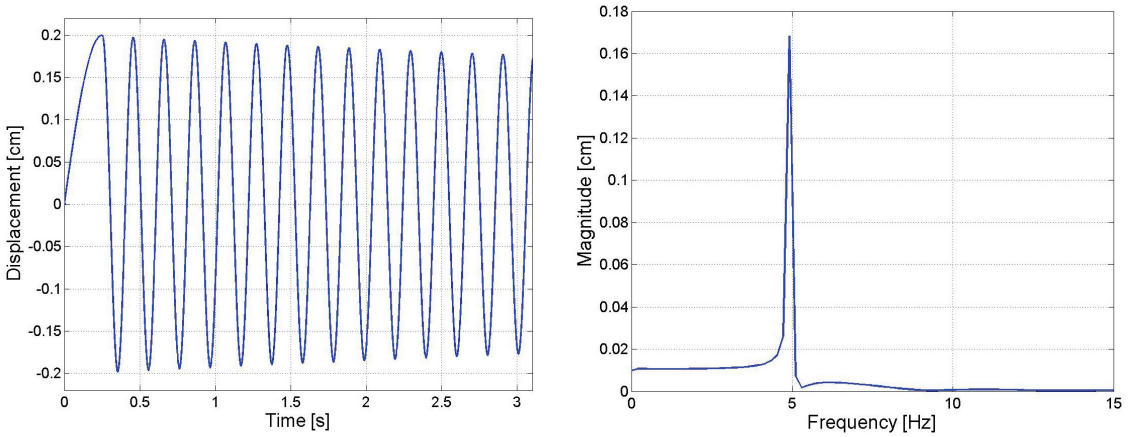

Fig. 7-7: (a) Movement of pile node number 1 after initial deflection by 0.2 cm as a function of time. (b) Fast Fourier Transform of the oscillation shown in (a) indicating the natural frequency of the system.

7.5 Main calculation: dynamic loading

Since the numerical analysis should simulate the experimental test series carried out within this research, the pile modelled in the numerical analysis has to be deflected by a certain displacements and with a certain frequency as it was done in the test series. However, a standard command is not available for the application of a displacement-driven loading to structural pile nodes. Therefore, the FISH language embedded in FLAC was used to assign those loading conditions to the pile element variables by accessing the pile structural element data using the so-called "STR.FIN" file. From this list of structural element data, the data structure of the pile elements, i.e., the offsets for displacements, velocities, forces, etc., can be read and manipulated. Hence, the desired deflection was prescribed and assigned to the upper node of the pile. This deflection applied in FLAC corresponds to the x_s-deflection that was measured in the experimental tests series. The numerically calculated pore pressure is analysed at four levels as response to the cyclic loading.

8 Analysis and results of the numerical simulation

In the numerical studies analysed within this chapter, the pile was cyclically deflected with a displacement of ±0.15 cm and a frequency of 1.0 Hz. Thus, it corresponds to the experimental test series labelled with $x_w = \pm 0.5$ cm and $f = 1.0$ Hz. This test was chosen to be simulated since, transferred to offshore conditions, its input parameters fall within the range of parameters representing in situ conditions which are very likely to occur (compare the test program given in Section 5.5 and Fig. 6-30).

FLAC offers the possibility to allow fluid flow (drained conditions) or to inhibit it (undrained conditions). Since dissipation of pore water is very unlikely to occur during seismic excitation, earthquake studies normally assume undrained conditions. But as it was already seen within the analyses of the test series, this is not the case within the problem under consideration. Here, dissipation definitely occurs as it is obvious from Fig. 8-1 which exemplarily shows the pore pressure signal F3 of the experimental test series mentioned above.

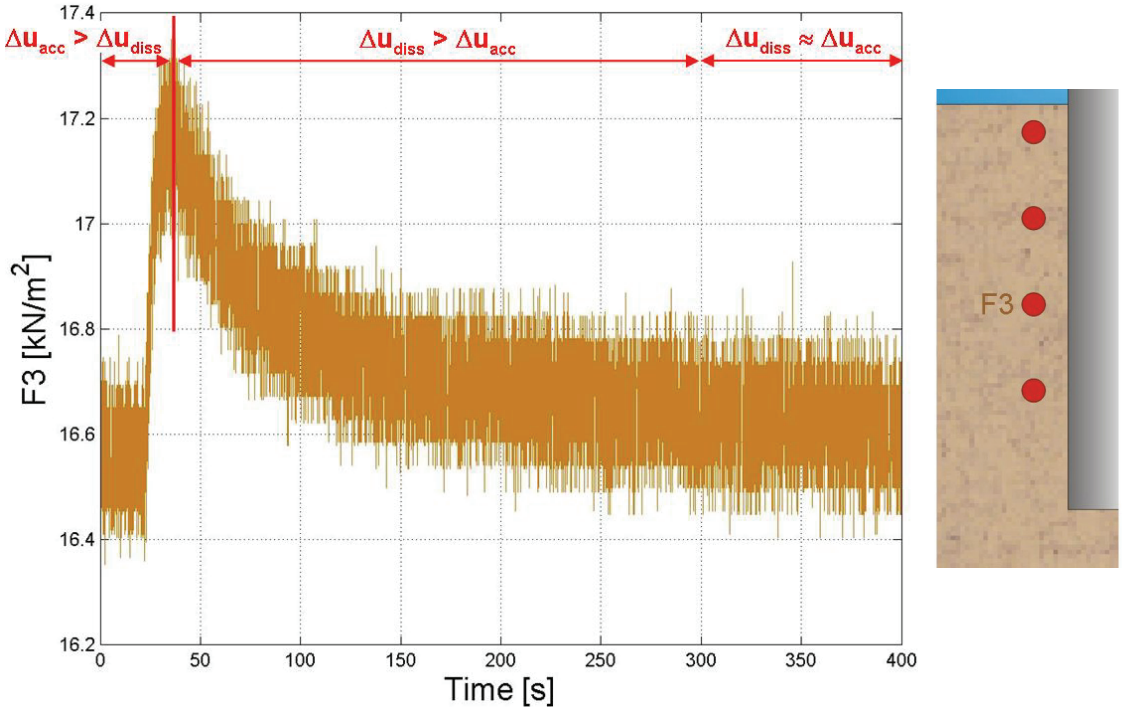

Fig. 8-1: First 400 s of pore pressure F3 measured in a test series with $x_w = \pm 0.5$ cm and $f = 1.0$ Hz.

According to the test series, the loading was started at t = 21.5 s. In the first phase (here: t = 20-35 s), the rate of pore pressure accumulation is higher than the rate of dissipation and, thus, the pore pressure increases. In the second phase (35-300 s), the rates of dissipating pore pressure are higher than the rates of accumulating pore pressure. Hence, the pore pressure decreases. In the last phase (300 s until the end), both rates are approximately equal. Therefore, the numerical simulation is split into two parts. Undrained conditions are assumed during the first phase of the numerical simulation and drained conditions are assumed after that phase. This chapter is organized accordingly.

8.1 Analysis I: Analysis of t = 20-35 s

In order to compare the numerical with the measured signals, the 15 s after the beginning of load application (t = 21.5 s) are considered in this first section. As discussed above, fluid flow is not allowed in this phase. This assumption corresponds to the results of the test series.

8.1.1 Pore pressure

The pore pressure measured in the experimental test series is shown in Fig. 8-2 for the levels 1 to 4. In Fig. 8-3, the corresponding pore pressure calculated within the numerical simulation is represented. In order to consider the measurement signals and the results of the simulation in more detail, the pore pressure should be looked at for all levels individually.

Fig. 8-4 shows of the pore pressure measured in the test series at level 1-4 (F1 – F4) on its left-hand side whereas the right-hand side represents the results of the corresponding FLAC simulation ($F1_{FLAC}$ – $F4_{FLAC}$). The first 15 s after load application are to be considered since this is the duration of predominant pore pressure accumulation. However, 20 s are plotted in the figure in order to see how the pore pressure further develops. As can be seen, the initial values of pore pressure are equal in the test series and the simulation since they represent the hydrostatic water pressure. However, the signals slightly differ in their progression with time. In order to better compare the signals measured within the test series and calculated with FLAC, the mean pore pressure u_{35s} and the transient pore pressure Δu_{trans} at t = 35 s is indicated in the plots.

As can be seen for all levels, the pore pressures measured in the test series do not increase further after 35 s at the latest. The simulated pore pressures, in contrast, increase further since pore pressure dissipation is not allowed. Regarding level 1, the mean value of F1 and the mean value of $F1_{FLAC}$ at t = 35 s are approximately equal, namely 11.26 kN/m^2 and 11.34 kN/m^2, respectively. Nevertheless, the amplitude of transient pore pressure is slightly overpredicted by the FLAC simulation (by $\Delta(\Delta u_{trans})$ = ±0.10 kN/m^2). At level 2 and 3, the pore pressure accumulation simulated with FLAC is less than in the test series (level 2: u_{35s} = -0.51 kN/m^2 and level 3: u_{35s} = -0.34 kN/m^2). Whereas at level 2, the transient pore pressure Δu_{trans} simulated with FLAC is smaller than the measured pore pressure (±0.44 kN/m^2 versus ±0.95 kN/m^2), the transient oscillation is almost identical for the measured pore pressure and the simulated one at level 3. At level 4, FLAC slightly overpredicts the pore pressure accumulation (u_{35s} = +0.14 kN/m^2) but underpredicts the transient pore pressure (Δu_{trans} = ±0.19 kN/m^2).

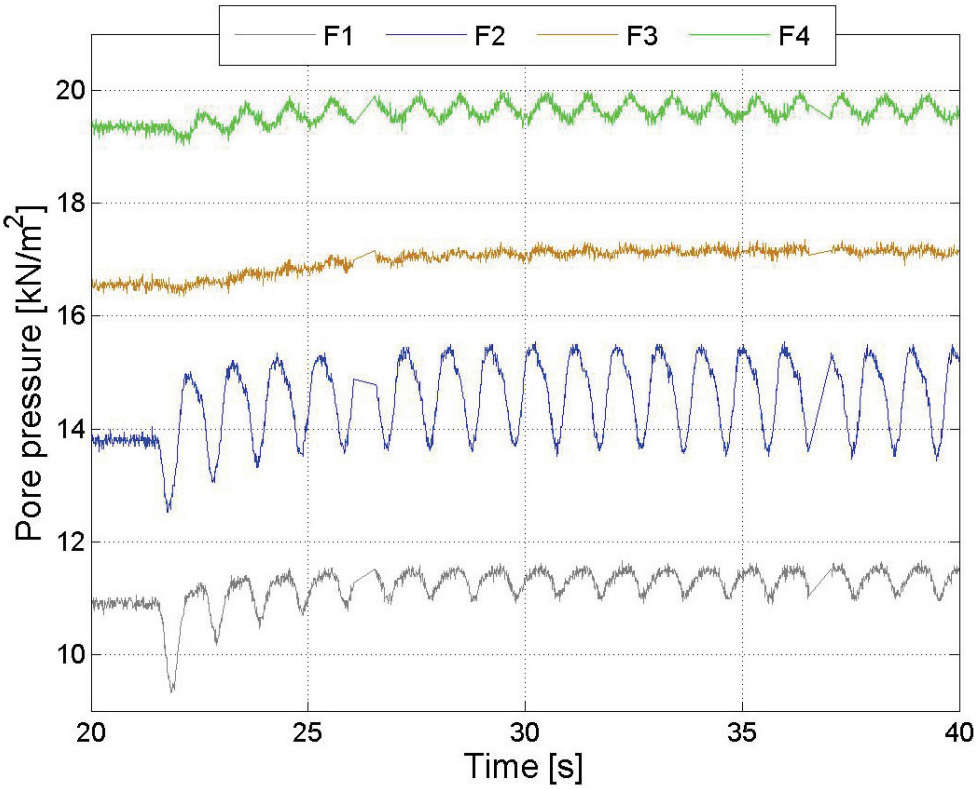

Fig. 8-2: Pore pressure F1 – F4 measured in a test series with $x_w = \pm 0.5$ cm and $f = 1.0$ Hz over t = 20-40 s.

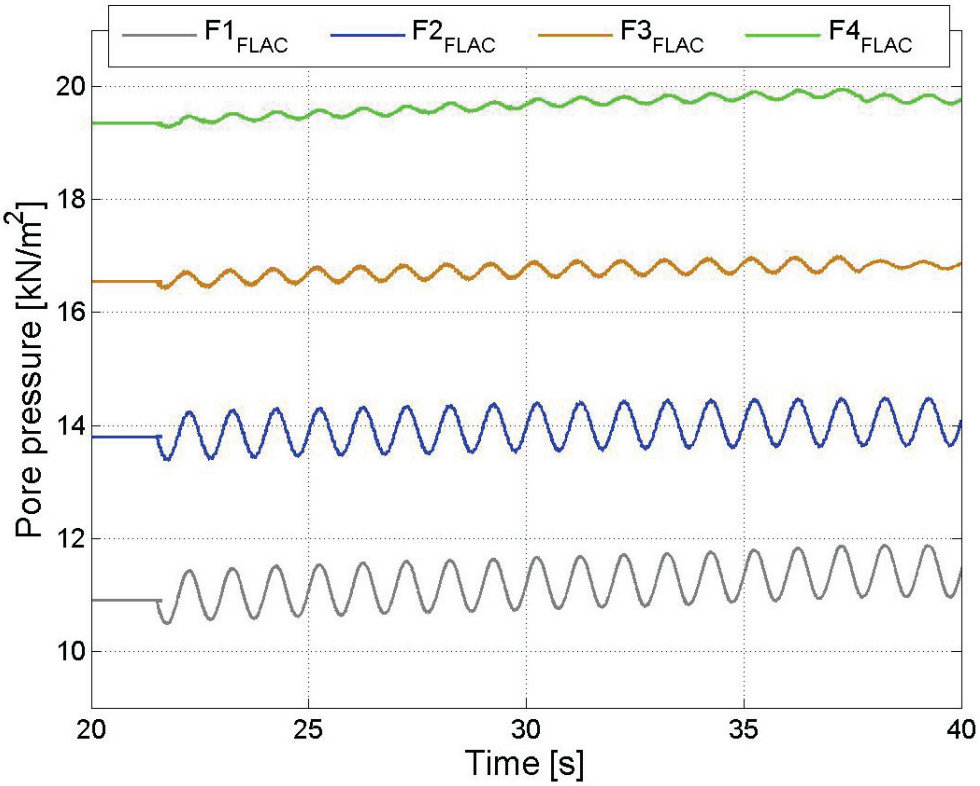

Fig. 8-3: Pore pressure $F1_{FLAC}$ – $F4_{FLAC}$ calculated with FLAC for the numerical simulation of a test series with $x_w = \pm 0.5$ cm and $f = 1.0$ Hz over t = 20-40 s.

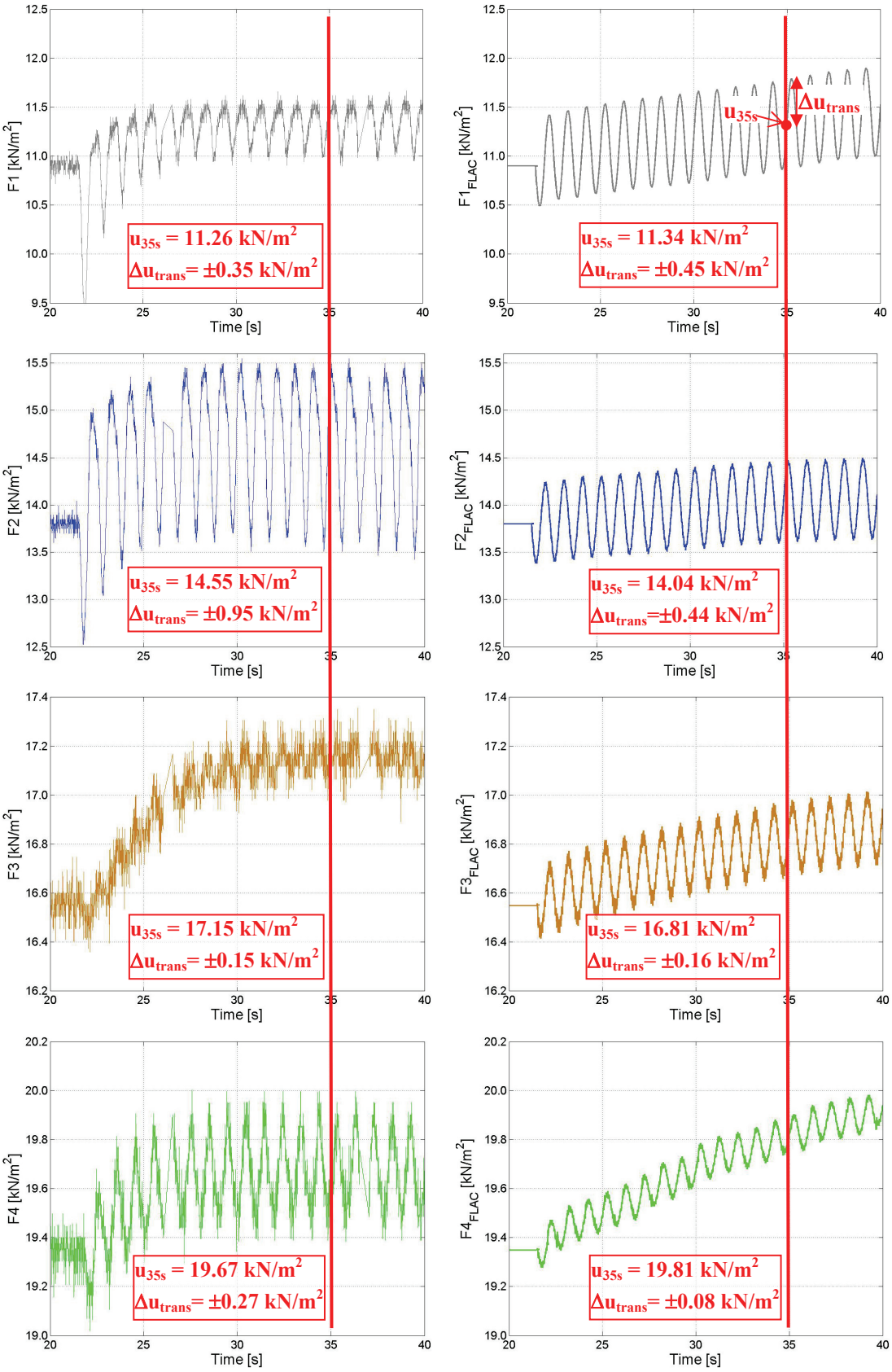

Fig. 8-4: Comparison of measured pore pressure (left: F1 – F4) and simulated pore pressure (right: $F1_{FLAC}$ – $F4_{FLAC}$) over t = 20-40 s (x_w = ±1.0 cm and f = 1.0 Hz). The mean and the transient pore pressure at t = 35 s are indicated.

8.1.2 Pore pressure and volumetric strain

In order to control the dependency of the simulated pore pressure on the volumetric strain in the corresponding zone (compare Section 3.4.3), those two parameters are shown exemplarily for level 2 in Fig. 8-5. Since the loading was always applied to the test pile such that the pile firstly moves towards the pore pressure sensors of group B and then towards the sensors of group F (Section 6.3.1), the zone adjacent to sensor F2 first experiences dilatation and then compression. This can be seen by the progression of the volumetric strain increment signal ε_{vd} and the pore pressure signal $F2_{FLAC}$. If the soil experiences dilation (positive ε_{vd}), $F2_{FLAC}$ decreases. If the soil is compressed (negative ε_{vd}), $F2_{FLAC}$ increases. The amount of pore pressure change after the pile has reached, for example, its first maximum deflection can be derived by use of Eq. (3-12) and with the volumetric strain shown in Fig. 8-5 (first maximum: $\Delta\varepsilon_{vd} = 0.84 \cdot 10^{-7}$):

$$\Delta u = \frac{K_w \cdot \Delta\varepsilon_{vd}}{n} = \frac{2 \cdot 10^6 \, kN/m^2 \cdot 0.84 \cdot 10^{-7} \, m/m}{0.4} = 0.42 \, kN/m^2 . \qquad (8\text{-}1)$$

Thus, the pore pressure can be determined to 13.8 kN/m²-0.42 kN/m² = 13.38 kN/m². This corresponds to the pore pressure calculated by the numerical simulation as can be seen in Fig. 8-5.

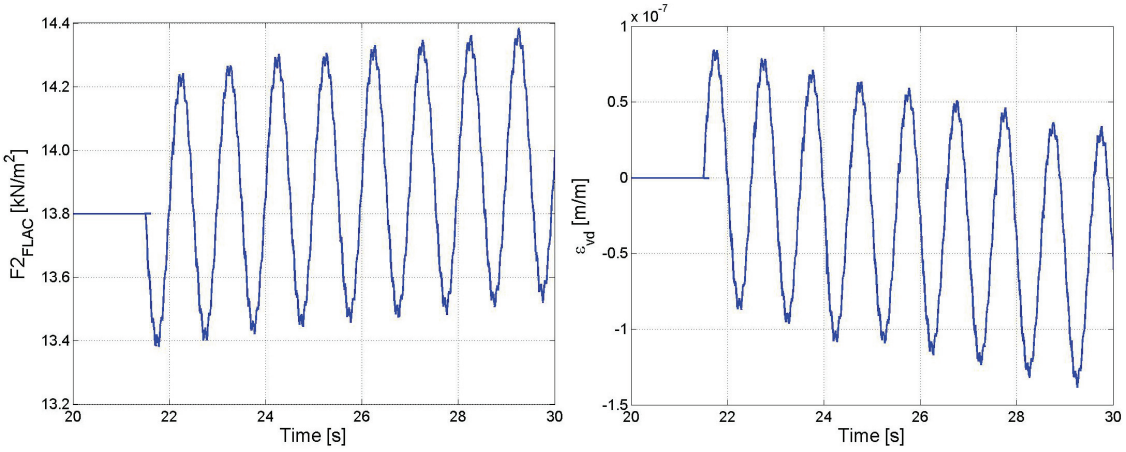

Fig. 8-5: Pore pressure $F2_{FLAC}$ and volumetric strain ε_{vd} of the corresponding zone over t = 20-40 s.

8.1.3 Pore pressure and deflection of the pile

The dependency of the pore pressure on the volumetric strain is also noticeable by considering the relation of the deflection of the pile and the pore pressure adjacent to the pile. Fig. 8-6 shows the horizontal deflection of the pile nodes when node 1 is deflected to the right (slightly less than 0.15 cm). Apart from the deflection of the pile, the distribution of pore pressure in the soil is shown as contour plot for the same time. Two facts can be observed: Firstly, the upper pile nodes experience a deflection to the right which decreases with depth. In contrast, the lower nodes are deflected to the left. Thus, corresponding to the results of the analysis of the test series, there must be a rotation point. This rotation point lies at approximately 1.25 m and is indicated in the figure. Its position is slightly deeper than it was assumed in the analysis of the test series (≈ 1.34 cm). Secondly, it is apparent that the deflection of the pile causes a sudden change in the pore pressure (see increases and decreases indicated by the colours). As it was already

shown for the test series, a deflection of the pile towards the soil causes compression of the soil and, therewith, an increase in pore pressure. In the contour plot, the pore pressure increases on the right side of the upper part of the pile whereas in the soil around the lower pile nodes, the pore pressure increases on the left side. Thus, this dependency is equal in the test series and in the numerical simulation.

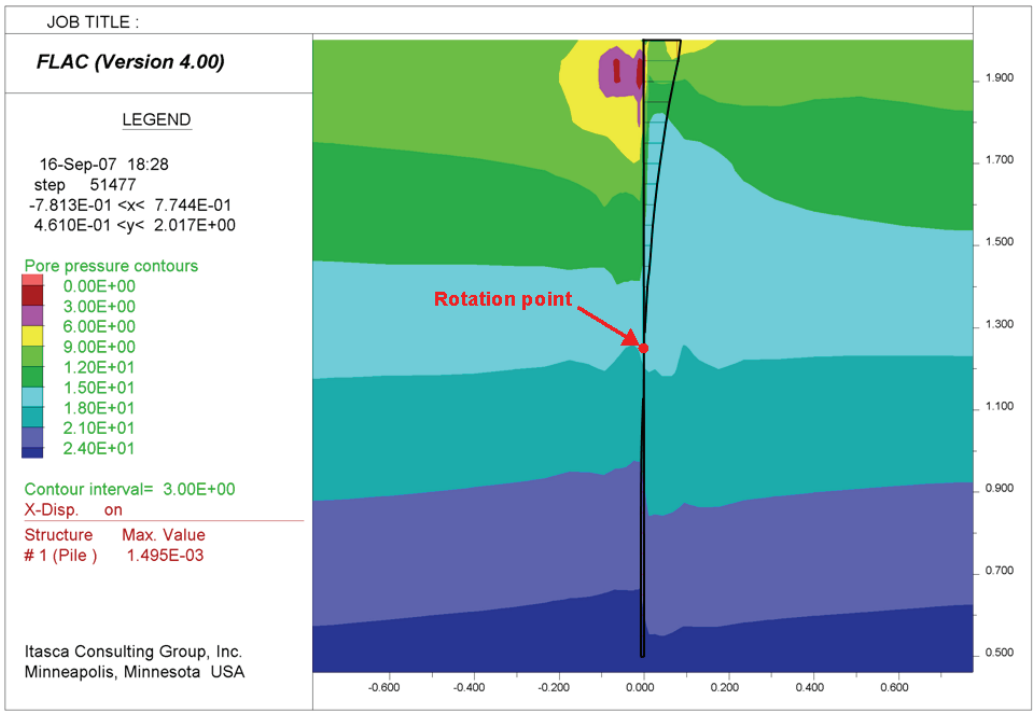

Fig. 8-6: Horizontal deflection of the pile and resulting pore pressure shown as contour plot.

8.1.4 The effect of varying input parameters

In the analyses of the experimental test series, it was found that the progression of pore pressure at the levels 2 to 4 depends on the input parameters, i.e., on the amplitude of forced deflection and on the frequency of loading. As summarized in Table 6-3, an increase of either x_w or f results in an increase of the maximum pore pressure as well as in an increase of the amplitude of transient pore pressure and vice versa. For level 1, a dependency on x_w and f could not be observed. This section investigates whether those dependencies are also valid in the numerical simulation. Therefore, the numerical simulation shown in Fig. 8-4 is taken as reference simulation ($x = \pm 0.15$ cm and $f = 1.0$ Hz) and two simulations varying in displacement and two simulations varying in frequency are carried out for studying the influence of the input parameters.

8.1.4.1 Amplitude of deflection

Two comparative simulations were conducted in which the amplitude of deflection was varied and the frequency was held constant. Fig. 8-7 exemplarily shows the pore pressure $F2_{FLAC}$ simulated for the reference simulation (second plot, compare Fig. 8-4) and for the two additional simulations (first plot: $x = \pm 0.1$ cm and third plot: $x = \pm 0.2$ cm). The mean pore pressure u_{35s} as well as the transient amplitude of pore pressure Δu_{trans} at $t = 35$ s is indicated. Obviously, the

dependencies observed in the test series are also valid for the FLAC simulation. With increasing forced displacement, the mean pore pressure as well as the transient pore pressure increase.

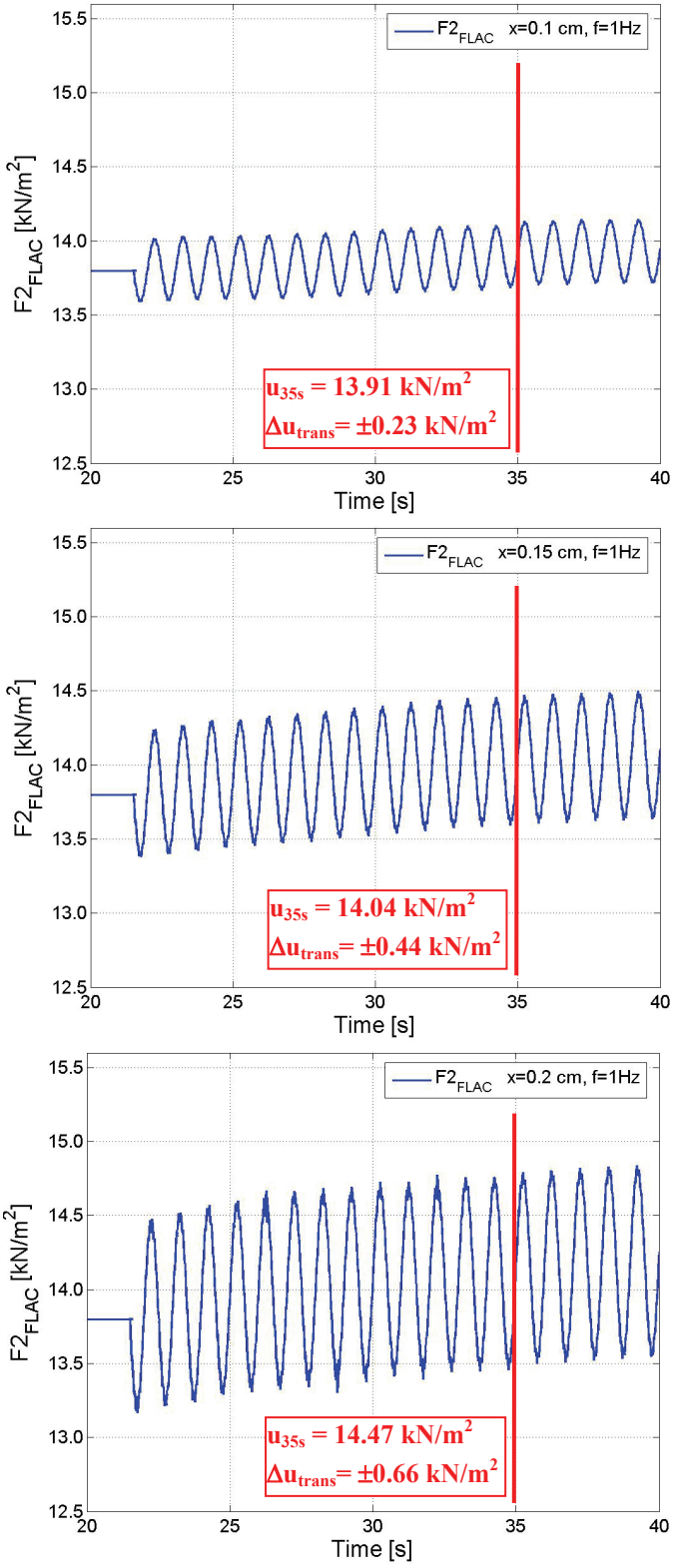

Fig. 8-7: Pore pressure $F2_{FLAC}$ for variations of forced displacement ($x = \pm 0.1$ cm, $x = \pm 0.15$ cm and $x = \pm 0.2$ cm) during the accumulation phase of the pore pressure, $t = 20$-40 s. The mean and the transient pore pressure at $t = 35$ s are indicated.

The same behaviour (increasing u_{35s} and Δu_{trans} for increasing input parameters) was also detected for the other levels. Nevertheless, only the results of the levels 2 to 4 are considered in this analysis since the here-assumed undrained conditions were seen to be not appropriate for level 1 (compare Section 6). In Fig. 8-8, the deviations of u_{35s} due to the variation of the forced displacement expressed as a percentage of u_{35s} from the reference simulation ($x = \pm 0.15$ cm and $f = 1.0$ Hz) are shown for the levels 2 to 4. The frequency is held constant. In Fig. 8-9, the deviations of Δu_{trans} are represented. As can be seen for both parameters and all levels represented in the figures, an increase in the amplitude x of the deflection causes increased values of u_{35s} and Δu_{trans}.

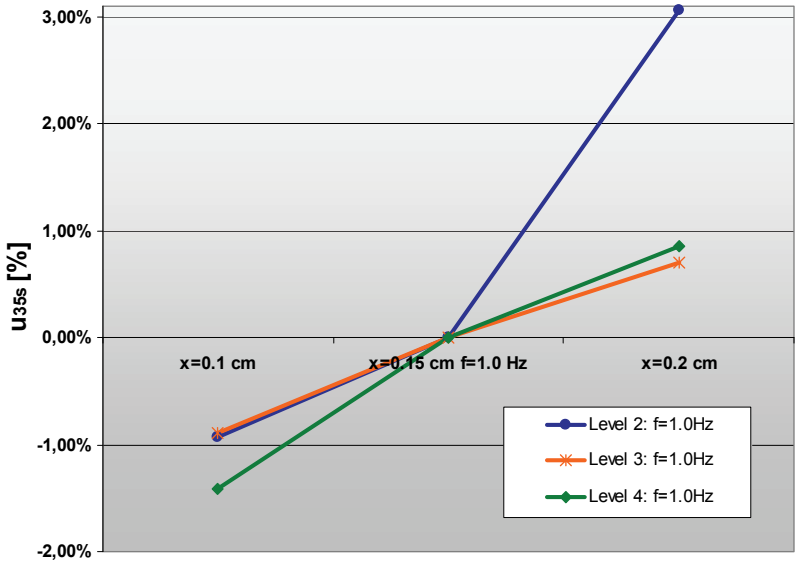

Fig. 8-8: Deviations of u_{35s} for variations of forced displacement ($x = \pm 0.1$ cm and $x = \pm 0.2$ cm) compared to reference simulation ($x = \pm 0.15$ cm and $f = 1.0$ Hz).

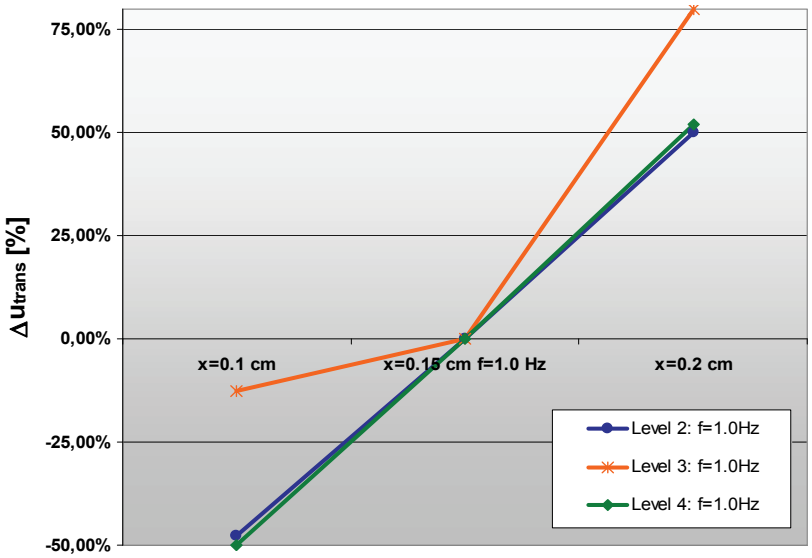

Fig. 8-9: Deviations of Δu_{trans} for variations of forced displacement ($x = \pm 0.1$ cm and $x = \pm 0.2$ cm) compared to reference simulation ($x = \pm 0.15$ cm and $f = 1.0$ Hz).

8.1.4.2 Frequency

Within a second study, the frequency was varied in two additional simulations and was set to $f = 0.5$ Hz and $f = 1.5$ Hz, respectively. The amplitude of the deflection was held constant. The results of those simulations in terms of the pore pressure $F2_{FLAC}$ are exemplarily represented in Fig. 8-10. Also here, the mean pore pressure as well as the amplitude of pore pressure oscillations at $t = 35$ s are indicated in the figure. Corresponding to the results of the test series, an increase in frequency also results in an increase of u_{35s} and Δu_{trans}. Nevertheless, whereas the test series revealed an equally strong dependency of u_{35s} and Δu_{trans} on both input parameters at level 2 (compare Table 6-3), the dependency of $F2_{FLAC}$ on the frequency is less strong in the FLAC simulation than the dependency on the forced displacement (compare Section 8.1.4.1).

The consideration of the other levels in the following will show that this is only valid for the transient pore pressure oscillations and that the influence on u_{35s} is approximately equally strong for x and f. Nevertheless, a difference between the conditions underlying the test series and the conditions underlying the numerical studies should be reflected. For the experimental test series to be simulated in this chapter, it was seen that the maximum pore pressure was reached at approximately the time $t = 35$ s. Thus, also the pore pressure in the corresponding FLAC simulation is supposed to reach its maximum then and hence, the calculation is stopped at this time. This approach is justifiable for the simulation of the test series to be modelled. Nevertheless, it can lead to errors when examining the results of numerical calculations with other input parameters (as it is done in Section 8.1.4.1 and 8.1.4.2). Although, the input parameters x and f chosen in those sections do not differ too much from the parameters of the reference simulation (±0.05 cm and ±0.5 Hz), the time when the maximum pore pressure is reached can be different.

Nevertheless, a dependency either of the number of cycles needed to cause liquefaction nor of the duration until the maximum pore pressure is reached on the input parameters could not be determined for the test series (compare Section 6.2.1). Therefore, it was seen appropriate to compare the maximum pore pressure and its transient amplitude of the reference test at $t = 35$ s with the values read-out for the same time for the simulations with varying input parameters. Hence, the comparison of the mean value and the transient amplitude of the pore pressure reveals dependencies on the input parameters. Those dependencies are, as far as possible, in good agreement with the results of the experimental test series.

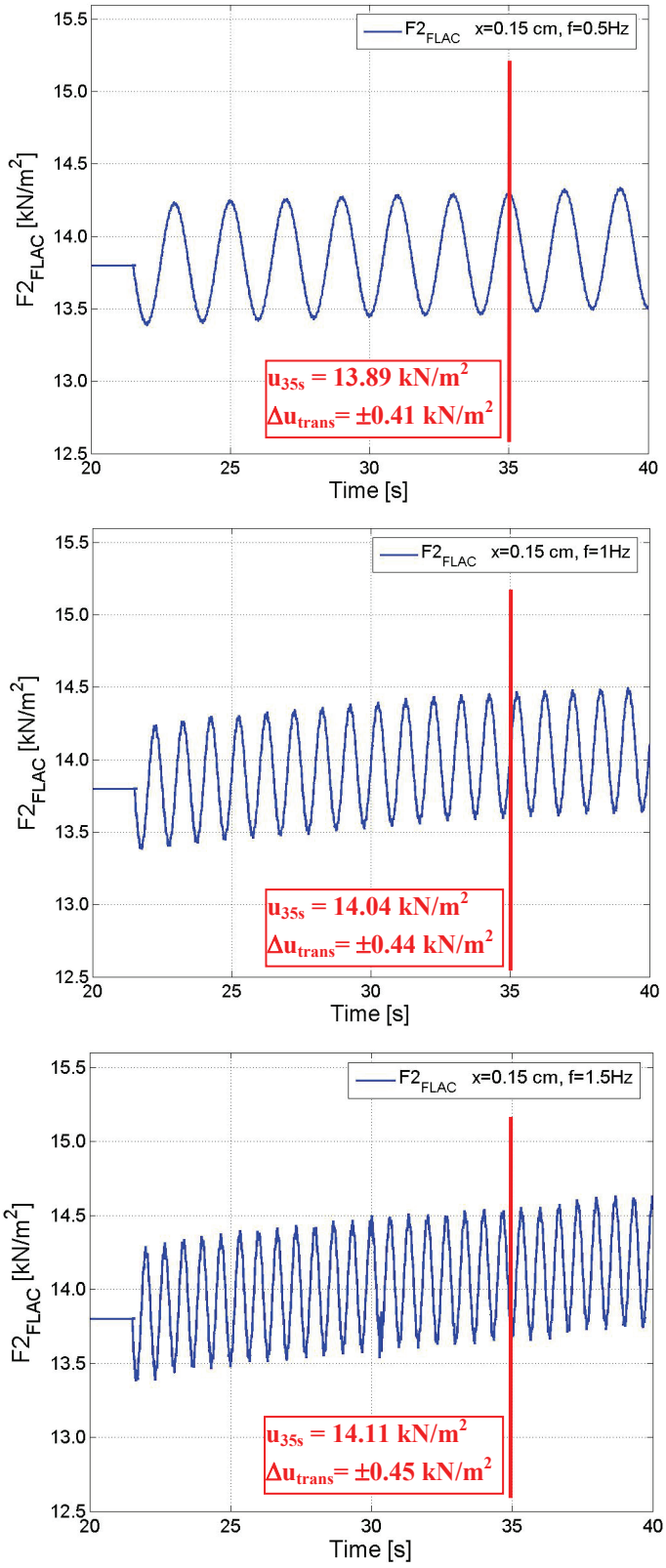

Fig. 8-10: Pore pressure $F2_{FLAC}$ for variations of the loading frequency (f = 0.5 Hz, f = 1.0 Hz and f = 1.5 Hz) during the accumulation phase of the pore pressure, t = 20-40 s. The mean and the transient pore pressure at t = 35 s are indicated.

The deviations of u_{35s} and Δu_{trans} for variations in the loading frequency at the levels 2 to 4 compared to the reference simulation are shown in Fig. 8-11 and Fig. 8-12, respectively. The consideration of the dependencies at the levels 3 and 4 confirms one fact observed for level 2: The value Δu_{trans} depends stronger on the amplitude of deflection than on the loading frequency. In contrast, u_{35s} seems to depend almost equally strong on x and f. The deviations of this parameter lie in the range of ±1.5 % for changes of both input parameters. Only for the simulation with x set to 0.2 cm, the deviation of u_{35s} exceeds +3.1 % at level 2 compared to the reference simulation.

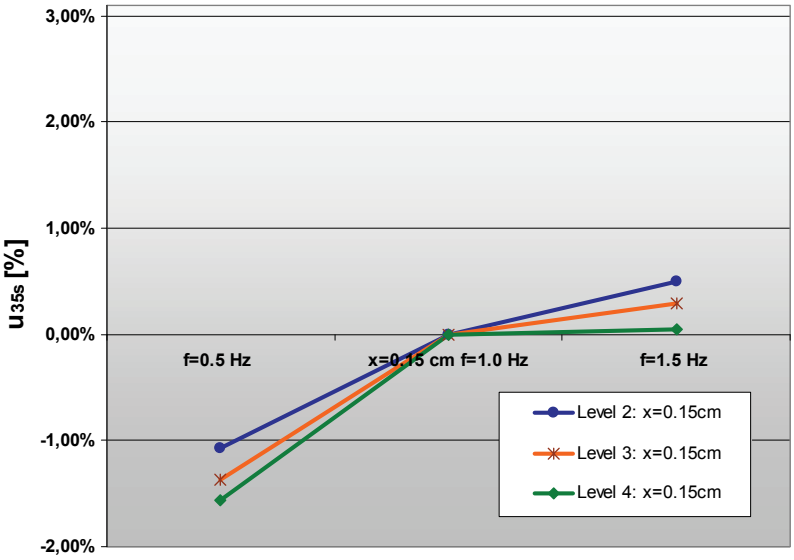

Fig. 8-11: Deviations of u_{35s} for variations of the loading frequency (f = 0.5 Hz and f = 1.5 Hz) compared to reference simulation (x = ±0.15 cm and f = 1.0 Hz).

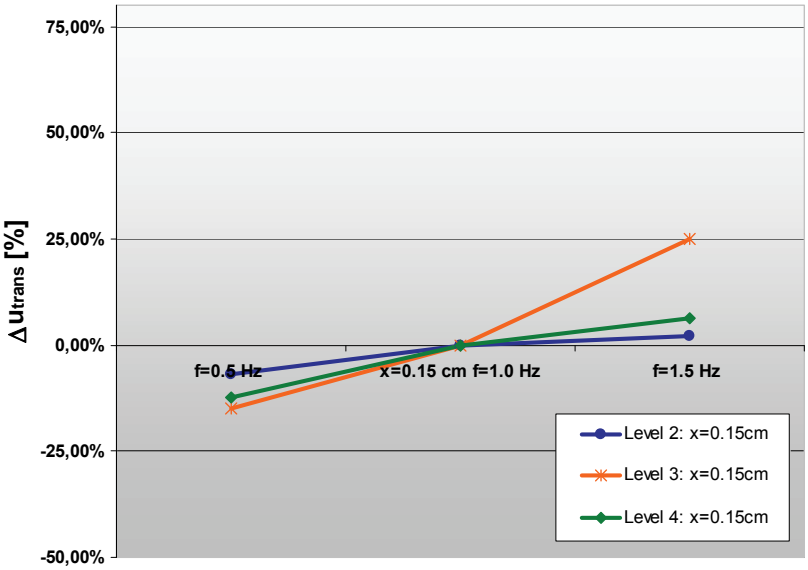

Fig. 8-12: Deviations of Δu_{trans} for variations of the loading frequency (f = 0.5 Hz and f = 1.5 Hz) compared to reference simulation (x = ±0.15 cm and f = 1.0 Hz).

8.2 Analysis II: Analysis of t = 35-300 s

As discussed before, the second phase indicated in Fig. 8-1 is characterized by higher pore pressure dissipation than accumulation. Therefore, fluid flow is allowed in this phase. Although, this section especially considers the phase of t = 35-300 s, the figures show the pore pressure changes from the beginning of the loading on in order to see both processes, the pore pressure accumulation and the pore pressure dissipation.

8.2.1 The effect of drainage and permeability

In contrast to earthquake studies in which the assumption of undrained conditions is justifiable over the entire duration of seismic loading, the loading considered within the present research can be simulated with undrained conditions only during the first phase of loading and is later rather marked by drained conditions or partial drainage, i.e., by conditions between full and no drainage. Therefore, the drainage property of the soil is changed at t = 35 s of loading by setting the flow on. By doing so, the pore water begins to dissipate according to the theory of consolidation given by Eq. (7-22). The pore pressure at level 1 during t = 20-55 s is shown in Fig. 8-13. The first 15 s correspond to the $F1_{FLAC}$-plot shown in Fig. 8-4. The onset of fluid flow is marked by the red vertical line and can be recognized very easily in the progress of the pore pressure over time.

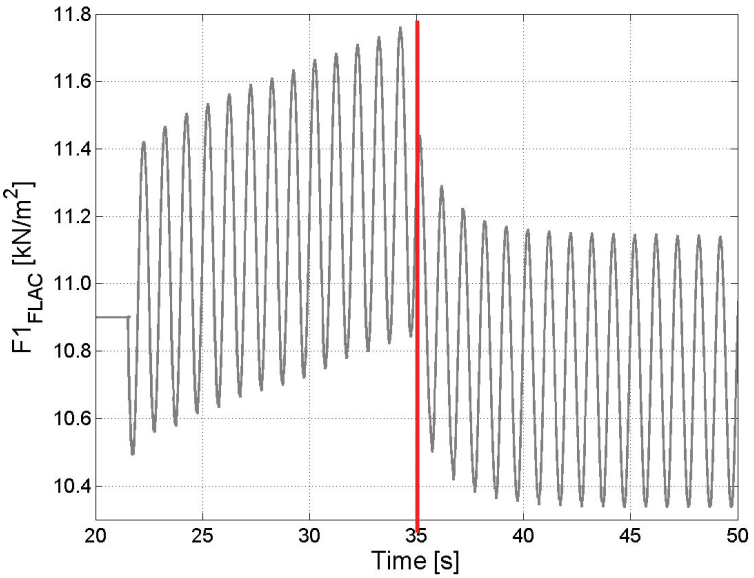

Fig. 8-13: Dissipation of pore water simulated at level 1 at t = 35 s by allowing fluid flow in FLAC.

Nevertheless, it is obvious that the situation shown in this figure does not reproduce the real conditions very well since the pore water dissipation is simulated too fast. The situation shown here corresponds more to the dissipating pore water when the pile loading is stopped as it was investigated in the experimental test series described in Section 6.2.3. But with ongoing loading, it is not an abrupt reduction that suddenly takes place, but rather a smooth process of pore water dissipation. This abrupt decrease represented here is firstly due to the fact that the flow in FLAC can only be set on or off but the simulation of partial drainage is not possible. Secondly, it is due

to an inadequacy of the Finn and Byrne Model: The value of the porosity of the soil as well as its permeability is not adjusted during the calculation but always stays constant. Recalling the consolidation theory again, the decrease of pore pressure faces an increase in effective stress by the same amount. This increase, in turn, causes a compression of the soil layer and, therewith, a settlement. Therefrom results a reduction of the porosity and the permeability of the soil which continuously takes place. In the test series, a settlement around the pile was observed which attests this assumption. Hence, with progressive pore water dissipation, the drainage ability is reduced due to the settlement of the soil. And thus, the dissipation process slows down. Therefore, not only the fluid flow has to be set on but also the porosity and the permeability have to be adjusted. Since the consolidation is an ongoing process, those parameters have to be adjusted step-by-step and this reduction has to be implemented in the Finn and Byrne Model.

8.2.2 Pore pressure

In Fig. 8-14, the pore pressure measured in the test series is shown on the left-hand side for the first 300 s of the test. The simulated pore pressure is depicted on the right-hand side. Whereas dissipation is suppressed during the first 15 s of loading, fluid flow is allowed afterwards and the permeability is simultaneously reduced to $\kappa = 1 \cdot 10^{-10}$ m^2/Pa·s. Hence, not only the pore pressure accumulation but also the dissipation can be simulated relatively well. At $t = 300$ s, the signals $F1_{FLAC}$ – $F4_{FLAC}$ reach approximately the same values as in the test series. After this time until the end of the test, the pore pressure only oscillates around its mean value. Apart from the fact Δu_{trans} slightly varies in amplitude, the simulation is in good agreement with the measurement data from the test series.

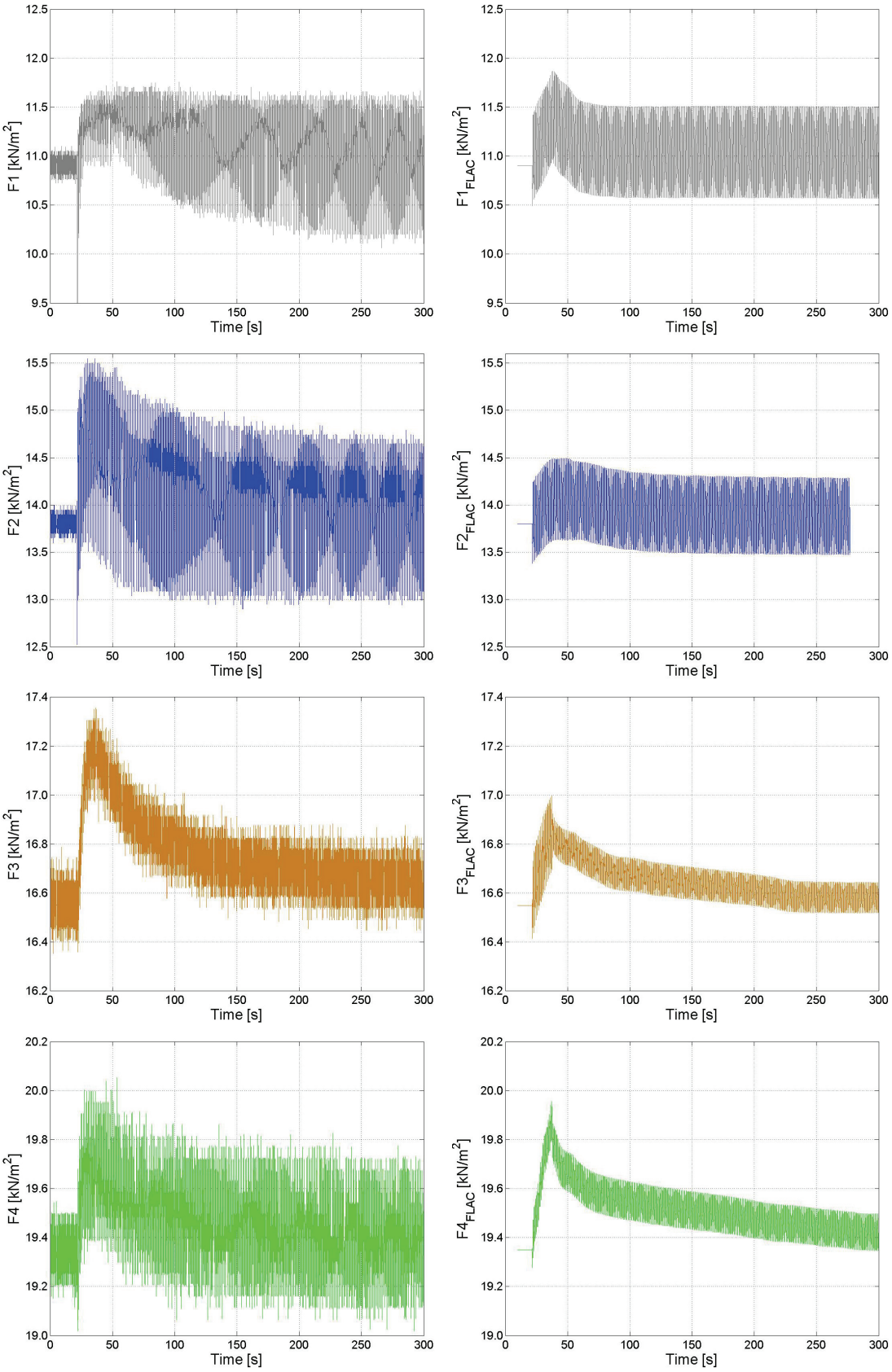

Fig. 8-14: Comparison of measured and simulated pore pressure at four levels. Left: first 300 s of pore pressure F1 – F4 in a test series with $x_w = \pm 1.0$ cm and $f = 1.0$ Hz. Right: pore pressure $F1_{FLAC}$ – $F4_{FLAC}$ simulated with FLAC for a corresponding test.

8.3 Key results of the numerical simulation

Within the numerical analyses, the cyclically loaded pile was simulated and the resulting pore pressure changes were analysed in order to investigate whether the pore pressure measured in the test series can be simulated numerically. Since the signals of the pore pressure in the experimental test series could be divided into two phases (first phase characterised by pore pressure accumulation, second phase characterised by pore pressure dissipation), the drainage capabilities of the FLAC simulation were designed accordingly. Thus, fluid flow was allowed in the first phase and inhibited in the second phase.

The FLAC simulation of the pore pressure during the first 15 s of loading (compare Section 8.1) showed an accumulation of pore pressure at all levels. Thus, it was seen that not only seismically induced pore pressure increases can be simulated but also the accumulation of pore pressure due to the cyclic deflection of a structure. At some levels, the mean value of the pore pressure and the amplitude of transient pore pressure at $t = 35$ s is slightly different in the FLAC simulation compared to the measurement signals. Hence, further investigations should focus on the analysis of this phase. Thereby, it is most important to find a tool which allows defining the time at which the maximum pore pressure is reached since this is the value which indicates if liquefaction occurs or not.

In further studies, it was controlled whether the pore pressure reacts to changes in volumetric strain as postulated in Section 3.4.3. It was seen that compression of a zone results in an increase of the corresponding pore pressure whereas dilatation of the soil causes a decrease of pore pressure. It was also shown that the deflection of the pile leads to changes in volumetric strain and, therewith, to pore pressure changes adjacent to the pile. The rotation point of the pile was seen to lie slightly above the location assumed for the experimental test series.

In order to investigate whether the dependency of the pore pressure on the input parameters equals to the dependency observed in the test series, further simulations varying in x and f were carried out. In accordance to the results of the test series, the simulated pore pressure was observed to be influenced by the amplitude of forced displacement as well as by the loading frequency. The influence of x and f was found to be approximately equally strong on u_{35s} but differently strong on Δu_{trans} (higher influenced by x than by f). Further investigations with different combinations of input parameters should investigate those dependencies in more detail.

For the simulation of the pore pressure during the second phase (compare Section 8.2), the fluid flow was set on. It was seen that when only the flow is set on, the dissipation process goes on very fast and is simulated unrealistically since a reduction of the permeability of the soil is not implemented in the Finn and Byrne Model. Thus, not only fluid flow was allowed but also the permeability coefficient was adjusted for the simulation of the pore pressure during the phase of predominant dissipation. By doing so, the resulting pore pressure calculated in the FLAC simulation was found to be in satisfying good agreement with the pore pressure measured in the test series. Nevertheless, future investigations should concern with this topic by implementing the reduction of permeability, and also of void content, into the Finn and Byrne Model.

9 Summary and outlook

Soil liquefaction and its severe consequences on buildings and infrastructure are at least known since the strong earthquakes in Asia and in Alaska in the 1960s. The risk of soil liquefaction around offshore structures is self-evident since all boundary conditions for such risks are given: firstly, the subsoil consists of sandy saturated soil which is, thus, prone to liquefaction; secondly, dynamic loading is present which can initiate liquefaction; and thirdly, structures which are affected by this loading and which can be damaged are regarded. The very few wind turbines that were installed in the ocean up to now, were constructed near the shore. Previous test series and other investigations mainly concern with caisson foundations. Hence, experiences are not available how the cyclic deflections of the offshore pile structures affect the pore pressure in the soil. Neither it is evidenced whether an increase in pore pressure causing soil liquefaction is likely to occur. The present research work contributes to these open questions by supplying the results of experimental and numerical investigations on a cyclically loaded pile foundation.

The **experimental investigations** carried out within this research work are the first of their kind and, therefore, supply important information on those questions. In an extensive test program, the pore pressure induced by the cyclic loading of the pile was analysed. Therefore, the pore pressure was measured at four levels: at the levels 1 (upper level) to 4 (bottom level). The deflection of the pile was varied in its amplitude and frequency. A wide range of input parameters was considered in order to examine their influences on different pore pressure characteristics.

In contrast to pore pressure measurements carried out beneath caisson breakwaters, it was observed that there is no residual pore pressure at the end of each test series but that the maximum of the pore pressure is reached directly after the beginning of loading. This maximum pore pressure is the most important characteristic value of the pore pressure since it indicates whether soil liquefaction occurs or not. The investigation of this maximum value showed that although a dependency on the input parameters could not be observed for level 1, this upper level was most frequently stroke by soil liquefaction (in 75 % of the test series). At deeper locations, the maximum value was found to increase with increasing amplitude of deflection and loading frequency, but to decrease with depth and with horizontal distance to the test pile. Hence, in still 60 % of the test series, the soil liquefied at both levels 1 and 2, whereas level 3 was only affected in 35 % and level 4 in 15 % of the tests series. Nevertheless, although when liquefaction did not occur, it was observed that the deflection of the pile mostly led to pore pressure in-

creases at all levels and that the pile had a rotation point close to level 3. Furthermore, it was found that also the duration of liquefaction and the duration of excess pore pressure (duration until the pore pressure has decreased to half of its maximum value) were the longest at the upper level and decreased with increasing depth.

Regarding the tests which reproduce the deflections and frequencies that can be encountered offshore, liquefaction was only observed at the upper level. This means that the soil liquefied down to a depth of at least 6.7 % of the embedding of the pile (level 1) or of at most 25.3 % of this length (level 2). At first sight, this seems to be a lot. Nevertheless, it was seen that another phenomenon, namely the scour phenomenon, even affects larger fractions of the embedded length of the pile. Nevertheless, since also scour is not finally examined yet, further investigations on the soil liquefaction phenomenon should be conducted in order to verify those assumptions. For further research on this field, the following recommendations are provided in order to improve future test series:

- Conduction of force-driven and non-uniform loading conditions (storm profile).
- Improved measurement of the settlement of the soil around the pile over the entire duration of a test series in order to obtain additional information on the dissipation process.
- Additional test series with the pore pressure transducers being installed at different distances to the test pile in order to further investigate the lateral spreading of excess pore pressure.
- Application of strain gauges at the pile in order to determine the deflection of the pile over its entire length or, alternatively, development and installation of further displacement transducers that are able to measure the deflection of the pile under the sand surface.

Apart from the realisation of the experimental test series and their analyses, a **numerical model** has been developed in order to simulate the results of the test series numerically. Therefore, the finite-difference program FLAC was used. The Finn and Byrne Model was applied to simulate the behaviour of the soil due to the cyclic deflection of a pile structure. It could be shown that by means of this program and model, pore pressure changes due to this cyclic deflection can be successfully simulated. The pore pressure accumulation and its dissipation were modelled by defining different conditions for the fluid flow and were analysed at the locations corresponding to those of the test series. It was shown that the simulated pore pressure depends on the changes in volumetric strain and, corresponding to the results of the experimental investigations, that the maximum values of mean and transient pore pressure depend on the amplitude of deflection and on the frequency of loading.

The numerical studies should be continued with the objective to simulate a real offshore structure with the there-present loading conditions and to determine the probability of soil liquefaction for this special location. Hence, the following recommendations are provided to focus on:

- Further investigation of the pore pressure accumulation and dissipation and implementation of a coupling between the settlement of the soil and the decrease in porosity and permeability (based on additional measurement data from test series, see above).
- Application of non-uniform, force-driven loading (see recommendations for test series).
- Simulation of a real offshore structure in a 1:1 scale and validation with the measurement data gained from projects as presented, e.g., in STAHLMANN et al. (2007).
- Determination of the probability of soil liquefaction for 1:1 structure.

The realisation of those recommendations for the experimental and the numerical investigations is certainly complex and expensive. Nevertheless, regarding the high number of offshore wind farms that is expected to be built in the next years, it is important to gain further knowledge and to go on with research in this field. The present research provides important information on the occurrence of liquefaction due to the cyclic horizontal deflection of a pile and supplies a sound basis for those future research works.

Appendix A

Duration of liquefaction

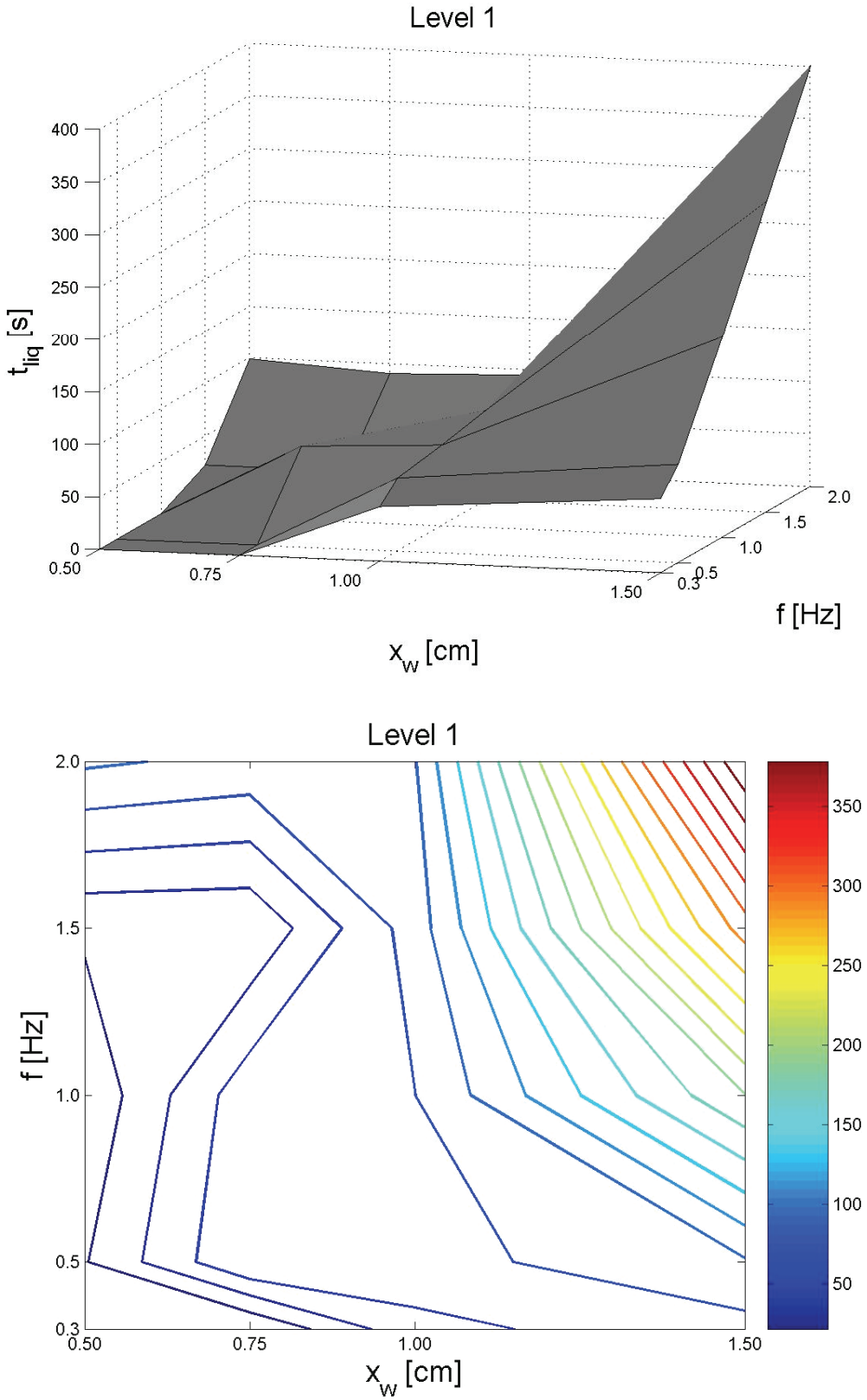

Fig. A-1: Above: Duration of liquefaction t_{liq} for level 1 versus displacement x_w and frequency f. Below: Isolines of duration of liquefaction t_{liq} for level 1 as a function of displacement x_w and frequency f.

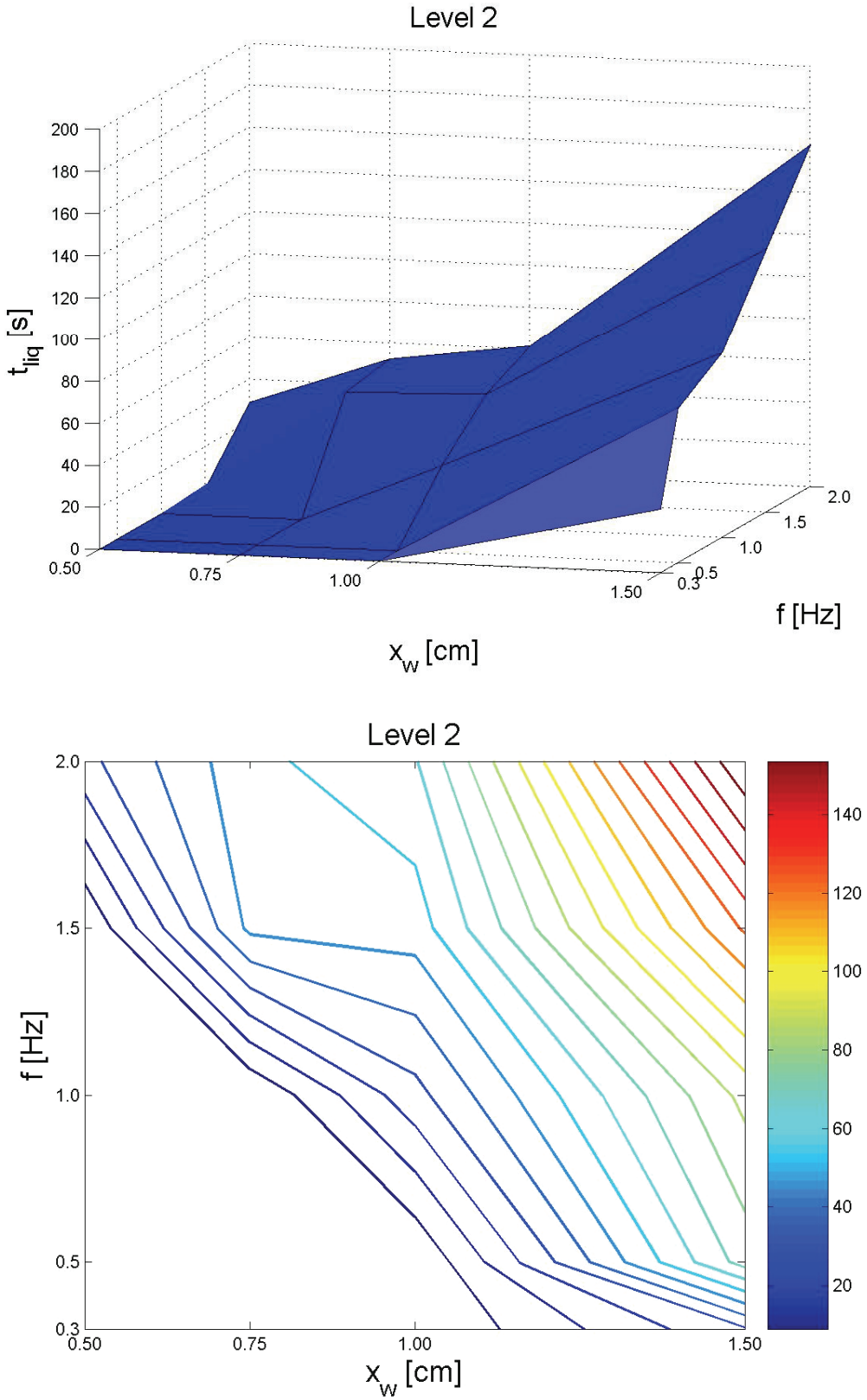

Fig. A-2: Above: Duration of liquefaction t_{liq} for level 2 versus displacement x_w and frequency f. Below: Isolines of duration of liquefaction t_{liq} for level 2 as a function of displacement x_w and frequency f.

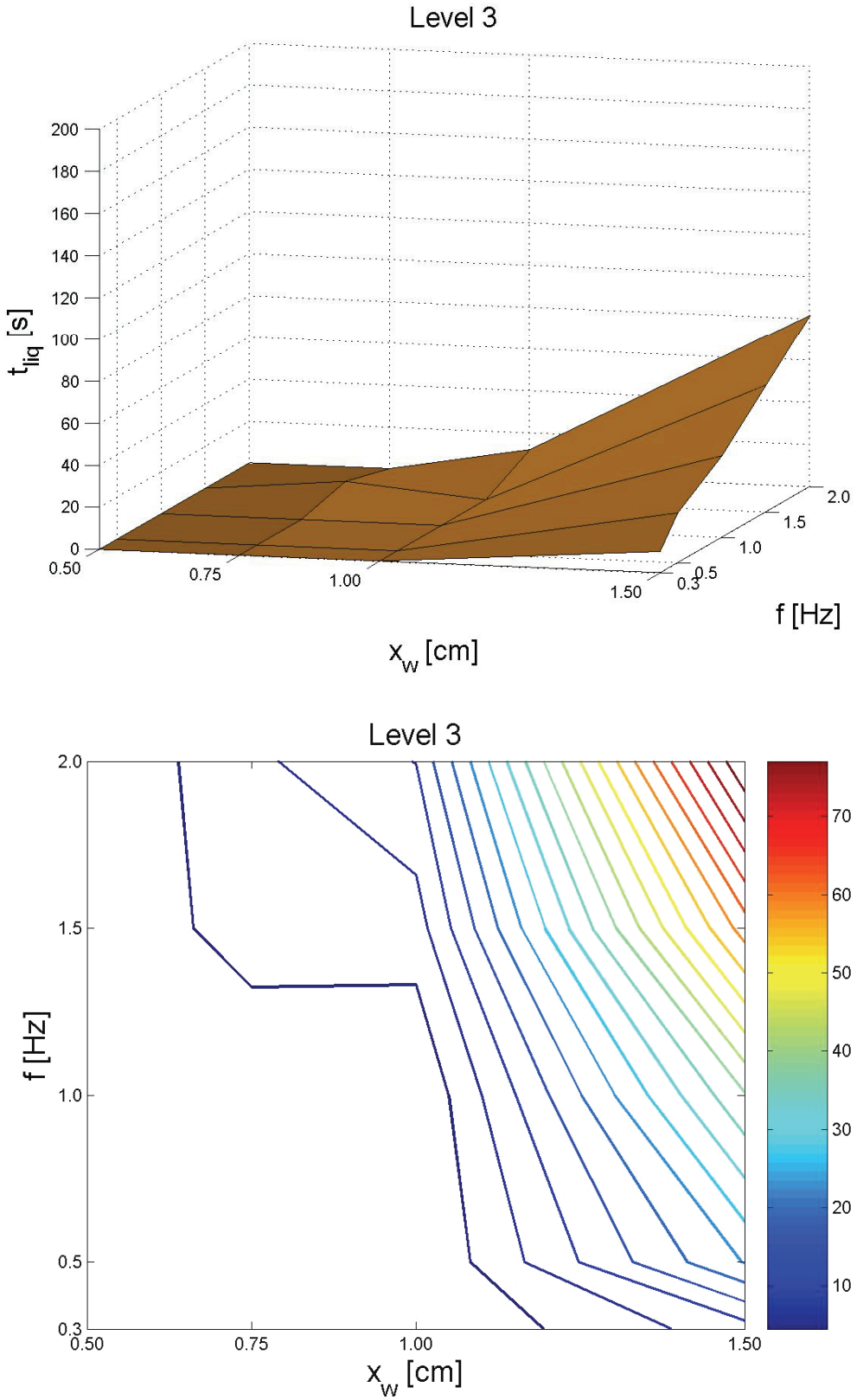

Fig. A-3: Above: Duration of liquefaction t_{liq} for level 3 versus displacement x_w and frequency f. Below: Isolines of duration of liquefaction t_{liq} for level 3 as a function of displacement x_w and frequency f.

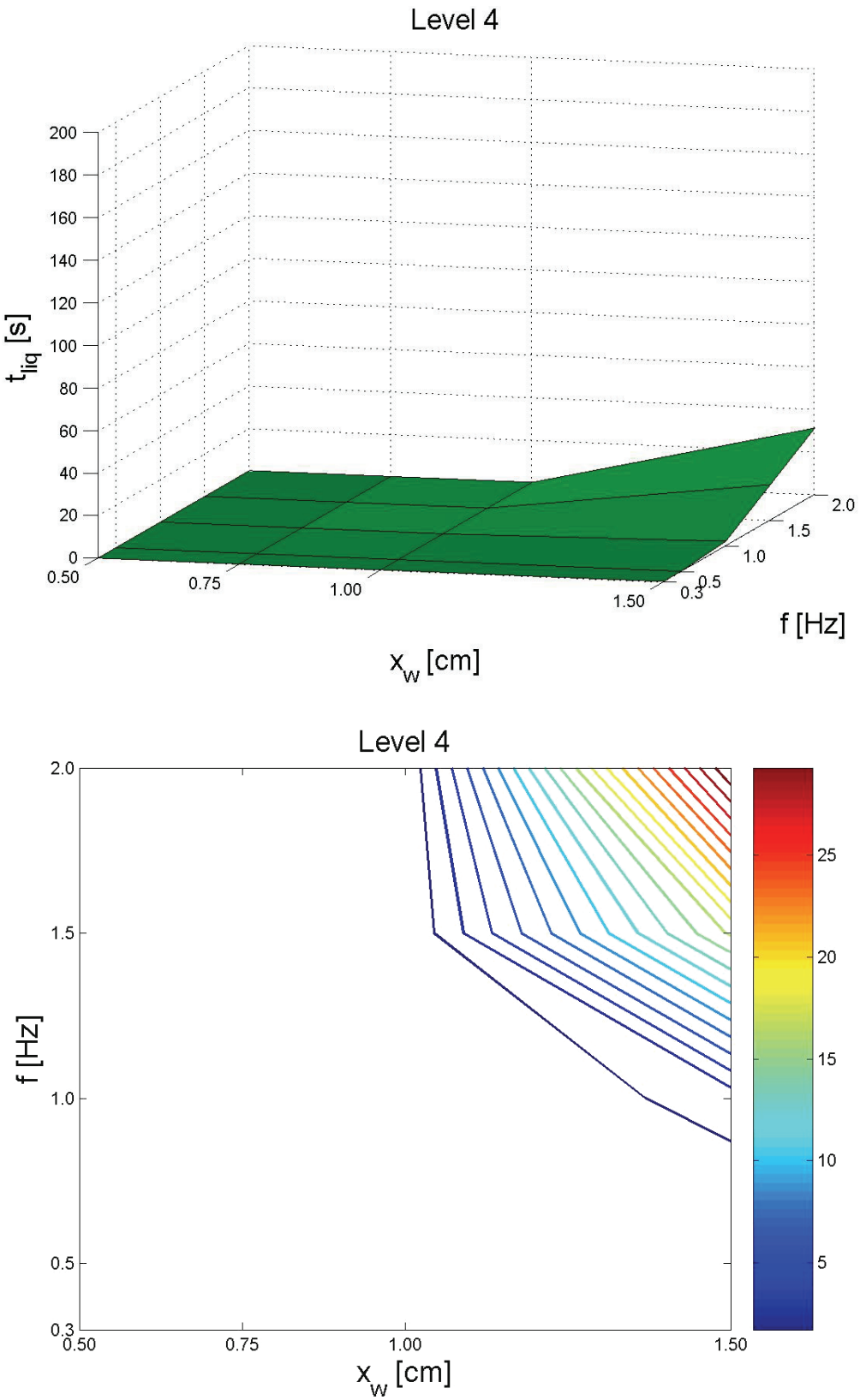

Fig. A-4: Above: Duration of liquefaction t_{liq} for level 4 versus displacement x_w and frequency f. Below: Isolines of duration of liquefaction t_{liq} for level 4 as a function of displacement x_w and frequency f.

Appendix B

Duration of excess pore pressure

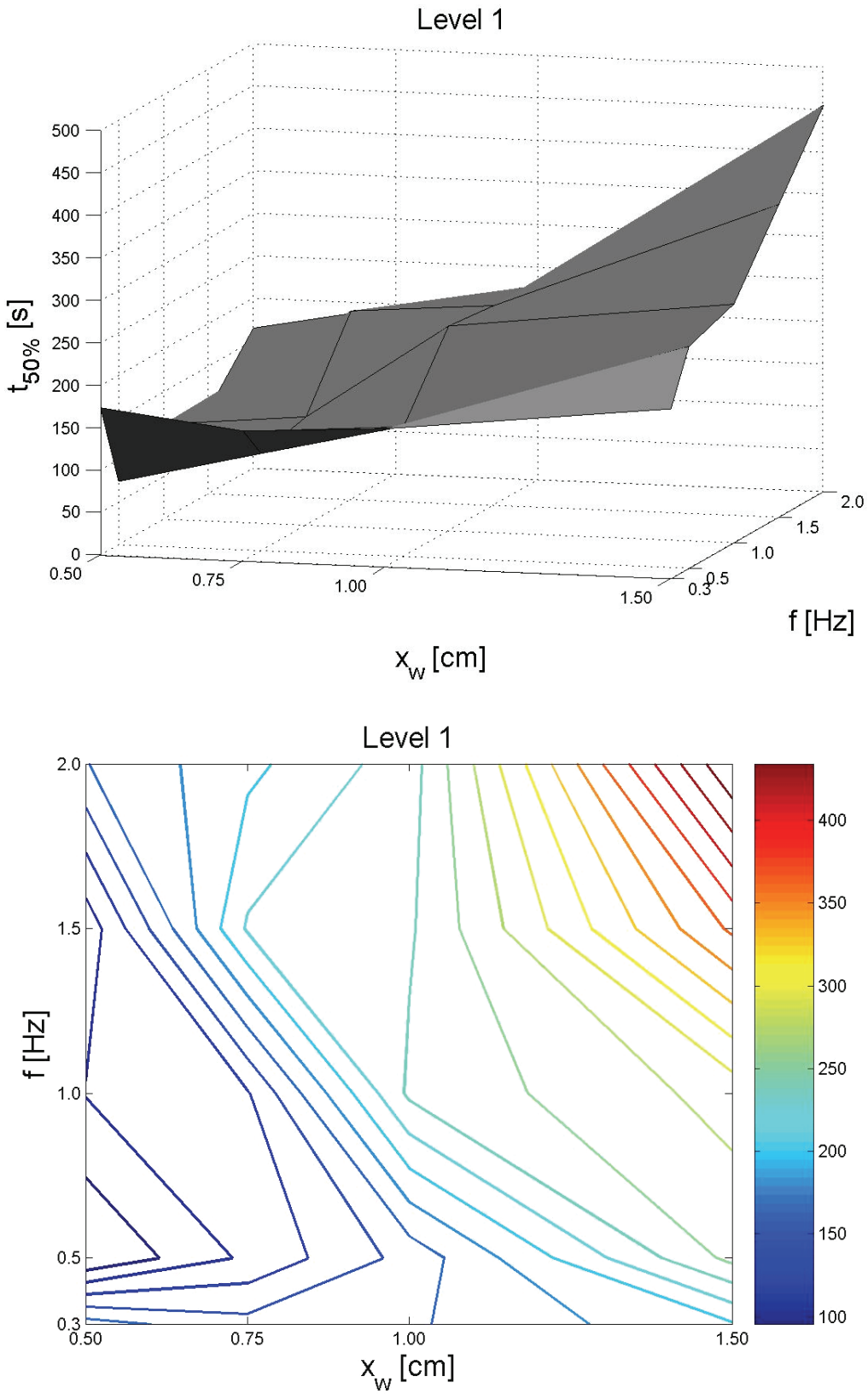

Fig. B-1: Above: Duration of excess pore pressure $t_{50\%}$ for level 1 versus displacement x_w and frequency f. Below: Isolines of duration of excess pore pressure $t_{50\%}$ for level 1 as a function of displacement x_w and frequency f.

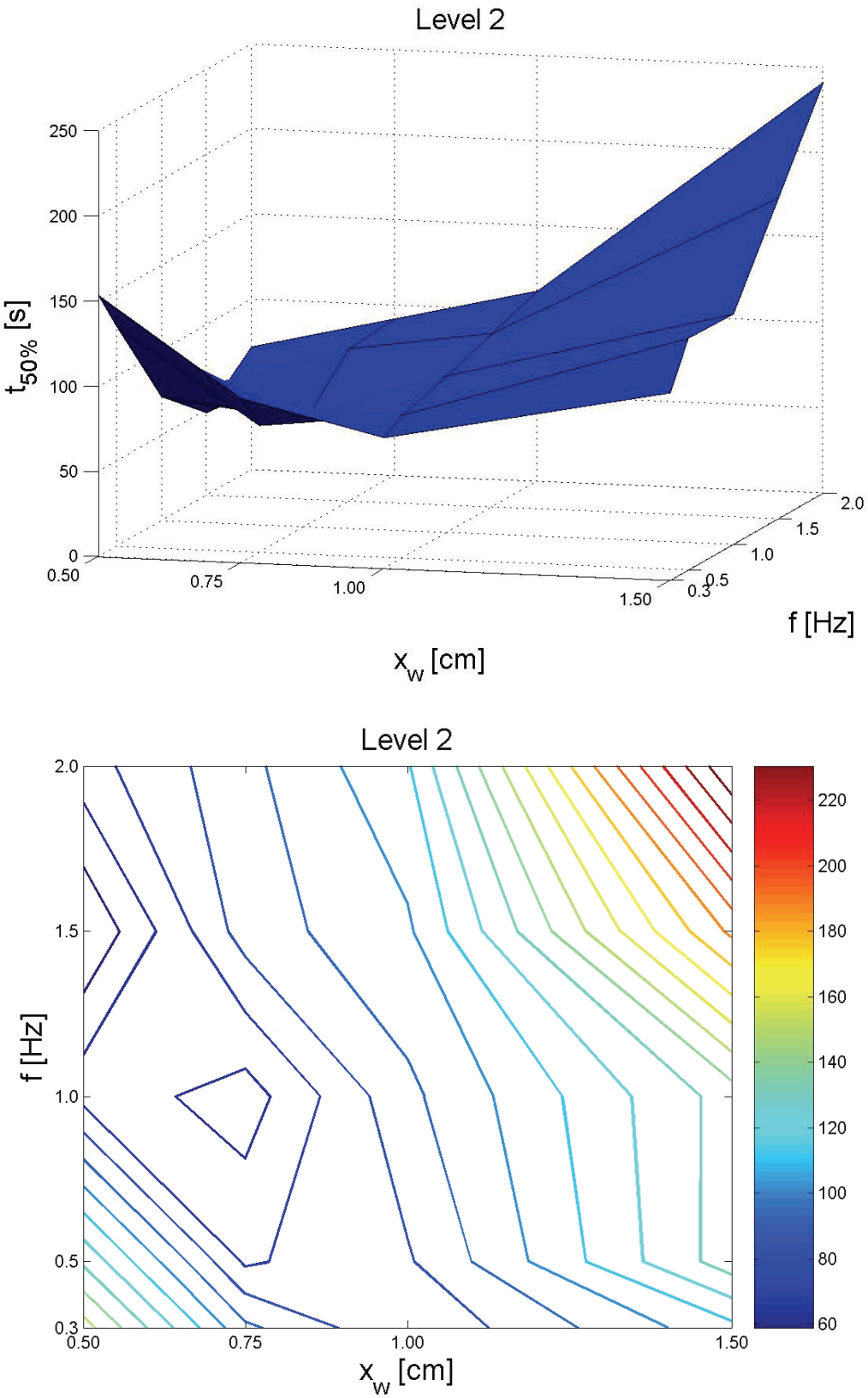

Fig. B-2: Above: Duration of excess pore pressure $t_{50\%}$ for level 2 versus displacement x_w and frequency f. Below: Isolines of duration of excess pore pressure $t_{50\%}$ for level 2 as a function of displacement x_w and frequency f.

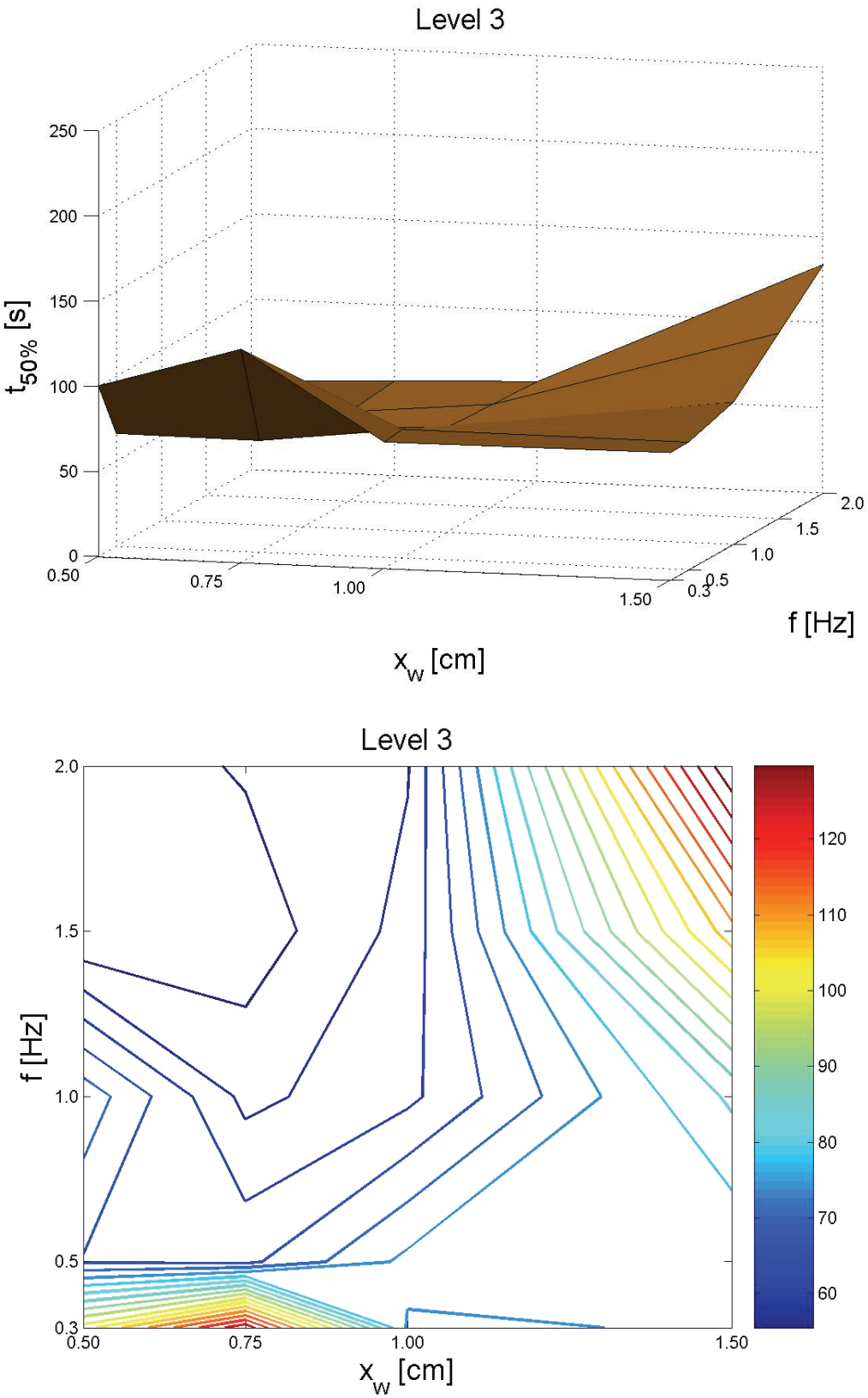

Fig. B-3: Above: Duration of excess pore pressure $t_{50\%}$ for level 3 versus displacement x_w and frequency f. Below: Isolines of duration of excess pore pressure $t_{50\%}$ for level 3 as a function of displacement x_w and frequency f.

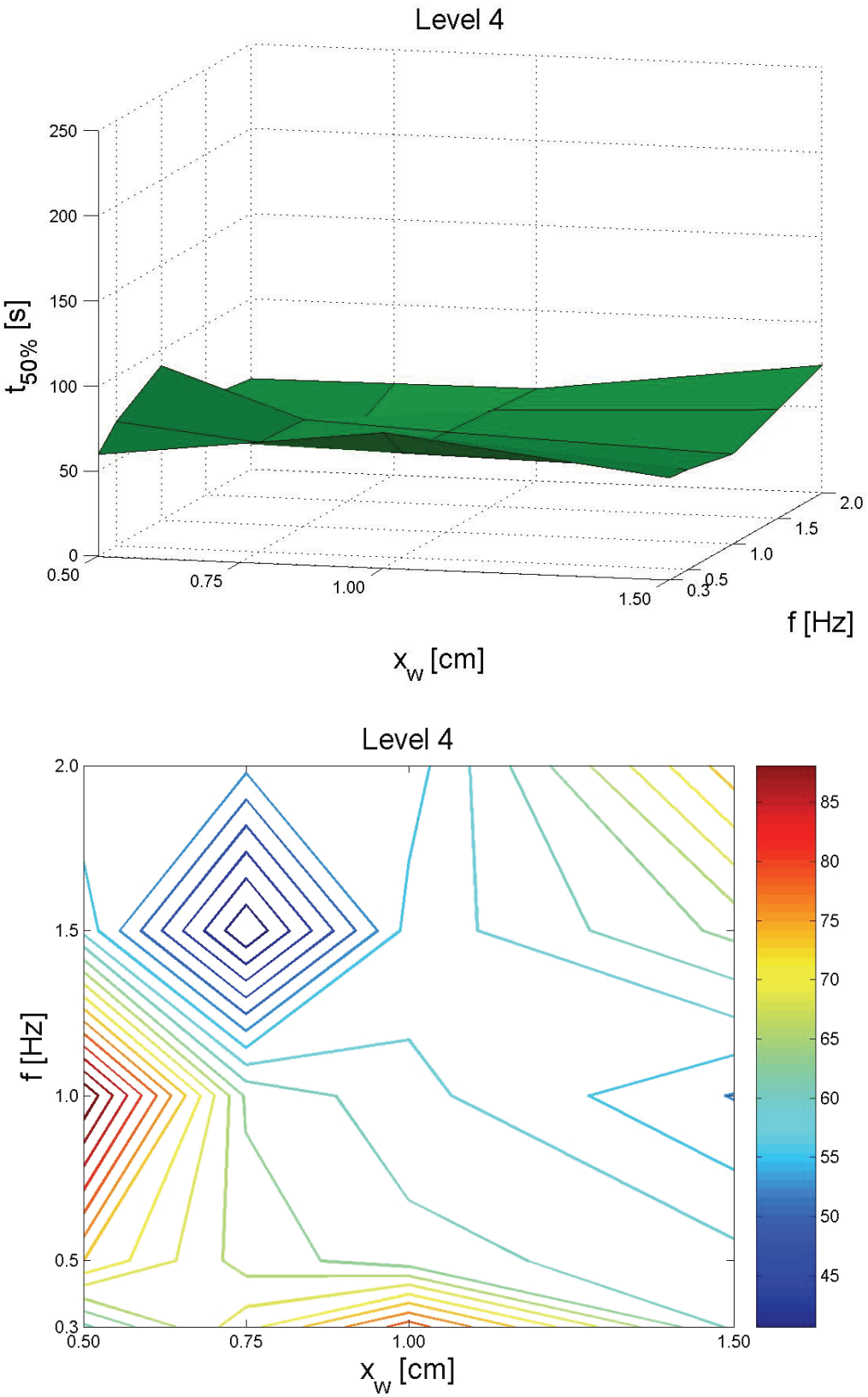

Fig. B-4: Above: Duration of excess pore pressure $t_{50\%}$ for level 4 versus displacement x_w and frequency f. Below: Isolines of duration of excess pore pressure $t_{50\%}$ for level 4 as a function of displacement x_w and frequency f.

Appendix C

Amplitudes of transient pore pressure

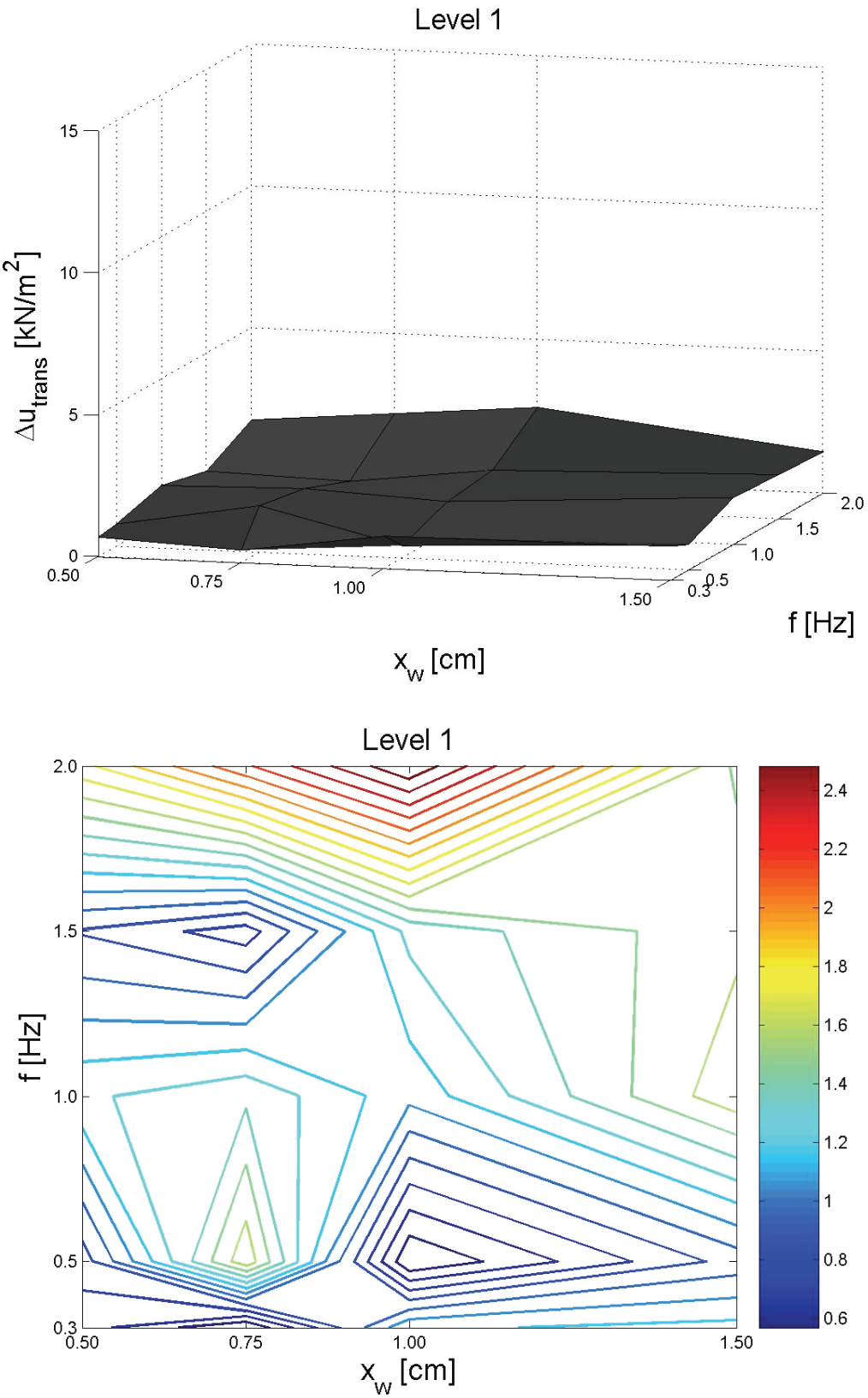

Fig. C-1: Above: Transient part of the pore pressure Δu_{trans} for level 1 versus displacement x_w and frequency f. Below: Isolines of the transient pore pressure Δu_{trans} for level 1 as a function of displacement x_w and frequency f.

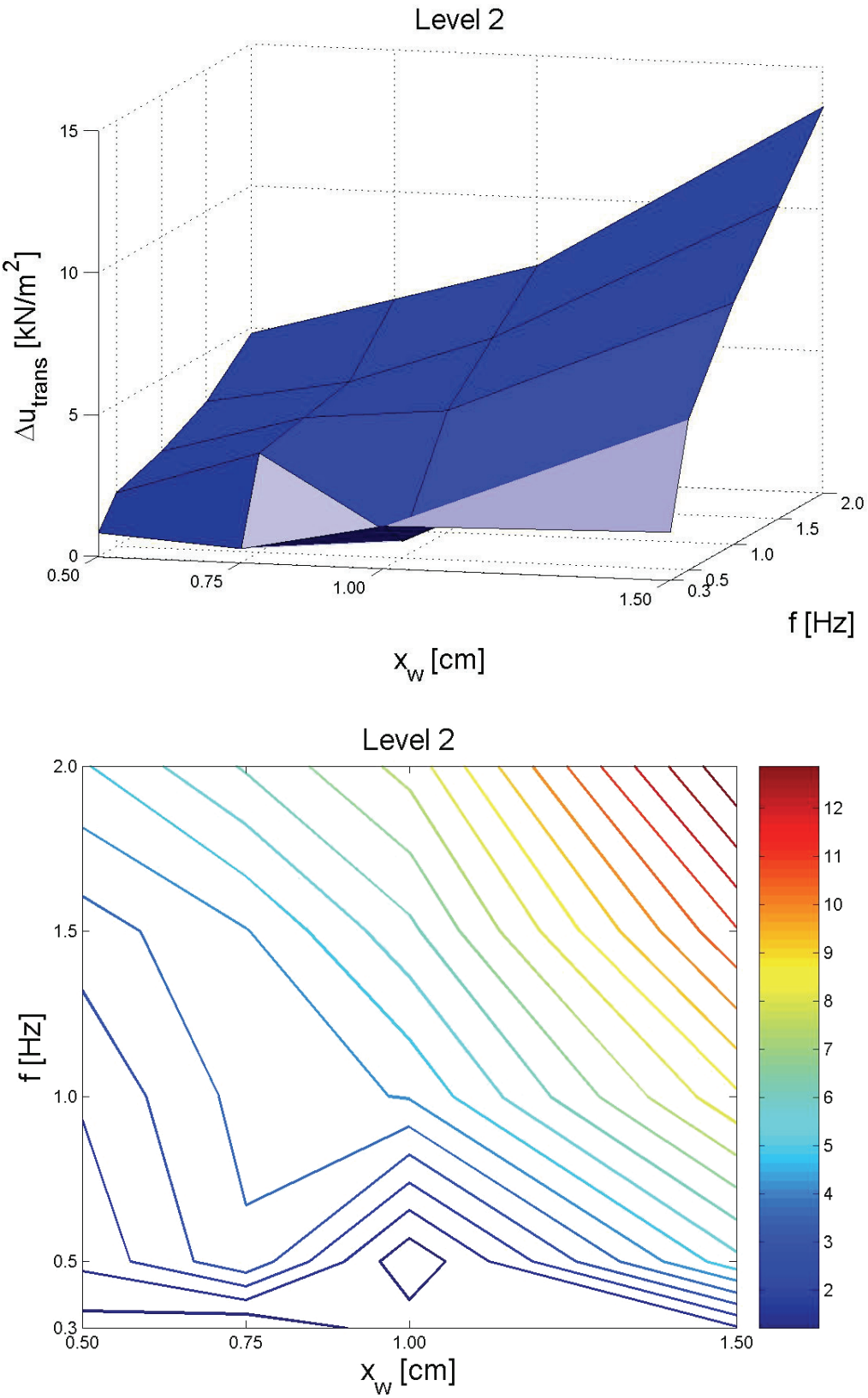

Fig. C-2: Above: Transient part of the pore pressure Δu_{trans} for level 2 versus displacement x_w and frequency f. Below: Isolines of the transient pore pressure Δu_{trans} for level 2 as a function of displacement x_w and frequency f.

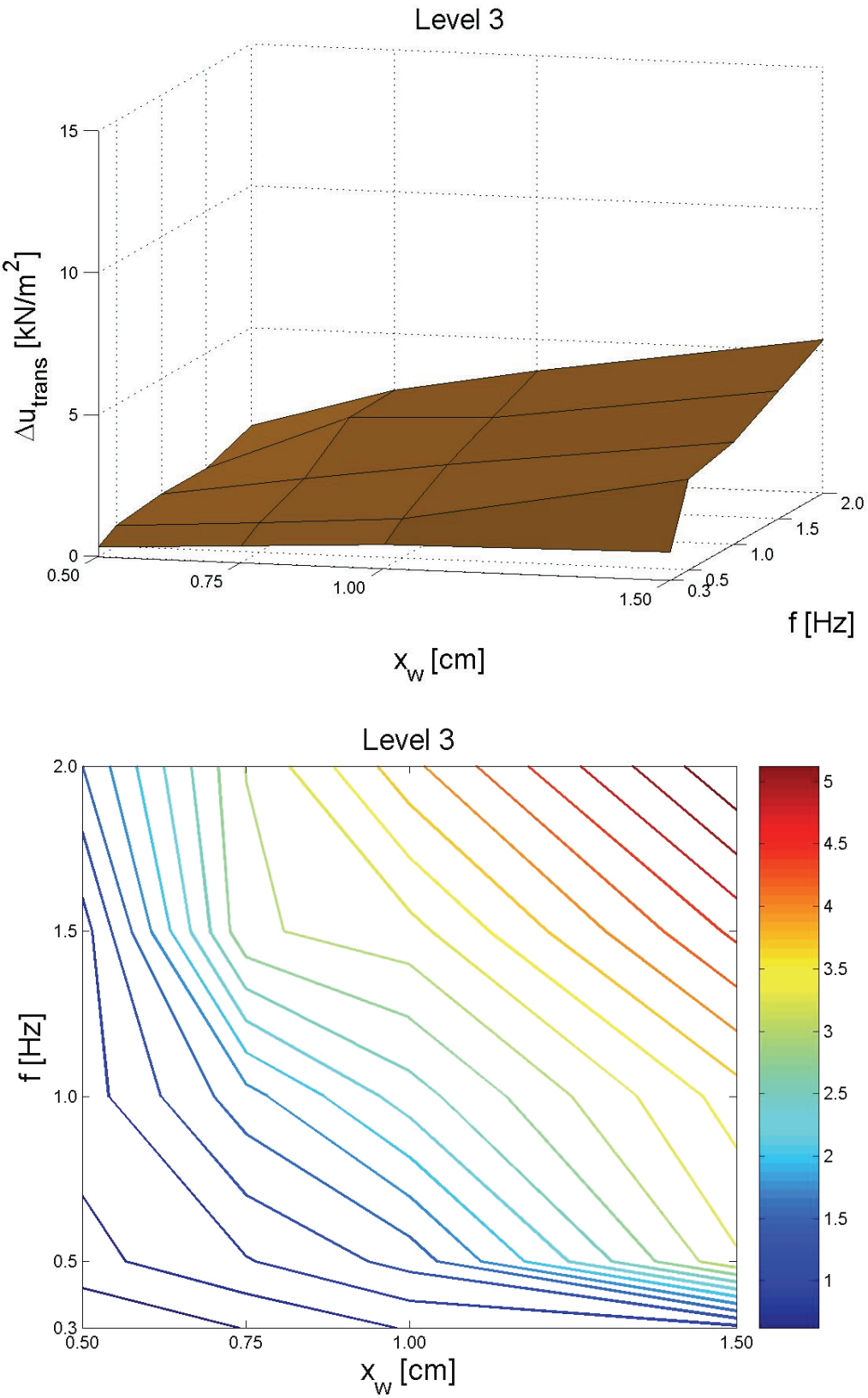

Fig. C-3: Above: Transient part of the pore pressure Δu_{trans} for level 3 versus displacement x_w and frequency f. Below: Isolines of the transient pore pressure Δu_{trans} for level 3 as a function of displacement x_w and frequency f.

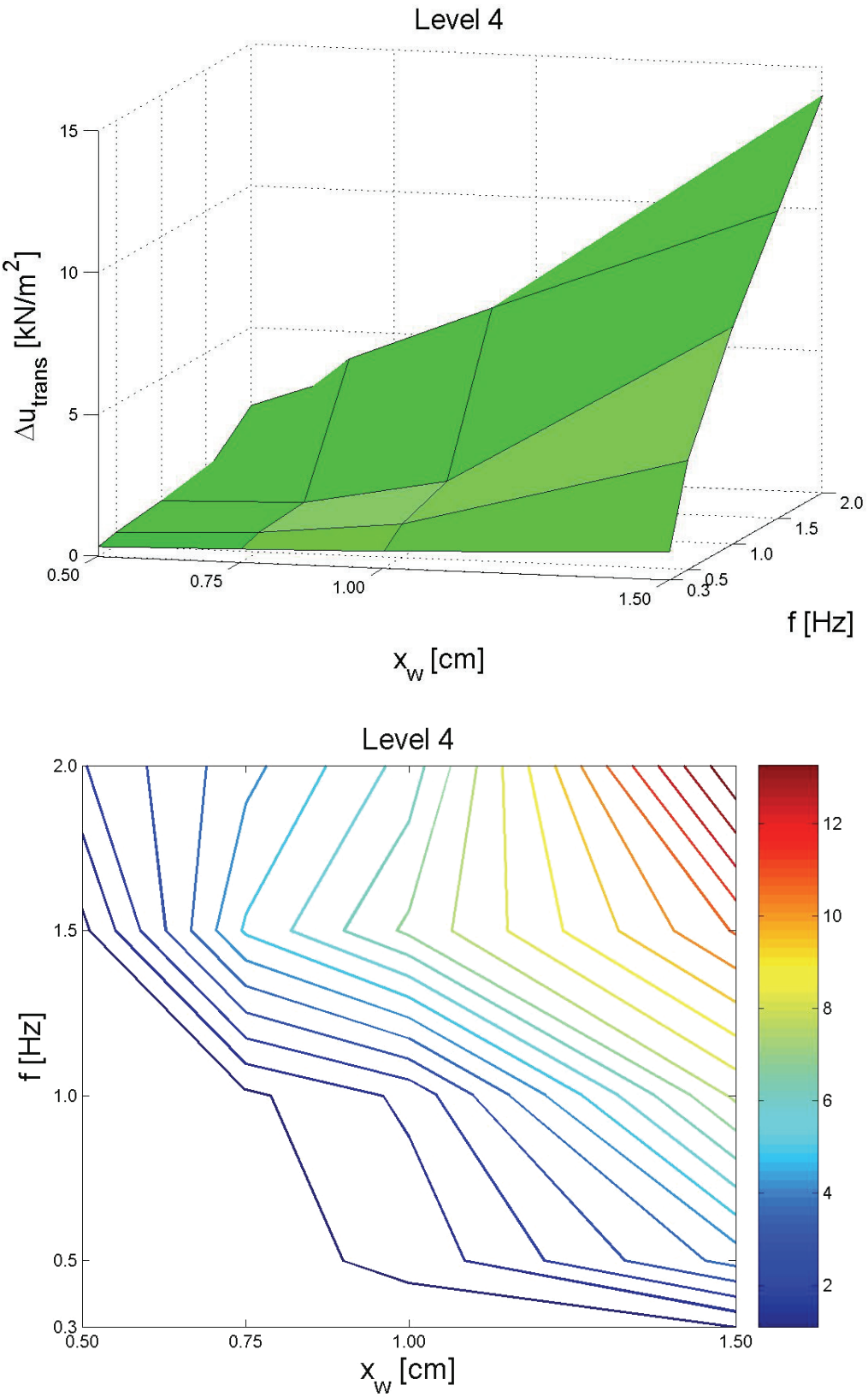

Fig. C-4: Above: Transient part of the pore pressure Δu_{trans} for level 4 versus displacement x_w and frequency f. Below: Isolines of the transient pore pressure Δu_{trans} for level 4 as a function of displacement x_w and frequency f.

Nomenclature

Notations and abbreviations introduced in Chapter 0:

E(D)	Expected value of damage
P_O	Probability of occurrence
R	Risk

Notations and abbreviations introduced in Chapter 2:

EEG	Renewable Energy Sources Act
EEZ	Exclusive Economic Zone
H	Height of a wave
H_i, H_1 to H_5	Different height of waves
H_m	Mean wave height
H_{max}	Maximum wave
H_S	Significant wave
$H_{1/10}$	Mean value of the 10% highest waves
$H_{1/100}$	Mean value of the 1% highest waves
$H_{1/3}$	Significant wave, mean value of the 33% highest waves
P(H)	Probability density function of the wave height H
T	Period of a wave
T_i, T_1 to T_5	Different periods of waves
T_{max}	Maximum wave period
T_{mean}	Mean wave period
T_{min}	Minimum wave period
$u_{mud,max}$	Maximum deflection of the pile at the mudline level

Notations and abbreviations introduced in Chapter 3:

Index 0	Initial value of a parameter
C_1, C_2, C_3, C_4	Experimentally determined constants (Finn / Byrne Constitutive Law)
D_r	Relative density
E_r	Tangent modulus of the one-dimensional unloading curve
FE	Failure envelope
FLS	Flow liquefaction surface
FS	Factor of safety

G	Shear modulus
G_{max}	Maximum shear modulus
G_{sec}	Secant shear modulus
h	Height of a soil sample
Δh	Change in height of a soil sample
K_0	Coefficient of earth pressure at rest
K_W	Bulk modulus of water
K_m, m	Factors (Byrne Constitutive Law)
M	Rebound constrained tangent modulus
m, n and k_2	Experimentally determined constants (Finn Constitutive Law)
N	Number of loading cycles
n	Porosity of a soil sample
N_{60}	Standard penetration test
P_a	Atmospheric pressure
r_u	Pore pressure ratio
S_r	Degree of saturation
$s_u(LIQ)$	Liquefied shear strength
t	Time
t_0, t_1, t_2, t_{2*}	Different points in time during liquefaction process
u	Pore pressure, i.e., neutral stress
u_1,u_2	Pore pressure at different points in time
u_g	Generated pore pressure
u_h	Hydrostatic water pressure
Δu	Excess pore pressure, pore pressure increment for one cycle
z	Depth in the soil
ε	Strain
ε_{vd}	Accumulated volumetric strain under drained conditions
ε_{vr0}	Recoverable volumetric strain under initial conditions
$\Delta\varepsilon_{vd}$	Incremental volumetric strain under drained conditions
$\Delta\varepsilon_{vd}^{p}$	Increment of plastic volumetric strains under drained conditions
$\Delta\varepsilon_{vr}$	Increment of recoverable volumetric strain
γ	Shear strain
γ_c	Shear strain of a certain cycle
γ_{cyc}	Cyclic shear strain
γ_h	Hyperbolic strain
γ_l	Limit shear strain
γ_s'	Unit weight of the soil under buoyancy
γ_V	Threshold shear strain amplitude
γ^*	Shear strain amplitude (Byrne Constitutive Law)
φ	Inner friction angle
σ	Total stress

σ_h	Horizontal stress
σ_v	Vertical stress
σ'	Effective stress
σ'_h	Horizontal effective stress
σ'_m	Mean effective stress
σ'_v	Vertical effective stress
μ	Poisson's ratio
τ	Shear strength
τ_{cyc}	Cyclic shear stress
τ_{hv}	Cyclic shear stress
τ_{max}	Maximum shear stress
ξ	Damping ratio

Notations and abbreviations introduced in Chapter 4:

H	Wave height
h	Water depth
k	Wave number
L	Wave length
p	Pressure oscillations due to water waves
p_0	Amplitude of the pressure oscillations due to water waves
T	Wave period
z	Depth of the sea bed
ω	Circular frequency

Notations and abbreviations introduced in Chapter 5:

A	Area of the object of interest
E	Modulus of elasticity
D	Diameter of the pile
d_{10}	Grain size of 10 % passing
e_{min}	Void ratio of the soil sample at densest packing
e_{max}	Void ratio of the soil sample at densest packing
F	Force
f	Frequency of the loading
I	Moment of inertia
K	Permeability
Index m	Characteristic of the model
Index o	Characteristic of the original system
l_e	Embedded length
l_p	Length of a pile
l_w	Water level

l	Length of the object of interest
M	Moment
n_{min}	Porosity of the soil sample at densest packing
n_{max}	Porosity of the soil sample at loosest packing
P	Line load
t	Time
v	Velocity
V	Volume of the object of interest
x_w	Deflection of the pile at the point of the load application
x_s	Deflection of the pile at the embedded of the pile
γ_s	Specific unit weight of the soil
φ	Friction angle
λ	Geometric scaling factor
ν	Viscosity
$\rho_{d,min}$	Density at densest packing
$\rho_{d,max}$	Density at loosest packing

Notations and abbreviations introduced in Chapter 6:

B1 – B4	Labelling of pore pressure transducers of group B
F1 – F4	Labelling of pore pressure transducers of group F
d	Distance of pore pressure sensors to the test pile
g	Gradient
Index n	Number of a loading cycle
Index N	Signifies a normal test
R_{xy}	Cross correlation
$r_{u,max}$	Maximum value of the pore pressure ratio
$r_{u,max,ref}$	Reference value of the maximum pore pressure ratio
Index S	Signifies a test in which the loading was stopped before the normal time
$signal_i$	Signal of pore pressure transducer with the number i
t_{liq}	Duration of liquefied state
$t_{50\%}$	Time until the pore pressure ratio is released to its half
Δu_{acc}	Accumulating pore pressure per cycle
Δu_{diss}	Dissipation pore pressure per cycle
$\Delta u_{(1\ cycle)}$	Pore pressure rate per loading cycle
Δu_{trans}	Transient part of the pore pressure changes Δu
x,y	Functions to be cross-correlated
γ_w	Unit weight of the water
ρ_{xy}	Cross correlation coefficient
σ_x, σ_y	Standard deviation of a function x and y
τ	Time shift

Notations and abbreviations introduced in Chapter 7:

A_z	Area of a zone
A	Area
b, f, c	Indices indicating the forward, backward and centred approximation
f_n	Natural frequency
c	Cycle
C	Speed of wave
Cp	Speed of compression waves
C_s	Speed of shear waves
c_v	Coefficient of consolidation
D	Critical damping
D_+	Secant line for the forward approximation
D_-	Secant line for the backward approximation
D_0	Secant line for the centred approximation
$GP_{1,2}$	Grid points
h	Grid size
I	Moment of inertia
j	Grid point number
k	Permeability
Δl	Spatial element size
Δl_{max}	Maximum spatial element size
M, C, K	System matrices
n_i^t	Unit vector in strain space
K	Bulk modulus
O	Error of an approximation
Index pile	Related to the properties of the pile
r	Radial direction
Index soil of s	Related to the properties of the soil
Index total	Related to the properties of the pile as full section pile
T	Time
t	Time step (number)
Δt	Time step (duration)
Δt_{crit}	Critical time step
Z	Zone in which the volumetric strain and pore pressure are analysed
α_l	Local damping coefficient
ε_1 - ε_6	Strain measures
κ	Mobility coefficient
λ	Wavelength
ρ	Mass density

Notations and abbreviations introduced in Chapter 8:

u_{35s}	Pore pressure at t = 35 s

References

ACHMUS et al. (2007). Achmus, M.; Abdel-Rahman, K.; Kuo, Y.-S.; Peralta, P.: Untersuchungen zum Tragverhalten von Monopilegründungen unter zyklischer Belastung, Pfahlsymposium 2007, Fachseminar am 22./23.02.07 in Braunschweig, Mitteilung des Instituts für Grundbau und Bodenmechanik, TU Braunschweig, Heft 84, S. 95-114, 2007

BENDAT and PIERSOL (2000). Bendat, J.S.; Piersol, A.G.: Random data: analysis and measurement procedures, 3rd edition, Wiley, New York, 2000

BMU (2004). Gesetz über den Vorrang erneuerbarer Energien, 2004

BMU (2006, a). Bundesministerium für Umwelt, Naturschutz und Reaktorsicherheit: Umweltpolitik, Erneuerbare Energien in Zahlen – nationale und internationale Entwicklungen, www.bmu.de, 2006

BMU (2006, b). Bundesministerium für Umwelt, Naturschutz und Reaktorsicherheit: Entwicklungen der erneuerbaren Energien 2005 – Aktueller Sachstand, www.bmu.de, 2006

BMU (2006, c). Bundesministerium für Umwelt, Naturschutz und Reaktorsicherheit: Erneuerbare Energien Gesetz - Entwicklungen der Stromerzeugung aus erneuerbaren Energien bis zum Jahr 2020 und finanzielle Auswirkungen, www.bmu.de, 2006

BMU (2007). Bundesministerium für Umwelt, Naturschutz und Reaktorsicherheit: Offshore wind power deployment in Germany, www.bmu.de, 2007

BSH (2003). Bundesamt für Seeschifffahrt und Hydrographie: Standard Baugrunderkundung, Mindestanforderungen für die Gründung von Offshore-Windenergieanlagen und die Verlegung der stromabführenden Kabel, BSH-Nr. 7004, Hamburg und Rostock, 2003

BSH (2006). Bundesamt für Seeschifffahrt und Hydrographie http://www.bsh.de/de/Meeresnutzung/Wirtschaft/CONTIS-Informationssystem/ContisKarten/NordseeDeutscherFestlandsockelAWZ.pdf, Download on January 19th, 2006

BSH (2007). Bundesamt für Seeschifffahrt und Hydrographie: Standard, Konstruktive Ausführung von Offshore-Windenergieanlagen, BSH-Nr. 7005, Hamburg und Rostock, 2007

BJERRUM (1973). Bjerrum, L.: Geotechnical problems involved in foundations of structures in the North Sea, Géotechnique, Vol. 23, No. 3, pp. 319-358, 1973

BUCKINGHAM (1915). Buckingham, E.: The principle of similitude, Nature, Vol. 96, pp. 396-397, 1915

BYRNE (1991). Byrne, P.M.: A cyclic shear-volume coupling and pore pressure model for sand, Proceedings of the 2nd international conference on recent advances in geotechnical earthquake engineering and soil dynamics, St. Louis, Missouri, 1991

CASTRO (1975). Castro, G.: Liquefaction and cyclic mobility of saturated sands, Journal of the Geotechnical Engineering Division, ASCE, Vol. 101, No. 6, pp. 551-569, 1975

CHANEY and FANG (1991). Chaney, R.C.; Fang, H.Y.: Liquefaction in the coastal environment: an analysis of case histories, Marine Geotechnology, Vol. 10, pp. 343-370, 1991

CHENG et al. (2001). Cheng, L.; Sumer, B.M.; Fredsøe, J.: Solutions of pore pressure build up due to progressive waves, International journal for numerical and analytical methods in geomechanics, Vol. 25, pp. 885-907, 2001

CLAUSEN et al. (1975). Clausen, C.J.F.; Digiagio, E.; Duncan, J.M.; Andersen, K.H.: Observed behaviour of the Ekofisk oil storage tank foundation, Proceedings of the 7th Offshore Technology Conference, Houston, pp. 399-413, 1975

CHAWLA (2003). Chawla, G.: Seismic response simulation of geostructures in Mid America: a consequence based engineering approach, Georgia Institute of Technology May, 2003

COM (2005). Commission of the European Communities: The support of electricity from renewable energy sources, Brussels, 2005

COOKE (2000). Cooke, H.G.: Ground improvement for liquefaction mitigation at existing highway bridges. PhD thesis, Faculty of the Virginia Polytechnic Institute and State University, Blacksburg, 2000

CORTE (2006). Corte, C.: Numerische Simulation von Seegangs- und Windbelastung auf Offshore-Windkraftanlagen, Dissertation an der TU Braunschweig, 2006

CRESPELLANI and MADIAI (2002). Crespellani, T.; Madiai, C.: Liquefaction hazard during earthquakes at Nocera Scalo, Italy – Part II: Total and effective stress analyses for liquefaction potential assessment, Rivista italiana di geotecnica, Vol. 4, pp. 48-67, 2002

CRESPELLANI et al. (2002). Crespellani, T.; Madiai, C.; Vannucchi, G.: Liquefaction hazard during earthquakes at Nocera Scalo, Italy – Part I: Assessment of liquefaction potential using simplified procedures, Rivista italiana di geotecnica, Vol. 4, pp. 26-47, 2002

D'ACUNTO (2004). D'Acunto, B.: Computational methods for PDE in mechanics, In: Series on Advances in Mathematics for applied sciences, No. 67, ISSN: 1793-0901, 2004

DET NORSKE VERITAS (2004). Offshore Standard DNV-OS-J101, Design for offshore wind turbine structures, Offshore standard dnv-os-j101, Det Norske Veritas, 2004

DGGT (2002). Deutsche Gesellschaft für Geotechnik e.V. (DGGT): Empfehlungen des Arbeitskreises "Baugrunddynamik", Berlin, 2002

DHAKAL (2004). Dhakal, S.: Empirical relations for earthquake response of slopes, Dissertation Delft, 2004

DISYNET (2007). Disynet: Sensor-Kompendium, Version 2.10, 2007, www.Disynet.de, Download on August 23rd, 2007

DOBRY and LADD (1980). Dobry, R.; Ladd, R.S.: Discussion to "Soil liquefaction and cyclic mobility evaluation for level ground during earthquakes", by H.B. Seed and "Liquefaction potential: science versus practice" by R.B. Peck, Journal of the Geotechnical Engineering Division, ASCE, Vol. 106, No. 6, pp. 720-724, 1980

EAU (1996). Empfehlungen des Arbeitsausschusses „Ufereinfassungen" Häfen und Wasserstraßen, 6. Auflage, Ernst und Sohn, Berlin, 1996

EWEA (2007). European wind energy association, www.ewea.org, Download on April 26th, 2007

FARDIS and VENEZIANO (1982). Fardis, M.N.; Veneziano, D.: Probabilistic analysis of deposit liquefaction, Journal of the Geotechnical Engineering Division, ASCE, Vol. 108, No. 3, pp. 395-417, 1982

FERRITO et al. (1999). Ferrito, J.; Dickenson, S.; Priestly, N.; Werner, S.; Taylor, C.: Seismic criteria for California marine oil terminals, Technical Report, TR-2103-SHR, Naval Facilities engineering Center, Shore Facilities Department, Structures Division, Port Hueneme, CA 93043, 1999

FINN et al. (1977). Finn, W.D.L.; Lee, K.W.; Martin, G.R.: An effective stress model for liquefaction, Journal of the Geotechnical Engineering Division, ASCE, Vol. 103, No. 6, pp. 517-533, 1977

FINO (2007). Fino – Forschungsplattformen in der Nord- und Ostsee, http://www.fino-offshore.de, 2007

GERMANISCHER LLOYD (2004, a). Germanischer Lloyd: Guideline for the certification of offshore wind turbines. Technical report, Germanischer Lloyd Windenergie, 2004

GERMANISCHER LLOYD (2004, b). Germanischer Lloyd: Research Project OPTI-PILE, Final report regarding certification of the Q7 monopile design, Germanischer Lloyd Windenergie, 2004

GRABE et al. (2004). Grabe, J.; Dührkop, J.; Mahutka, K.-P.: Monopilegründungen von Offshore-Windenergieanlagen – Zur Bildung von Porenwasserüberdrücken aus zyklischer Belastung, Bauingenieur, Band 79, pp. 418-423, 2004

HARDING and DRNEVICH (1972). Hardin, B.O.; Drnevich, V.P.: Shear modulus and damping curves in soils: Design equations and curves, Journal of the Soil Mechanics and Foundations Division, ASCE, Vol. 98, No. 7, 1972

HAUPT (1986). Haupt, W.: Bodendynamik, Grundlagen und Anwendung, Friedr. Vieweg & Sohn, Braunschweig / Wiesbaden, 1986

HETTLER (1981). Hettler, A. : Verschiebungen starrer und elastischer Gründungskörper in Sand bei monotoner und zyklischer Belastung, Veröffentlichungen des Instituts für Bodenmechanik und Felsmechanik der Universität Fridericiana in Karlsruhe, Heft 90, 1981

ISHIHARA (1993). Ishihara, K: Liquefaction and flow failure during earthquakes, Géotechnique 43, No. 3, pp. 351-415, 1993

ISHIHARA and YAMAZAKI (1984). Ishihara, K.; Yamazaki, Y.: Wave-induced liquefaction in seabed deposits of sand, in Seabed Mechanics, B. Denness (ed.), pp. 139-48, London: Graham & Trotman, 1984

ITASCA (2002). User's Guide, Itasca Consulting Group, Inc., 2002

JAPANESE GEOTECHNICAL SOCIETY (1998). Japanese geotechnical society: Remedial measures against soil liquefaction – From investigation and design to implementation, A.A. Balkema, Rotterdamm, ISBN: 90-5410-668-9, 1998

JESSBERGER and JORDAN (1980). Jessberger, H.L.; Jordan, P.: Bodenmechanische Aspekte für die Standsicherheitsbetrachtung von Offshore-Bauwerken, Bautechnik, 57. Jahrgang, Heft 6, Berlin, 1980

KAGAWA et al. (1981). Kagawa, T.; Kraft, L. M.: Modelling the liquefaction process, Journal of the Geotechnical Engineering Division, ASCE, Vol. 107, No. 12, pp. 1593-1607, 1981

KOSHLA and WU (1976). Khosla, V.K.; Wu, T.H.: Stress-strain behaviour of sand, Journal of the geotechnical engineering division, ASCE, Vol. 102, No. 4, pp. 303-321, 1976

KOHLHASE et al. (2005). Kohlhase, S.; Dede, C.; Weichbrodt, F.; Radomski, J.: Buhnenbau: Beanspruchung und Bemessung von Holzpfählen im Küstenwasserbau, Schlussbericht, Rostock, 2005

KRAMER (1988). Kramer, S.L.: Initiation of soil liquefaction under static loading conditions, Journal of Geotechnical Engineering, Vol. 114, No. 4, pp. 412-430, 1988

KRAMER (1996). Kramer, S.L.: Geotechnical earthquake engineering, Prentice Hall, Inc., ISBN 0-13-374943-6, 1996

KUHLEMEYER and LYSMER (1973). Kuhlemeyer, R. L.; Lysmer, J.: Finite element method accuracy for wave propagation problems, Journal of the Soil Mechanics and Foundations Division, ASCE, Vol. 99, No. 5, pp. 421-427, 1972

LANG et al. (2007). Lang, H.-J.; Huder, J.; Amann, P.; Puzrin, A.M.: Bodenmechanik und Grundbau, Das Verhalten von Böden und Fels und die wichtigsten grundbaulichen Konzepte, 8. Auflage, Springer-Verlag, Berlin, 2007

LEE and FOCHT (1975). Lee, K.L.; Focht, J.A.: Liquefaction potential at Ekofisk tank in North Sea, Journal of the Geotechnical Engineering Division, ASCE, Vol. 101, No. 1, pp. 1-18, 1975

LEE and POULOS (1988). Lee, C.Y.; Poulos, H.G.: Influence of excess pore pressures on axial offshore pile response, Behaviour of foundations in calcareous sediments, Bulletin GB6, University of Sydney, pp. 73-93, 1988

LESNY et al. (2002). Lesny, K.; Richwien, W.; Wiemann, J.: Gründungstechnische Randbedingungen für den Bau von Offshore-Windenergieanlagen in der Deutschen Bucht, Bauingenieur, Band 77, pp. 431-483, 2002

LEVEQUE (2005). LeVeque, R.J.: Finite difference methods for differential equations, University of Washington, 2005

LONG and VANNESTE (1994). Long, J.H.; Vanneste, G.: Effects of cyclic lateral loads on piles in sand, Journal of the Geotechnical Engineering Division, ASCE, Vol. 120, No. 1, pp. 225-245, 1994

MARINE SAFETY AGENCY (1993). Marine Safety Agency: Formal Safety Assessment MSC 66/14, submitted by the U.K. to the IMO Maritime Safety Committee, Southampton, U.K., 1993

MARTIN et al. (1975). Martin, G.R.; Finn, W.D.L.; Seed, H.B.: Fundamentals of liquefaction under cyclic loading, Journal of the Geotechnical Engineering Division, ASCE, Vol. 101, No. 5, pp. 423-438, 1975

MARTIN et al. (1978). Martin, G.R.; Finn, W.D.L.; Seed, H.B.: Effects of system compliance on liquefaction tests, Journal of the Geotechnical Engineering Division, ASCE, Vol. 104, No. 4, pp. 463-479, 1978

MARTIN et al. (1980). Martin, G.R.; Lam, I.; Tsai C.-F.: Pore-pressure dissipation during offshore cyclic loading, Journal of the Geotechnical Engineering Division, ASCE, Vol. 106, No. 9, pp. 981-996, 1980

MARTINO and SCARASCIA MUGNOZZA (2005). Martino, S.; Scarascia Mugnozza, G.: The role of the seismic trigger in the Calitri landslide (Italy): historical reconstruction and dynamic analysis, Soil Dynamics and Earthquake Engineering No. 25, pp. 933-950, 2005

MITTENDORF (2006). Mittendorf, K.: Hydromechanical design parameters and design loads for offshore wind energy converters, Institut für Strömungsmechanik und Elektronisches Rechnen im Bauwesen der Leibniz Universität Hannover; Bericht Nr. 71, 2006

MITZLAFF and UECKER (2002). Mitzlaff, A.; Uecker, J.: Gründungsstrukturen für Offshore-Windenergieanlagen, HANSA, Vol. 139, No. 11, pp. 63-70, 2002

NAGO and MAENO (1987). Nago, H.; Maeno, S.: Pore pressure and effective stress in a highly saturated sand bed under water pressure variation on its surface, Natural disaster science, Vol. 9, No. 1, pp. 23-35, 1987

NATARAJA and GILL (1983). Natarajah, M.S.; Gill, H.S.: Ocean wave-induced liquefaction analysis, Journal of Geotechnical Engineering, Vol. 109, No. 4, pp. 573-590, 1983

NGI (1996). Norwegian Geotechnical Institute: Foundation design of caisson breakwaters, Nr. 198, Oslo, 1996

OUMERACI (1994). Oumeraci, H.: Wasserbauliches Versuchswesen II – Modelle im Küsteningenieurwesen, Vorlesungsumdruck für das Vertiefungsfach „Hydromechanik und Küsteningenieurwesen“, Ausgabe Dezember 1994

OUMERACI and KUDELLA (2004). Oumeraci, H.; Kudella, M.: Wave-induced pore pressure in the sandy seabed underneath a caisson breakwater – Experimental results of large-scale model tests, Technical Report LIMAS (Liquefaction around marine structures), Braunschweig, 2004

POULOS (1988). Poulos, H.G.: Marine Geotechnics, Unwin Hyman, London, 1988

QUAST (2003). Quast, P.: Gründungen für Offshore-Windenergieanlagen, 1. EFUC-Konferenz in Suderburg, 2003

RAHMANN et al. (1977). Rahman, M.S.; Seed, H.B.; Booker, J.R.: Pore pressure development under offshore gravity structures, Journal of the Geotechnical Engineering Division, ASCE, Vol. 103, No. 12, pp. 1419-1436, 1977

RAJU (1994). Raju, V.R.: Spontane Verflüssigung lockerer granularer Körper – Phänomene, Ursachen, Vermeidung. Veröffentlichungen des Institutes für Bodenmechanik und Felsmechanik der Universität Fridericiana in Karlsruhe, Heft 134, 1994

REESE et al. (1988). Reese, L.C.; Wrigth, S.G.; Roesset, J.M.; Hayes, L.H.; Dobry, R.; Vallabhan, C.V.G.: Analysis of piles subjected to lateral loading by storm-generated waves, Engineering for calcareous sediments, Eds Jewell & Khorshid, pp. 647-654, 1988

RICHWIEN et al. (2002). Richwien, W.; Lesny, K.; Wiemann, J.: Nachweise und Sicherheitskonzepte für die Gründung von Offshore-Windenergieanlagen in der Deutschen Bucht, 2. Symposium Offshore – Windenergie, Hannover, 2002

SAVIDIS et al. (2004). Savidis, S.; Rackwitz, F.; Richter, T.; Röhner, J.; Schneider, N.: Verhalten von Pfählen in wassergesättigten Sanden unter zyklischen Horizontallasten, Bauingenieur, Band 79, pp. 383-385, 2004

SCHUPPENER (1980). Schuppener, B.: Porenwasserüberdrücke im Sand unter Wellenbelastungen auf Offshore-Bauwerke, Dissertation an der TU Braunschweig, 1980

SCHÜTTRUMPF (1973). Schüttrumpf, R.: Über die Bestimmung von Bemessungswellen für den Seebau am Beispiel der südlichen Nordsee. Mitteilungen des Franzius-Instituts für Wasserbau und Küsteningenieurwesen der Technischen Universität Hannover, Heft 39, 1973

SEED and IDRISS (1970). Seed, H.B.; Idriss, I.M.: Soil moduli and damping factors for dynamic response analysis, Report No. EERC70-10, University of California, Berkeley, 1970

SEED and IDRISS (1982). Seed, H.B.; Idriss, I.M.: On the importance of dissipation effects in evaluating pore pressure changes due to cyclic loading, in Soil mechanics – transient and cyclic loads, Pande, G.N. and Zienkiewicz, O.C. (ed.), John Wiley & Sons Ltd, 1982

SEED et al. (1976). Seed, H.B.; Martin, P.P.; Lysmer, J.: Pore-water pressure changes during soil liquefaction, Journal of the Geotechnical Engineering Division, ASCE, Vol. 102, No. 4, pp. 323-346, 1976

SEED et al. (1978). Seed, H.B.; Pyke, R.M.; Martin, G.R.: Effect of multidirectional shaking on pore pressure development in sands, Journal of the Geotechnical Engineering Division, ASCE, Vol. 104, No. 1, pp. 27-44, 1978

STAHLMANN and KLUGE (2003). Stahlmann, J.; Kluge, K.: Theoretische Überlegungen zur Porenwasserdruckausbildung im Gründungsbereich von Offshore-Pfählen, 5. FZK-Kolloquium 'Seegang, Küstenschutz und Offshorebauwerke' am 08. März 2005 in Hannover, Herausgeber: Forschungszentrum Küste (FZK), ISSN 1610-5249, S. 129-140, 2005

STAHLMANN et al. (2007). Stahlmann, J.; Gattermann, J.; Kluge, K.: FINO 3 – Forschungsansätze für Offshore Windenergieanlagen, Pfahl-Symposium 2007, Fachseminar am 22./23.02.07 in Braunschweig, Mitteilung des Instituts für Grundbau und Bodenmechanik, Technische Universität Braunschweig, Heft 84, S. 207-223, 2007

STREIF (1990). Streif, H.: Das ostfriesische Küstengebiet – Nordsee, Inseln, Watten und Marschen. Sammlung geologischer Führer, Band 57, 2. Auflage, Gebr. Borntraeger, Berlin, 1990

STUDER and ZIEGLER (1986). Studer, J.; Ziegler, A.: Bodendynamik, Grundlagen und Kennziffern, Probleme. Springer-Verlag, Berlin, 1986

SUMER and FREDSØE (2002). Sumer, B.M.; Fredsøe, J.: The mechanics of scour in the marine environment, Advanced series on ocean engineering, Vol. 17, World Scientific, 2002

TAIEBAT (1999). Taiebat, H. A.: Three dimensional liquefaction analysis of offshore foundations, Dissertation University of Sydney, 1999

TAIEBAT and CARTER (2000). Taiebat, H. A.; Carter, J. P: A semi-empirical method for the liquefaction analysis, International journal for numerical and analytical methods in geomechanics, Vol. 24, No. 13, pp. 991-1011, 2000

TERZAGHI (1936). Therzaghi, K.: The shearing resistance of saturated soils. In Proceedings of the First International Conference on Soil Mechanics and Foundation Engineering, Vol. 1, pp. 54.56, 1936

UW (2000). University of Washington, http://www.ce.washington.edu/~liquefaction/html/main.html, Download on April 10th, 2004

VERRUIJT (1982). Verruijt, A: Approximations of cyclic pore pressures caused by sea waves in a poro-elastic half-plane, in Soil mechanics – transient and cyclic loads, Pande, G.N. and Zienkiewicz, O.C. (ed.), John Wiley & Sons Ltd, 1982

VERRUIJT and SONG (1991). Verruijt, A. ; Song, E.X.: Finite element analysis of pore pressure build-up due to cyclic loading, Deformation of soils and displacement of structures, Proceedings of the 10th European Conference on Soil Mechanics and Foundation Engineering, pp. 277-280, 1991

VUCETIC (1994). Vucetic, M.: Cyclic threshold shear strains in soils, Journal of geotechnical engineering, ASCE, Vol. 120, Nr. 12, pp. 2208-2229, 1994

WAGNER (1990). Wagner, P.: Meerestechnik, Ernst & Sohn Verlag, Berlin, 1990

WALZ (1982). Walz, B.: Bodenmechanische Modelltechnik als Mittel zur Bemessung von Grundbauwerken, Bericht Nr. 2 der Forschungs- und Arbeitsberichte aus den Bereichen Grundbau, Bodenmechanik und Unterirdisches Bauen an der Bergischen Universität-GH Wuppertal, S. 45-90, 1982

WIEMANN et al. (2002). Wiemann, J.; Lesny, K.; Richwien, W.: Gründung von Offshore-Windenergieanlagen – Gründungskonzepte und geotechnische Grundlagen, Mitteilungen aus dem Fachgebiet Grundbau und Bodenmechanik, Hrsg.: W. Richwien, Heft 29, Verlag Glückauf GmbH, 2002

WILL (1999). Will, J.: Beitrag zur Standsicherheitsberechnung im geklüfteten Fels in der Kontinuums- und Diskontinuumsmechanik unter Verwendung impliziter und expliziter Berechnungsstrategien, Dissertation Uni Weimar, 1999

ZEN et al. (1998). Zen, K.; Jeng, D.S.; Hsu, J.R.C.; Ohyama, T.: Wave-induced seabed instability: difference between liquefaction and shear failure, Soils and Foundations, Vol. 38, No. 2, pp. 37-47, June 1998

Standards

DIN 1054 (2005-01). Baugrund – Sicherheitsnachweise im Erd- und Grundbau

DIN 18126 (1996-11). Baugrund, Untersuchung von Bodenproben - Bestimmung der Dichte nichtbindiger Böden bei lockerster und dichtester Lagerung